New Photonics Technologies for the Information Age

The Dream of Ubiquitous Services

For a listing of recent titles in the *Artech House Optoelectronics Library*,
turn to the back of this book.

New Photonics Technologies for the Information Age

The Dream of Ubiquitous Services

Shoichi Sudo
Katsunari Okamoto
Editors

Artech House, Inc.
Boston • London
www.artechhouse.com

Library of Congress Cataloging-in-Publication Data

A catalog record of this book is available from the U.S. Library of Congress.

British Library Cataloguing in Publication Data
International Symposium on New Frontiers for Ubiquitous IT Services (2003: Atsugi R&D Center)
New photonics technologies for the information age: the dream of ubiquitous services.—(Artech House optoelectronics library)
1. Photonics—Congresses 2. Ubiquitous computing—Congresses
3. Optical communications—Congresses
I. Title II. Sudo, S. (Shoichi) III. Okamoto, Katsunari, 1949–
621.3'6

ISBN 1-58053-696-4

Cover design by Igor Valdman

Chapter 6 is not subject to copyright in the United States.

International Standard Book Number: 1-58053-696-4

10 9 8 7 6 5 4 3 2 1

A human being is only a reed, the weakest in nature, but he is a thinking reed. To crush him, the whole universe does not have to arm itself. A mist, a drop of water, is enough to kill him. But if the universe were to crush the reed, the man would be nobler than his killer, since he knows that he is dying, and that the universe has the advantage over him. The universe knows nothing about this.

All our dignity consists therefore of thought. It is from there that we must be lifted up and not from space and time, which we could never fill.

So let us work on thinking well. That is the principle of morality.
—Blaise Pascal, *Pensées*

None is of freedom or of life deserving
Unless he daily conquers it anew.
—Johann Wolfgang von Goethe, *Faust*

Contents

Preface

History has seen the development of many important types of technology, including ships, trains, cars, electricity, and telecommunications. Ubiquitous information technology (IT) services should eventually join this group but at present they seem to be just a dream for the future. *Webster's Dictionary* defines ubiquitous as "being or existing everywhere at the same time," and so ubiquitous IT services appear to indicate a kind of dream world where we possess abilities that are beyond time and space.

If we are to realize such super abilities, ubiquitous IT services will require a number of very specific tools, for example, photonic, electrical, and micromechatronic tools, various sensing tools, and a new communication tool.

At the same time, we believe that a substantial change is taking place in IT services, namely, from a small "i" and a large "T" to a large "I" and a small "t," as shown in Figure P.1. This represents an expansion of human abilities and a customer-centered structure. We are confident that ubiquitous IT services correspond precisely to this change in IT services, because they are not only network services but also "I-centered" or "human-centered" services designed to promote individual empowerment. Ubiquitous IT services are just beginning to emerge and the time is coming when we will launch a new IT age that can provide such services. We will then be able to utilize IT services everywhere simultaneously whenever we so desire.

The International Symposium on New Frontiers for Ubiquitous IT Services introduced many excellent technologies in fields including photonics, electronics, micromechatronics, sensing, new networks, and new communication schemes, with the goal of realizing such ubiquitous IT services for the future.

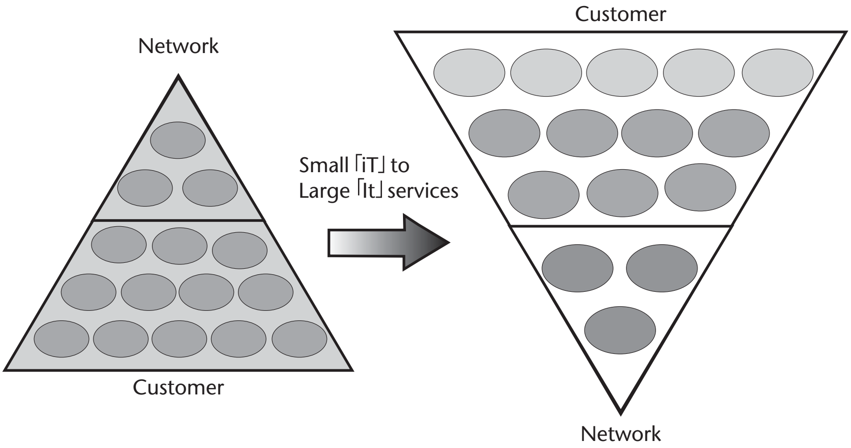

Figure P.1 What is happening to IT services now?

This international symposium was realized through the help of many people. We express our sincere thanks to Nippon Telegraph and Telephone (NTT) Corporation and its executives, all of whom offered their support, with special thanks to Dr. Yoh'ichi Tohkura, former executive manager of the NTT Science and Core Technology Laboratory Group. We also offer our gratitude to Dr. T. Nagatsuma, Dr. M. Kitamura, Dr. Y. Sato, Dr. T. Haga, Dr. J. Kobayashi, Ms. M. Sasaki, and Ms. K. Yamazaki for their enthusiastic work in helping to organize this symposium and realize this book. Moreover, we express our deep appreciation to Mr. Mark Walsh and Mrs. Christine Daniele of Artech House for their quick decision-making, critical comments, and encouragement with respect to the development and publication of this book.

Shoichi Sudo,
Kanagawa, Japan
Katsunari Okamoto,
Ibaraki, Japan
September 2004

CHAPTER 1

The Dream of Ubiquitous IT Services

Shoichi Sudo
NTT Microsystem Integration Laboratories

Introduction

A worldwide revolution has taken place in the field of information technology. This has been brought about largely through the arrival of three great technologies. The first of these is optical technology, which includes wavelength division multiplexing (WDM) transmission systems capable of very large transmission capacities. The second is wireless technology, in particular low-power wireless transmission technology and codec (coder/decoder) technology. The third is Internet technology, which includes the Transmission Control Protocol/Internet Protocol (TCP/IP) and various kinds of software. Of course, these technologies have been realized based on the rapid and stable growth of very large scale integration (VLSI) technology.

The merger of these technologies has led to a new age in which the ability to communicate and handle information is directly related to human activities and well being. This “Information Age” is now clearly upon us. For example, optical fiber communication has had a dramatic impact on the ability to transmit information, and wireless communication has enabled us to realize very convenient access between locations. In addition, the Internet provides us with a reliable communication scheme even if the network is slightly unstable. Consequently these great technologies have the potential to offer us ubiquitous IT services. The time is coming when we will launch a new age in which ubiquitous information technology and services will be available to all. At present, this may appear to be a kind of dream world where we possess abilities that are beyond time and space. However, this is just the beginning; we are approaching the dawn of the new information age.

Scope of This Book

We have collected together the stimulating papers that were presented at the International Symposium on New Frontiers for Ubiquitous IT Services held at NTT’s Atsugi R&D Center from May 27–28, 2003. A number of eminent speakers came all the way from the United States and Europe, and also from within Japan to contribute to this symposium’s success. Those who attended enjoyed some excellent presentations and discussions regarding this pioneering technology whose goal is to usher in a new age of ubiquitous IT services.

The topics covered by the meeting and this book include:

- The renaissance of physics and technology for ubiquitous IT services;
- New photonics, electronics, and micromechatronics applications for biology and ubiquitous medical sensing;
- New communication schemes for ubiquitous IT services.

The Dream of Ubiquitous IT Services

The dream of ubiquitous services may appear to be an ambitious and perhaps slightly fantastic title, but it is based on the premise that we are about to enter a new age of information technology. First, we must ask ourselves the questions: What is science? and What is technology? to clarify the foundations on which this new age will be built. Science is a branch of pure learning. Its aim is intellectual satisfaction, the clarification of unknown fields, and the discovery of new aspects of nature and human society. Technology focuses more directly on practical applications that are useful to mankind.

One important way of meeting that requirement could be provided by ubiquitous IT services. Throughout history we have developed many important types of technology including ships, trains, cars, electricity, and telecommunications, and ubiquitous IT services could be next in this line. *Webster's Dictionary* defines "ubiquitous" as "being or existing everywhere at the same time." This seems to transport us into a kind of dream, since ubiquitous IT services should be able to provide us with superhuman abilities. "Ubiquitous" suggests abilities that are beyond time and space and perhaps makes us think of that great childhood hero, Superman, and his ability to travel beyond time and space.

However, Superman needs very specific tools to provide him with his superpowers. He needs, for example, photonic, electrical, and micromechatronic tools, various sensing tools, and a new communication tool. These tools have very specific properties. For example, the photonic toolrequires an extremely pure light with an ultranarrow spectrum and a very wide frequency tuning range.

In scientific terms, quantum mechanics itself is ubiquitous. Those involved in developing and improving quantum mechanics are indicating that the wave function exists everywhere simultaneously, in the same way as a ubiquitous state. The Einstein, Podolsky, and Roden (EPR) paradox [1] and Bell's theorem are notable for indicating an implied mechanism in quantum mechanics and nature's characteristics [2, 3]. A renowned physicist, David Bohm, wrote books entitled *Wholeness and the Implicate Order* [4] and *The Undivided Universe* [5], and J. S. Bell wrote a book entitled *Speakable and Unspeakable in Quantum Mechanics* [6]. Their works suggest that nature itself is a ubiquitous state at a deep level. However, the main goal of our meeting and this book is not scientific discussion, it is to present and discuss new frontiers for ubiquitous IT services, and this brings us back to information technology.

Currently, IT services are undergoing a great change, focusing less on the "T" and more on the "I." This represents the expansion of human abilities and a customer-centered structure.

Ubiquitous IT consists of “I-centered” technologies and services. In part, this means the expansion of human power and abilities, sometimes called human empowerment. It also means a content revolution, and achieve this we need many basic technologies. Eventually we will be able to develop this power beyond time and space.

Ubiquitous IT services are just beginning. The time is coming when we will launch a new information technology age in which such services are available. Then we will be able to utilize IT services everywhere at the same time whenever we need them.

Moreover, ubiquitous IT services are not only network services but also I-centered or human-centered services designed to promote individual empowerment. One of the keys to ubiquitous IT services is that “anyone, anything, anywhere” and “only for you, only for us” services should be realized, because they are of particular importance. That is, they are I-centered or human-centered services that satisfy the requirements of both convenience and privacy.

As shown in Figure 1.1, we will need many excellent technologies to realize such ubiquitous IT services, including those in the fields of photonics, electronics, micromechatronics, sensing, new networks, and new communication schemes. These technologies should in turn lead to other developments such as the ad hoc network of wireless technology in which individuals, sensors, and cellular phones communicate directly without the need for a backbone network. We eagerly await the arrival of such new technologies for ubiquitous services.

We hope this book will give readers the chance to take a look at the cutting edge technology that will be used to realize ubiquitous IT services. Of course, ubiquitous

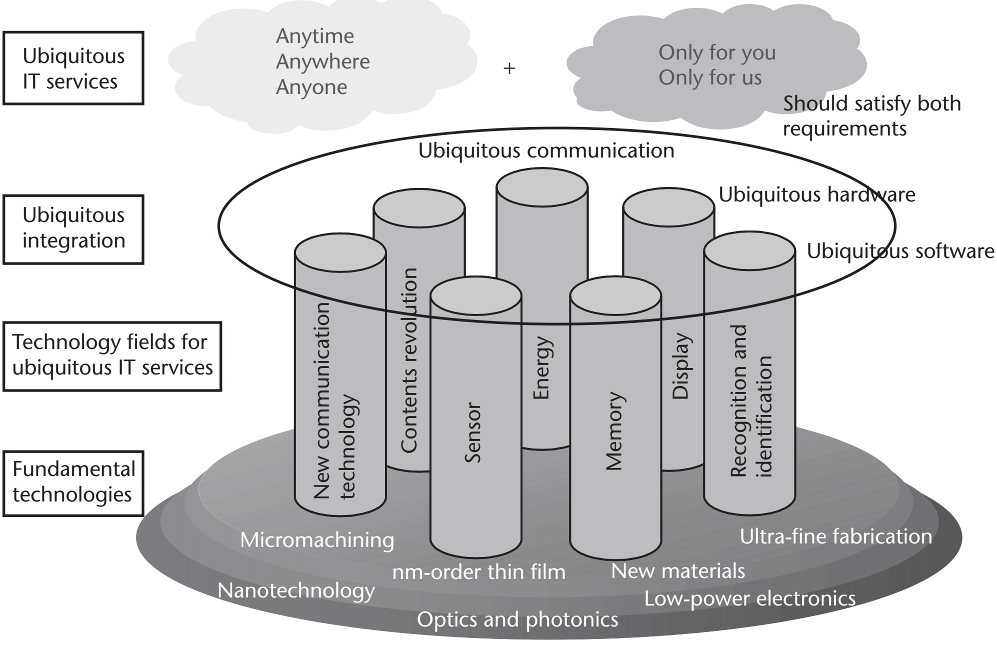

Figure 1.1 Key technologies for ubiquitous IT services.

IT services require development over a much wider technical spectrum than described in this book. They cover fields including software technology, security, and network architecture that are beyond the scope of our symposium and this book. Nevertheless, we sincerely hope that this book will be the trigger for other international symposia and discussions that will lead ultimately to ubiquitous IT services that will benefit us all.

References

[1] Einstein, A., B. Podolsky, and N. Rosen, “Can Quantum-Mechanics Description of Reality Be Considered Complete?” *Phys. Rev.*, Vol. 47, 1935, pp. 777–780.

[2] Bell, J. S., “On the Impossible Pilot Wave,” *Found. Phys.*, Vol. 12, 1982, pp. 989–999.

[3] Bell, J. S., “Against Measurement,” *Phys. World*, Vol. 3, 1990, pp. 33–40.

[4] Bohm, D., *Wholeness and the Implicate Order*, New York: Routledge, 1992.

[5] Bohm, D., and B. J. Hiley, *The Undivided Universe: An Ontological Interpretation of Quantum Theory*, New York: Routledge, 1993.

[6] Bell, J. S., *Speakable and Unspeakable in Quantum Mechanics*, Cambridge, England: Cambridge University Press, 1993.

CHAPTER 2

New Frontiers of Discovery and Innovation

Robert L. Byer
Stanford University
Stanford, California

Introduction

Although I am not an expert on IT, I appreciate the dream of ubiquitous IT services. To achieve this dream we begin with technical achievements, innovation and invention. These technical achievements are often motivated by audacious goals that place the dream into a context and points to the future that extends beyond technology to include global political and economic systems.

Since we are technologists, I will start on familiar turf and discuss the process of discovery and innovation. I use as examples the outcomes of research in progress during the year Dr. Sudo spent at Ginzton Laboratory as a visiting scientist. Through a series of evolutionary steps, his early work led to developments that ranged from quasi-phase-matched nonlinear interactions to laser remote sensing and to the ultimate in precision measurements, the goal of detecting and observing gravitational waves generated at the beginning of time and space.

At the next level we must motivate a community to adopt a new idea or a new approach by sharing a vision of the future. We must understand the context in which we plan, develop, and commercialize technology. In this chapter, I refer to Silicon Valley as a successful economic model for the development of technology for commercial applications, and discuss the way in which Silicon Valley has gone global and the role it might play in NTT's dream of ubiquitous IT services. I then explore the role that Stanford University has played in the success of Silicon Valley. I close with a brief discussion of technology adoption and the time frames for achieving widespread application and significant impact on society.

I would first like to say something about Dr. Sudo of NTT. He arrived at Stanford in 1987. I had met him a year earlier when I visited his laboratory at NTT. During that visit he shared his dream regarding the next generation of optical fibers for telecommunications. Subsequently, he came to Stanford for a year to study in our group with a view to understanding some of the science and technologies that we were studying in our laser research programs.

In 1987, Dr. Sudo presented me with a book that he coauthored with Dr. Izawa [1]. At that time we were both thinking about the important research ideas that lay ahead of us. That book was based upon a breakthrough in technology—the optical fiber—that when properly engineered, transmits lightwaves over extraordinarily long distances and conducts information at an unprecedented rate. This is a fundamental technology breakthrough that happens perhaps once every 25 to 50 years. Using this breakthrough as a foundation, technologists have built the fiber optic communication networks that are the basis for what might be called ubiquitous IT technology.

Inventions, Inventors, Patents, and Copyrights

Each year I present a lecture to graduate students at Stanford entitled "Invention, Inventors, Patents, and Copyrights." The aim of the lecture is to suggest ways of realizing an invention, and to show how the invention can be developed and serve the community in an important way. Asking the right question motivates the process of invention. The problem to be solved must be understood in an overall context. A far-seeing inventor recognizes that the application of current technology is at an end and a new approach is needed.

I pose the following questions to the students in my lecture. First, What is an invention? An invention involves fundamental ideas, perhaps a novel combination of ideas. Next, How does one approach making an invention? Most students do not ask themselves this question. One part of the answer relates to the big picture. Can you imagine a future where your invention will be critical? Another part of the answer relates to understanding the problem that for which a solution is sought. This enables the inventor to ask the critical question that may lead to a discovery. However, realizing an invention may still require considerable persistence. Hugh Aitken said, "What is new about the invention is the novelty of the combination—the way the elements are put together." He wrote this in his history of radio called *The Continuous Wave*. One hundred and twenty years ago the radio had just been invented and the words coherence, heterodyne, and superheterodyne were coined. The discovery, development, and the universal acceptance of the radio are an apt illustration of invention, technology development, and adoption to widespread use with an impact on society.

In 1986, a patent was issued to coinventors in my research group and Professor Martin Fejer [2]. The patent was for an invention related to the growth of single-crystal optical fibers; fibers that might be used to generate, amplify, and transmit light. When Dr. Sudo visited the Ginzton Laboratory we were investigating laser heated pedestal growth to prepare single-crystal fibers of the nonlinear crystal lithium niobate. To do this we employed a carbon dioxide laser to provide a small molten zone from which we grew a single-crystal fiber. These oriented single-crystal fibers could be submillimeter in diameter. At the time our goal was to create nonlinear optical fibers that could act as guided wave structures and thus realize more efficient nonlinear frequency conversion.

Dr. Sudo selected an area of study based on the notion that if we are going to fabricate guided wave single-crystal fibers, we must invent a cladding for the fibers to realize the propagation of light at low loss. His work led to a coinvention, with Stanford faculty members and students, of claddings for single-crystal optical fibers [3].

Unfortunately, but not unlikely in retrospect, this patent has had no commercial value. Perhaps only one patent in fifty leads to commercial success. However, this patent prepared the groundwork for a subsequent patent that was issued a couple of years later for a guided wave optical fiber amplifier. Professor Shaw and Michel Digonnet are the inventors of a patent for the WDM pumped guided wave optical fiber amplifier. That patent has proved to be of considerable value to Stanford University.

Professor N. Bloembergen, a Nobel laureate, founded the field of nonlinear optics in 1962. In 1968 he was granted a patent for a basic idea entitled “Apparatus for Converting Light Energy from One Frequency to Another” [4]. This patent describes the idea of phasematching by periodically varying the sign of the nonlinear coefficient, now referred to as quasi-phasematching (QPM). However, by the time quasi-phasematching was realized experimentally in the laboratory, Bloembergen’s fundamental patent had expired. As often happens, his patent was too early.

It was Professor Fejer who realized that the lithium niobate crystal fibers grew with a fixed orientation of their ferroelectric polarization domain. He suggested that by modulating the temperature or the growth rate we might be able to grow periodically reversed ferroelectric domains and thus realize quasi-phasematching for efficient nonlinear frequency conversion. One of the early structures that we prepared by modulated growth was a periodically poled lithium niobate single-crystal fiber with a 4-μm domain period. That fiber was used to generate blue radiation by second harmonic generation [5].

If quasi-phasematched nonlinear materials can be fabricated in quantity and low cost then there are potential applications to ubiquitous IT for signal processing. Single-crystal fibers are no longer used for frequency conversion, but the research opened new approaches and led to quasi-phasematched devices based on low-cost wafer scale processing using well-developed lithographic tools. Today we routinely prepare wafers of periodically poled lithium niobate from which we fabricate nonlinear chips. Based on the rapid progress at the time, I made a prediction in 1993 that by the end of the decade quasi-phasematched nonlinear optical devices would be in widespread use. I was wrong. It did not happen that quickly. The best we can do is to prepare the way for a new technology and be persistent in moving toward applications.

Big Audacious Goals

Remote air pollution sensing motivated our early work on tunable lasers [6]. We used flash lamp pumped Nd:YAG lasers to pump 1.4- to 4.3-μm tunable parametric oscillators and were successful in detecting atmospheric CO_2, SO_2, carbon monoxide, methane, water vapor, and temperature. An outcome of our early work was to ask the question: What is the most important remote sensing experiment that we can envision? We elected to take a global view.

After considerable discussion, we decided that the most important measurement, over the long term, was global wind sensing. If we could make a laser transmitter with less than 1-MHz linewidth, 10% electrical efficiency, and 100W of average power, and fly it on a satellite at 400 km, we could perform global wind sensing. The capability would have a major impact on what we know about the Earth's atmosphere as a whole. This is an example of a big, audacious, and far-reaching goal.

Another example of an audacious goal in fundamental science is the detection of gravitational waves. We have joined with scientists at the Laser Interferometer Gravitational Wave Observatory (LIGO), and the Laser Interferometer Space Antenna (LISA) to develop precision laser interferometers capable of detecting gravitational waves. I discuss the progress toward the detection of gravitational waves below.

Another audacious goal that fits comfortably on this list is the realization of ubiquitous IT services on a global scale.

Global Wind Sensing

Our goal for the past 20 years has been to invent, demonstrate, and fabricate a laser source that would meet the global wind sensing requirements and that could be launched into orbit around the earth. The laser transmitter and telescope receiver would use coherent laser radar, to sense the direction of the wind above the surface of the earth as first proposed by Milton Huffaker in 1978 [7]. This was an extremely difficult technical challenge when we began the research effort in 1980.

The challenge prompted ideas and new approaches to solid-state lasers. Motivated by remote wind sensing, we undertook the first experimental steps to investigate a diode-pumped solid-state laser in 1984 to meet the efficiency, operational reliability, and linewidth requirements for a space-based laser transmitter [8]. For our very first experiment we borrowed a laser diode from Toshiba Corporation. We focused this diode into a small crystal of Nd:YAG and we realized an output power of 2 mW. Figure 2.1 shows the components of that first laser diode-pumped Nd:YAG laser [8]. The penny in the background represents the relative cost of fundamental research in a university laboratory.

Figure 2.1 Photograph of the three elements of the first laser diode-pumped Nd:YAG laser constructed at Stanford. The laser operated with 2 mW of output power at 25% slope efficiency. (*After:* [8].)

Big, audacious goals such as global wind sensing using coherent laser radar reminds me of a quote from Edwin Land, the founder and president of Polaroid Corporation. He said, “Don’t undertake a project unless it’s manifestly important and nearly impossible.” We must challenge ourselves to think about problems that seem nearly impossible but are very important to solve.

Our first step on the road to accomplishing global remote sensing was to undertake a ground-based coherent laser radar experiment. For that we needed three elements: Invent a local oscillator with a narrow linewidth, invent a power amplifier, and find a way of realizing a heterodyne receiver. The combination of these three elements would allow us to take the first step toward global remote sensing. The first thing to emerge from our consideration of the coherent laser radar problem was the invention of a device called a monolithic isolated ring resonator [9]. We now call the device a single-frequency nonplanar ring oscillator or NPRO. The Nd:YAG NPRO is the master oscillator for the laser transmitter. It has become the master oscillator for the gravitational wave detectors described below.

Figure 2.2 is a photograph of an Nd:YAG NPRO crystal. The size scale is set by a 1-cm diameter American dime. The NPRO laser devices became commercially available in 1986 and have been on the market since that time. We used a zigzag slab Nd:YAG crystal gain medium as the power amplifier. In addition, we used optical fiber for our heterodyne receiver and mixer. This was one of the earliest applications of optical fiber in a coherent detection system. It is worth noting that the elements

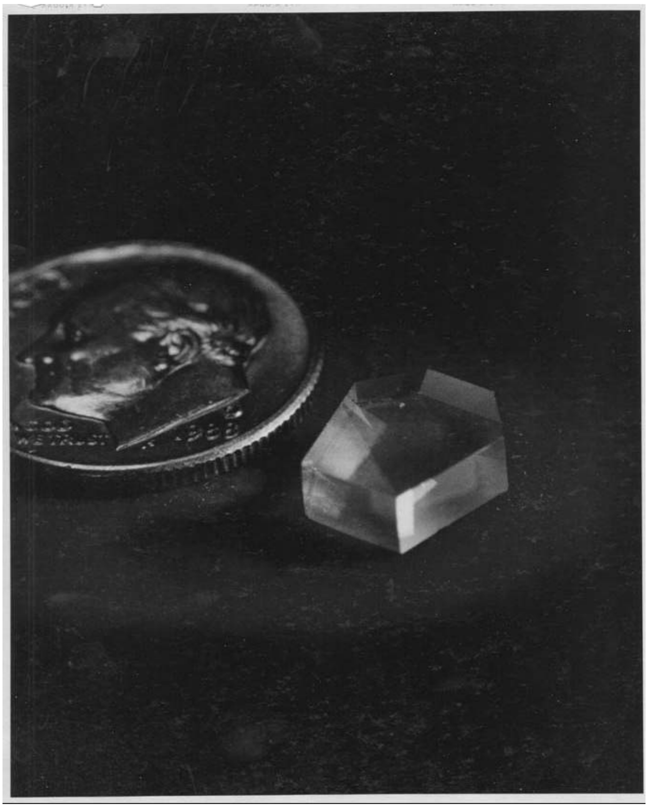

Figure 2.2 Photograph of the monolithic nonplanar Nd:YAG ring laser, NPRO, that operates in a single frequency with a linewidth less than 10 kHz. (*After:* [9].)

required for coherent laser radar are the same elements needed for coherent optical communication. With these components we successfully demonstrated wind sensing using a ground-based Nd:YAG transmitter [10].

Another outcome of my random walk through research came from a meeting with Art Schawlow (professor of physics at Stanford) in 1979. Dr. Schawlow told me, “Someday a solid state laser will provide the narrowest linewidth of any laser source.” I made a note of his comment so I would remember it.

A few years later, in 1992, Dr. Ady Arie, a postdoctoral scholar from Israel, realized that if we used a frequency-doubled, single-frequency Nd:YAG NPRO oscillator, we could frequency stabilize the laser on the Doppler-free hyperfine lines of molecular iodine. We were successful in frequency stabilization of an Nd:YAG NPRO laser to a part in 10^{13} [11]. For example, the frequency stabilized Nd:YAG laser demonstrated an absolute frequency stability of better than 15 kHz. This result would become important for gravitational wave detection.

Subsequently, Dr. Sudo applied this approach to frequency lock the telecommunication frequency band laser diodes to an absolute frequency reference based on molecular acetylene gas to meet telecommunication frequency stabilization requirements.

LIGO, LISA, and Gravitational Waves

We then turned to the next big, audacious idea, namely finding a way to detect gravitational waves. Peter Bender is an astrophysicist who loves to think about black holes and the fact that black holes can radiate gravitational waves. In 1988, Dr. Bender introduced me to the proposed LISA project designed to observe gravitational waves emitted by massive black holes that exist at the core of virtually every galaxy in the universe.

Figure 2.3 shows an early sketch of the LISA concept posted on Dr. Bender’s laboratory wall with my added notes about the requirements. The proposed plan was to build and fly three satellites in orbit about the sun and trailing earth. The three satellites would fly in formation in the form of a triangle with subwavelength precision and with a 5-million-km separation. A single-frequency, 1-W, Nd:YAG laser would be used to illuminate the interferometer to probe for gravitational waves, particularly waves emitted at very low frequencies from 0.1 to 100 MHz by binary massive black holes.

Dr. Bender asked me if I could provide him with a 1-W, single-frequency laser by 1998 when it was expected that the proposed LISA mission would be launched. The mission was not launched in 1998 but it is due to be launched approximately one decade from now. Nevertheless, we demonstrated for Peter Bender a precisely frequency stabilized laser that met the requirements for the LISA mission. A description of the LISA mission is available at the LISA Web site [12].

In addition to the space-based antenna, we joined the LIGO project in 1992. LIGO is a ground-based gravitational wave interferometer with sensitivity in the 10- to 1000-Hz frequency region. The LIGO 4-km length interferometers are located at two sites in the United States: one in the desert in Hanford, Washington, and the other in the swamps in Livingston, Louisiana.

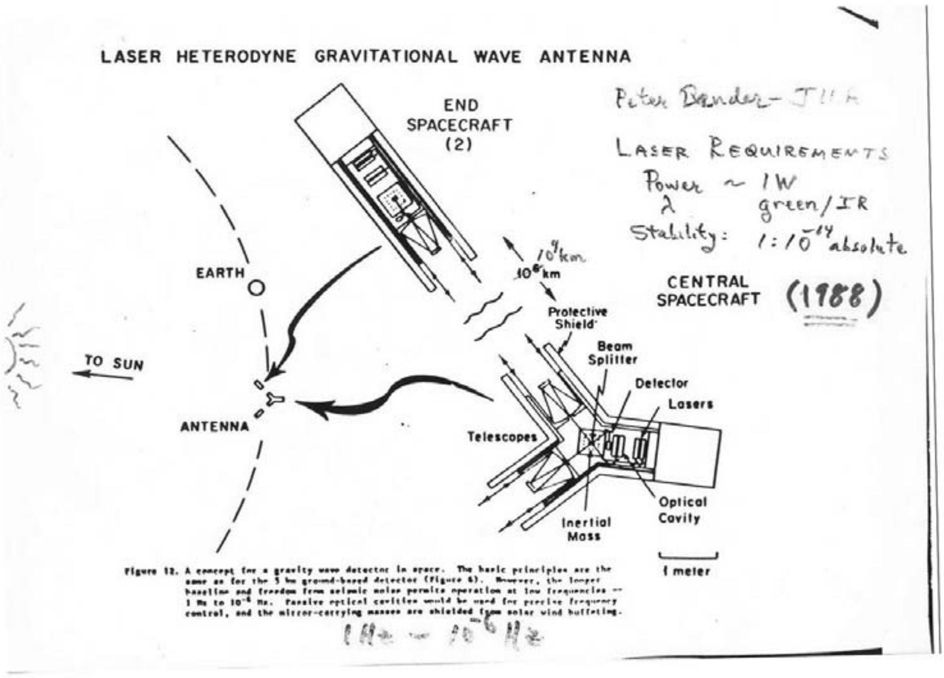

Figure 2.3 Diagram of the LISA project as sketched in 1988. (Courtesy of Peter Bender, JILA, University of Colorado, Boulder, Colorado.)

Figure 2.4 shows a photograph of the two LIGO sites from the air. The LIGO project has been underway for about one decade and represents an investment of about \$360 million for construction of the two 4-km long Michelson interferometers at the two sites. LIGO is now conducting its third science run. The description and progress of the LIGO project is available at the LIGO Web site [13].

The LIGO interferometer is illuminated by a single frequency Nd:YAG laser that is mode matched into the 4-km-length Michelson interferometer with Fabry-Perot interferometers in each arm. Optical mirrors are suspended at each end of the inteferometer to act as test masses for incident gravitational waves. The interferometer is capable of measuring a relative displacement distance between the two arms of the interferometer to one part in 10^{21}. One part in 10^{21} is equivalent to dividing a 1-μm optical wavelength by a part per billion relative to 4 km. For scale, it corresponds to measuring the diameter of an atom on the surface of the earth from the distance of the sun. Gravitational waves are very weak and their measurement is extremely challenging.

At Stanford we undertook the research challenge to design the Nd:YAG laser system to be used in LIGO. The Stanford research program showed that a single-frequency Nd:YAG NPRO oscillator followed by an amplifier would offer the best approach to a reliable, power-scalable laser for LIGO. A commercial laser company engineered the final laser system to meet the performance and long-term reliable operation requirements for LIGO. The engineered 8-W TEMoo mode Nd:YAG NPRO master oscillator, power amplifier (MOPA) lasers were installed at the LIGO site 5 years ago and have met all of the LIGO requirements since that time.

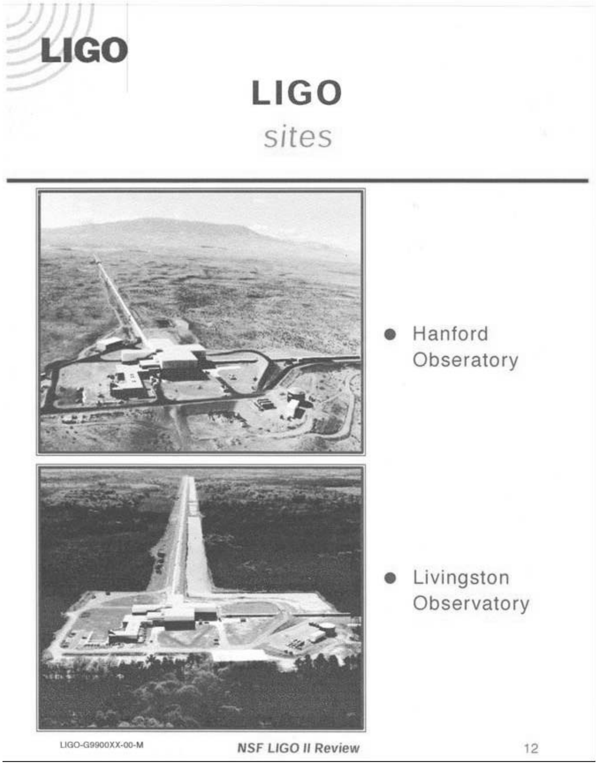

LIGO

LIGO
sites

- Hanford
Obseratory

- Livingston
Observatory

LIGO-G9900XX-00-M NSF LIGO II Review 12

Figure 2.4 Photograph of the two LIGO interferometers. One interferometer is located in Hanford, Washington; the other is in Livingston, Louisiana. The interferometers operate in coincidence to reduce noise during the search for gravitational waves.

The laser is but one subsystem of an advanced LIGO interferometer that is being developed to improve the detection sensitivity of LIGO by an order of magnitude. Advanced LIGO requires an upgrade in laser power from 8 to 200W while maintaining the single-frequency, diffraction-limited operation. This challenge has forced us to think about new approaches to laser design that would allow power scaling while maintaining quantum limited noise performance with diffraction limited beam quality. Asking the right question led to the concept of the edge-pumped slab laser [14].

Figure 2.5 is a photograph of an edge-pumped Nd:YAG slab laser that has operated with more than 100W of output power at 42% optical-to-optical efficiency. The edge-pumped slab laser has the potential for average power scaling to greater than 100 kW [15]. It is ironic that a project with fundamental science as its goal has led to a laser concept that allows power scaling of solid-state lasers to unprecedented levels.

The gravitational wave detection event rates scale as the probed volume of the universe or as third power of sensitivity improvement. Thus we expect that advanced LIGO, when operational late in this decade, will have a thousandfold increase in event rate and therefore a high probability of observing gravitational waves. The big, audacious goal is to detect gravitational waves that are radiated by binary neutron stars, neutron star black hole binary systems, and black hole black hole binary systems to learn more about our universe. Gravitational waves will pro-

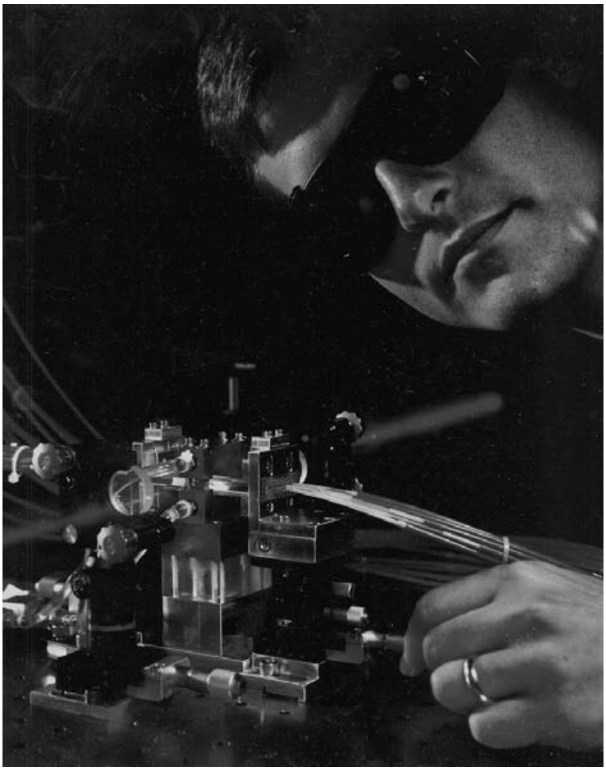

Figure 2.5 Photograph of the edge-pumped conduction cooled Nd:YAG slab laser. (*After:* [15].)

vide a new window on the universe that could allow observations back to 10^{-30} seconds after the big bang, very close to the beginning of time and space.

The Big Picture: Silicon Valley Goes Global

I now move from my random walk through discovery and research to a different level and explore the environment in which inventions make the transition to commercial products that may have an impact on society. To illustrate the process by which technology finds it way into widespread use, I will focus on Silicon Valley as an example of a technology-driven, regional economy. I explore the role that Stanford University has played in the success of Silicon Valley and consider the question of whether the Silicon Valley concept can be adapted and adopted to other economic regions around the world.

When Dr. Sudo visited Stanford, he was working day to day on technology in Ginzton Laboratory. However, he was concerned about larger issues. One day he said he wanted to speak with me and ask some questions about Stanford. His first question was, "What is the spirit of Stanford?" This is not a technical question but a question about an institution and its place in northern California. We discussed his question for some time. I think he remembered the some of the points brought up in that discussion. One was that Stanford was built on a model of doing fewer things but doing them very well. We call this model steeples of excellence, a term coined by

Fred Terman, former dean of engineering and provost of Stanford. The other point was that we should focus on our mission as a private research university. Our product, in the language of business, is educated students. Since Stanford is located in a region that includes Silicon Valley, the development of the Valley has had an impact on the university. Silicon Valley was an outgrowth of a new approach to business created by David Packard and Bill Hewlett, the founders of Hewlett-Packard. The Hewlett-Packard Company was very innovative in the early days, not only in technology but also in a business model often referred to as the "HP way."

What did Hewlett-Packard contribute to the region that makes Silicon Valley special? One example of the impact of Hewlett-Packard is the extraordinary mission statement prepared by the company on behalf of Stanford University. It says, "Hewlett-Packard is committed to enhancing and supporting the mutual and strategic interests of Stanford and HP." The company states its interest in supporting the university, which is quite extraordinary: "Building new partnerships on the bases of our traditional relations with Stanford students, faculty and administration we expect to continue and expand efforts to increase Stanford's position as a premier educational research institution in keeping with Stanford's strategic goals." The company is concerned about contributing to the well being of the local community. The HP business model is one reason why Silicon Valley evolved so successfully. Hewlett-Packard has been called "The DNA of Silicon Valley."

A second issue that Dr. Sudo and I discussed was what Stanford contributed to Silicon Valley. In my talks about Stanford and Silicon Valley, it is often assumed that Stanford's principle contribution is technology. I was asked this question at a meeting of the Sendai Cosmos Club in 1994. I explained that Stanford contributes a small amount of technology to Silicon Valley. A young woman in the audience in Sendai, a student of technology transfer, expressed some doubt about my statement. I replied that we had studied the question in great detail and that only one company out of twenty uses Stanford technology either directly or indirectly. Educated students are Stanford's principle contribution to the success of Silicon Valley.

What are the factors for success in Silicon Valley? The list is not long but each factor is important. One is entrepreneurial attitude; that is, the expectation that individuals will go out and start something new. Another is land resources to allow for growth. High on the list are educated people and the institutions of learning from two-year college to major research universities. It is also important to have venture capital funds and individuals who are willing to risk capital, now referred to as "angel" investors. Investment capital is usually in short supply but it enables new companies to be started. We also had legal help in the region, which is essential for organizing and managing a company. A very important factor is a community that encourages risk and allows for failure. In Silicon Valley, if the company you have started fails, people will sympathize and then ask when you plan to start your next company. We have government investment in the technology of the region in the form of federal research laboratories such a Lawrence Berkeley Laboratory, Lawrence Livermore Laboratory, and the Stanford Linear Accelerator Center (SLAC). We also have the advantage of a diverse and mobile workforce. In the world today, a diverse workforce with representation from all corners of the globe is essential for success.

A few years ago I had the opportunity to join in a conversation with the science minister of New Zealand. We were having lunch with a group of entrepreneurs and businessmen from companies representing Silicon Valley. At the end of the lunch I asked the minister, “If you had Silicon Valley in New Zealand could you celebrate it as a success?” After thinking about it for a while, his answer was “No.” He said that in New Zealand the attitude would be that if your company was successful then you must have taken something from somebody else. He said that New Zealanders would have a hard time celebrating success. In Silicon Valley we celebrate success. When people do things that are interesting and successful the whole valley celebrates. This is a very interesting and important factor with regard to Silicon Valley.

The next question to ask is: Does the Silicon Valley economic model transfer to the rest of the world? A decade ago the answer was unclear but today we know that the answer is yes. We now have many examples of global economic hot spots. Silicon Valley has been reinvented in places as diverse as Tel Aviv, Taipei, Munich, Tokyo, Kyoto, Singapore, and Helsinki. There are many places that have adopted and adapted the economic model of Silicon Valley. They are using the model to grow regional economies successfully. One good example is Munich. Today, Munich has its own form of technological development with a major emphasis on medicine and medical applications as well as lasers and biotechnology. It was not clear a decade ago whether this kind of entrepreneurial development was possible in Japan. Masahiko Aoki, Professor of Economics both at Stanford and Kyoto University, said, “Real change must and can occur in business organizations. The role of government is to facilitate this change.” Several years ago, Professor Aoki offered several reasons why Japan was lagging behind. I believe that the younger generation will make changes that will lead to the creation of new business opportunities in this country. In Japan the younger generation has an entrepreneurial spirit and a global outlook about business opportunities. Perhaps Japan’s high-tech hope is in the region of Nara and Kyoto, where a new type of Silicon Valley is taking hold. NTT has a presence there.

Technology Adoption

At this symposium we discussed a big, audacious goal to change society in a very significant way through ubiquitous IT. We must be prepared for a long process of adoption because it will not be realized overnight. On July 7, 1997, Forbes business magazine published a figure that plotted the percentage penetration into the marketplace of a new technology relative to the number of years following the fundamental discovery. The graph showed that automobiles took 100 years before they penetrated 80% of the market in the United States, Europe, and elsewhere. Airplanes took 90 years and electricity took 80 years before they reached full penetration. These are infrastructure changes that fundamentally affect the way in which we live. Such changes take a century to be fully adopted. This means that if we are to dream about changes that alter the fundamental way in which we live we have to plan for change over times measured in the units of a century.

There is another kind of technology that is introduced much more quickly. Examples include the radio, television, and personal computers. These technologies took only about 30 years to find their way into widespread use. These technologies build on an existing infrastructure and so can be adopted more quickly. Therefore, if we take advantage of a technology that builds on an existing infrastructure we can achieve 80% penetration in about 30 years or the professional lifetime of an engineer at NTT.

There are examples of technologies that can be adopted even more quickly because they not really new technologies but combinations of existing technologies. For example, the cell phone is a combination of a personal radio transmitter and radio receiver. The public often adopts new combinations of existing technologies to create new capabilities in a relatively short time, for example, 10 to 15 years.

Concluding Remarks

We are fortunate to live in a world not imagined 30 years ago when I began my career at Stanford. It is now a world in which I can board an aircraft and be in Japan the next day, participate in the symposium, and have a conversation with friends from the other side of Earth. If technology is to fuel our growth and our well-being in the future, then universities and industry—in collaboration with government—must work together to overcome the barriers to adopting these new technologies and to facilitating change.

References

[1] Izawa, T., and S. Sudo, *Optical Fibers: Materials and Fabrication,* Tokyo, Japan: KTK Scientific Publishers, 1987.

[2] Byer, R. L., and M. M. Fejer, “Apparatus for Growing Crystal Fibers,” U.S. patent 4,421,721, issued December 20, 1983; J. L. Nightengale, M. M. Fejer, R. L. Byer, “Apparatus for Translating Crystal Fibers,” U.S. patent 4,607,776, issued August 26, 1986.

[3] Byer, R. L., et al., “Claddings for Single Crystal Optical Fibers and Devices and Apparatus for Making Such Claddings,” U.S. patent 5,037,181 issued August 6, 1991; also “Method of Cladding Single Crystal Optical Fiber,” U.S. patent 5,077,087, issued December 31, 1991.

[4] Bloembergen, N., “Apparatus for Converting Light Energy from One Frequency to Another,” U.S. patent 3,384,433, issued May 31, 1968.

[5] Magel, G. A., M. M. Fejer, and R. L Byer, “Quasi-Phasematched Second Harmonic Generation of Blue Light in Periodically Poled LiNbO3,” *Appl. Phys. Lett.,* Vol. 56, January 1990, pp. 108–110.

[6] Byer, R. L., “Nonlinear Optics and Solid State Lasers: 2000” (invited paper), *IEEE J. Selected Topics Quantum Electronics,* Vol. 6, November/December 2000, pp. 911–930.

[7] Huffaker, R. M., (ed.), “Feasibility Study of Satellite Borne Lidar Global Wind Monitoring System,” NOAA, Washington D.C., Tech. Memo. ERL WPL-37, 1978; R. M. Huffaker, “Feasibility Studies for a Global-Wind Sensing Measuring Satellite System (Winsat), Analysis of Simulated Performance,” *Appl. Opt.,* Vol. 23, August 1984, pp. 2523–2536.

[8] Zhou, B., et al., “Efficient Frequency-Stable Laser-Diode-Pumped Nd:YAG Laser,” *Opt. Lett.* Vol. 10, February 1985, pp. 62–64.

[9] Kane, T. J., and R. L. Byer, “Monolithic, Unidirectional, Single-Mode, Nd:YAG Ring Laser,” *Opt. Lett.,* Vol. 10, February 1985, pp 65–67.

[10] Kane, T. J., et al., “Coherent Laser Radar at 1.06 Micrometers Using Nd:YAG Lasers,” *Opt. Lett.,* Vol. 12, April 1987, pp. 239–241.

[11] Arie, A., and R. L. Byer, "Laser Heterodyne Spectroscopy of $^{127}I_2$ Hyperfine Structure Near 523 nm," *J. Opt. Soc. Amer. B,* Vol. 10, November 1993, pp. 1990–1997.

[12] http://lisa.jpl.nasa.gov/.

[13] http://www.ligo.caltech.edu/.

[14] Tulloch, W. M., T. S. Rutherford, and R. L. Byer, "Transverse-Pumped Slab Laser Amplifier," U.S. patent 6,134,558, issued October 17, 2000.

[15] Rutherford, T. S., et al., "Edge-Pumped Quasi-Three-Level Slab Lasers: Design and Power Scaling," *J. Quant. Electron.,* Vol. 36, February 2000, pp. 205–219.

CHAPTER 3

Photonic Crystal Fibers in Communications and Sensing

Philip Russell
Department of Physics
University of Bath, United Kingdom

Introduction

This chapter focuses on photonic crystal fibers (PCFs), a new technology that has applications in almost every area of science involving light [1, 2]. Figure 3.1 is an optical micrograph of one of the very first hollow core PCFs. The picture was taken by placing a short length of the fiber in a microscope and focusing white light into the fiber core from below. As can be seen, colored light remains within an empty channel surrounded by glass. For anyone who has worked in guided wave photonics, this seems rather strange because light normally tends to refract into a higher index regions, whereas in this case it "chooses" to remain inside a small hollow channel, and not just over short distances—it is currently possible to transmit light along several hundred meters of fiber in a channel only 10 μm in diameter [3, 4]. The guidance mechanism is of course the photonic band gap.

I will discuss several topics under the general heading of photonic crystal fibers. Although these fibers are also sometimes known as holey fibers or microstructure fibers, today the name PCF is generally preferred. The structures of PCFs vary greatly, coming in many different shapes and forms, some appearing less like crystals than others; a selection of representative micrographs is given in Figure 3.2. On the bottom right is one of the first PCFs we made in 1995 [5]. It has quite small air holes (on order of 200 nm in diameter), an interhole spacing of 2,300 nm, and in the center a missing air hole forms a core. This particular structure is single-mode at every wavelength of guidance; that is, "endlessly single-mode" [6]. On the bottom left of the figure, the far-field pattern is shown for such a fiber into which several different colors of laser light are simultaneously launched; this pattern remains steady even when the fiber is twisted or bent. We have also fabricated fibers with very small cores (the one on the left in the middle has a core only 800 nm in diameter), as have other groups, such as a group at Lucent (now OFS) [7, 8]. We have also recently made fibers out of soft glasses [9]. The top left of Figure 3.2 shows a fiber made from Schott SF6 glass, which has some interesting applications. We have made polarization-maintaining fibers by creating twofold symmetry through the introduction of two enlarged holes on opposite side of the core (the fiber illustrated, bot-

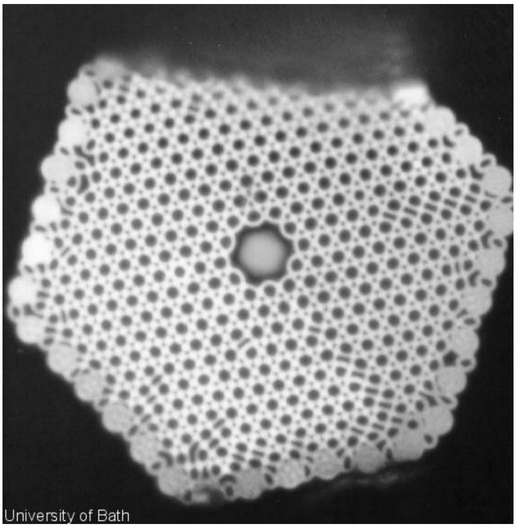

Figure 3.1 One of the first hollow-core PCFs. A short length of fiber is placed in a microscope and illuminated from below with white light. In this case, only yellow-green light is trapped in the core by a photonic band gap.

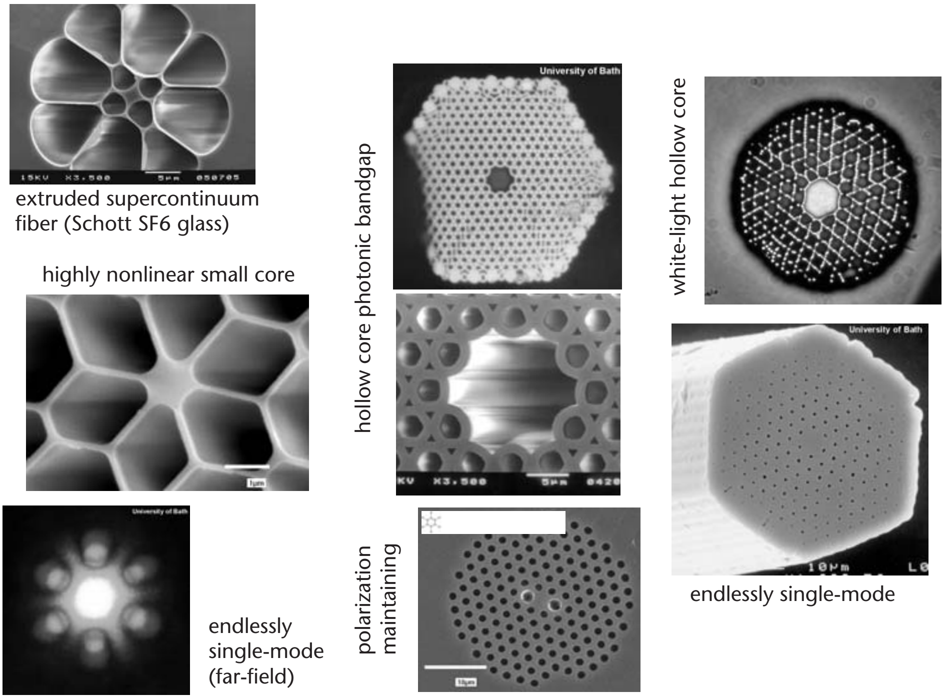

Figure 3.2 A selection of PCFs.

tom center, was made by BlazePhotonics Ltd.) [10]. We have recently fabricated another type of hollow core fiber (top right-hand corner) that can transmit a very wide range of optical wavelengths (the very first fibers transmitted only narrow bands of wavelengths). The cladding structure in this fiber has a very low density of states, but not a full photonic band gap [11].

Fabrication Techniques

So how do we actually make PCFs? Very briefly, we use two main techniques. The most common and popular, at least for silica glass, is the stack-and-draw method where we stack tubes and rods of glass to create the required crystal "preform." The spacing between the rods and tubes is roughly 1 mm. We can insert doped glass or thicker tubes of glass or we can leave out a tube of glass to form a hollow core. The stack-and-draw approach is very versatile, allowing straightforward building up of complex structures very precisely at the preform stage (Figure 3.3). The preform stack then is put into a fiber drawing system (Figure 3.4), the tubes fused together, and the whole structure reduced in size to form the final fiber with overall collapse ratios of about 10^4 or 10^5. We can make nanoscopic holes as small as 25 nm in diameter and hundreds of meters long. Such small thin holes are quite remarkable, and may prove to be a useful template for studying, for example, chemistry in constrained systems.

Band Structure of the Photonic Crystal Cladding

Now I briefly look at the properties of the cladding of a fiber with a regular triangular lattice of air holes. It may be viewed as a composite material with its own dispersion. An important quantity is the axial wave vector component, β which is conserved in every region of the fiber. Naturally, it is possible to calculate the transverse wave vector in each case and establish whether the light is traveling or evanescent in the holes or in the glass. We calculated the dispersion of this defect-free structure [12], and plotted the result on a diagram of frequency versus wave vector (Figure 3.5). In each region of the structure, for fixed frequency, light propagates when the wave vector β is small enough. For example, on the right-hand side of the slanting "vacuum" line, light is evanescent in air (i.e., unable to propagate). The line for silica glass is further to the right in the figure, and for the composite structure, which is a mixture of glass and air, the refractive index of the holey photonic crystal fiber cladding lies somewhere in between—as might be expected.

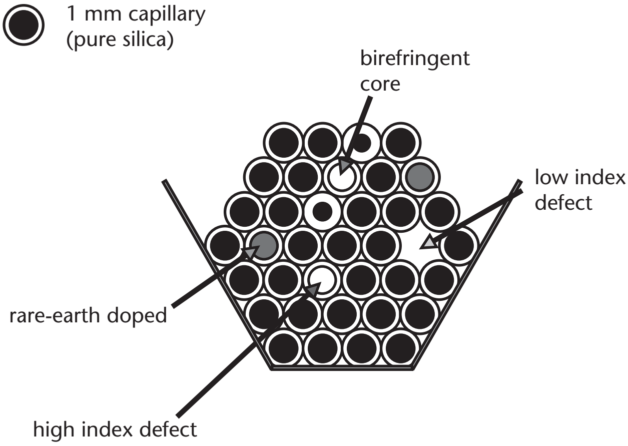

Figure 3.3 Stacking the preform from tubes and rods of silica glass.

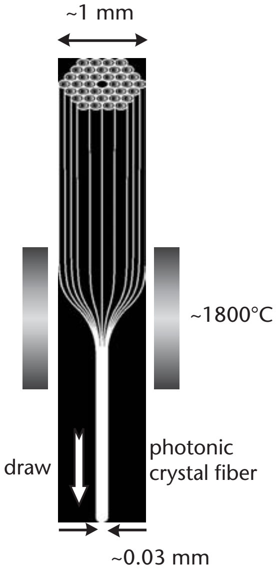

Figure 3.4 The final PCF drawing stage. Overall collapse ratios as high as 10,000 times are possible, with hole diameters as small as 25 nm.

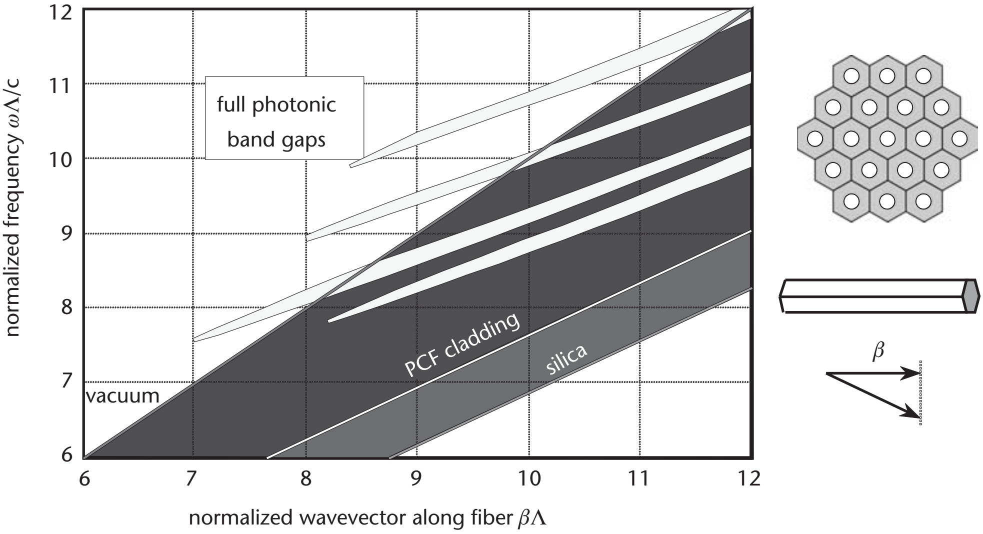

Figure 3.5 Band edge diagram for a triangular lattice of air holes in silica glass with 45 % volume filling fraction of air. The interhole space is Λ and ω/c is the vacuum wave vector.

In addition, we have photonic band gaps, which are shown in the figure by the "fingers" extending down from the top right. These can appear in regions where the light is normally able to propagate. It is clear that the propagation of light is quite complicated in these photonic crystal structures. The same diagram for a standard single-mode fiber is plotted for comparison in Figure 3.6. The fiber is surrounded by a vacuum, the cladding is pure silica glass, and the core is Ge-doped. The entire telecommunications revolution happened within the very narrow guidance strip indicated on the diagram. If we compare this with the diagram for PCFs in Figure 3.5, we can begin to see why photonic crystal fibers are so much richer in terms of their

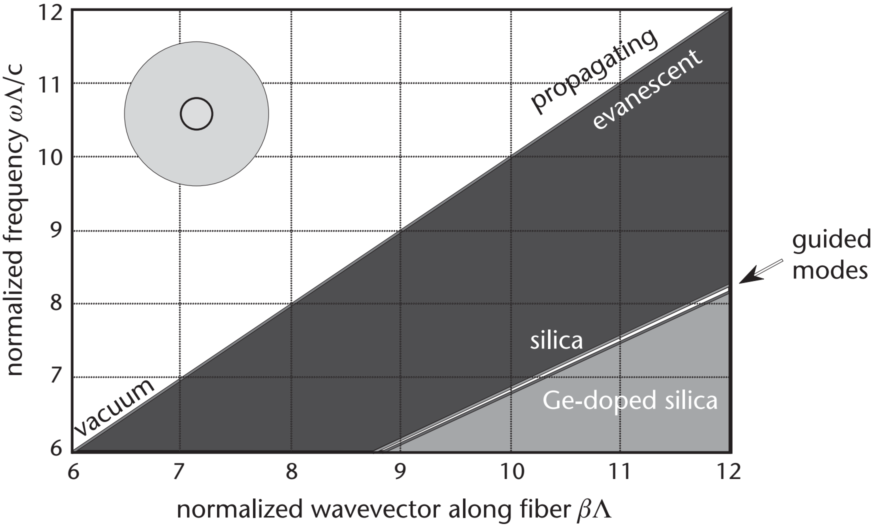

Figure 3.6 Propagation diagram for a standard single-mode fiber.

possibilities. This diagram includes features (e.g., the photonic band gaps) that that do not exist at all in the single-mode fiber case.

Modal Filtering: An Endlessly Single-Mode PCF

Our first discovery, which was serendipitous, was the endlessly single-mode fiber [6]. This is shown in Figure 3.7. In November 1995 we formed the structure shown on the left in the figure and could not initially decide whether this would be a waveguide because there are clear pathways where the light can leak away between the holes. And yet, on the other hand, the average refractive index is lower in the cladding than in the core so there is a refractive index difference. Having made the PCF, we found it was very easy to test, and discovered experimentally that it was single-mode at every wavelength of excitation. This indicated that the azimuthally discontinuous core-cladding interface had a very important effect on the guidance. I explain this by noting that the fundamental mode has a transverse effective wavelength roughly equal to twice the core diameter. The light is thus unable to escape because it cannot "image" the gaps between the air holes; that is, it cannot squeeze between them (note that the air holes are very strong barriers to light under these circumstances). The fundamental mode is then effectively trapped inside a "sieve," whereas the higher-order modes, with smaller transverse effective wavelengths, can leak away rapidly through the gaps between the air holes [1]. In summary, the spatial resolution of the light is higher for the higher-order modes than it is for the fundamental mode. So we have a new mechanism for guiding light, which appears to be total internal reflection but with a very interesting and unexpected twist.

If the hole is taken away from the center (i.e., filled in) we are operating (refer to Figure 3.5) between the refractive index of the composite cladding and the refractive index of the silica. Plotting axial refractive index instead of β (and neglecting mate-

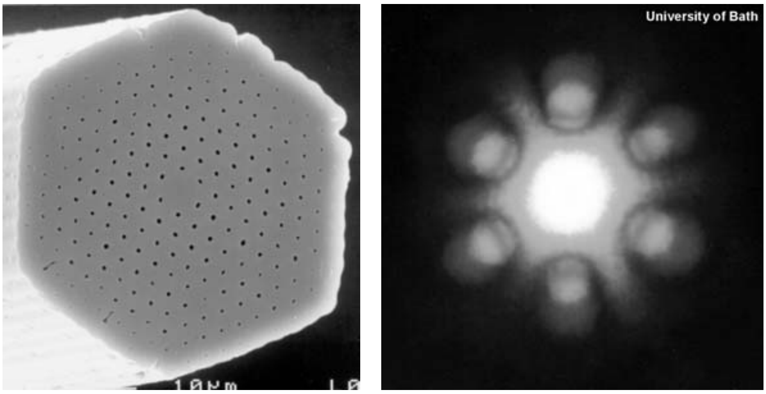

Figure 3.7 Scanning electron micrograph (left) and far-field pattern of guided light in an endlessly single-mode PCF. The interhole spacing is 2.3 μm.

rial dispersion for simplicity), we obtain the diagram in Figure 3.8. It is clear that the refractive index difference between core and cladding falls as the wavelength gets shorter. If the fiber is designed correctly (the ratio of hole diameter to spacing must be less than 0.4), single-mode guidance is maintained at every wavelength of operation.

We can also use this approach to make a fiber that fails to guide short wavelengths; that is, it cuts off the guidance of light at shorter wavelengths [13]. The diagram in Figure 3.9 shows wavelength versus refractive index for the pure silica core (once again material dispersion is neglected) and the photonic crystal fiber cladding. If we now dope the core with fluorine we can reduce its refractive index, and wavelength regions appear where the core-cladding index difference is positive (longer wavelengths) or negative (shorter wavelengths). For wavelength below a certain value, the fiber ceases to guide light. We tested this in a series of experiments at wavelengths from 633 to 458 nm. The near-field mode patterns in Figure 3.9 were taken by keeping the fiber extremely straight—even if only slightly bent, the light rapidly leaves the core at the shorter wavelengths. This is a radically new kind of

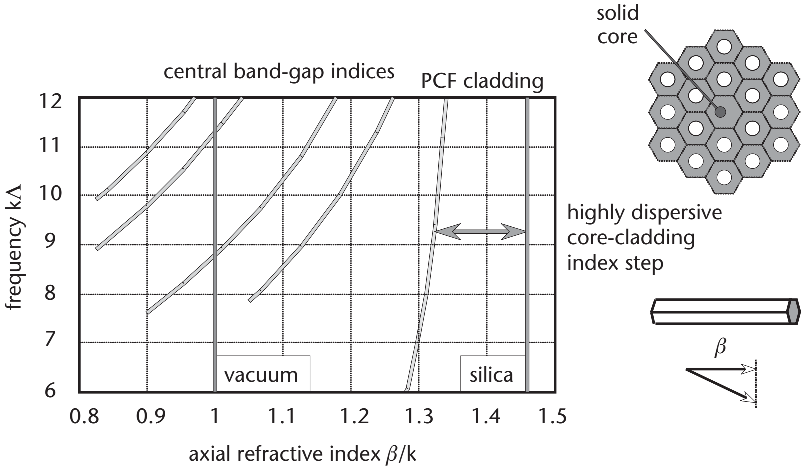

Figure 3.8 Plot of frequency versus axial refractive index for a PCF with a solid glass core and a holey cladding. The core-cladding refractive index difference is highly dispersive.

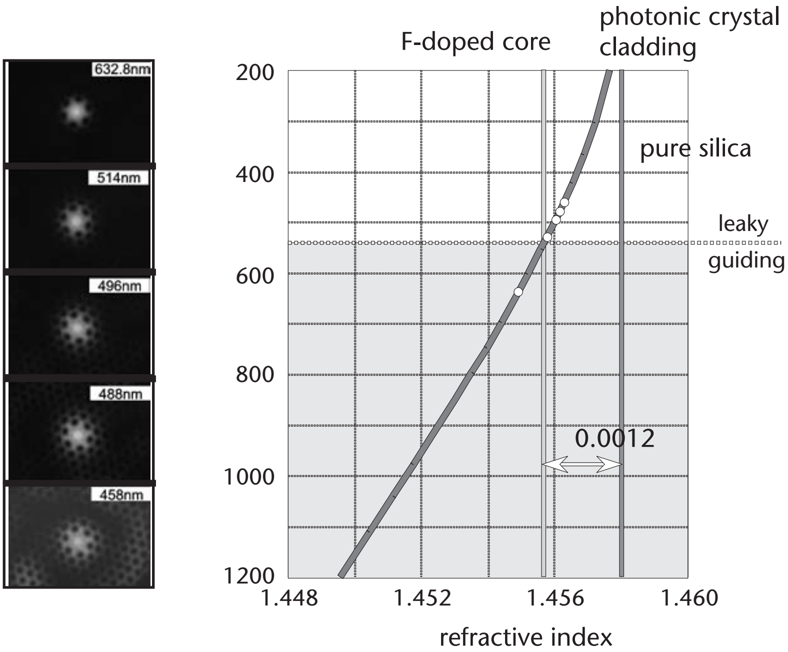

Figure 3.9 Designing a PCF with a short wavelength cutoff. The light of the wavelength that is shorter than a certain value is not guided at all.

single-mode fiber that filters out shorter wavelengths, something that is impossible in traditional fiber optics.

It is of course vital with any kind of optical fiber to consider attenuation loss. Figure 3.10 shows results reported by BlazePhotonics Ltd in 2002, in a postdeadline paper at the ECOC meeting in Europe [14]. The measured attenuation was 0.58 dB/km at 1,550 nm (to put this in context, the very first fibers we made, in 1995, had losses of about 1 dB/m). The different components of the loss are analyzed in the figure. After eliminating the effects of OH absorption (caused by water in the structure, which can be eliminated if required), there remains a residual loss of 0.46 dB/km, caused we believe by scattering at the air/glass interfaces. More recently (at OFC in 2003), NTT reported a loss of 0.37 dB/km at 1,550 nm in a similar PCF [15]. It seems likely that the attenuation will continue to fall, as this has been the trend in fiber optics, and it will be interesting to see how low it can go.

Supercontinuum Generation

One of the most useful and intriguing applications of PCF is to the generation of broadband supercontinuum light from short-pulse laser systems. This is made possible by a combination of ultrasmall cores and dispersion zeros that can be shifted to coincide with the pump laser wavelength. In Figure 3.11, the group velocity dispersion is plotted against wavelength in the range from 500 to 1,000 nm. Bulk silica glass has normal dispersion in this range. However, if we form a PCF with an ultrasmall core (800 nm in diameter; see the inset in the figure), the dispersion is changed beyond recognition. The sign is reversed compared to that of bulk silica, the zero

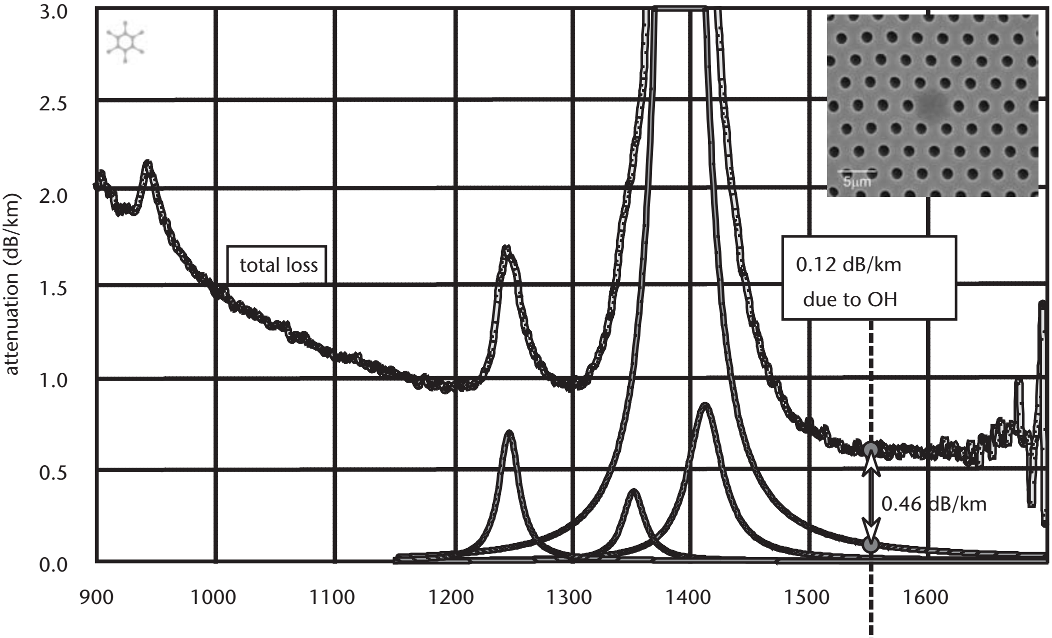

Figure 3.10 Attenuation spectrum in a solid-core PCF with hole diameter 2.89 μm and hole spacing 4.1 μm. The attenuation is 0.58 dB/km at 1,550 nm, caused predominantly by scattering at the air-glass interfaces.

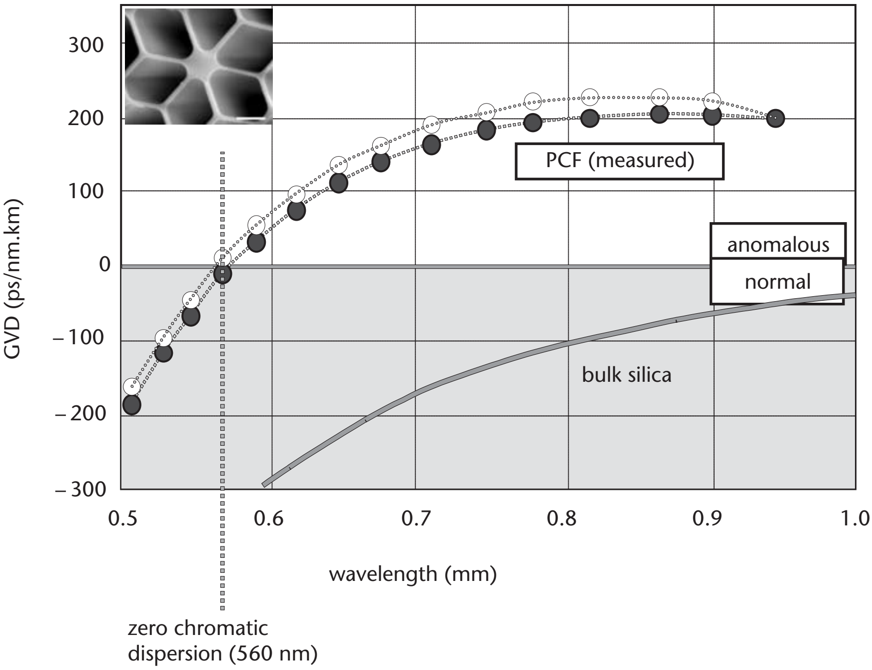

Figure 3.11 The effect of microstructuring on the dispersion profile of silica glass. The core is 800 nm in diameter (see inset).

dispersion wavelength is shifted down to 560 nm, and indeed the whole dispersion landscape is completely changed (the bidispersion is caused by slight birefringence in the core, due to geometrical distortion). As the holes become bigger the core becomes increasingly isolated and begins to look like a strand of silica glass sitting in vacuum. The waveguide dispersion of such a strand is very strong compared with the material dispersion.

The combination of very high effective nonlinearity (per unit power) and zero dispersion at Ti-sapphire laser wavelengths (around 800 nm) leads to efficient supercontinuum generation, as first reported in 2000 [8]. The results were very dramatic: using an unamplified, high repetition rate, mode-locked Ti:sapphire laser, the supercontinuum light is both extremely bright and extremely broad spectrally (Figure 3.12). It behaves something like a sunlight laser (it has very high coherence compared to sunlight) and indeed represents a new kind of optical source [16]. I now describe its applications.

One very important application of a broadband, very bright source is in medical imaging. This source is already being used in optical coherence tomography [17]. It is also employed for many kinds of spectroscopy and quite recently has been successfully applied to the field of frequency metrology [18]. Menlo Systems of Munich have marketed a device to measure frequency with extremely high accuracy. In fact, the current Austrian frequency standard is based on this Menlo Systems device, which contains a piece of our fiber. The reason that this device works is that the supercontinuum spectrum consists of many steps in frequency, that is, a frequency "ladder" or "ruler." The spacing between the individual frequencies corresponds to the pulse rate or repetition rate of the laser. There are laboratories in Japan, the United States, and throughout the world using this supercontinuum ladder to measure frequency.

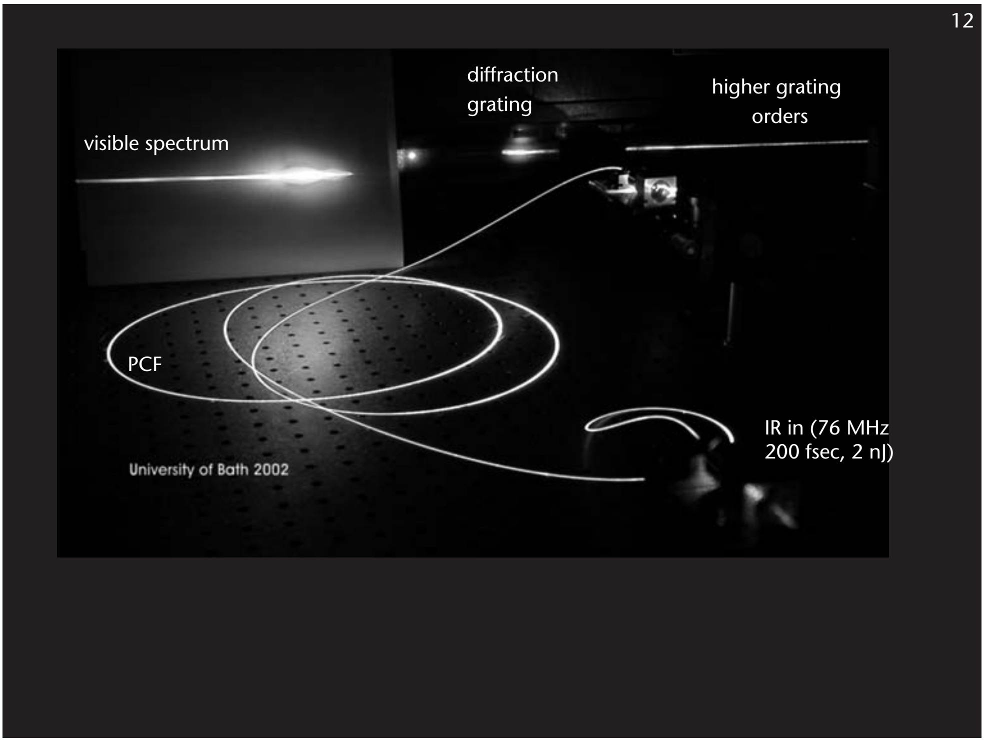

Figure 3.12 Supercontinuum spectrum generated from a Ti:sapphire laser using a small-core highly nonlinear PCF.

More recently, we have been looking at generating a supercontinuum in PCFs made from soft glasses using an extrusion technique. Molten bulk glass is forced through a die and converted directly (with one further step to bulk-out the cladding) into fiber. The extruded PCF shown in the inset in Figure 3.13 is made from Schott SF6 glass and has an attenuation spectrum over the 500- to 1,700-nm wavelength range that, with the exception of the usual water peak, is within a factor of two of that of the bulk glass.

Compared to silica glass, the dispersion of SF6 glass is strongly normal over the wavelength range 1,300 to 1,600 nm (Figure 3.14). This provides a considerable benefit in that, by adjusting the core diameter, we can shift the zero dispersion wavelength to any point we require in the important 1,550-nm band. This means that we can pump this fiber with a femtosecond laser source at 1,550 nm wavelength (such as a fiber laser [19]) and generate a supercontinuum. Figure 3.15 shows our first result, obtained in collaboration with the Los Alamos National Laboratory in the United States [9]. The supercontinuum spectrum in this case extends from 350 to at least 2,200 nm and probably much further, which represents a considerable improvement over results achieved in pure silica PCF. It is interesting to note that most of this conversion occurs in the first few tens of centimeters, which look white in color. The fiber becomes increasingly red in appearance as the light travels along it. This is because the shorter (bluer) wavelengths are differentially absorbed.

Earlier I described a radically new class of fiber-based light source. It is exciting to conjecture what will happen when we use PCFs made from other glass-forming systems, such as tellurites, which are transparent out to 4.5 μm. Perhaps we will be able ultimately to produce a supercontinuum covering the entire midinfrared range, a result that would have huge implications in many types of sensing.

Sound and Light in PCF

The next topic—the control of sound in PCF—digresses slightly, but not completely, from the photonics theme. Very high frequency sound can be particularly useful for

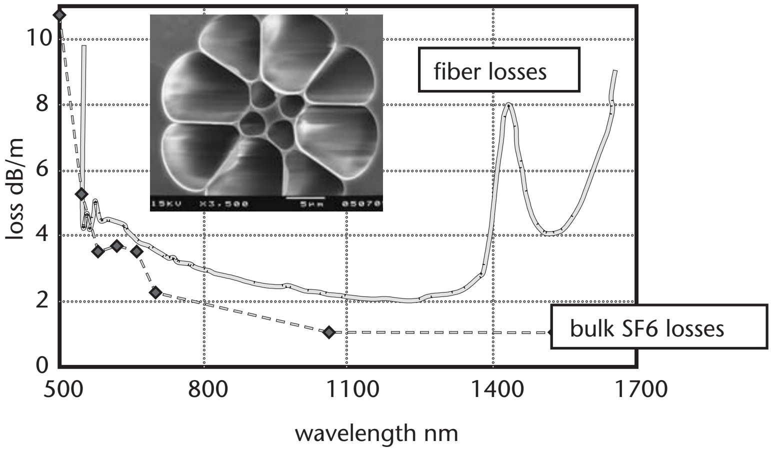

Figure 3.13 The microstructure and attenuation spectrum of a PCF extruded from Schott SF6 glass. The core diameter is roughly 2 μm.

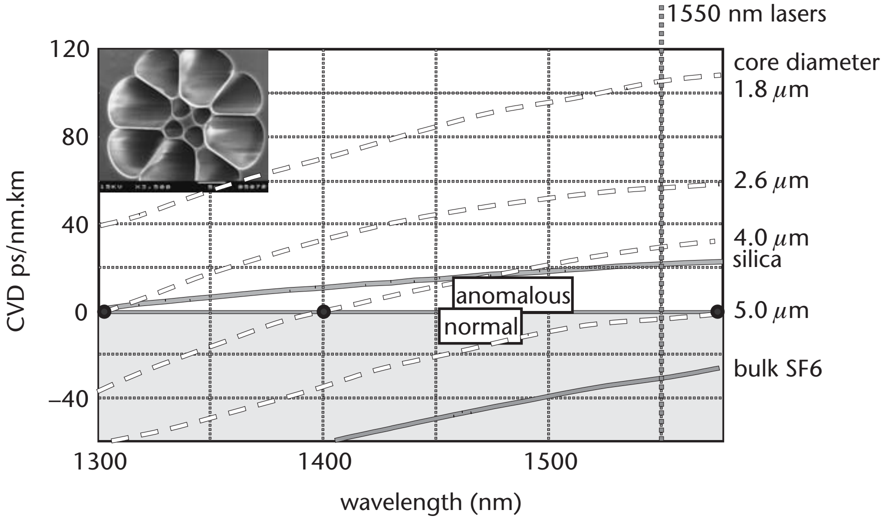

Figure 3.14 Group velocity dispersion of pure silica glass, Schott SF6 glass, and a PCF extruded from SF6. The core diameter can be chosen to place the dispersion zero at 1,550 nm.

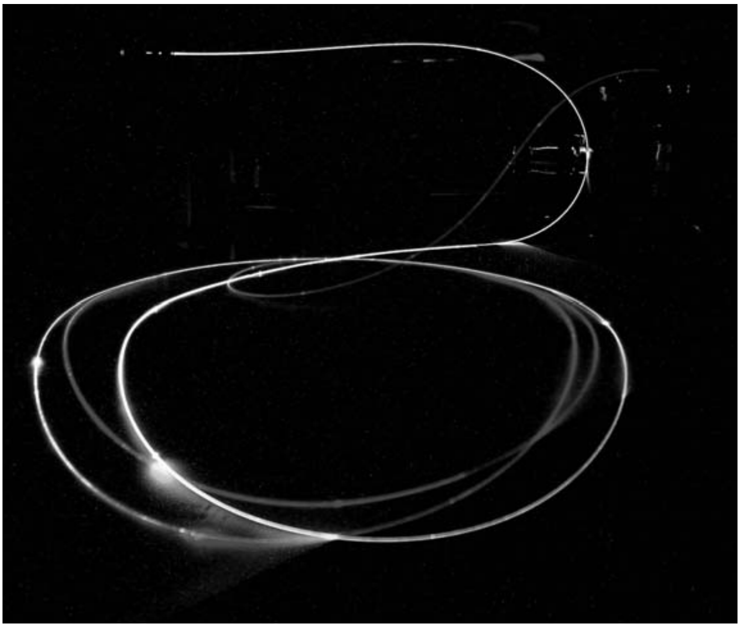

Figure 3.15 Extruded SF6 PCF producing a white-light supercontinuum from a 1,550-nm 100-fs pulsed laser. The spectrum extends form 350 to at least 2,200 nm.

modulating light, though sound and light do not “talk to each other” very well; their interaction (via electrostriction) is quite weak. Therefore, any technique that can enhance their interaction is of interest. One way to achieve an enhancement is to trap the acoustic vibrations in a very small space along with the light. Recently we completed some experiments on sound-wave manipulation in a PCF preform with a square lattice of air holes (see inset in Figure 3.16) [20]. There was a spacing of about 0.1 mm between the holes in the preform, and the structure was made with two solid cores. We placed a piezoelectric transducer at the side of the preform, and

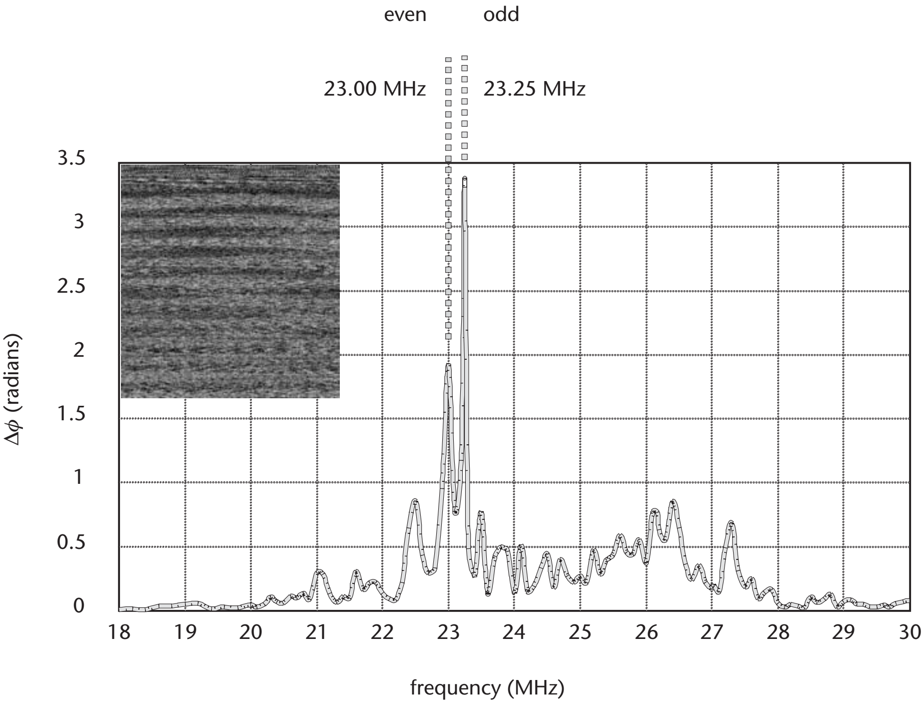

Figure 3.16 Spectrum of the phase change induced in a two-core square-lattice PCF preform by vibrations in the range of 18 to 30 MHz. A laser beam was passed along one of the cores in one arm of a Mach-Zehnder interferometer.

launched a laser beam along one of the cores, in a Mach-Zehnder interferometer arrangement. Measuring the phase modulation as a function of transducer frequency produced the spectrum in Figure 3.16. Two sharp resonances are apparent, one at 23 MHz and other at 23.25 MHz. These are the even and odd vibrational modes of the coupled cores, the sound being trapped in the cores by a phononic band gap created by the square array of holes in the cladding. Calculations of the phononic band structure confirm that this is so. This opens up the possibility of engineering sound in the same way as we engineer light.

Hollow-Core PCFs

This section focuses on hollow-core PCFs, where the only possible guidance mechanism is a photonic band gap. Even though this type of fiber was our first goal back in 1991, it took the longest time to realize. Referring again to Figure 3.5, the idea is that we operate at a frequency where one of the “fingers” extends to the left-hand side of the vacuum line. Under these conditions, a photonic band gap prevents light from penetrating into the photonic crystal cladding while permitting it to form a mode in the hollow core. A scanning electron micrograph of the very first successful hollow-core fiber we made (reported in 1999) is given in Figure 3.17 (left-hand side) [3]. It had characteristically narrow bands of guidance, giving rise to vividly colored near-field core modes when white light was launched (see Figures 3.1 and 3.2). More recently, hollow-core PCFs have become commercially available and the losses have dropped dramatically. In 2002, Corning reported a loss of 13 dB/km at 1,550 nm in

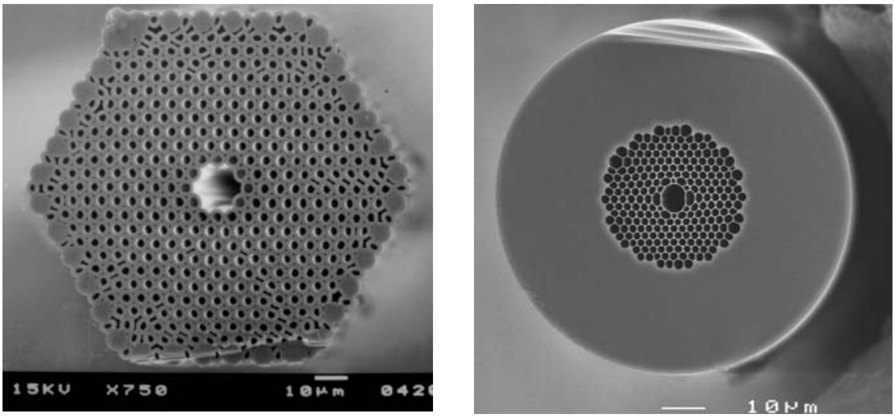

Figure 3.17 State-of-the-art hollow-core photonic band gap PCFs in 1999 (left) and 2003 (right). The right-hand PCF guides light in the 830-nm band with losses of ~180 dB/km.

a 100-m length of hollow-core fiber [21]. The right-hand micrograph in Figure 3.17 is a recent PCF designed for 830-nm transmission and produced at the University of Bath [4]. BlazePhotonics Ltd has recently published specification sheets for its own hollow-core fiber on the Web [22]. Figure 3.18 shows a commercial hollow-core fiber designed for transmitting 1,060-nm light. The center-band attenuation is 60 dB/km and the transmission bandwidth is 150 nm.

A second type of hollow-core fiber, recently developed in Bath, has a very broad transmission band, which is important for some applications [11]. Strictly speaking, it operates not by a photonic band gap, but by a low "density-of-states" mechanism

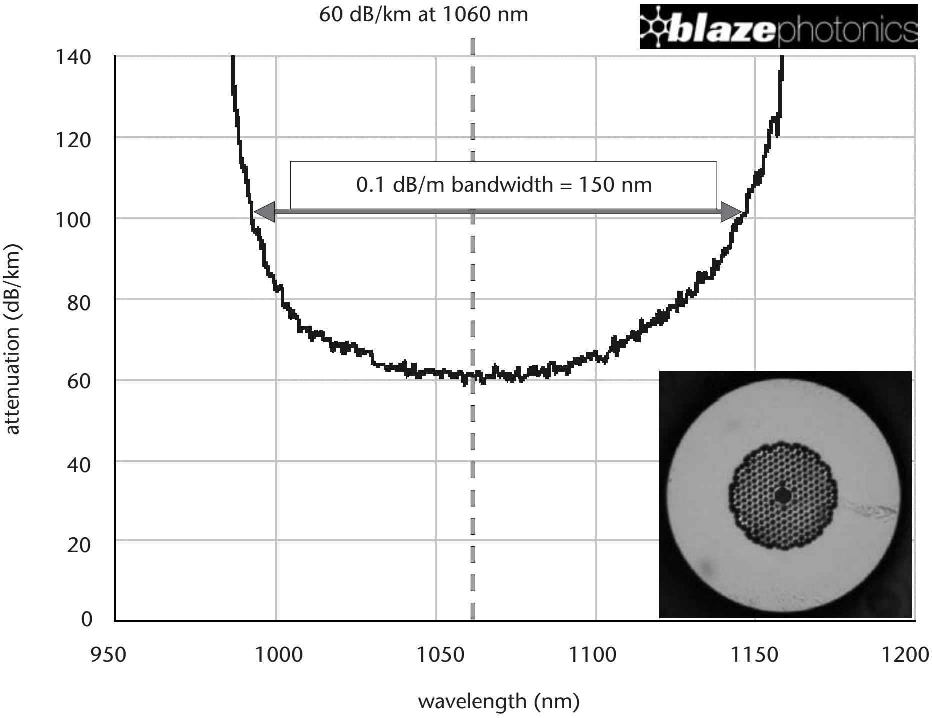

Figure 3.18 Transmission attenuation spectrum of a commercial hollow-core PCF made by BlazePhotonics Ltd.

in the cladding. This means that it can guide white light. Figure 3.19 shows the structure and transmission spectrum of one of these fibers. From 400 to 1,600 nm the losses are of the order of 1 dB/m, our best results lying somewhat below this value. These characteristics are valuable in experiments where one needs to guide widely different wavelengths in the hollow core.

Applications of Hollow-Core PCFs

Next, I look at two applications and then briefly discuss some intra-PCF devices. An attractive feature of hollow-core fiber is that it can maintain very high intensities over long lengths in a very small bore channel (of the order of 10 μm in diameter). Simple glass capillaries leak very strongly in this regime, because loss goes as the inverse of the bore radius to the power of 3 [23]. If we reduce the bore from around 200 μm (when it is highly multimode, with losses of order 1 dB/m) to 10 μm, the loss increases 8,000 times. This means that single-mode capillaries (which must have bores of diameter of a few microns) are simply impractical.

In laser tweezer experiments (the next topic), the particle trapping forces are greatest where the intensity gradient is highest, so that the higher the intensity and the smaller the mode diameter the stronger the forces. A hollow-core PCF is thus a perfect vehicle for transporting microscopic particles in laser light. We performed an experiment using a population of micron-sized polystyrene particles on a vibrating glass plate [24]. As seen in Figure 3.20, a laser beam enters from below and is focused into the fiber core, passing through a horizontal glass plate supporting the particles. Turning on the transducer makes the particles separate and bounce around, releasing them from Van der Waal's forces, and occasionally a particle becomes trapped in the laser beam and is propelled up into the fiber. The small white

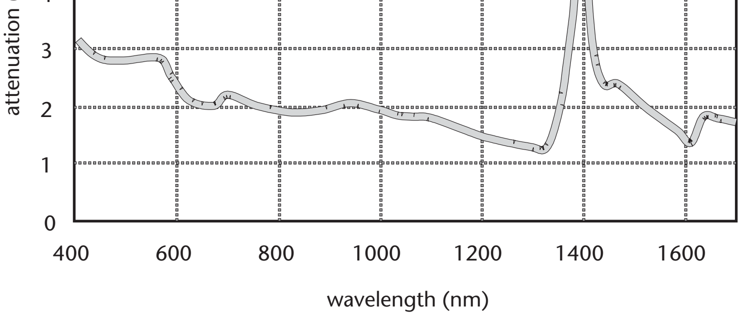

Figure 3.19 Attenuation spectrum of a hollow-core PCF guiding light by a low density-of-states in the cladding. It has a very broad transmission band, guiding white light (see insets for electron and optical micrographs). The core is roughly 12 μm in diameter.

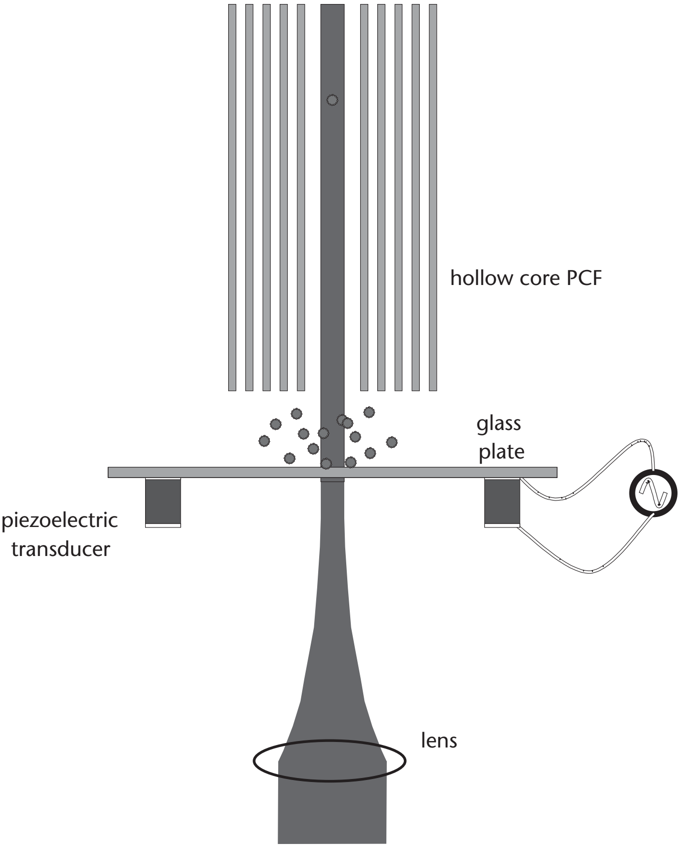

Figure 3.20 Laser trapping and propulsion of micron-sized particles inside a hollow-core PCF.

dot visible in Figure 3.21 is a particle progressing along the core at a terminal velocity (limited by the viscosity of air) of about 1.5 cm/sec. The arrows indicate its position in each frame. The PCF had a 20-μm diameter hollow core, the particles were 5-μm diameter polystyrene spheres, and the laser power was 80 mW at 514 nm. We have not yet performed an experiment where the fiber is curved. It would be interesting to see if the particles can negotiate bends without crashing into the walls. Many interesting experiments remain to be done on this subject. Guiding cold atoms is a related area of considerable scientific interest, as is the idea of guiding biological particles, or viruses, along a liquid-filled fiber.

The advent of low-loss hollow-core PCF is revolutionizing the field of nonlinear optics in gases. We can compare simple capillaries with hollow-core PCF using the following figure of merit: $\text{FoM} = \lambda L_{\text{loss}}/A_{\text{eff}}$ where L_{loss} is the loss length (how far does the light travel before it is absorbed or lost?), A_{eff} the effective core area (should be very small to obtain high intensities), and λ is the vacuum wavelength. FoM is plotted against bore radius in Figure 3.22 for a simple capillary and three different hollow-core PCFs, each with a different attenuation constant. The curve for the capillary is rather peculiar, because it indicates that the nonlinear interaction actually improves as the intensity drops. In other words, capillaries operate better when the light intensity is lower. This is because their performance is completely dominated

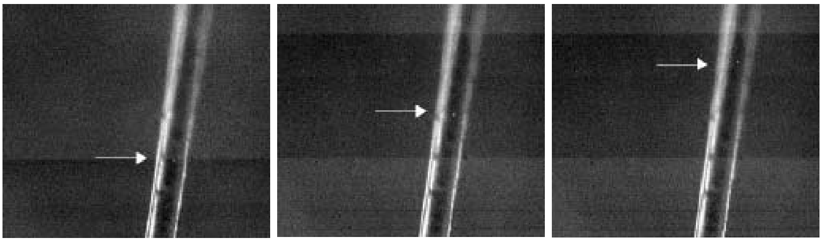

Figure 3.21 Individual video frames of a particle moving along inside the hollow-core PCF.

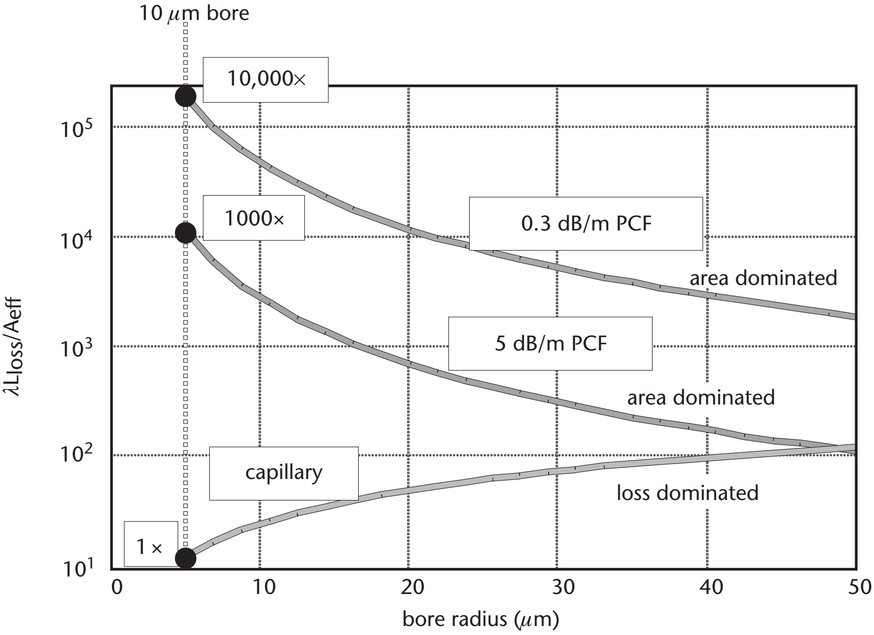

Figure 3.22 Nonlinear figure of merit for capillaries and hollow-core PCF, plotted against hole radius.

by loss. If we take a hollow-core PCF, on the other hand, it behaves more sensibly: as the bore radius increases, the effectiveness of the nonlinear interaction falls off. The factors of improvement over simple capillaries are quite startling. For example, a 10-μm bore PCF with 0.3-dB/m loss provides a 10^4 enhancement in nonlinear figure of merit compared to capillary. Using the recent Corning result of 13 dB/km, the factor is 10^5. Such huge factors of improvement are very rare in nonlinear optics, and are giving rise to many revolutionary new opportunities in applications where a tight focus must be maintained over long distances. For example, with a length of hollow-core PCF we could perform efficient high harmonic generation in inert gases at low power—an exciting goal that has yet to be realized. Of course, people have been doing this for years in gas-filled capillaries. Perhaps now we can hope for high harmonic generation of X-rays and ultraviolet light in a gas-filled hollow-core PCF pumped by a compact diode-pumped femtosecond laser.

We recently carried out experiments on stimulated Raman scattering in a hydrogen-filled hollow PCF [11]. Gas was pumped into a length of hollow-core fiber at pressures up to 50 bar. Nanosecond pulses at wavelength 532 nm were launched into the gas-filled core and the output monitored as the pulse energy was increased. The PCF used was the broadband white-light guiding fiber in Figure 3.19. Figure 3.23 shows the experimental setup, together with photographs of the green pump light, the red Stokes light, and the blue anti-Stokes light emerging from the core of the 30-cm-long fiber. What is remarkable about this result is that, without too much effort, we achieved a factor of 100 times reduction in the threshold energy required to generate efficient conversion to the Stokes wavelength. It should be possible to increase this factor considerably. We believe that this is just the first step into a very exciting new arena for gas-based laser optics.

Another rather simpler application of hollow-core PCF is in the transmission of very high average powers and pulse energies for, as an example, industrial machining applications. The absence of any solid material in the core means that extremely high intensities can be supported without damage. This is an area of increasing technological interest worldwide [25, 26].

Intra-PCF Devices

To realize the potential of all these new developments in fiber optics, we need, as in conventional fiber optics, intrafiber devices of many sorts. We have been working on a range of such devices recently. An example is a birefringent rocking filter [27]. Here we take a length of polarization-maintaining fiber and scan a carbon dioxide

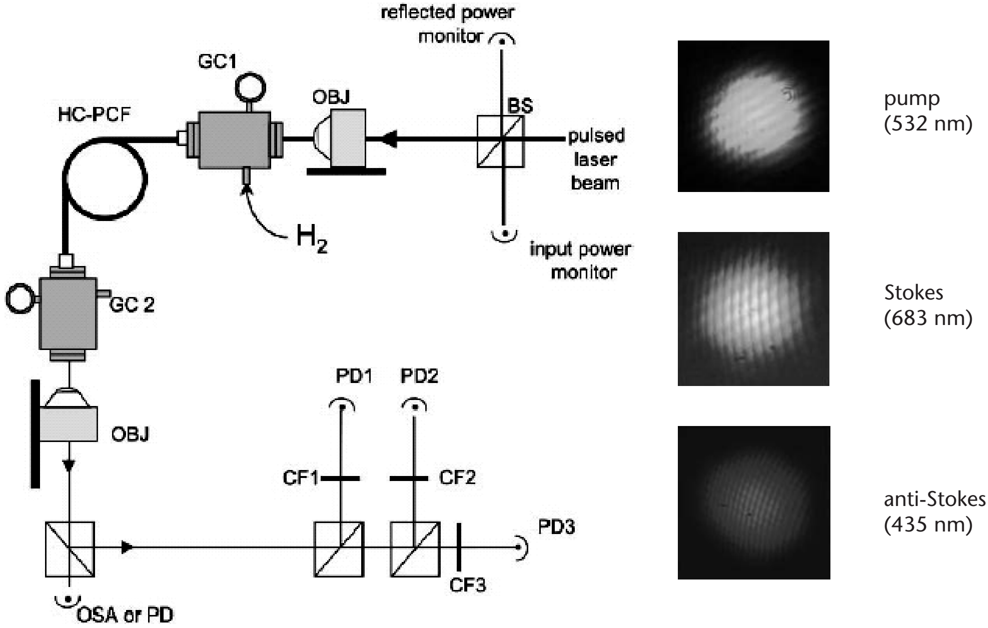

Figure 3.23 Setup for the stimulated Raman scattering measurement in a hydrogen-filled hollow-core PCF. On the right-hand side are photographs of the near-field patterns emerging from the core.

laser beam along it while twisting the fiber to and fro periodically (see Figure 3.24). The glass softens when the carbon dioxide laser hits it and then freezes back with a permanent twist (this process does not work with conventional polarization-maintaining fiber because the fiber destroys itself due to the internal stresses that are used to create birefringence). Figure 3.25 shows the conversion efficiency (between orthogonal polarization states) versus wavelength for one such device. The center-band suppression is 24 dB, and since the devices do not rely on photosensitivity, but involve a morphological change in the structure, there are no aging effects. Since they are made entirely from one material—pure silica glass—there are no temperature-induced stresses and the devices are highly temperature stable. Because we are working with the very large air-glass index difference we can make very short beat lengths. This means that, for a given bandwidth, the device length can be very short. We can manufacture these devices in a few seconds, at a rate of many thousand per day, making this an interesting area for commercial exploitation. We can also make many other different devices such as dual-core couplers and core-cladding couplers using this approach [28–30].

Final Comments

In summary, PCFs offer major new opportunities in many areas of physics and photonics, only a few of which have been mentioned here: frequency metrology, nonlinear optics, gas-laser interactions, cold atom guiding, particle guidance, fiber optics itself, dispersion control, solitons at new frequencies, fiber sensors, nonsilica fibers, polymer fibers, fiber lasers and amplifiers, supercontinuum generation, and intrafiber devices. The rapid pace of development means that is it difficult to keep up with all the current developments. The already very long and exciting list continues to grow by the week.

Acknowledgments

I would like to acknowledge all the many individuals who have contributed to the success of this work over the years, in particular my colleagues Dr. Tim Birks and Professor Jonathan Knight, who joined the work at a time when nobody even knew whether it was possible to fabricate such fibers. Since then many other people have

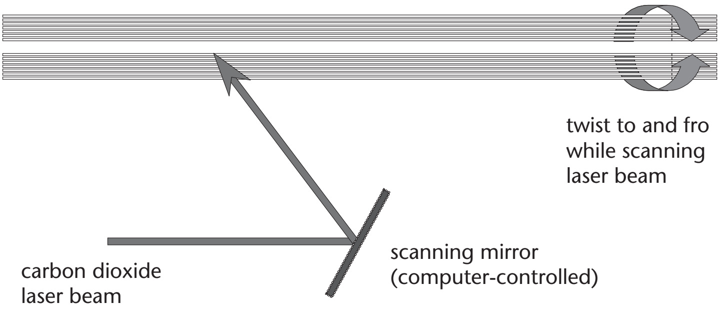

Figure 3.24 Setup for making a rocking filter.

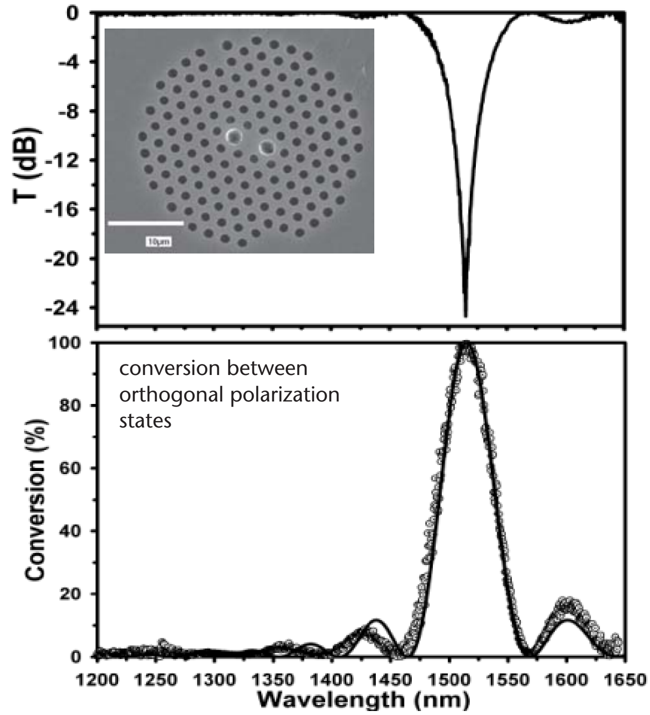

Figure 3.25 Performance of a rocking filter realized in a polarization-maintaining PCF made by BlazePhotonics Ltd.

become involved and funding has been provided from multiple sources including the UK Engineering & Physical Sciences Research Council, the Higher Education Funding Council for England, the UK Joint Infrastructure Fund, the Defence Evaluation and Research Agency (now QinetiQ), Lawrence Livermore National Laboratory, and Naval Research Laboratory in the United States, as well as several commercial companies.

References

[1] St. J. Russell, P., "Photonic Crystal Fibers," *Science*, Vol. 299, 2003, pp. 358–362.

[2] Knight, J. C., "Photonic Crystal Fibers," *Nature*, Vol. 424, 2003, pp. 847–85.

[3] Cregan, R. F., et al., "Single-Mode Photonic Band Gap Guidance of Light in Air," *Science*, Vol. 285, 1999, pp. 1537–1539.

[4] Bouwmans, G., et al., "Properties of a Hollow-Core Photonic Bandgap Fiber at 850 nm Wavelength," *Opt. Exp.*, Vol. 11, 2003, pp. 1613–1620.

[5] Knight, J. C., et al., "All-Silica Single-Mode Fiber with Photonic Crystal Cladding," *Opt. Lett.*,Vol. 21, 1996, pp. 1547-1549; Errata, *Opt. Lett.*, Vol. 22, 1997, pp. 484–485.

[6] Birks, T. A., J .C. Knight, and P. St. J. Russell, "Endlessly Single-Mode Photonic Crystal Fiber," *Opt. Lett.*, Vol. 22, 1997, pp. 961–963.

[7] Knight, J. C., et al., "Anomalous Dispersion in Photonic Crystal Fibers," *IEEE Phot. Tech. Lett.*, Vol. 12, 2000, pp. 807–809.

[8] Ranka, J. K., R. S. Windeler, and A. J. Stentz, "Visible Continuum Generation in Air-Silica Microstructure Optical Fibers with Anomalous Dispersion at 800 nm," *Opt. Lett.*, Vol. 25, 2000, pp. 25–27.

[9] Ravi Kanth Kumar, V. V., et al., "Extruded Soft Glass Photonic Crystal Fiber for Ultrabroad Supercontinuum Generation," *Opt. Exp.*, Vol. 10, 2002, pp. 1520–1525.

[10] Ortigosa-Blanch, A., et al., "Highly Birefringent Photonic Crystal Fibers," *Opt. Lett.*, Vol. 25, 2000, pp. 1325–1327.

[11] Benabid, F., et al., "Stimulated Raman Scattering in Hydrogen-Filled Hollow-Core Photonic Crystal Fiber," *Science*, Vol. 298, 2002, pp. 399–402.

[12] Birks, T. A., et al., "Full 2-D Photonic Band Gaps in Silica/Air Structures," *Electron. Lett.*, Vol. 31, 1995, pp., 1941–1942.

[13] Mangan, B. J., et al., "Fundamental-Mode Cutoff in a Photonic Crystal Fiber with a Depressed-Index Core," *Opt. Lett.*, C+Vol. 26, 2001, pp. 1469–1471.

[14] Farr, L., et al., "Low Loss Photonic Crystal Fiber," postdeadline paper PD1.3, *European Conference on Optical Communications* (*ECOC'02*), Copenhagen, Denmark, September 2002.

[15] Tajima, K., et al., "Ultra Low Loss and Long Length Photonic Crystal Fiber," *Optical Fiber Communication Conference (OFC 2003)*, postdeadline paper PD1, Atlanta, GA, March 2003.

[16] Wadsworth, W. J., et al., "Supercontinuum Generation in Photonic Crystal Fibers and Optical Fiber Tapers: A Novel Light Source," *J. Opt. Soc. Am. B*, Vol. 19, 2002, pp. 2148–2155.

[17] Povazay, B., et al., "Enhanced Visualization of Choroidal Vessels Using Ultrahigh Resolution Ophthalmic OCT at 1050 nm," *Opt. Exp.*, Vol. 11, 2003, pp. 1980–1986.

[18] Holzwarth, R., et al., "Absolute Frequency Measurement of Iodine Lines with a Femtosecond Optical Synthesizer," *Appl. Phys. B*, Vol. 73, 2001, pp. 269–271.

[19] Hundertmark, H., et al., "Supercontinuum Generation with 200 pJ Laser Pulses in an Extruded SF6 Fiber at 1560 nm," *Opt. Exp.*, Vol. 11, 2003, pp. 3196–3201.

[20] St. J. Russell, P., et al., "Sonic Band Gaps in Pcf Preforms: Enhancing the Interaction of Sound and Light," *Opt. Exp.,* Vol. 11, 2003, pp. 2555–2560.

[21] Smith, C. M., et al., "Low-Loss Hollow-Core Silica/Air Photonic Bandgap Fiber," *Nature*, Vol. 424, 2003, pp. 657–659.

[22] http://www.blazephotonics.com.

[23] Renn, M. J., and R. Pastel, "Particle Manipulation," *J. Vac. Sci. Technol. B*, Vol. 16, 1998, pp. 3859–3863.

[24] Benabid, F., J. C. Knight, and P. St. J. Russell, "Particle Levitation and Guidance in Hollow-Core Photonic Crystal Fiber," *Opt. Exp.*, Vol. 10, 2002, pp. 1195–1203.

[25] Shephard, J. D., et al., "High Energy Nanosecond Pulses Delivered Single-Mode Through Hollow-Core PBG Fibers," *Opt. Exp.*, Vol. 12, 2004, pp. 717–723.

[26] Ouzounov, D. G., et al., "Generation of Megawatt Optical Solitons in Hollow-Core Photonic Band-Gap Fibers," *Science*, Vol. 301, 2003, pp. 1702–1704.

[27] Kakarantzas, G., et al., "Structural Rocking Filters in Highly Birefringent Photonic Crystal Fiber," *Opt. Lett.*, Vol. 28, 2003, pp. 158–160.

[28] Kakarantzas, G., et al., "Directional Coupling in a Twin Core Photonic Crystal Fiber Using Heat Treatment," *Proc. QELS*, 2001, pp. 125–126.

[29] Kakarantzas, G., T. A. Birks, and P. St. J. Russell, "Structural Long-Period Gratings in Photonic Crystal Fibers," *Opt. Lett.*, Vol. 27, 2002, pp. 1013–1015.

[30] Birks, T. A., et al., "Photonic Crystal Fiber Devices," *Proc. SPIE (Fiber-Based Component Fabrication, Testing and Connectorization),* 2002, Vol. 4943, pp. 142–151.

CHAPTER 4

Femtosecond Pulse Processing and Applications to Optical Communications

Andrew M. Weiner
School of Electrical and Computer Engineering
Purdue University
West Lafayette, Indiana

This chapter focuses on optical signal processing—specifically, work at the subsystems level where we are trying to apply some unique ideas involving interactions between temporal degrees of freedom, spatial degrees of freedom, and frequency domain degrees of freedom in optical signals. In other words, my subject relates to Fourier optic types of ultrafast optical signal processing.

Specific topics include synthesis of arbitrarily shaped ultrafast optical waveforms, serial-parallel and parallel-serial conversion for ultrafast waveforms, and equalization methods for correction of signal distortion including chromatic dispersion and polarization-mode dispersion (PMD). I will also touch briefly on optical code-division multiple-access. In addition to optical communications applications, I will also mention some recent work using our ultrafast optical technologies with a view to introducing new capabilities in the area of radio frequency photonics.

First, I will describe the motivation for our work in optical signal processing. Figure 4.1 shows the progress made in commercial lightwave systems in terms of capacity versus year, up to about 2 years ago [1]. First, there have been tremendous advances in single-channel data rates, from about 600 Mbps to about 40 Gbps in commercial systems, over a little less than a 15-year period. There have been even more dramatic advances when we consider wavelength division multiplexing (WDM) with commercial capacities that have risen well into the Tbit/s range. WDM in fact constitutes a simple but extremely successful form of optical signal processing, where the key is the ability to either combine or separate signals based on optical wavelength. Thus, optical signal processing is the essence of WDM, which is responsible for the remarkable rate of progress shown in the figure.

In my group we are primarily interested in optical signal-processing methods in the ultrafast domain. That is, we are interested in new enabling optical signal-processing technologies that can potentially contribute to further improvements for ultrafast communications such as TDM. Impressive results in which ultrafast optical signal processing is applied in a systems context are reviewed in [2]. In this chapter I survey our own unique contributions to optical signal processing involving

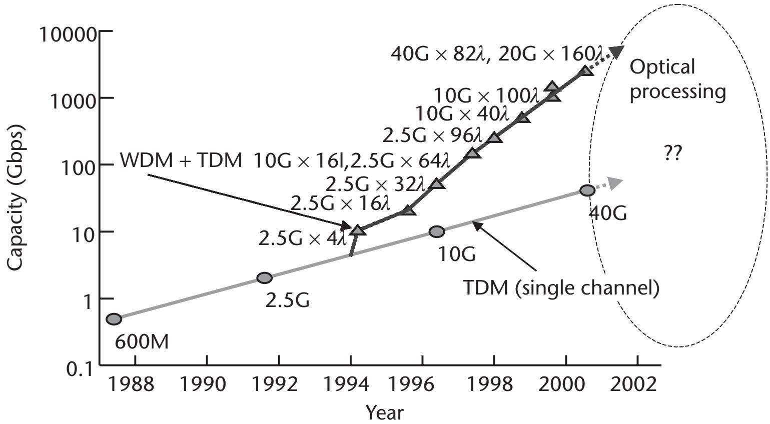

Figure 4.1 Progress in commercial lightwave systems over an approximately 15-year period. (Courtesy of Tingye Li [1].)

combinations of interactions between space, frequency, and time. A general review of this topic from several years ago is given in [3].

It is worth introducing some of the research issues for subpicosecond optical communications. A key point is that as we approach speeds significantly beyond 40 Gbps, we meet real bottlenecks from the electronic processing point of view. The rate of electronics is just not fast enough. Therefore, if we want to go much faster we must have new tools, and so we are looking at optical signal-processing tools to try to alleviate these bottlenecks. In an attempt to categorize the different topics that I discuss, Figure 4.2 shows a very simple diagram of a transmission system. The system consists of a transmitter, a channel, and a receiver. If we are thinking about very fast communications with subpicosecond pulse durations, then there are very significant issues with respect to all the parts of this system. For example, in the transmitter there is the problem that the data cannot be directly modulated fast enough to get into a single data stream, so we need optics for multiplexing or data aggregation. In this regard I will describe work we have undertaken on optical pulse shaping and parallel-to-serial conversion, which can potentially address the transmitter issue. After the transmitter we come to the fiber, which is, of course, an absolutely beautiful medium. However, when the demands placed on the fiber are sufficiently severe, certain problems emerge. For very high rates, various signal distortions must be corrected in order to achieve high-quality communications. In this regard I will describe our work on arbitrarily tunable chromatic dispersion compensators and some new work that is starting to provide results aimed at solving polarization-mode dispersion compensation problems. Finally, if we assume success at addressing transmitter and fiber issues and then turn to the receiver, we have the problem that data is arriving too fast for direct electronic processing. This means we need to employ optics to reduce the information rate or to convert from serial to parallel to try to interface with the speeds of electronics. Therefore, I will describe some of our schemes that are aimed at realizing serial-to-parallel conversion and briefly mention some other types of decoding relevant to optical code-division-multiple access.

I have already mentioned the words "time," "frequency," and "space." In my group, on the one hand we are trying to look at novel architectures for optical signal processing. On the other hand, rather than just demonstrating novel architectures, Alleviate "electronics bottlenecks" via new optical signal processing technologies for ultrafast and broadband lightwave signals.

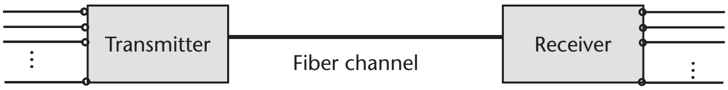

- Transmitter: data must be aggregated into an ultrafast data stream
    - Parallel-to-serial conversion
- Channel: lightwave signal distortions must be corrected
    - Chromatic dispersion and PMD compensation
- Receiver: data must be preprocessed optically prior to electronics
    - Serial-to-parallel conversion, O-CDMA decoding

Figure 4.2 Research issues for subpicosecond optical communications: opportunities for impact from optical signal-processing technologies.

we are trying very hard to engineer them in a way that we hope can ultimately have an impact in real systems. This means working not in the visible wavelength region but in the lightwave band and striving for compatibility with required speeds at realistic powers. In certain cases we still have some distance to go, but that is our goal.

I start by describing how we make very high-speed signals. It involves work on pulse-shaping or femtosecond waveform synthesis (see Figure 4.3) that I have been interested in and associated with for quite a number of years [3–6]. This provides a good introduction and presents a core idea that permeates much of our work. We (and now researchers in many other laboratories as well) start with a short pulse from our favorite mode-locked laser. This pulse could be in the range of picoseconds down to just a few femtoseconds (for applications in the ultrafast science community). Most of our work described here is in the subpicosecond range relevant to ultrafast optical communications. The idea is to start with a short pulse and transform it into a new waveform of our choosing. The technique involves sending a short pulse to a spectrally dispersive element, most commonly a diffraction grating, which causes the different frequencies or wavelengths in the pulse to spread out along different angles. With the help of a lens, they are then focused down to small spots, providing us with a continuum of optical frequencies spread out along a line. Our innovation is the introduction of a spatially patterned object. This was originally a fixed microlithographically defined mask, but for many years now a modulator array technology, namely, a spatial light modulator, has been preferred. The idea of the modulator array is to control the phase and/or the amplitude of the spectrum on a wavelength-by-wavelength basis. This allows us to manufacture very complex spectra according to our desires. By employing additional optics, we can put the wavelengths all back together. This results in a new waveform shape, as given by the Fourier transform of the pattern transferred by the spatial object onto the spectrum.

Figure 4.3 includes two nice examples. One trace shows what I like to call a femtosecond data sequence [7]. A single short pulse, here about 100 fs, goes through a mask whose Fourier transform is a sequence of pulses. We can imagine that this waveform is made up of four ones, a zero, and four more ones coming out at a few hundred femtosecond-bit spacing. In another example we place a pseudorandom

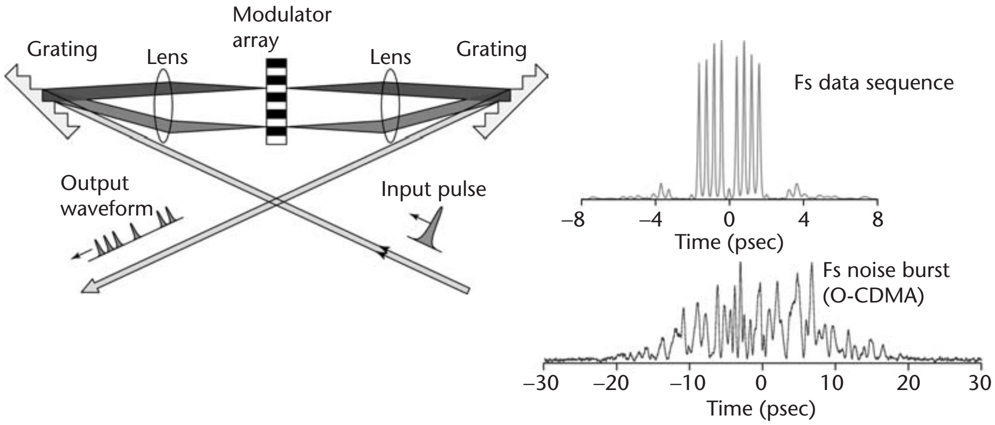

- Fourier synthesis via parallel spatial/spectral modulation
- Numerous spatial masking technologies:
  liquid crystal arrays, acousto-optics, deformable mirrors, fixed masks, MEMS arrays, galvanometers, holograms, nonlinear optics …
- Diverse applications: fiber communications, coherent quantum control...

Figure 4.3 Femtosecond Fourier transform pulse-shaping apparatus and representative-shaped femtosecond waveforms [3–6].

phase pattern onto the spectrum [4, 8]. A mode-locked pulse has a beautiful phase-locked spectrum. If we make that spectrum pseudorandom in phase, it transforms the clean modelocked pulse into what looks like a pseudonoise burst. I will return to waveforms of this sort when I talk about code-division multiple access. In general, a very wide variety of waveforms is possible.

Currently a number of spatial masking technologies are available [6]. Probably the most commonly used are liquid crystal arrays [5, 9, 10], which are the primary tool that we use in my laboratory. Acousto-optic technologies are also successfully used [11], and deformable mirrors are sometimes employed for very short pulse applications [12]. There are also a number of other devices, such as fixed masks, MEMS arrays, and galvanometers. I will even mention some work involving holograms or nonlinear optics that is starting to increase the range of functionality, allowing more complicated sorts of processing to be performed in pulse-shaping geometries.

The main focus of my group has been to look at applications related to information technology, such as fiber communications, and that is what I focus on here. But pulse-shaping has had considerable penetration in several other areas, particularly in areas of ultrafast science. One notable example is the area of coherent quantum control where physical chemists, for example, are tying to use specially engineered laser waveforms to control the course of chemical reactions [13–20]. This is a tremendously active research field at this point. Pulse-shaping is one of the key enabling technologies that nearly all the experimental research groups in coherent control are using.

Figure 4.4 shows the layout of the liquid crystal modulator arrays, which we often use in our work. The specific example of a phase modulator array is shown [5, 9]. Similar to display devices, the array consists of a sandwich of a few micron-thick

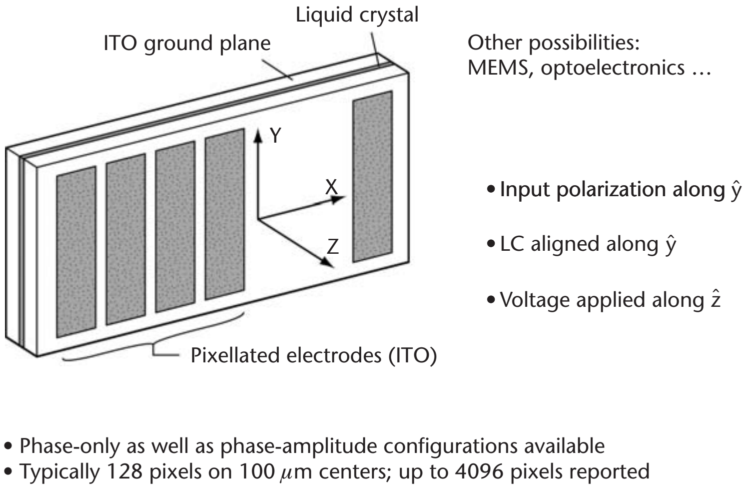

Figure 4.4 Layout of liquid crystal phase modulator arrays used for programmable femtosecond pulse-shaping [5, 9].

liquid crystal layers sandwiched between two pieces of glass. The individual liquid crystal molecules have a rodlike shape and are aligned in a particular direction. The idea is that the molecules have a relatively higher refractive index for light polarized along the molecules and a relatively smaller refractive index for light polarized the other way. This makes the liquid crystal layer birefringent. To use the device as a phase modulator, we align the liquid crystals along the y-direction (for example) and use input light along the same polarization. At zero voltage this gives a relatively large phase. Now, if we apply a longitudinal voltage, we can rotate the molecules. The voltage is applied using a set of pixellated electrodes on one piece of glass and a transparent ground plane on the other, both made from transparent indium tin oxide (ITO) films. Now the light sees a changed index of refraction and a changed phase. This results in a phase modulator where we can control the phase at each pixel independently, from zero to 2π, so we can impose nearly any spectral phase we want. By using another configuration [10], essentially taking two of these liquid crystal arrays and gluing them back-to-back (and with different, appropriately selected orientations for the molecules), it is possible to control both phase and amplitude completely independently, again on a pixel-by-pixel basis. Concerning some of the other parameters, the most typical commercial arrays consist of 128 pixels on 100-μm centers. Other commercial products with increased pixel count in a phase-only geometry have been introduced. One version that we are evaluating has up to 4,096 independent pixels. Thus, liquid crystal arrays provide a great number of degrees of freedom that can be used for pulse shaping. Liquid crystal arrays are a relatively slow technology, with reprogramming times in the millisecond range. Therefore, applications of this technology in ultrafast optical communications emphasize signal conditioning rather than data modulation.

Figure 4.5 illustrates one application using liquid crystal modulator arrays in the signal conditioning arena, namely for dispersion compensation. When a pulse is launched into a single-mode fiber, dispersion means that different frequency components have different velocities; as a result the pulse spreads out. In commercial systems dispersion is often an issue even at 10 Gbps for transmission lengths exceed-

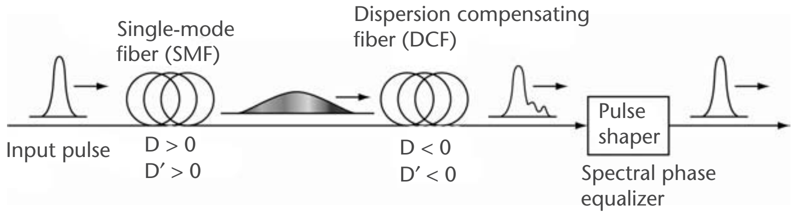

- Coarse dispersion compensation using matched lengths of SMF and DCF
- For fs applications, both dispersion and dispersion slope must be matched
- Fine-tuning using a pulse shaper as a programmable spectral phase equalizer

$$\boxed{\tau(\omega)=\frac{-\partial\psi\,(\omega)}{\partial\omega}}$$

Figure 4.5 Conceptual representation of subpicosecond pulse dispersion compensation experiments based on dispersion compensating fiber and a programmable pulse shaper acting as a spectral phase equalizer.

ing 100 km or so. Therefore, such systems rely on dispersion compensation. The tool that is most commonly used to accomplish this commercially is dispersion compensating fiber, which is a fiber that is engineered to have the opposite sign of dispersion compared to standard single-mode fiber. The fast frequencies in the first fiber are the slow frequencies in the second fiber. By matching the lengths of these two fibers appropriately, the frequencies that are spread out in one fiber come back together at the end of the second. In my group we became interested in the short pulse limits of this dispersion compensation methodology. Therefore, instead of working at 10 Gbps, we started doing experiments in the range from below 100 fs up to about half a picosecond [21–24].

When we employ an ultrashort pulse with a very broad bandwidth, it becomes essential not only to compensate the dispersion itself, but also the variation of dispersion with wavelength (commonly termed dispersion slope). Since it is generally difficult to realize perfect simultaneous dispersion and dispersion slope compensation via a fixed fiber solution, we end up with some small amount of distortion. We then use our pulse shaper in a mode that we call a spectral phase equalizer. This provides a mechanism to fine-tune out any distortion that is left after the dispersion compensating fiber. The basis for our spectral phase equalization scheme is given by the following equation:

$$\tau(\omega)=-\frac{\partial\psi(\omega)}{\partial\omega}$$

We see that the frequency dependent delay $\tau(\omega)$,which represents dispersion, is related to the spectral phase $\psi(\omega)$ through a frequency derivative. Therefore, by constructing an appropriate phase versus frequency variation in the pulse shaper, we can manipulate frequency dependent delay.

Figure 4.6 shows one example from a few years ago [23]. This represents one of a series of experiments in our laboratory where we have investigated pulses of about one-half picosecond duration transmitted through a few kilometers of standard single-mode fiber. The dispersion is extremely strong for these ultrashort pulses, with the pulse initially spreading by several hundred times. By carefully matching

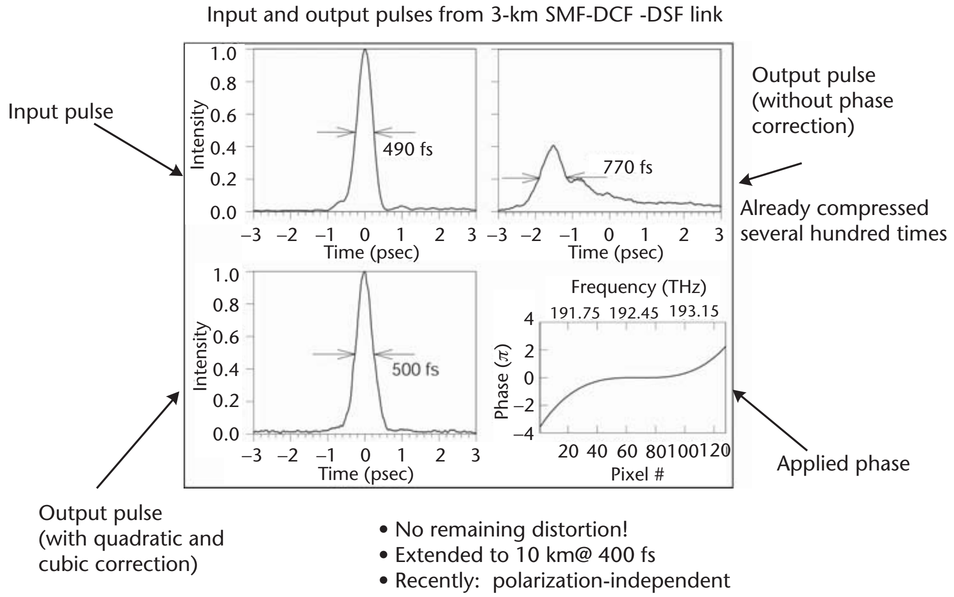
Input and output pulses from 3-km SMF-DCF -DSF link

Input pulse

Output pulse (without phase correction)

Already compressed several hundred times

Output pulse (with quadratic and cubic correction)

Applied phase

- No remaining distortion!
- Extended to 10 km@ 400 fs
- Recently: polarization-independent

Figure 4.6 Subpicosecond pulse dispersion compensation: experimental results. Input pulses approximately 500 fs in duration are propagated without distortion through a 3-km fiber link, by using dispersion compensating fiber in conjunction with spectral phase equalization realized via a programmable pulse shaper [23].

the dispersion compensating fiber to the single-mode fiber, we achieve well above 99% correction, thus ending up with a pulse that is actually rather good and only broadened by about 50%. Nevertheless, we would still like to correct that. Figure 4.6 shows a measurement of a 480-fs input pulse emerging from a 3-km single-mode fiber/dispersion-compensated fiber/dispersion-shifted fiber link. The output pulse has an asymmetric distortion that is indicative of cubic spectral phase (a phase that varies with the third power of frequency offset). Therefore, in the modulator array we program a phase versus pixel (phase versus frequency) profile that is equal and opposite to the phase causing the distortion. When we do that, the pulse is restored to a very clean, distortion-free waveform. Although this result is very good, I believe we are still far from the limits of this technique. For example, in a later experiment we used slightly shorter (400 fs) input pulses and propagated them over a 10-km fiber link [24]. As before, a distortion-free output waveform was obtained after spectral phase equalization. Even in the 10-km experiment, my estimate is that the liquid crystal modulator acting as a spectral phase equalizer was still about a factor of ten away from reaching its dynamic range limits. Therefore, full dispersion compensation using this approach may be possible out to ~100 km for 400-fs pulses! I would also point out that we have recently learned how to run the spectral phase equalizer in a mode that is independent of input polarization [25]. This is very important from a practical point of view, since polarization is usually scrambled during fiber-optic transmission.

Figure 4.7 shows a photograph of a recent version of our pulse shaper [25]. Light first emerges from a fiber, passes through a collimator, and impinges on a diffraction grating. After the grating the different frequencies contained in the input pulse spread out. A lens then focuses these different frequencies. Here we are using a reflection geometry; instead of having two gratings, we only have one grating and

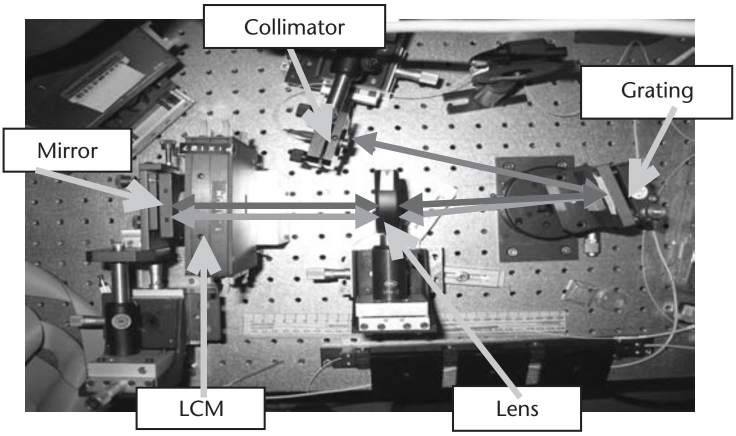

- Smaller, with reduced component count, substantially easier alignment
- 5.1 dB insertion loss (2.9 dB from shaper, 2.2 dB from circulator)
- Low PDL grating, polarization-independent operation of modulator array

Figure 4.7 Photograph of a low-loss, fiber-coupled, reflection-mode pulse shaper. The circulator used to separate the output from the input is not shown [25].

we double pass through the apparatus. We are also double passing through a commercial liquid crystal modulator array. The output light is coupled back into the original fiber and then separated using a circulator. We are able to realize a fiber-to-fiber insertion loss of ~5 dB. About 2 dB comes from the circulator; therefore, less than 3-dB loss comes from the optics and from coupling in and out of fiber. This is an acceptable level of loss for most systems applications. By using a low polarization-dependent loss grating and developing a new operating mode for these modulator arrays, we can achieve dispersion correction in a polarization insensitive way, as mentioned above.

There are a number of industrial groups, several of them in Japan, which are now working on this pulse-shaping inspired approach for dispersion compensation. A key motivation is to develop technology to tune out the dispersion slope in WDM systems. Some of the first work in this area has been accomplished at the NTT Laboratories in Atsugi over the last few years [26]. The novelty of that work involves the use of a modified arrayed waveguide grating structure to act as an integrated optic equivalent of the grating and lens used in bulk optic pulse shapers. Used together with an external fixed spatial phase mask, this provided a means to compensate dispersion slope on a channel-by-channel basis. Other work is also of interest. Shirasaki et al. from Fujitsu-Avanex have reported on a pulse shaping arrangement in which the grating is replaced by an etalon-based device called a virtual image phased array or VIPA [27]. Basically, the VIPA is a spectral disperser that can provide finer-grained wavelength resolution than a grating. They use a fixed-curved mirror in the pulse shaper to impose a wavelength-dependent phase, again for the purpose of dispersion slope compensation. Finally, in a very recent example, a Sumitomo group has investigated a reflection-mode grating pulse shaper in which they incorporate a novel MEMS modulator array [28]. The new feature of their work is that each array element is a deformable mirror that is electrostatically actuated and can bend. Their device supplies a programmable curvature at each pixel, which in a pulse shaper is equivalent to a programmable quadratic spectral phase. By applying different curvatures at different pixels, they are able to compensate dispersion slope.

I would now like to turn to polarization mode dispersion (PMD) [29]. Compensation for PMD is quite a challenging undertaking and of great current interest for industry. We have now begun to address PMD compensation in my group and are starting to make some progress; however, much remains to be done. Fundamentally, polarization mode dispersion arises from random spatially distributed birefringences in a fiber. Figure 4.8 depicts this using a simple random wave-plate model [30]. We must imagine that we have a large number of birefringent wave plates, each of which for example has random orientation. When light enters a single wave plate, we know that it experiences a polarization rotation (unless it happens to be polarized exactly along an optical axis). That polarization rotation or transformation is wavelength-dependent. If the light passes through a whole cascade of wave plates, the polarization not only becomes scrambled but it becomes scrambled in a very highly frequency-dependent way. In addition, since each wave plate is defined by a fast and a slow axis, different input polarization states of light experience different delays. Therefore, when we couple in a short pulse with a broad frequency spectrum, the result is a complex distortion in which the output signal exhibits a frequency-dependent state of polarization and frequency and input polarization dependent delay. Many in industry are trying to combat PMD because its effects become very critical for systems operating at 40 Gbps and above. Most existing compensation approaches are limited to relatively small delay distortions, which are only a fraction of the input pulse width or bit duration.

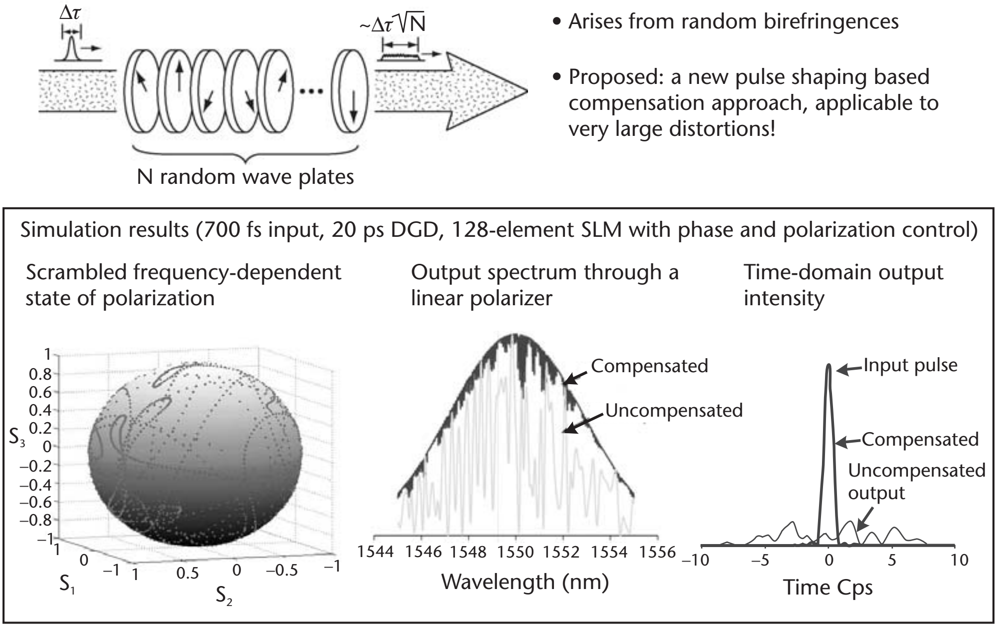

Figure 4.8 Conceptual depiction of PMD via the random wave-plate model (top). Simulation results [30] for a 700-fs input pulse after propagation through a medium with PMD with 20 ps mean differential group delay (bottom). The frequency-dependent polarization state and the output temporal waveform are severely distorted, but can in principle be corrected nearly completely if an SLM providing 128 pixels of independent polarization and phase control is available.

In my group we are focusing on a novel approach that is based on pulse shaping to provide the corrections on a frequency-component by frequency-component basis. A key goal is to realize a method applicable to compensation of very severe PMD distortion, such that the distortion in time is much longer than the duration of the input signal. To illustrate this, Figure 4.8 includes representative simulation results obtained using the random wave-plate model. For the simulations we assumed a 700-fs input pulse and a 128-element liquid crystal modulator array in a new configuration that provides not only spectral phase control but also wavelength-by-wavelength state-of-polarization control. In addition, we took 20 ps as the characteristic time scale for the delay distortions (formally this is termed the mean differential group delay). This is sufficiently large compared to the input pulse duration that most or all of the existing compensation approaches would fail. In our simulation we used a fixed input polarization state, which would correspond to a single point on the Poincaré sphere. The figure shows a Poincaré sphere representation of the output polarization, where each point represents a different frequency component. The main point to notice is that the polarization as a function of frequency is scattered over most of the surface of the sphere, which means that the polarization is completely scrambled. This illustrates the very complex frequency dependent polarization distortion we expect from large PMD.

Another way to illustrate this is to view the simulated transmission through a polarizer as a function of wavelength. Even though we start with a smooth spectrum, passing the output light through the polarizer causes the power spectrum to become completely jagged. Therefore, any polarization-dependent elements in a system would cause a huge problem. The simulations show that if we were able to use 128 independent pixels, each of which is set to correct the polarization state at that pixel, then we would obtain the result shown as the darker curve in the figure. The results are actually quite good. The reason that the simulated compensation is not prefect has to do with the finite number of degrees of freedom of the spatial light modulator (i.e., the finite number of pixels). When the wavelength variation of the polarization distortion is fast compared to equivalent pixel width, then imperfections start to appear in the compensated output. Thus, for a 20-ps differential group delay and a 700-fs input pulse, the wavelength variation is beginning to become too fast, even for 128 pixels. This effect provides the fundamental limit on the amount of differential group delay that can be compensated for a given input pulse duration.

The simulation at the bottom right of Figure 4.8 shows the temporal intensity profiles of the assumed input pulse and the simulated output waveforms, both with and without compensation. Without compensation, the pulse is completely pulled apart, both because of polarization versus frequency effects and also because of frequency-dependent delay effects. If we were able to correct both the spectral polarization profile and the spectral phase with 128-pixel resolution, the simulation predicts that we should be able to compress the pulse almost completely. Such a result would be a very significant achievement, although much further work is needed before this result can be realized.

As depicted in Figure 4.9, for the experimental implementation we envision a broadband light source being input into a fiber subject to PMD, which we would like to compensate. One possible scenario is to employ a sensor, which must have several functions. It has to sense polarization on a frequency-by-frequency basis, and

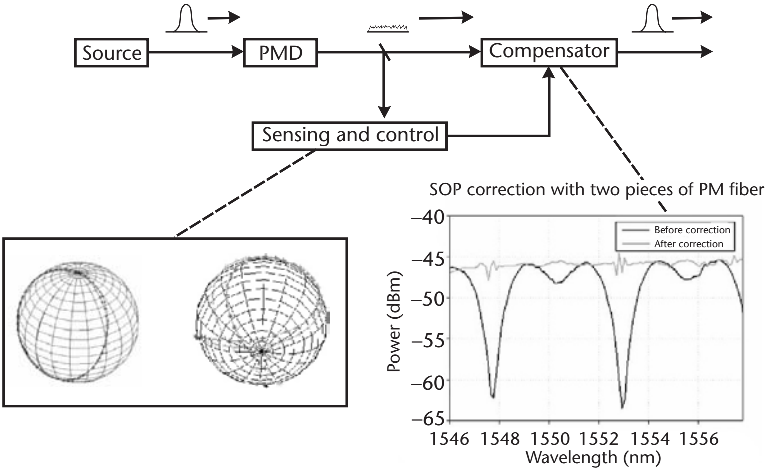

- A new wavelength-parallel polarimeter that can measure complete state of polarization for >100 wavelengths, potentially in <1ms
- A new liquid crystal modulator array permitting wavelength-by-wavelength polarization correction

Figure 4.9 Early experimental results on a new wavelength-parallel polarization sensor (left) [32] and on a wavelength-by-wavelength polarization corrector (right) [31].

it has to sense the spectral phase variation as well. This would then be fed into the compensator, which would correct all those degrees of freedom and consequently output a nice restored pulse. For real-world applications, it should complete this operation fairly quickly, since the PMD is not fixed in time. Although the required response time for PMD compensators is still under discussion, time scales for change in PMD effects due to environmental variations and especially artificial disturbances can be as fast as milliseconds. Therefore, we view millisecond response as a target for our compensator.

Our initial efforts are directed at sensing and correcting the wavelength-dependent polarization state. Future efforts will aim at demonstrating correction of the delay effects. Below I describe some new results on polarization sensing and polarization correction that we have recently reported in detail for the first time [31, 32]. On the sensing front, we have been able to build a new polarimeter that works much faster than existing technologies. All existing polarimeters are single channeled; they achieve at best perhaps a few thousand measurements per second. We have built a novel multichannel polarimeter taking advantage of arrayed InGaAs detector technology and fast ferroelectric liquid-crystal-switchable wave plate technology that allows us to cycle through the different aspects of a polarization measurement very quickly [32]. This provides the potential to measure the complete state of polarization of 256 different wavelength components in parallel in under 1 ms (though the actual operation is currently limited to a few milliseconds by software). In this first demonstration, we set up the apparatus to cover a spectral range of about 100 nm, but that can be scaled to other values. Figure 4.9 shows two examples of data. In one case, a single piece of polarization-maintaining fiber causes the output polarization as a function of wavelength to lie on a circular trajectory round the Poincaré sphere, as expected. In a second example with a more complicated polarization distorter, the wavelength-dependent polarization exhibits a more varied trajectory. In both cases, our apparatus is able to measure this in milliseconds.

We also have results on the polarization corrector system [31]. For these experiments we have performed measurements using conventional polarimeter technology; we intend to integrate our wavelength-parallel polarization sensor with our polarization corrector in future work. We are performing polarization correction by using a new liquid-crystal modulator array geometry obtained through a collaboration with CRI, Inc., a vendor of liquid crystal modulator arrays. Our approach allows us to take any input state of polarization and restore it to fixed linear polarization, for example pointing vertically. We first measure the polarization state as a function of wavelength and then correct it on a wavelength-by-wavelength basis, as shown in Figure 4.9. In these first experiments we used transmission through a polarizer as a metric for wavelength-dependent polarization. Without correction there was greater than 15-dB variation in the transmission through the polarizer. With the help of our array, we can equalize this and obtain a flat output spectrum through the polarizer within 1 to 2 dB. Thus, we already have some experimental success. We are looking forward to further progress in our future work.

I will now discuss work related to the receiver problem for ultrafast optical communications. Figure 4.10 shows a schematic for a time-to-space converter or serial-to-parallel converter. Here we imagine an incoming stream of ultrafast optical data, for example at a few hundred gigabits per second. In contrast to conventional demultiplexer techniques, where one switches out one time slot at a time, to arrive for example at 10-Gbps demultiplexed data in a serial stream, I will focus on an architecture organized around frame-by-frame or block-by-block conversion. We therefore have a single reference or sampling pulse. Instead of just acting on the one pulse that is lined up with it, the reference pulse interacts with a frame of pulses and converts them into parallel. This constitutes a time-to-space converter with applications to waveform measurement or frame oriented serial-to-parallel operation. I will show experiments demonstrating this basic functionality and then describe our efforts to address the practical problems, such as working at communication wavelengths. The most difficult challenge involves the need to scale the power down to where we can run this full duty cycle at the desired average power levels.

So how does this work? What I describe is not in fact spectral nonlinear optics, which is what we really do now, but something called spectral holography [33, 34], which is easier to explain. This work was undertaken several years back with Martin

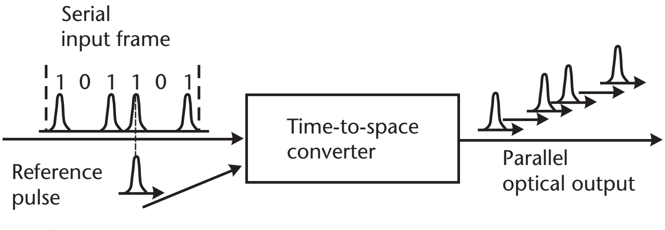

Applications
- Waveform measurement
- Frame-by-frame conversion for parallel detection or processing

Requirements for lightwave
- Speed: conversion process must be intrinsically fast
- Sensitivity: must scale to Gframes/sec at realistic power
- Wavelengths: 1.55 μm band

Figure 4.10 Conceptual diagram of a time-to-space or serial-to-parallel converter that performs frame-by-frame conversion of ultrafast serial input data for parallel detection or processing.

Nuss [35], who was at Bell Laboratories at that time. The idea is that we have the first half of a pulse shaping setup, namely a grating and a lens, as shown in Figure 4.11. However, instead of a modulator array we now have a dynamic holographic medium. This will act like a mask that is written by the incoming information. Instead of just having one beam coming in, we actually have two beams, which is analogous with normal spatial holography. We call our approach spectral holography. In normal holography we have a plane wave, which is just a spatially uniform beam. In spectral holography we have a reference pulse, which is simply an unshaped short pulse whose spectrum is essentially flat; this is approximately a spectral plane wave. The second beam, which we call a signal pulse, has information of interest that we can view in either the time domain or frequency domain. Both beams impinge on the grating and are both spread out so their frequencies are dispersed along the line. At the Fourier plane the different beams interfere with each other on a frequency-by-frequency basis and write a hologram. Our work was performed using a dynamic multiple quantum well holographic medium. This medium has a response on a millisecond to microsecond time scale, which is quite fast for a holographic material but still slower than we want. The spectral hologram that is recorded encodes information about the signal pulse spectrum. Then we read out with a continuous-wave plane wave. The hologram is now interpreted as spatial information. The readout beam diffracts off the hologram and then goes through a Fourier transform lens, which produces an output with a spatial pattern that is a scaled version of the spatial Fourier transform of the hologram. However, the hologram is the Fourier transform of the input temporal pattern. So with this approach, there are two Fourier transforms. This brings us back to where we started, except that instead of having a pattern in time we have a pattern in space. As one simple example, Figure 4.11 shows data from a series of experiments where the signal pulse was simply delayed with respect to the reference [35]. Here the relative delay constituted the information. When we look at the output on a CCD camera, we find that as we delay the signal pulse with respect to the reference, the output spot moves across the screen, so this really performs a time-to-space conversion.

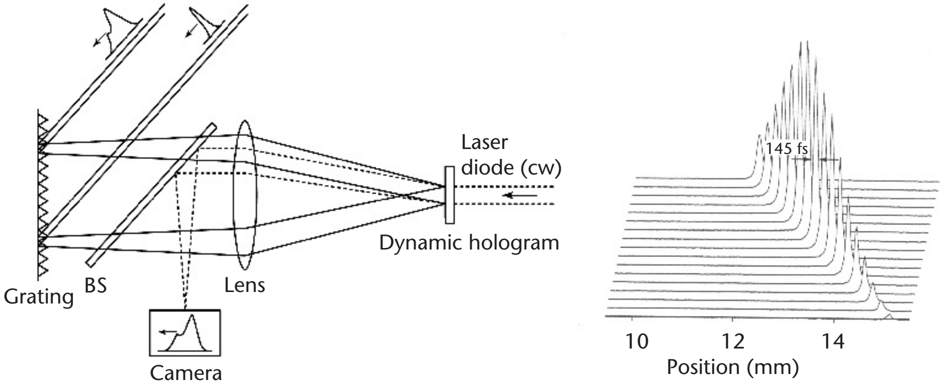

The temporal profile of the input signal pulse is converted into a spatial profile at the output.

Changing the delay of the signal pulse causes the output spot observed on a CCD camera to move across the screen in real time

Figure 4.11 Setup for time-to-space mapping via spectral holography (left) and experimental results in which the delay of a signal pulse is converted to a shift in spatial position (right) [35].

As I have already mentioned, even if holograms are dynamic, they are not fast enough. We are really interested in frame rates that are well into the subnanosecond regime. A path to realizing that involves spectral nonlinear optics, where we replace the slow holographic media with faster nonlinear optical crystals. Specifically, we are pursuing second harmonic generation in our research. The experimental apparatus is a little more complex than that for spectral holography, but the basic idea is quite similar. Figure 4.12 shows cases where we built up simple data frames of ultrashort pulses to act as the signal beam [36]. The individual pulses were a few hundred femtoseconds in duration at 1,550 nm, separated by about 2 ps. The figure shows images of these pulses that all come out in parallel for three different inputs: four ones, two pairs of ones with a zero in between, and so forth. This was the first time this time-to-space conversion was accomplished via spectral nonlinear optics in the lightwave band. Historically, the first experiments performing spectral nonlinear optics using the second harmonic nonlinearity were reported by the Fainman group at University of California at San Diego, who worked with a titanium:sapphire laser [37]. In our work, we translated this scheme to the lightwave band [36] and identified a way to increase the nonlinear optical efficiency by more than two orders of magnitude [38]. This is important since efficiency and sensitivity are usually key issues associated with nonlinear optics in the rather unusual geometry of a time-to-space converter.

In one set of experiments, we placed a photodiode at the spatial location corresponding to one of the stripes seen in the figure and observed the output with a fast oscilloscope [36]. A key result is that we were able to detect the individual pulses with beautiful signal to noise, in real time and with no signal averaging, directly at the 80-MHz rate corresponding to the laser source used in these experiments. Although further progress is needed, we are beginning to approach an average power and repetition rate regime that would be suitable for real high-performance applications.

For further progress I believe that we need to scale from bulk nonlinear materials, such as the 2-cm-long bulk periodically-poled lithium niobate (PPLN) crystal used in the current experiments, to more sophisticated PPLN waveguide chips, as

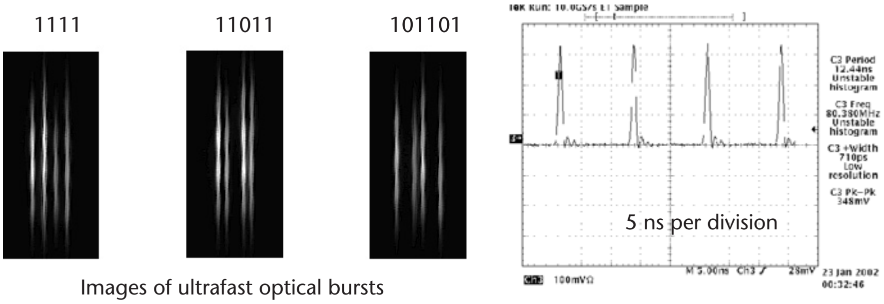

Images of ultrafast optical bursts
(2 ps pulse separations)

- First spectral nonlinear optics time-to-space converter in the lightwave band!
- Power in time-to-space image is sufficient for real-time detection with good signal to noise!

Figure 4.12 Experimental results with time-to-space mapping via spectral nonlinear optics operating in the lightwave communications band [36]. Left: images of three different ultrafast data packets. Right: real-time detection of one pixel in a time-to-space mapping image in real time with no signal averaging.

described in the article by Professor Fejer in [39]. One area that we are very excited about would involve development of new geometries for PPLN technology, planar waveguide geometries for example, that would be compatible with the types of optical processing that I have been describing. Professor Fejer and I have submitted a joint funding proposal which, if funded, would allow us to embark on this research. The waveguide approach could really reduce the power levels to a point that would allow practical applications for high duty cycle demultiplexing, for example. In terms of technologies, if we really want to achieve this, there are many interesting packaging issues. Probably a very nice way to address them would be to utilize hybrid planar lightwave circuit (PLC) and PPLN approaches, as described by Professor Fejer in [39].

Another research activity related to the receiver problem in ultrafast optical communications involves optical code-division multiple-access (O-CDMA) [40–43]. CDMA is a communication technology that is widely used in cellular radio. For example, many cell phones use CDMA, which basically involves using different coded signals, in other words different complicated noise bursts, to distinguish between different users and to share the communications medium. For several years I have been interested in finding out whether this could be accomplished in ultrafast fiber optics [8, 40, 41, 44, 45]. One driving motivation was that our pulse shapers provide a unique enabling technology needed to accomplish the very fast optical encoding and decoding that would be required.

Recently the Defense Advanced Research Projects Agency (DARPA) has invested in this research; they now have a new program funding several groups that are trying to develop O-CDMA demonstrations and to explore potential unique advantages of this approach. One can imagine advantages such as information security at the physical layer, soft-limited capacity, and so forth. At this point I do not think anybody has really studied this topic in enough depth to know if there are any hugely beneficial advantages, but part of the exercise is to better understand the potential advantages. Our work is a collaborative program involving my group and that of Professor Fejer at Stanford, since we are using PPLN channel waveguide chips [46] as the decoder technology. A key issue is that we have different coded waveforms with very fast time structure, so we need some kind of specialized ultrafast nonlinear processing to distinguish one ultrafast waveform from another. We have shown that if we use second harmonic generation in a slightly unusual operation mode, we can actually perform this waveform discrimination operation [47–49]. Figure 4.13 shows examples of data that we have gathered and reveals that, with very good contrast, we can tell the difference between the desired waveform and an undesired waveform. In some of the experiments, we have actually reached about 30-dB contrast for desired and undesired users [47]. We can accomplish this operation at a very interesting power level, namely about one quarter of a picojoule per pulse, which at this 40-MHz rate is only about 10 μW [48]. Even at that very low average power level, we are already reaching a second harmonic conversion efficiency of several tens of percent. This is extremely efficient, and now under the DARPA program, we are trying to scale this up to the gigabit per second range. Our goal over about the next year and a half will be to try to run at per user rates of 2.5 Gbps with two to three users. If we are successful, then we hope to go beyond that in the future.

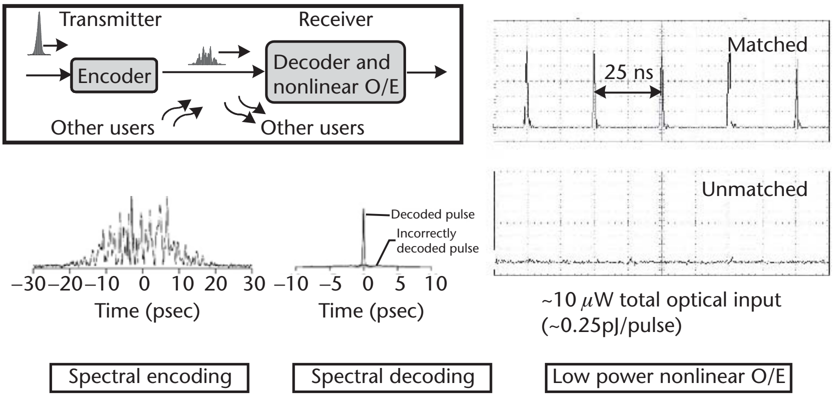

Figure 4.13 Femtosecond O-CDMA: schematic diagram, experimental coding and decoding results, and data from a low-power nonlinear discriminator (nonlinear O/E) that can be used to suppress multiaccess interference from improperly decoded signals [48].

Let me now return to ultrafast optical communications transmitter technology and describe a parallel-to-serial converter, as shown in Figure 4.14, which I sometimes call an ultrafast optical word generator or space-to-time converter. This is the converse to the time-to-space converter, although we still adopt the philosophy of frame-by-frame processing. Here we would like to have a box that we can connect to parallel data, for example electrical data words on a computer, and obtain a serial optical sequence in the time domain corresponding to this electrical data. In particular, I will describe here an optical subsystem that can be read out by a single ultrashort pulse to yield a time-domain pulse sequence corresponding to the parallel data pattern [50–52]. I have already briefly described Fourier transform pulse shapers that, in principle, can perform this function; however, such shapers work according to a Fourier transform relationship, which means that if we want a certain data pattern, we need to first determine its Fourier transform. Unfortunately, the time needed to calculate such Fourier transforms would prohibit operation at the desired subnanosecond frame rates. So we became interested in developing a direct mapping technology in which a spatial pattern in the pulse shaper is directly converted into the ultrafast time domain, without any Fourier transform. In our research to date we have used fixed static masks to perform the spatial masking function. However, the subsystem I will describe is inherently compatible with the use of subnanosecond

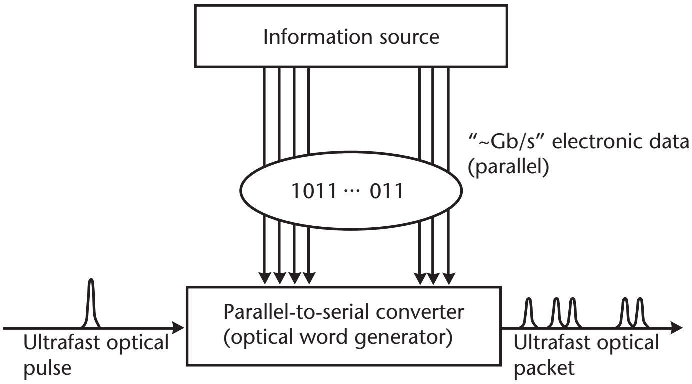

Figure 4.14 Conceptual diagram of a parallel-electronic-to-serial-optical converter.

optoelectronic array technologies for spatial patterning. In parallel with the work I will describe here, we are working within my laboratory to fabricate an array of optoelectronic modulators that we hope to be able to use in high-speed parallel-to-serial conversion experiments in the future.

I now describe the novel optical subsystems we have developed in this research. Figure 4.15 shows the layout of a direct space-to-time converter. There is some resemblance to a Fourier transform shaper, in that both contain a grating and a lens and have a short pulse coming in. The differences are that instead of there being a mask at the Fourier plane, there is just a simple slit. The layout is equivalent to a conventional spectrometer. If a short pulse comes in to a spectrometer, it is spectrally filtered; because it is filtered, we end up with a long pulse. This is well known. The new feature here is that we bring back our spatially patterned mask (or in the future, potentially a rapidly programmable modulator array), which now we place near the grating. What happens if we send in a short pulse, spatially pattern it, and pass it through our spectrometer? Well, it turns out that after completing the Fourier optic analysis, we obtain a new time domain waveform, which directly reflects the spatial pattern. There is a direct scaling between time and space, with no Fourier transform [50, 51]. A simple way to understand this is that whenever a short pulse emerges from a spectrally dispersive element, such as a grating, it has a tilted pulse front [53]. This means the time delay of the pulse varies with lateral spatial coordinate. Thus, space actually encodes delay. If you block different spatial elements of the beam, you block different time elements as well. Figure 4.16 shows some examples. We originally performed this experiment at 850 nm [50] and later transitioned to the lightwave band [52]. For the left side of Figure 4.16, we had a simple spatially patterned gold-on-glass mask at the input to the apparatus [50]. This completely blocked the light, except for 20 equally spaced windows where the mask was transparent, as defined by the lithography. The time domain trace shows one pulse for every opening on the mask. Figure 4.16 (lower left) shows what I call a data packet. Here we used a similar mask, except that some of the window locations are now filled in with gold, hence they are opaque. At each location where the window is filled in, the pulse disappears with beautiful contrast. These are very clear demonstrations of conversion from space to time.

Another point to notice is the temporal rolloff. This arises because the input had a Gaussian beam spatial intensity profile, which is also converted by the apparatus, resulting in the temporal rolloff.

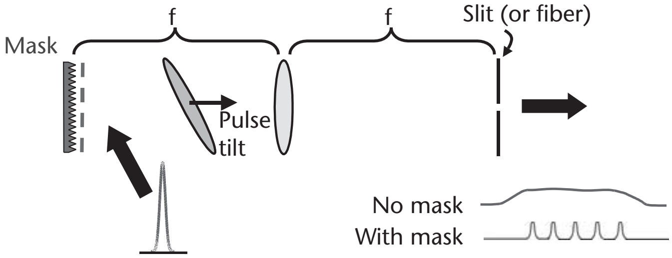

Figure 4.15 Layout of a direct space-to-time (DST) pulse shaper. The output temporal waveform generated in response to an ultrashort pulse input is a directly scaled version of the spatial pattern at the input. The encoding of delay onto the transverse spatial coordinate may be understood in terms of the tilted pulse front after the grating.

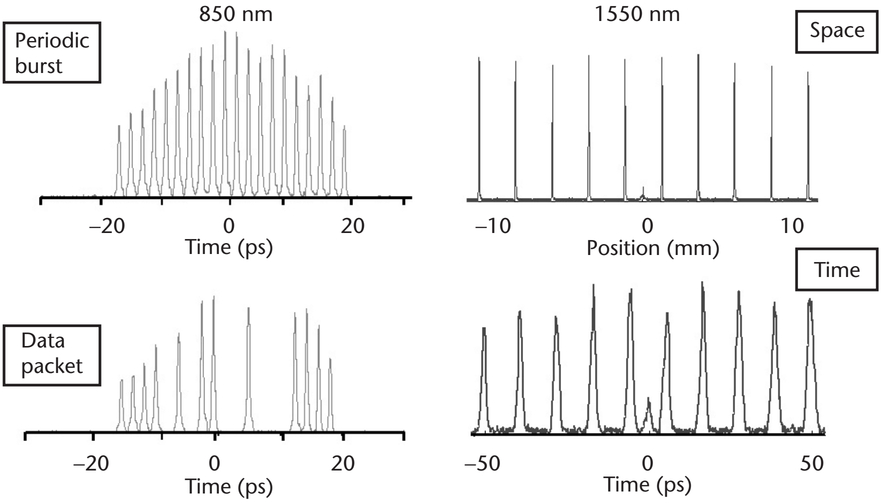

Figure 4.16 DST pulse shaper data. Left: Periodic pulse burst and modulated pulse burst (data packet) at 850 nm [50]. Right: Spatial profile at input to a 1,550-nm DST pulse shaper and corresponding output temporal profile [52].

For the data on the right-hand side of Figure 4.16 [52], we were interested not only in moving to 1,550 nm, but also in trying to correct the temporal rolloff. This was achieved by introducing custom diffractive optical elements prior to the DST pulse shaper to produce an array of equal intensity beams. For the example shown in the figure, the input consists of ten evenly spaced, equal intensity beams. The direct space-time pulse shaper maps this spatial input pattern into time fairly well. We can even notice imperfections in the input spatial profile that end up becoming imperfections in the time domain profile (see the small feature at 0 mm and 0 ps, respectively).

Our DST pulse shapers were read out initially using low-repetition-rate mode-locked lasers, either a Ti: sapphire laser at ~80 MHz or an erbium fiber laser at ~40 MHz. By using a higher repetition rate source, for example a 10-GHz mode-locked fiber laser, then instead of isolated pulse bursts, we can obtain pulse sequences with 100% duty cycle. Figure 4.17 provides examples of data from such

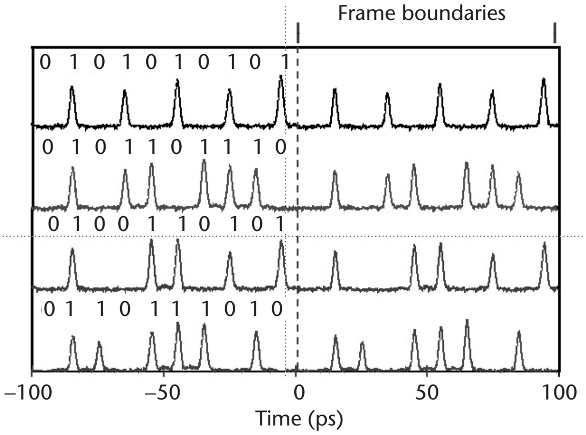

Figure 4.17 A 100-GHz optical word generation from a DST pulse shaper, read out at 10 GHz. The pulse sequence is arbitrary within one period and repeats at the source repetition rate [52].

experiments [52], each of which consists of different frames of data at 100 Gbps within a 100-ps frame. Because we are using a fixed mask, the temporal pattern repeats itself periodically every time we read it out (in these experiments, the readout rate was 10 GHz). In the future it should be possible to use synchronized modulator array technologies to change the spatial profile on a frame-by-frame basis, which would provide the ability to program independent data for every frame.

Thus far, all of our discussions on DST pulse shapers has been related to bulk optics. I now describe how this functionality can be accomplished in integrated optic, planar lightwave circuit technology [54–56]. Figure 4.18 shows the bulk optics setup along with a planar lightwave circuit implementation based on arrayed waveguide grating structures. The disc in the figures is a U.S. quarter to set the size scale. Clearly the planar lightwave circuit implementation has a major advantage in terms of compactness.

Figure 4.19 depicts an important analogy between the direct space-to-time pulse shaper and the AWG [57], which is an important component for multiplexing or demultiplexing optical frequencies in WDM communications. The AWG is a planar lightwave circuit based on silica-on-silicon material. At the input, a fiber connects to a channel waveguide, which then leads to a slab region where the light spreads laterally until it impinges on an array of waveguides. This array of waveguides incorporates a uniform delay step from one waveguide to the next, all the while maintaining phase coherence. This means that the delay is controlled to an extremely small fraction of a wavelength, which allows the AWG to function as an integrated optic grating. This is the first part of the analogy. The output ends of the waveguides in the array typically lie on a curved surface. This provides a focusing function, analogous to the lens that appears in the bulk DST pulse shaper. At the output of the AWG, there is a series of waveguides to accept the different demultiplexed optical frequencies. In terms of our DST pulse shaper, we view each of these output waveguides as a spatial slit. This essentially completes the analogy. With this insight, we started to look at time domain functionalities of these devices. In particular, based on this analogy, we anticipated that if an ultrashort pulse were coupled into an AWG, the output would be a sequence of pulses corresponding to a scaled version of the spatial pattern present at the output side of the waveguide array.

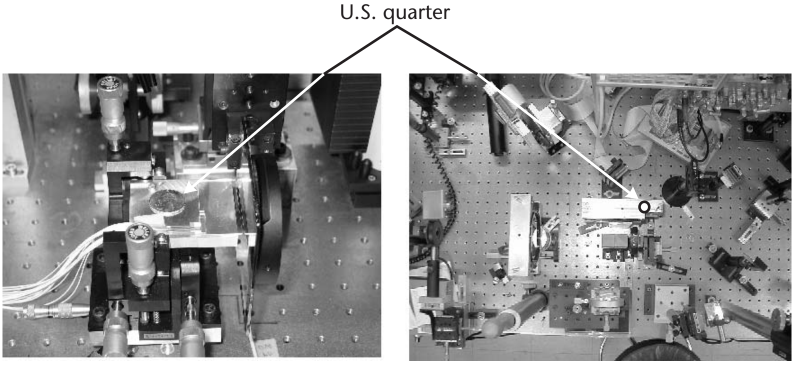

Arrayed waveguide grating (AWG) implementation

Bulk optics implementation

Figure 4.18 Photographs of bulk optics DST pulse shaper setup and an integrated implementation based on an arrayed waveguide grating (AWG) structure.

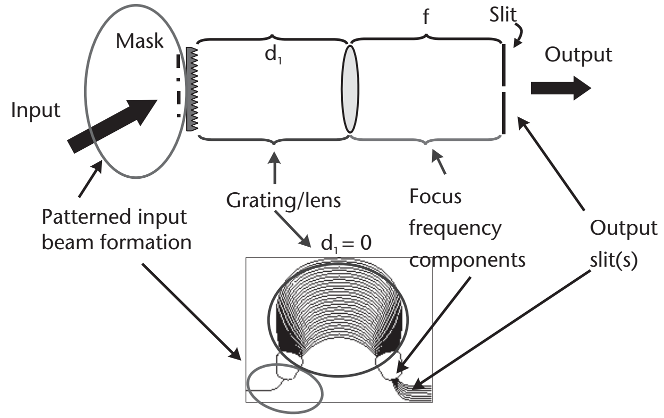

Figure 4.19 The femtosecond response of an AWG device may be understood through an analogy with the direct space-to-time pulse shaper.

Figure 4.20 explains this in another way, which we refer to as the "one guide, one pulse" design methodology. When we excite the AWG with a short input pulse, it excites all the waveguides in the array. Each waveguide that is excited contributes an individual pulse to the pulse sequence observed at any single output guide. There is a very clear mapping between each of the different waveguides in the array and each of the different pulses in the output pulse sequence. The delay of each output pulse depends on the delay of the corresponding waveguide in the array. The "one guide, one pulse" mapping also means that if we start to modify the waveguide array (e.g., if we cut off certain waveguides or insert loss), we can start to manipulate the pulses on a pulse-by-pulse basis. This is a spatial patterning idea originating from the direct space-to-time pulse shaper.

Our experiments testing these ideas were performed in close collaboration with Dr. Katsunari Okamoto, who was at NTT at that time, and has led to a number of publications [54–56, 58]. Figure 4.21 summarizes two key results. The first trace (left) describes a conventional AWG structure with parameters chosen to be compatible with our test pulses. The AWG takes a single pulse input and converts it to a

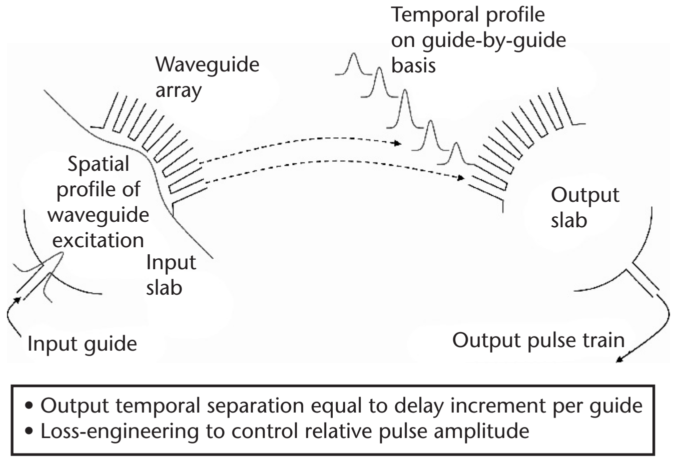

- Output temporal separation equal to delay increment per guide
- Loss-engineering to control relative pulse amplitude

Figure 4.20 One guide, one pulse design methodology for pulse sequence generation from an arrayed waveguide grating.

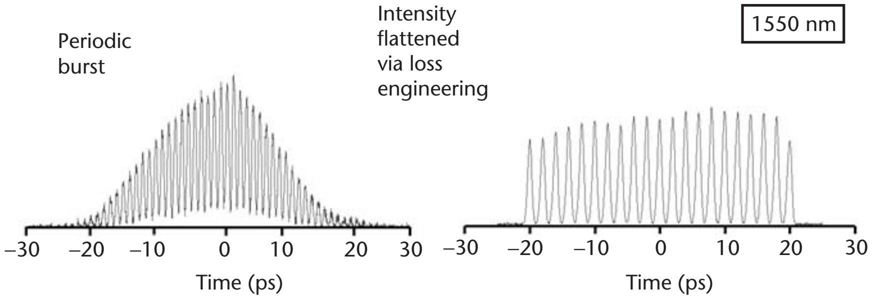

- New functionality for an established WDM technology
- Close analogy with DST pulse shaper provides insight for waveform engineering

Figure 4.21 Data demonstrating femtosecond pulse sequence generation using (left) a standard AWG and (right) a modified AWG structure [54, 55].

train of pulses. The pulse repetition rate is 1 THz, corresponding to 1-ps pulse spacing; this is equal to the 1-ps delay increment per guide, in accord with the one guide, one pulse concept. A temporal rolloff is observed, as with the direct space-to-time pulse shaper; here this can be understood as a result of the Gaussian excitation profile of the different waveguides in the array [54].

After this nice initial result, we were interested in trying to make intensity equalized output trains, similar to our research in bulk optic pulse shaping systems. For this research another group of devices was fabricated, where different fixed losses were inserted in different waveguides with a view to attenuating each pulse by just the right amount. The waveguide array was cut off outside the central 21 waveguides, resulting in an output pulse train consisting of 21 individual pulses (Figure 4.21, right). Here the repetition rate was 500 GHz, corresponding to the 2-ps delay increment per guide chosen in fabricating the modified AWG. The important point is that the intensity across the temporal profile is substantially equalized, as intended [55].

We have obtained two other sets of results recently. Figure 4.22 shows a new result in which intensity-equalized AWGs are employed in a unique approach to repetition rate multiplication [59]. In previous work, planar lightwave circuit technologies based on cascaded interferometer architectures have been used for repetition rate multiplication [60]. Our work with AWG structures provides a new set of

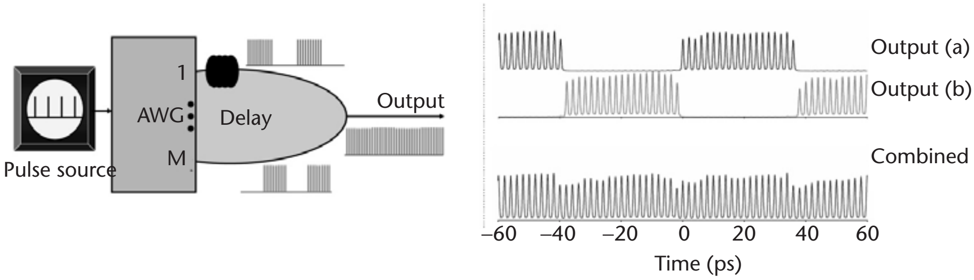

- Makes use of the multiple output property of AWG pulse train generators
- Engineered AWGs offer alternative to conventional cascaded interferometer architecture
- Offers potential for very large multiplication factors

Figure 4.22 Application of intensity-equalized AWG for repetition rate multiplication. An input pulse train at 13.2 GHz is multiplied up to 500 GHz [59].

tools with which to realize such functionalities, which expands the design space. As before, we read out the AWG with a short pulse, thereby generating output pulse trains. In this experiment, we were reading out the AWG with pulses whose repetition rate was in the range of 10 GHz and above. The individual output trains were on the order of 40 ps in duration. In the example shown in Figure 4.22, we were reading out at 13 GHz. For repetition rate multiplication, we take advantage of the fact that a family of output waveforms is observed at the different output guides. At each output guide the temporal intensity profiles are the same, although the waveforms are slightly frequency shifted with respect to each other by an amount that is much less than the total optical spectrum. It is possible to use all of these outputs (e.g., to recombine them). To demonstrate this, we recombined two of the outputs, which leads to a 500-GHz pulse train. These results demonstrate a 38-fold multiplication of the repetition rate of the incident pulse train.

One other new development was realized with the support of the Optoelectronic Industry Development Association under the Joint Optoelectronics Program, a program that facilitated exchange of precommercial component technologies between device groups and systems researchers in the United States and Japan. Figure 4.23 shows the concept for modified AWG devices that we actually designed before performing the other research described above [61]. These devices are a very direct analog of the bulk optic direct space-to-time pulse shapers. Essentially the device has a normal AWG structure, but with one of the facets cut off to provide direct optical access to the waveguide array. This provides the possibility to perform some external spatial patterning in order to control the spatial excitation profile in the waveguide array. The idea is that we focus an external short pulse beam onto the end facet, which can be patterned using spatially patterned masks. In the future we hope

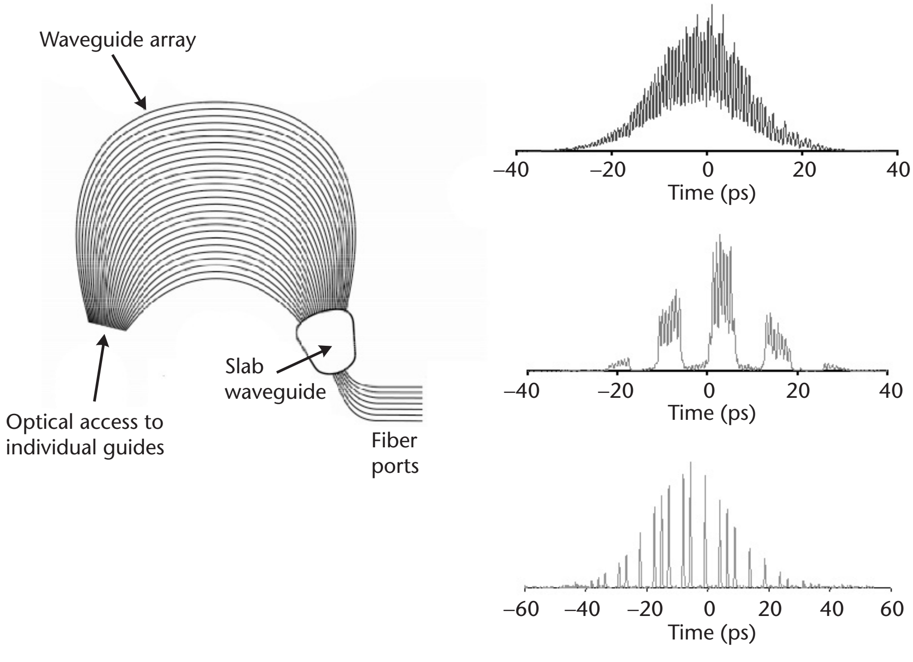

Figure 4.23 A modified AWG structure with one facet cut off to provide direct optical access to the waveguide array. Data with spatially patterned, short-pulse input beams demonstrate direct space-to-time pulse shaping action [61].

to be able to use modulator arrays to control which guides get excited. This would provide programmable control over the output intensity profile.

We have performed experiments using an AWG structure designed for 600-fs delay increment per guide. The input pulses were 300 fs in duration. The top trace in Figure 4.23 shows the output pulse sequence without using a spatial mask; the different pulses from each of the output guides are resolved, but just barely. By introducing a spatial mask, we can block excitation of some of the guides. Then, as shown in the center trace, we obtain a modulated burst of pulses; pulses corresponding to the nominally blocked waveguides are largely extinguished. Finally, in the most recent experiment, we had a configuration with a larger time increment between guides, which allowed us to cleanly resolve the individual output pulses. As shown in the bottom figure, we can now cleanly turn on and off individual pulses [61].

Our work is the first to look carefully at the short pulse time-domain behavior of AWG technology. I believe that we are just scratching the surface of some of the possible functionalities, and I hope to see this line of research go much further.

Finally, I briefly describe a new research field in which we have become involved. As I have described, the limited speed of electronics means that we need optical signal processing technologies to support ultrafast optical communications. In our recent work, we are asking whether our ultrafast optical signal processing approaches can provide any benefit to the world of radio frequency (RF) electronics. At present, we are exploiting optical arbitrary waveform generation (pulse shaping) as a tool for arbitrary RF waveform generation [62, 63]. As depicted in Figure 4.24, the idea is to start with modelocked laser pulses, which are shaped in an optical pulse shaper. Either a Fourier transform pulse shaper or a direct space-to-time pulse shaper will work. In our particular experiments, we chose the direct space-to-time pulse shaper. The idea is simply first to generate a shaped optical waveform and then use it to drive a high-speed optical to electrical converter (O/E). In the experiments I describe here, we use a 60-GHz commercial photodiode. An important point is that the photodiode response is slow compared to individual features in

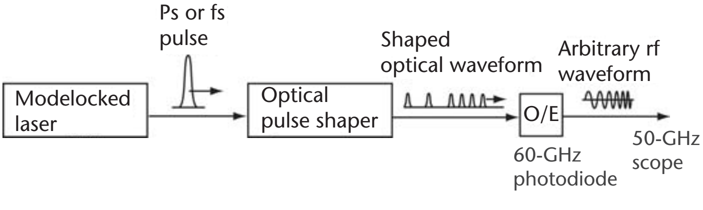

- Exploits optical pulse shaping technology, where we have very strong capability, for cycle-by-cycle synthesis of arbitrary waveforms in the mm-wave band
- Already demonstrated in the 25-50 GHz band; much higher than the commercial state of the art (~2 GHz)
- Can be extended to cover lower frequencies (e.g., 1-10 GHz)
- Potentially a new enabling technology for UWB wireless, pulsed radar, electronic countermeasures, …

Figure 4.24 Photonic synthesis of arbitrary radio-frequency electrical waveforms. Optical pulse shaping technology is employed in conjunction with a fast photodetector for cycle-by-cycle synthesis of structured electrical waveforms.

the optical waveform; consequently, the photodiode smoothes out the drive signal in converting it to an electrical waveform. The idea is that if we control the optical waveform correctly, it should be possible to synthesize interesting, very broadband RF waveforms. Significantly, it should be possible to access bandwidths much higher than the commercial state of the art, where arbitrary electronic waveform generators with bandwidths up to about 2 GHz are available. In the work I describe here, we are working in the 25- to 50-GHz band. In other research, we are working in the lower gigahertz range but still above the commercial solutions. It is too early to say specifically what the applications will be, but our idea is that if we can create new technologies in this important frequency range, there are likely to be applications in areas such as ultrawideband wireless communication and for defense applications such as electronic countermeasures and so forth.

I shall provide two examples of our results [62]. Figure 4.25 shows an example of millimeter-wave frequency modulation. Here the idea was to generate a simple optical pulse sequence and then use a fast photodiode to convert it to a smooth electrical signal. Changes in the pulse spacing in the optical waveform are converted into changes in the frequency of the millimeter-wave electrical waveform. In the first part of the waveform, we obtained three relatively high frequency ~48 GHz) sinusoidal cycles, with one electrical cycle per optical driving pulse. We chose the pulse train so that later in the waveform, pairs of pulses were grouped together too closely to be resolved electrically. This allowed us to stretch the duration of individual features in the electrical waveform. The result is two additional cycles at 24 GHz, which are at least a reasonable fit to a true sinusoid. So within a single very short waveform, we are already demonstrating synthesis of different frequencies on a cycle-by-cycle basis over quite a broad bandwidth.

Another interesting point with regard to this experiment is that different optical pulses are intentionally chosen to have different amplitudes. Although the experiment is still fairly crude at this point, we have nevertheless successfully manipulated the relative amplitudes of the optical pulses in order to equalize the amplitude of the electrical signal. Without this approach, the two 24-GHz cycles become significantly stronger than the 48-GHz cycles (e.g, due to the rolloff in the frequency response of

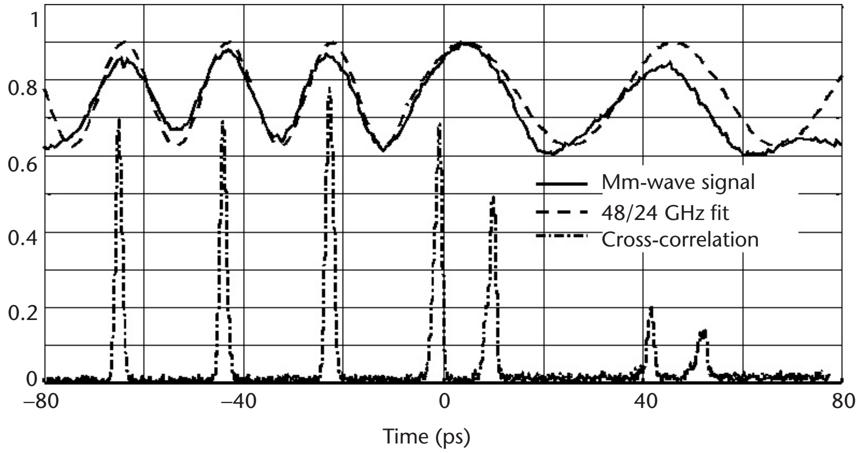

Figure 4.25 Abrupt millimeter-wave frequency modulation achieved via optical pulse shaping control [62].

the electrical system). This is an example of equalization: we apply control in the optical domain in order to predistort the input in such a way that the desired electrical signal is obtained at the output.

Figure 4.26 shows another example, where we insert abrupt π phase shifts into 48-GHz sinusoids. In this work, the phase shift can be controlled abruptly on a single-cycle basis, which is difficult to accomplish via other approaches. The optical driving waveforms consist of a train of six pulses. Between the first optical waveform and the second, we simply introduced a half period of delay between the second and third optical pulses. The resulting electrical waveform is a burst of six approximately sinusoidal cycles, where we obtain a π phase shift exactly at the position corresponding to the additional optical delay. Here optical timing is converted into radio-frequency electrical phase. As shown by the other waveforms in the figure, we can also insert the optical timing shifts at different locations, which in turn controls the location of the electrical phase shift.

We also have other examples of radio-frequency arbitrary waveform generation in our laboratory. In the experiments described above, we used low repetition rate modelocked lasers, which produce isolated burst optical and electrical waveforms. We have also performed similar experiments based on a modelocked laser with 10-GHz repetition rate. This allows us to generate continuously repeating versions of these waveforms [63]. With the right modulator technologies for use in our optical pulse shapers, we may be able to make completely arbitrary frames of electrical waveforms that can be reprogrammed on a frame-by-frame basis and then coherently stitched together. That is one of our challenging goals for the future.

In summary, I have described several examples of activities under way in my laboratory, in which we seek to take advantage of the relationships between time, space, and optical frequency to gain new capabilities for ultrafast optical signal processing relevant to high-speed manipulation of information. These time-space-frequency techniques represent a relatively unique approach that will enlarge the suite of available ultrafast optical signal processing tools.

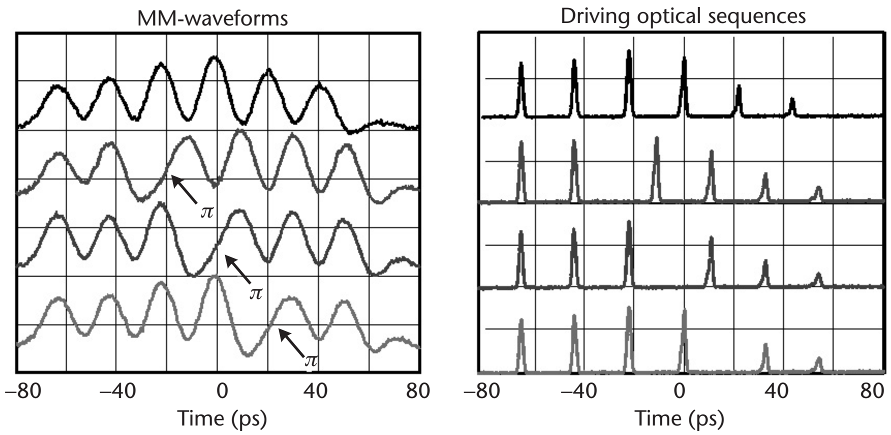

- Millimeter-wave phase shifts induced by timing shifts in the driving optical pulse sequence

Figure 4.26 Abrupt binary phase modulation in the millimeter-wave electrical domain achieved via optical pulse shaping control [63].

Acknowledgments

I am grateful to many different individuals who have contributed to this work, including many talented graduate students in my laboratory. I would also like to specifically acknowledge Dr. Dan Leaird at Purdue and our external collaborators Dr. Katsunari Okamoto and Professor Marty Fejer. This work was made possible by funding from the U.S. government, including funding from the National Science Foundation under grant ECS-0100949, the Army Research Office under grant DAAD19-00-1-0497, and DARPA under grant MDA972-03-1-0014. We also acknowledge support from the Optoelectronic Industry Development Association under the Joint Optoelectronics Program.

References

[1] Li, T., unpublished work.

[2] Kawanishi, S., "Ultrahigh-Speed Optical Time-Division-Multiplexed Transmission Technology Based on Optical Signal Processing," *IEEE J. Quantum Electron.*, Vol. 34, 1998, pp. 2064–2079.

[3] Weiner, A. M., "Femtosecond Optical Pulse Shaping and Processing," *Prog. Quantum Electron.*, Vol. 19, 1995, pp. 161–238.

[4] Weiner, A. M., J. P. Heritage, and E. M. Kirschner, "High-Resolution Femtosecond Pulse Shaping," *J. Opt. Soc. Amer. B*, Vol. 5, 1988, pp. 1563–1572.

[5] Weiner, et al., A. M., "Programmable Shaping of Femtosecond Pulses by Use of a 128-Element Liquid-Crystal Phase Modulator," *IEEE J. Quantum Electron.*, Vol. 28, 1992, pp. 908–920.

[6] Weiner, A. M., "Femtosecond Pulse Shaping Using Spatial Light Modulators," *Rev. Sci. Instr.*, Vol. 71, 2000, pp. 1929–1960.

[7] Weiner, A. M., and D. E. Leaird, "Generation of Terahertz-Rate Trains of Femtosecond Pulses by Phase-Only Filtering," *Opt. Lett.*, Vol. 15, 1990, pp. 51–53.

[8] Weiner, A. M., J. P. Heritage, and J. A. Salehi, "Encoding and Decoding of Femtosecond Pulses," *Opt. Lett.*, Vol. 13, 1988, pp. 300–302.

[9] Weiner, A. M., et al., "Programmable Femtosecond Pulse Shaping by Using a Multielement Liquid Crystal Phase Modulator," *Opt. Lett.*, Vol. 15, 1990, pp. 326–328.

[10] Wefers, M. M., and K. A. Nelson, "Generation of High-Fidelity Programmable Ultrafast Optical Waveforms," *Opt. Lett.*, Vol. 20, 1995, pp. 1047–1049.

[11] Tull, J. X., M. A. Dugan, and W. S. Warren, "High Resolution, Ultrafast Laser Pulse Shaping and its Applications," *Adv. Magn. Opt. Res*, Vol. 20, 1997, p. 1.

[12] Zeek, E., et al., "Pulse Compression by Use of Deformable Mirrors," *Opt. Lett.*, Vol. 24, 1999, pp. 493–495.

[13] Warren, W. S., R. Rabitz, and M. Dahleh, "Coherent Control of Quantum Dynamics: The Dream Is Alive," *Science*, Vol. 259, 1993, p. 1581.

[14] Weiner, A. M., et al., "Femtosecond Pulse Sequences Used for Optical Control of Molecular Motion," *Science*, Vol. 247, 1990, p. 1317.

[15] Meshulach, D., and Y. Silberberg, "Coherent Quantum Control of Two-Photon Transitions by a Femtosecond Laser Pulse," *Nature*, Vol. 396, 1998, pp. 239–242.

[16] Assion, A., et al., "Control of Chemical Reactions by Feedback-Optimized Phase-Shaped Femtosecond Laser Pulses," *Science*, Vol. 282, 1998, pp. 919–922.

[17] Bartels, R., et al., "Shaped-Pulse Optimization of Coherent Emission of High-Harmonic Soft X-Rays," *Nature*, Vol. 406, 2000, pp. 164–166.

[18] Dudovich, N., D. Oron, and Y. Silberberg, "Single-Pulse Coherently Controlled Nonlinear Raman Spectroscopy and Microscopy," *Nature*, Vol. 418, 2002, pp. 512–514.

[19] Brixner, T., et al., "Photoselective Adaptive Femtosecond Quantum Control in the Liquid Phase," *Nature*, Vol. 414, 2001, pp. 57–60.

[20] Levis, R. J., G. M. Menkir, and H. Rabitz, "Selective Bond Dissociation and Rearrangement with Optimally Tailored, Strong-Field Laser Pulses," *Science*, Vol. 292, 2001, pp. 709–713.

[21] Chang, C.-C., et al., "Broadband Fiber Dispersion Compensation for Sub-100-fs Pulses with a Compression Ratio of 300," *Opt. Lett.*, Vol. 21, 1996, pp. 1141–1143.

[22] Chang, C.-C., and A. M. Weiner, "Fiber Transmission for Sub-500-fs Pulses Using a Dispersion-Compensating Fiber," *IEEE J. Quantum Electron.*, Vol. 33, 1997, pp. 1455–1464.

[23] Chang, C.-C., H. P. Sardesai, and A. M. Weiner, "Dispersion-Free Fiber Transmission for Femtosecond Pulses Using a Dispersion-Compensating Fiber and a Programmable Pulse Shaper," *Opt. Lett.*, Vol. 23, 1998, pp. 283–285.

[24] Shen, S., and A. M. Weiner, "Complete Dispersion Compensation for 400-fs Pulse Transmission over 10-km Fiber Link Using Dispersion Compensating Fiber and Spectral Phase Equalizer," *IEEE Photon. Techol. Lett.*, Vol. 11, 1999, pp. 827–829.

[25] Nelson, R. D., D. E. Leaird, and A. M. Weiner, "Programmable Polarization-Independent Spectral Phase Compensation and Pulse Shaping," *Optics Express*, Vol. 11, 2003, pp. 1763–1769.

[26] Takenouchi, H., T. Goh, and T. Ishii, "8 THz Bandwidth Dispersion-Slope Compensator Module for Multiband 40 Gbit/s WDM Transmission Systems Using an AWGS and Spatial Phase Filter," *Electron. Lett.*, Vol. 37, 2001, p. 777.

[27] Shirasaki, M., and S. Cao, "Compensation of Chromatic Dispersion and Dispersion Slope Using a Virtually Imaged Phased Array," *Optical Fiber Communications,* Anaheim, CA, 2001.

[28] Sano, T., et al., "Novel Multichannel Tunable Chromatic Dispersion Compensator Based on MEMS and Diffraction Grating," *IEEE Photon. Technol. Lett.*, Vol. 15, 2003, pp. 1109–1110.

[29] Poole, C. D., and J. Nagel, "Polarization Effects in Lightwave Systems," in *Optical Fiber Telecommunications,* Vol. IIIA, I. P. Kaminow and T. L. Koch, (eds.), San Diego, CA: Academic Press, 1997.

[30] Akbulut, M., "Computer Modeling for Characterization, Emulation, and Compensation of Polarization Mode Dispersion in Single-Mode Fibers," Master's thesis, Purdue University, School of Electrical and Computer Engineering, West Lafayette, IN, 2001.

[31] Akbulut, M., et al., "Programmable Multi-Wavelength Polarization Corrector," *Conference on Lasers and Electro-Optics,* Baltimore, MD, 2003.

[32] Wang, X., and A. M. Weiner, "Wavelength-Parallel Polarization Sensor for Multi-Wavelength Optical Networks," *Conference on Lasers and Electro-Optics,* Baltimore, MD, 2003.

[33] Mazurenko, Y. T., "Holography of Wave Packets," *Appl. Phys. B*, Vol. 50, 1990, pp. 101–114.

[34] Weiner, A. M., et al., "Femtosecond Spectral Holography," *IEEE J. Quantum Electron.*, Vol. 28, 1992, pp. 2251–2261.

[35] Nuss, M. C., et al., "Time-to-Space Mapping of Femtosecond Pulses," *Opt. Lett.*, Vol. 19, 1994, pp. 664–666.

[36] Chung, J. H., and A. M. Weiner, "Time-to-Space Conversion of Ultrafast Optical Pulses Via Spectral Nonlinear Optics in the Communications Band," *Ultrafast Phenomena XIII*, Vol. 71, Springer Series in Chemical Physics, 2003, pp. 208–210.

[37] Sun, P. C., Y. T. Mazurenko, and Y. Fainman, "Femtosecond Pulse Imaging: Ultrafast Optical Oscilloscope," *J. Opt. Soc. Am. A*, Vol. 14, 1997, p. 1159.

[38] Kanan, A. M., and A. M. Weiner, “Efficient Time-to-Space Conversion of Femtosecond Optical Pulses,” *J. Opt. Soc. Am. B*, Vol. 15, 1998, pp. 1242–1245.

[39] Fejer, M.M., International Symposium on New Frontiers for Ubiquitous IT Services, Kanagawa, Japan, May 26–27, 2003.

[40] J. A. Salehi, A. M. Weiner, and J. P. Heritage, “Coherent Ultrashort Light Pulse Code-Division Multiple Access Communication Systems,” *J. Lightwave Tech*., Vol. 8, 1990, pp.A. M. 478.

[41] Sardesai, H. P., C.-C. Chang, and A. M. Weiner, “A Femtosecond Code-Division Multiple-Access Communication System Testbed,” *J. Lightwave Technol*., Vol. 16, 1998, pp. 1953–1964.

[42] Teh, P. C., et al., “Demonstration of a Four-Channel WDM/OCDMA System Using 255-Chip 320-Gchip/s Quarternary Phase Coding Gratings,” *IEEE Photon. Technol. Lett.,* Vol. 14, 2002, pp. 227–229.

[43] Sotobayashi, H., W. Chujo, and K. I. Kitayama, “1.6-b/s/Hz 6.4-Tb/s QPSK-OCDM/WDM (4 OCDM x 40 WDM x 40 Gb/s) transmission Experiment Using Optical Hard Thresholding,” *IEEE Photon. Technol. Lett*., Vol. 14, 2002, pp. 555–557.

[44] Shen, S., et al., “Bit-Error-Rate Performance of Ultrashort-Pulse Optical CDMA Detection Under Multi-Access Interference,” *Electron. Lett*., Vol. 36, 2000, pp. 1795–1797.

[45] Shen, S., and A. M. Weiner, “Suppression of WDM Interference for Error-Free Detection of Ultrashort-Pulse CDMA Signals in Spectrally Overlaid Hybrid WDM-CDMA Operation,” *IEEE Photon. Techol. Lett*., Vol. 13, 2001, pp. 82–84.

[46] Chou, M. H., et al., “1.5 Micron Band Wavelength Conversion Based on Cascaded Second Order Nonlinearity in LiNbO3 Waveguides,” *IEEE Photon. Techol. Lett*., Vol. 11, 1999, pp. 653–655.

[47] Zheng, Z., and A. M. Weiner, “Spectral Phase Correlation of Coded Femtosecond Phase Codes by Second Harmonic Generation in Thick Nonlinear Crystals,” *Opt. Lett*., Vol. 25, 2000, pp. 984–986.

[48] Zheng, Z., et al., “Low Power Spectral Phase Correlator Using Periodically Poled LiNbO3 Waveguides,” *IEEE Photon. Techol. Lett*., Vol. 13, 2001, pp. 376–378.

[49] Zheng, Z., and A. M. Weiner, “Coherent Control of Second Harmonic Generation Using Spectrally Phase Coded Femtosecond Waveforms,” *Chemical Physics*, Vol. 267, 2001, pp. 161–171.

[50] Leaird, D. E., and A. M. Weiner, “Femtosecond Optical Packet Generation Via a Direct Space-to-Time Pulse Shaper,” *Opt. Lett*., Vol. 24, 1999, pp. 853–855.

[51] Leaird, D. E., and A. M. Weiner, “Femtosecond Direct Space-to-Time Pulse Shaping,” *IEEE J. Quantum Electron*., Vol. 37, 2001, pp. 494–504.

[52] McKinney, J. D., D. S. Seo, and A. M. Weiner, “Direct Space-to-Time Pulse Shaping at 1.5 μm,” *IEEE J. Quantum Electron*., Vol. 39, 2003, pp. 1635–1644.

[53] Bor, Z., and B. Racz, “Group-Velocity Dispersion in Prisms and Its Application to Pulse-Compression and Traveling-Wave Excitation,” *Optics Communications*, Vol. 54, 1985, pp. 165–170.

[54] Leaird, D. E., et al., “Generation of High-Repetition-Rate WDM Pulse Trains from an Arrayed-Waveguide Grating,” *IEEE Photon. Techol. Lett*., Vol. 13, 2001, pp. 221–223.

[55] Leaird, D. E., et al., “Generation of Flat-Topped 500-GHz Pulse Bursts Using Loss Engineered Arrayed Waveguide Gratings,” *IEEE Photon. Technol. Lett*., Vol. 14, 2002, pp. 816–818.

[56] Leaird, D. E., et al., “High Repetition Rate Femtosecond WDM Pulse Generation Using Direct Space-to-Time Pulse Shapers and Arrayed Waveguide Gratings,” *Opt. Quantum Electron.,* Vol. 33, 2001, pp. 811–826.

[57] Okamoto, K., “Recent Progress of Integrated Optics Planar Waveguide Circuits,” *Opt. Quantum Electron*., Vol. 31, 1999, pp. 107–129.

[58] Leaird, D. E., et al., "Double-Passed Arrayed Waveguide Grating for 500-GHz Pulse Burst Generation," *IEEE Photon. Technol. Lett.*, Vol. 14, 2002, pp. 1451–1453.

[59] Seo, D. S., et al., "Continuous 500 GHz Pulse Train Generation by Repetition-Rate Multiplication Using Arrayed Waveguide Grating," *Electron. Lett.*, Vol. 39, 2003, pp. 1138–1140.

[60] Nakazawa, M., et al., "TDM Single Channel 640 Gb/s Transmission Experiment over 60 km Using 400 fs Pulse Train and Walk-Off Free, Dispersion Flattened Nonlinear Optical Loop Mirror," *Electron. Lett.*, Vol. 34, 1998, pp. 907–908.

[61] Leaird, D. E., and A. M. Weiner, "High Repetition Rate Femtosecond Direct Space-to-Time Pulse Shaping Using a Modified Arrayed Waveguide Grating,"*Conference on Lasers and Electro-Optics,* Baltimore, MD, 2003.

[62] McKinney, J. D., D. E. Leaird, and A. M. Weiner, "Millimeter-Wave Arbitrary Waveform Generation with a Direct Space-to-Time Pulse Shaper," *Opt. Lett.*, Vol. 27, 2002, pp. 1345–1347.

[63] McKinney, J. D., D. S. Seo, and A. M. Weiner, "Photonically Assisted Generation of Continuous Arbitrary Millimetre Electromagnetic Waveforms," *Electron. Lett.*, Vol. 39, 2003, pp. 309–311.

CHAPTER 5

Global Network: Prospects for the Future

Vincent W. S. Chan
Department of Electrical Engineering and Computer Science
Department of Aeronautics and Astronautics
Massachusetts Institute of Technology

Introduction

Ubiquitous communication of the future will be supported by a multitude of modality in the form of satellite, fiber, and wireless communication, as shown in Figure 5.1. These modalities are very different in terms of technology and the architectural construct of these particular subnetworks would be very different. The important notion is that for the future there will be only one network and that network would have to be an interconnection of all these different modalities. Users will have a choice of connecting to any one of them as they see fit.

Most of the traffic of the future will be computer data communications that is bursty and unscheduled, as shown in Figure 5.2. Traditional circuit-oriented traffic will only make up at most 10% of the volume. Thus, the network of the future must use architectures tuned to the nature of such traffic.

Fiber Networks

In the early 1990s, the drastic reduction in the cost of long-haul transmission fiber changed the equation of the Internet. It used to be that long-haul transmission was an expensive and precious commodity and the electronic packet-switching architecture of the Internet was designed to optimally use the long-haul transmission capacity. The deployment of WDM drove down the cost per bit, and finally crossed over with the cost of switching around 1987–1988, as shown in Figure 5.3. At present, the electronics switching architecture is what is dominant in terms of network costs. In the near future, optical switching in the core, using MEMs or linear photonic circuit devices, will reduce the cost of electronic switching at the major long-haul nodes. The next barrier encountered will be the electronic access cost. Even gigabit/Ethernet would run into this particular problem. The cost improvement rate will follow Moore's Law, which reduces costs by a factor of 2 approximately every 12 months, maybe every 18 months, and is too slow to catch up with the speeds at which WDM increases core capacities. We need to go to optical access to move beyond the Moore's Law limit on electronic access.

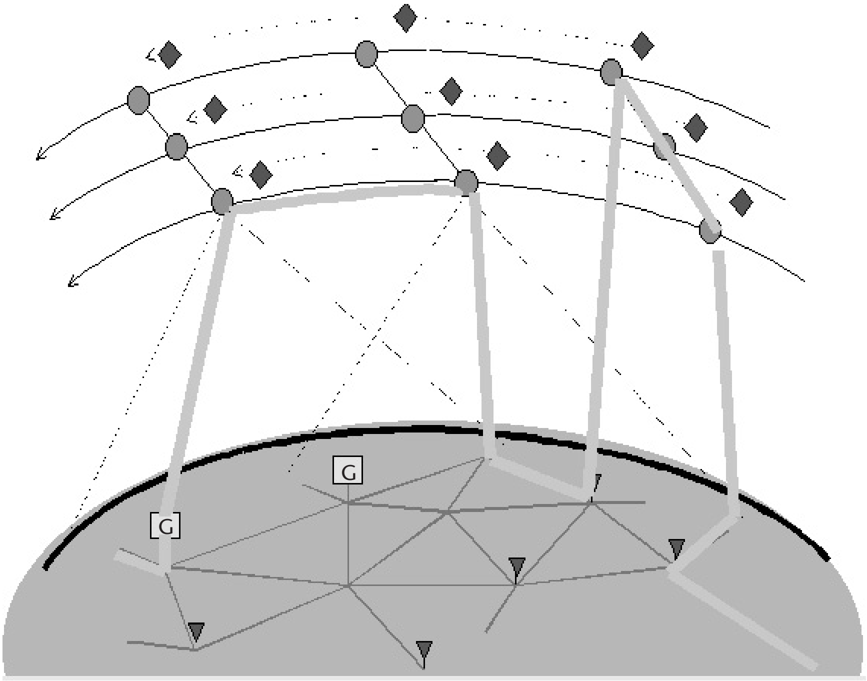

- Satellites, fiber, wireless, ...
- Interconnected network
- Emphasis on data communications

Figure 5.1 Ubiquitous network concept.

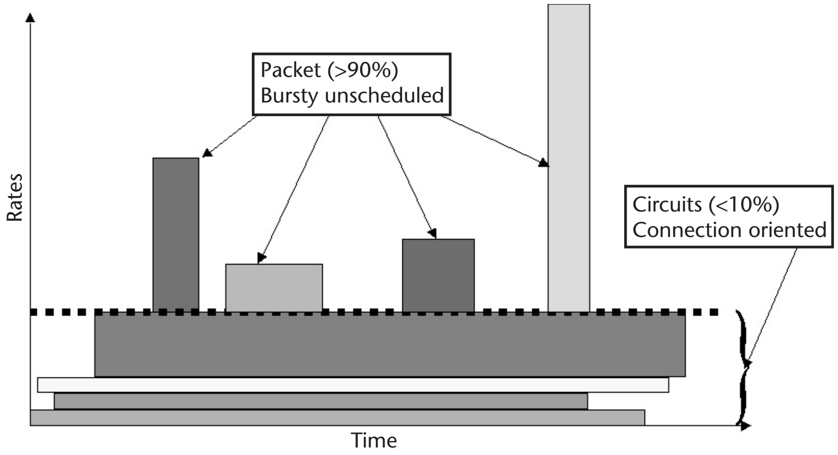

Figure 5.2 The nature of traffic of the future.

The long-haul fiber network of the future will not be not a ring network but a mesh network. Most long-haul networks today have a mesh physical topology but they are arranged in logical rings for protection and management. This architecture is simple but very inefficient (~50%). In the future, the network will be more aggres-

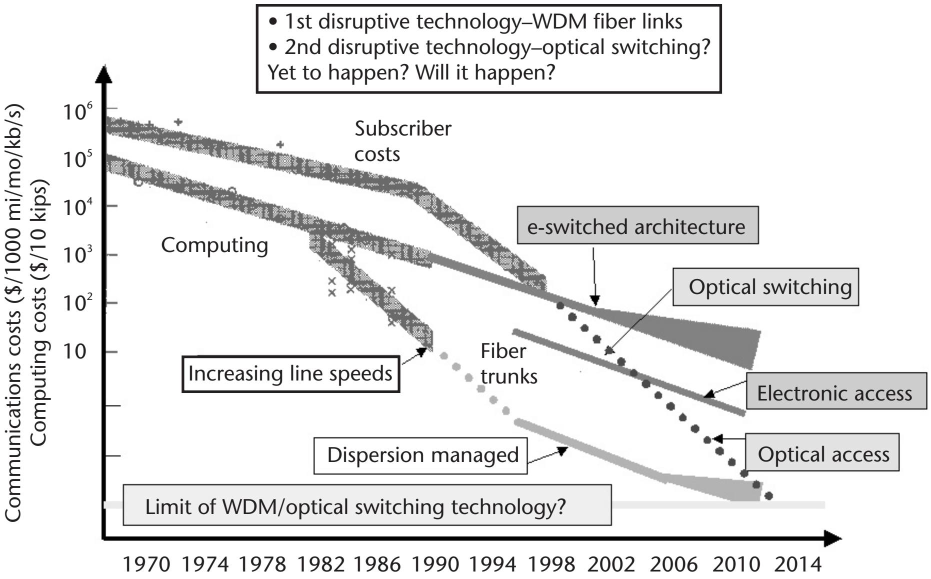

Figure 5.3 Optical network evolution and disruptive technologies.

sively arranged in mesh-logical topologies, and each node will consist of an optical cross-connect and an IP router sitting on top of the optical cross-connect, as shown in Figure 5.4. Optical switching would be used in the long haul for high-speed bypass. With such a construct, the long-haul transmission costs will still dominate because of the high precision of long-haul transmission equipment, optical amplifiers, and polarization dispersion management. Thus, it will continue to be important to use long-haul wavelengths efficiently.

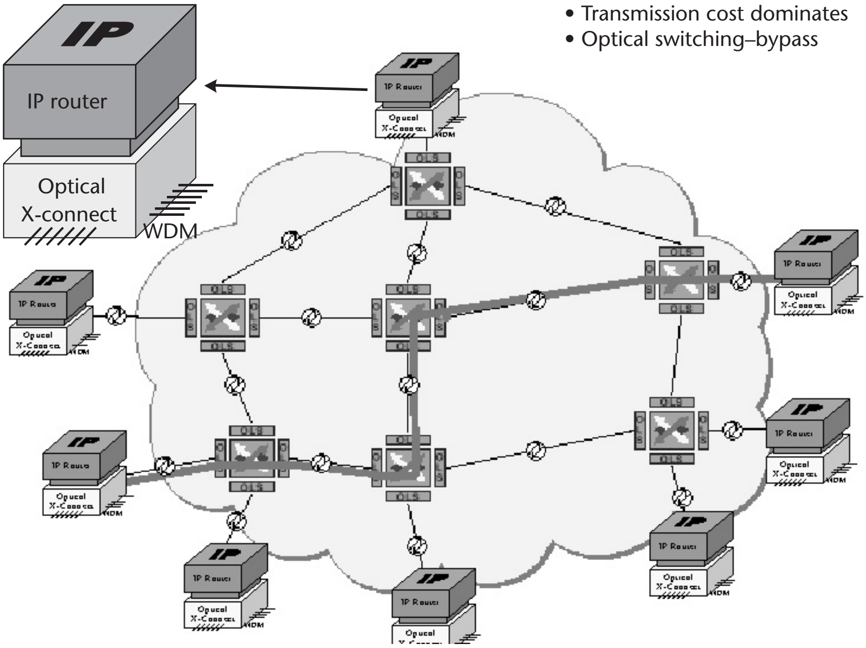

Figure 5.4 Wide area optical network.

In the future, three-dimensional MEM switches will use integrated internal circuits for sensing and feedback control without having to bring the signal out of the chip (Figure 5.5). Switching voltages of the order of a few volts can be achieved and is very compatible with C-MOS electronics.

In the future, hierarchical switching with multiple fibers coming into the switch will be used. The network management and control will use bundling techniques and switch, at the first level, fiber by fiber, each fiber with perhaps hundreds of wavelengths. Next, a frequency-selective switch will switch grouped wavelength bands and maybe individual wavelengths. This feature will reduce the number of ports of the optical switch and lower costs.

The frequency of occurrence distribution versus size of the computer transactions are not exponentially distributed as commonly modeled. Actually, they exhibit heavy tail statistics. The longest sessions, which are probably about 1% of all sessions, dominate the traffic volume. In fact, more than 95% of the traffic is contained in 1% of the transactions (Figure 5.6). Thus, to design an IP-based system that deals with four orders of increase in capacity, it is extremely uneconomical to break these large (> gigabyte) transactions into little IP packets of 1.5 KB each, switch them one by one and then reassemble them.

The simplest architecture notion is generalized multiprotocol label switching (GMPLS), where the router senses that there is a large transaction and opens up an end-to-end optical circuit to go from the entrance router to the exit router, bypassing all intermediate routers. This is the kind of network that is being thought about and being deployed in next generation optical networks. A more advanced view is that the user should not really have to talk to the access router and send the large transaction segmented into many 1.5-KB packets, but should negotiate directly with the network management and control system. Thus, the user can perform large transactions by directly opening up an optical circuit in the WDM layer and flow the transaction within 100 ms or longer (Figure 5.7).

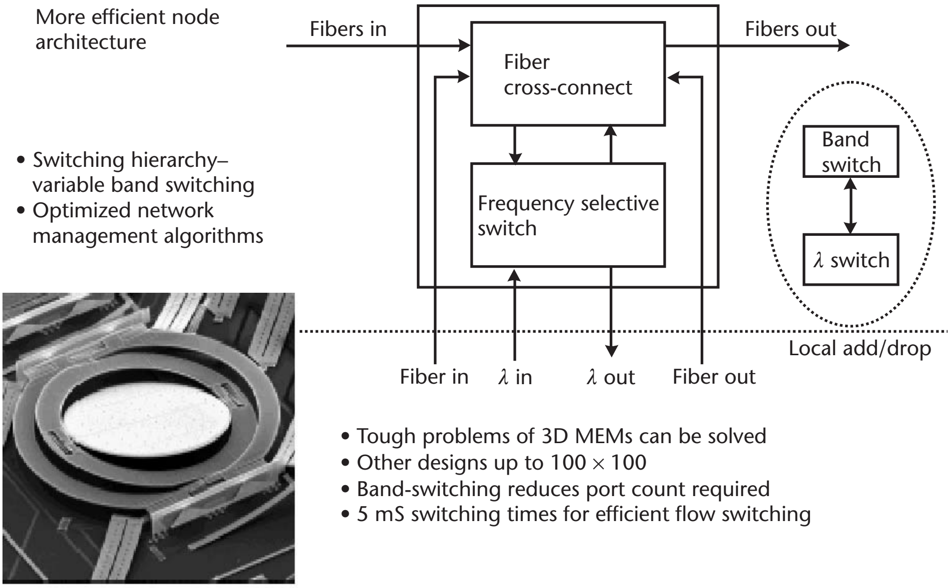

- Switching hierarchy–variable band switching
- Optimized network management algorithms

- Tough problems of 3D MEMs can be solved
- Other designs up to 100 × 100
- Band-switching reduces port count required
- 5 mS switching times for efficient flow switching

Figure 5.5 Future all-optical node architecture.

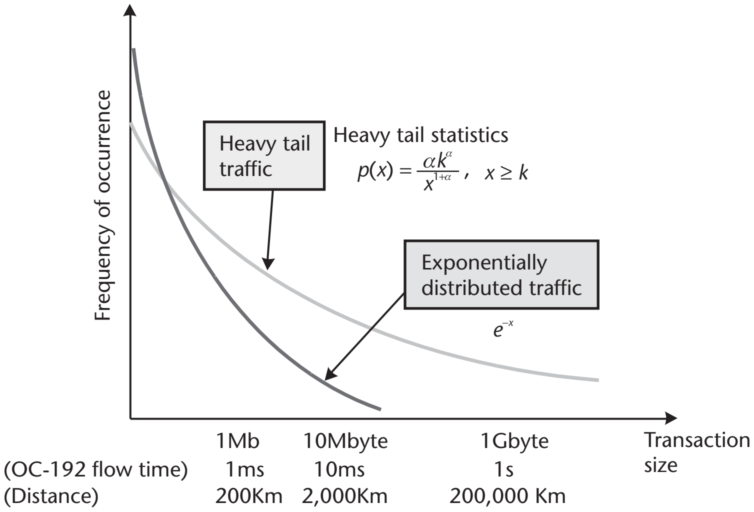

Figure 5.6 Heavy tail statistics.

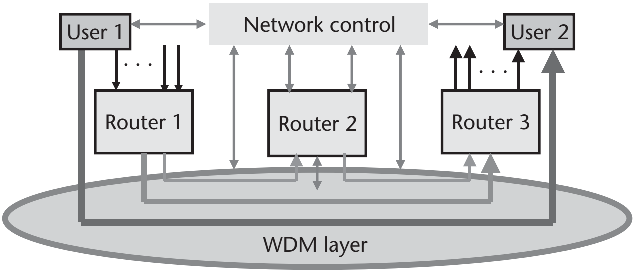

Figure 5.7 Flow switching.

Consider a network arranged in a wide-area network and an access network hierarchy where the access network also consists of a metropolitan-area network and a local-area network (LAN) (Figure 5.8). A user connected to one of the access nodes can send a flow session across the wide-area network to another access network by signaling to the network and management scheduler, as seen in Figure 5.9.

Ultrahigh Reliability LAN

One interesting special application of a LAN is using the optical network for the control of its engine and flight surfaces. The optical LAN can replace all the electronic lines and hydraulic lines in an airliner (Figure 5.10). Tremendous amounts of savings in weight and increased reliability can be realized. This network has to be a lot more reliable than the everyday LAN, so new features such as simultaneously using multiple independent routes distributed around the aircraft must be used to provide ultrahigh reliability.

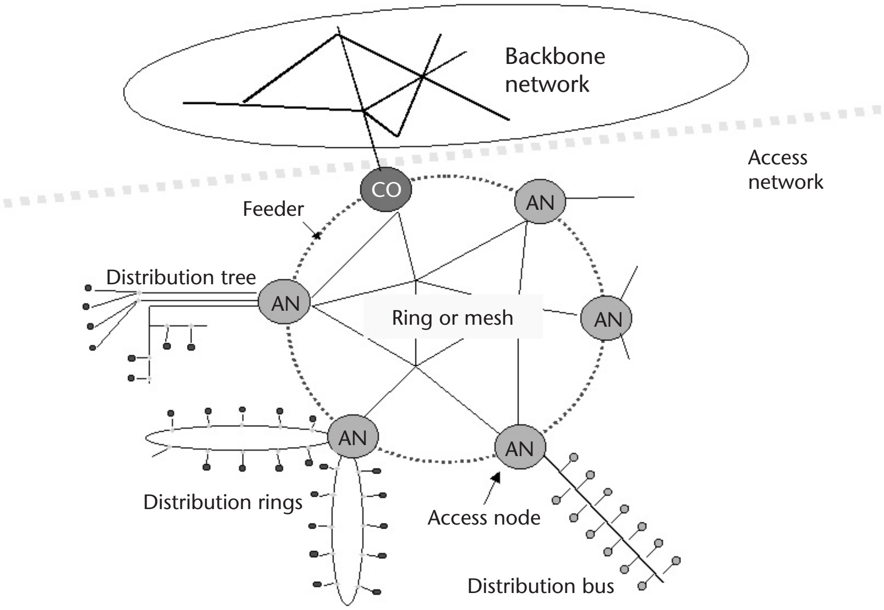

Figure 5.8 Optical access network.

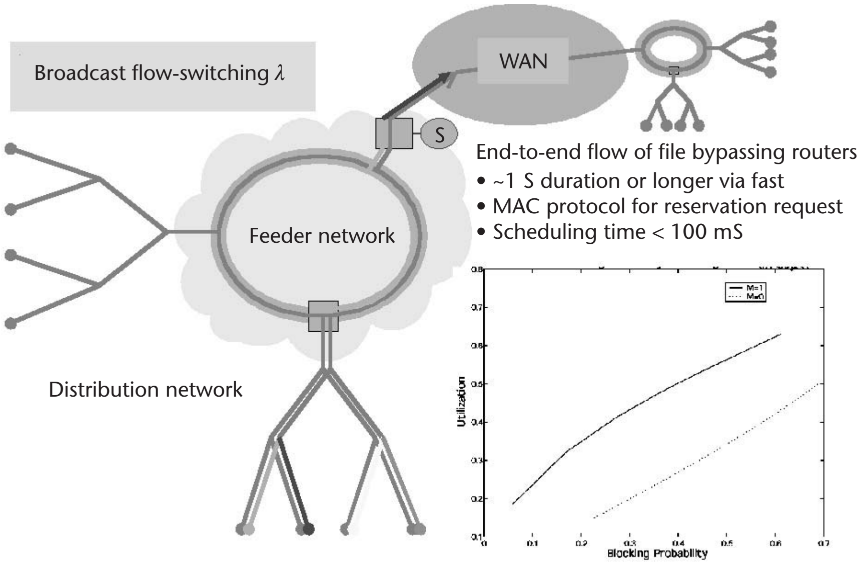

Figure 5.9 Flow switching across an access node and long-haul optical network.

Wireless Communications

Wireless has a long way to go before its maximum potential is realized. Multiple antennas in wireless both in the base station and at the user terminal will increase capacity or improve reliability (Figure 5.11). In some cases, multiple antennas are able to phase in such a way that more energy is received, resulting in better signal-to-noise ratio and therefore they can support high capacity. In a highly dispersive

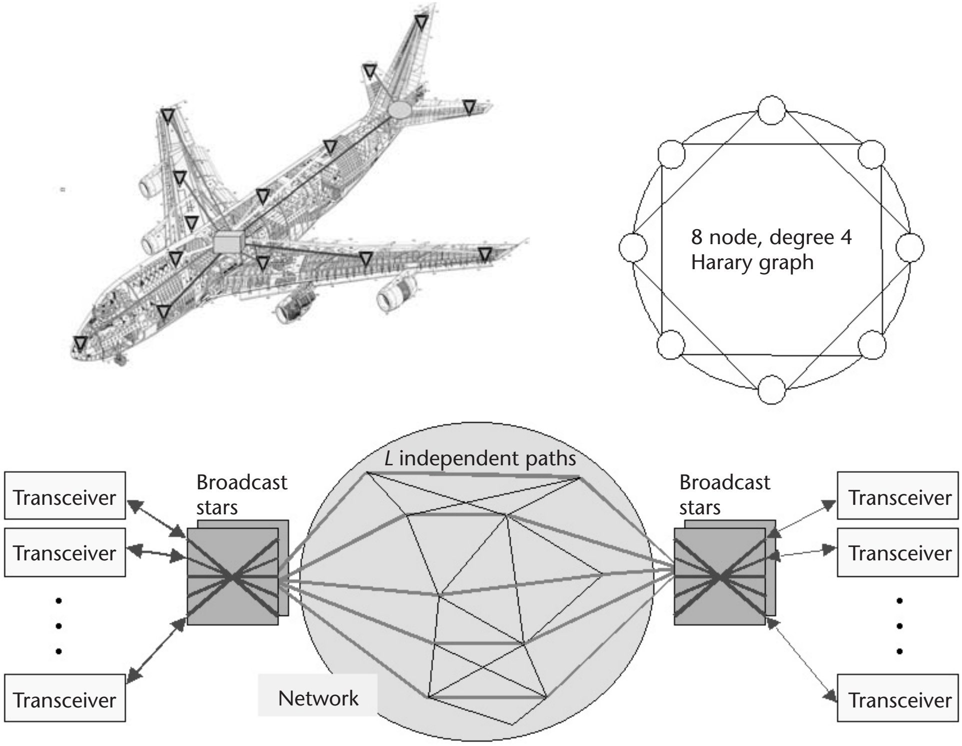

Figure 5.10 Ultrahigh reliability LAN.

multipath environment, multiple antennas can provide enough diversity in terms of path and frequency so that the session would never drop out. Current evolution and revolution in RF technology will improve significantly high-speed continuous reliable wireless communication.

Imagine a wireless system supported by the optical access network as shown in Figure 5.8. The RF signal received at each node can be transported using WDM to a processing center. Each user's RF signal could be picked up by multiple antennas, and the wireless processing center could perform the signal processing to provide rake receiver combining and increase the capacity of the system to multigigabits per second (Figure 5.12).

Space Networks

Multiple satellites can be interconnected to form a backbone in space as a duo to the backbone on the ground. High-speed RF trunks from space to ground will interconnect the space and terrestrial networks, as shown in Figure 5.13. A more aggressive use of free space RF and optical links is to provide access to mobile users in places such as aircraft, and users in areas where infrastructures are not available, such as oceans or mountains.

The key technology that makes this work is the space laser communication crosslink seen in Figure 5.14. It can interconnect geosatellites 80,000 km apart with

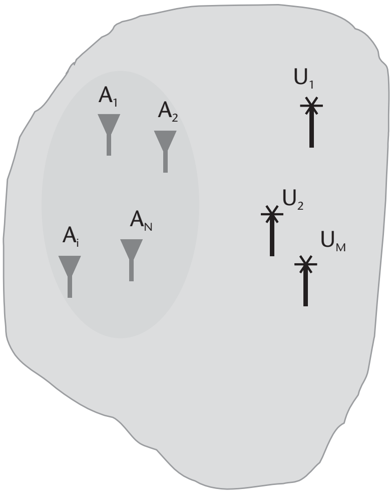

- Fading dispersive multipath channel
- Multiaccess/multiuser information theory
- Robust communications over unpredictable random channels

- Antenna and signal processing technology
- MAC protocol
- Spacetime coding
- Multilayer network design/optimization

Figure 5.11 Future radio systems.

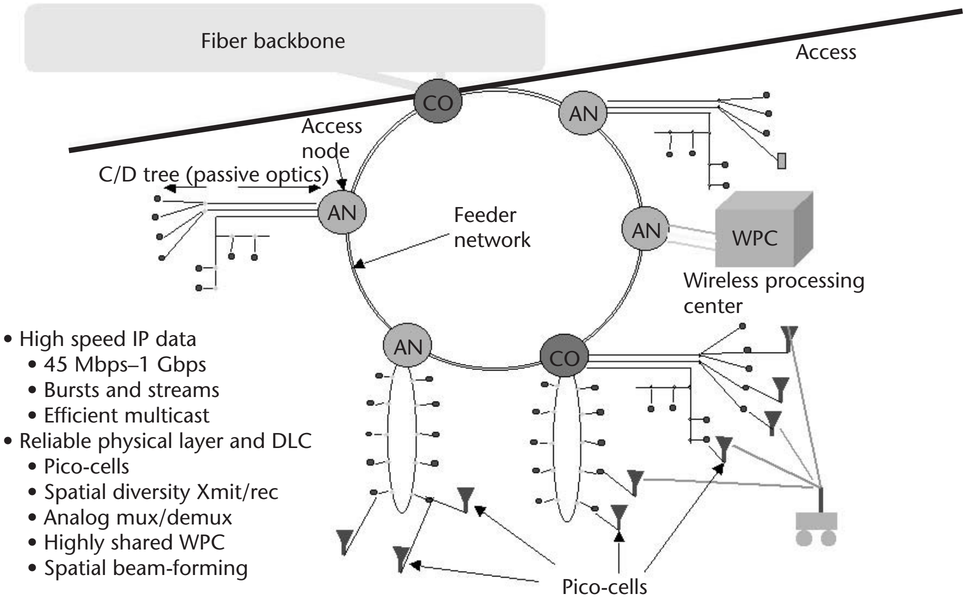

- High speed IP data
  - 45 Mbps–1 Gbps
  - Bursts and streams
  - Efficient multicast
- Reliable physical layer and DLC
  - Pico-cells
  - Spatial diversity Xmit/rec
  - Analog mux/demux
  - Highly shared WPC
  - Spatial beam-forming

Figure 5.12 Wireless access via optical access network infrastructure.

modest telescopes (~20 cm), made possible via a high-power optical amplifier (~10W), highly efficient modulation, and coding operating at the quantum limit of reception (which is about 20 dB better than a typical fiber-optics receiver).

With this backbone and new microwave phase array technology, a satellite system can support multiple narrow RF access beams (~ 50 km) with very high gain for high-speed users (Figure 5.15). Since this system will be used largely for data users, a matching data network set of protocols such as media access, routing, transport layer protocols, and network management and controls needs to be in place.

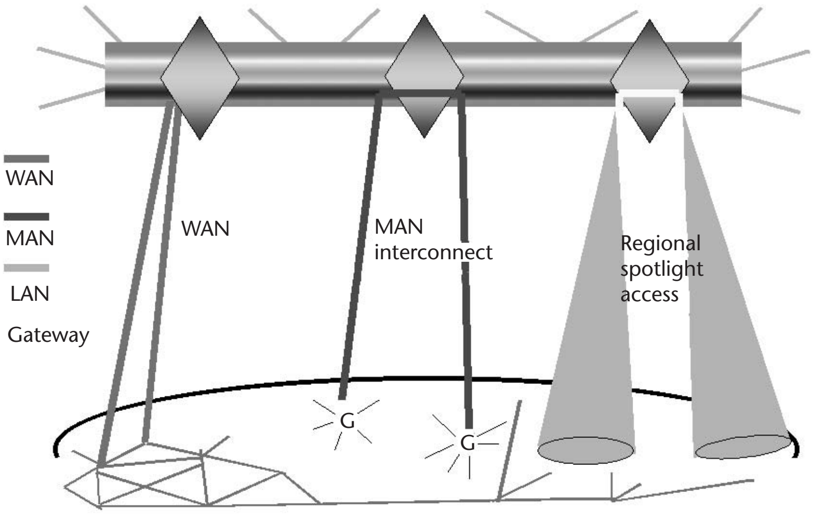

Figure 5.13 Globally integrated network.

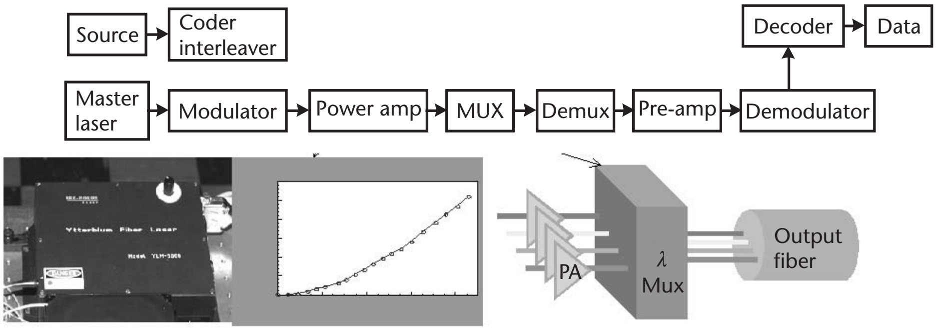

Figure 5.14 Optical space crosslink.

Innovative Space Architectures

In the near future, optical crosslinks will become much more economical and have higher rates than RF up-and-down links. Spaceborne sensors currently use RF downlinks to bring the data to processing centers on the ground. The high cost of high-rate RF downlinks from satellites, not the resolution of the sensors, will become the limiting factor on system resolution and sensed area rates. With an ultrahigh rate and economical optical satellite backbone in place, one can think about the concept of using shared spaceborne processing (Figure 5.16) to reduce the amount of data to be sent earthbound, and thus reduce the requirement for very costly high RF downlink data rates.

Modest RF downlinks can then be used for the processed and reduced data, substantially lowering the overall system cost and raising the resolution and coverage rate of the sensor. A progressive concept is to locate a processing satellite somewhere close to or within the backbone, with the most advanced processor at the time of launch, which would be periodically replaced and replenished. First, the

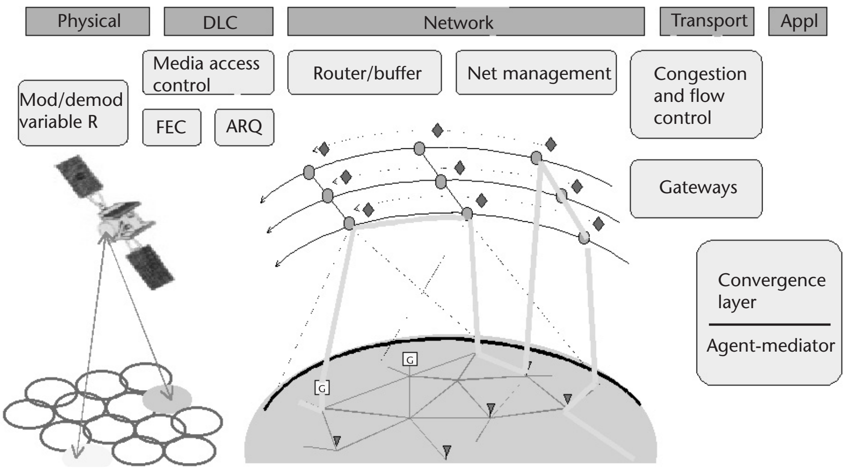

- Dynamic capacity
- Agile beams
- MAC

- Dynamic routing: deterministic and stochastic
- Heterogeneous network: Satcom, fiber, wireless
- Differentiated services: cost-based, time-deadline, ...

- Satellite resources extremely precious

Figure 5.15 Dynamic space/terrestrial network.

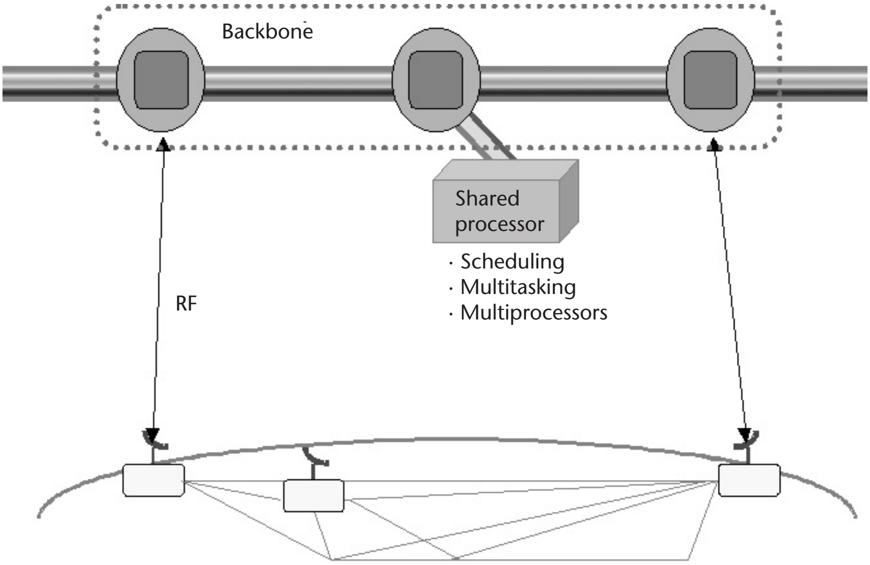

Figure 5.16 Shared processing in space.

sharing allows much more efficient utilization of the processing system, as well as reducing the need for 100% redundancy. Figure 5.17 shows such a satellite node that can be located in a convenient orbit.

Current practice has the terrestrial network tie together disparate modalities to form a single network. Satellite systems have not followed that paradigm. The main impediment has been that satellite systems have stovepipe designs that are not interoperable, and tying them together requires gateways or teleports on the ground that are not only costly but also tie up a significant fraction of the up-and-down link

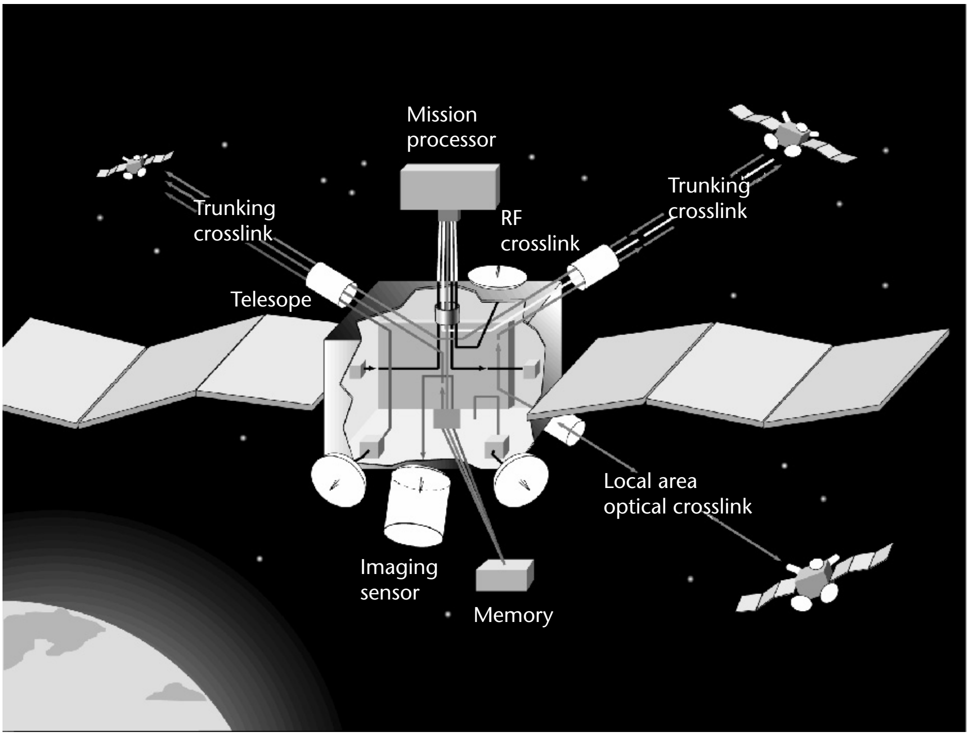

Figure 5.17 Satellite node concept.

resources for the connections to the conversion gateways. Moreover, interconnections at the application layer slow down the overall end-to-end network response. The high-speed optical satellite backbone and the processing satellite can be used to perform the conversion gateway function and tie the different satellite communication systems in space rather than on the ground (Figure 5.18). This will be the key technology that transforms the stovepiped satellite communication community to a data satellite network community serving many more users.

A satellite communication system's performance may be greatly improved if the receiving function can be distributed over more than one satellite. For example, two satellites can form the arm of a long baseline interferometer provided the two received signals can be brought together for coherent processing (Figure 5.19). This either requires fine quantization and significant data rate transmissions to preserve phase information or coherent analog transmission at high fidelity, sometimes known as transmission transparency. An analog link of an optical satellite network can provide such a service. In general, a distributed satellite system can substantially improve interference rejection, enhanced power efficiency, and data rate of small mobile terrestrial users.

Summary

Not very often, in the history of communications and networking, have there been truly transforming inventions that result in quantum leaps in the nature of services

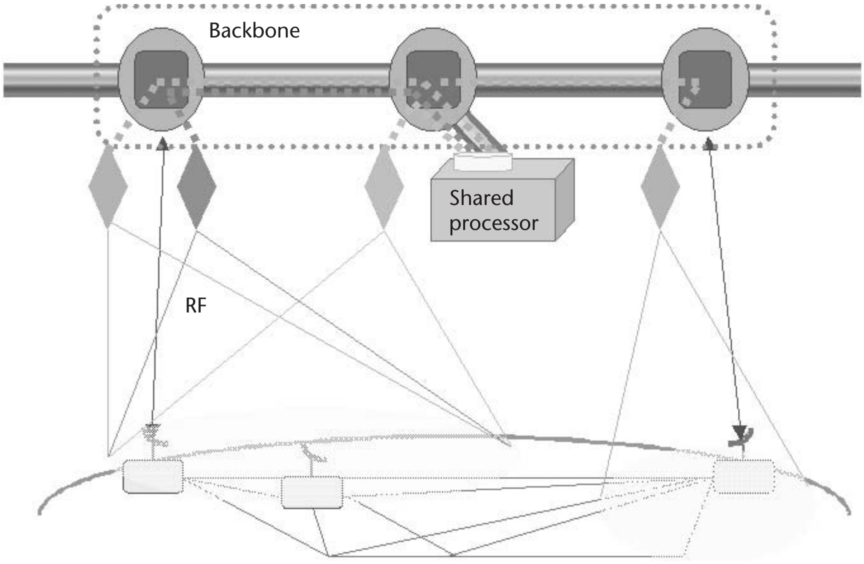

- Rapidly upgradable modulation and coding in space
- Data networking with packet switching and QoS (e.g., priority) in space
- Adapt to marketing needs at the time

Figure 5.18 Interoperable interconnected space communications.

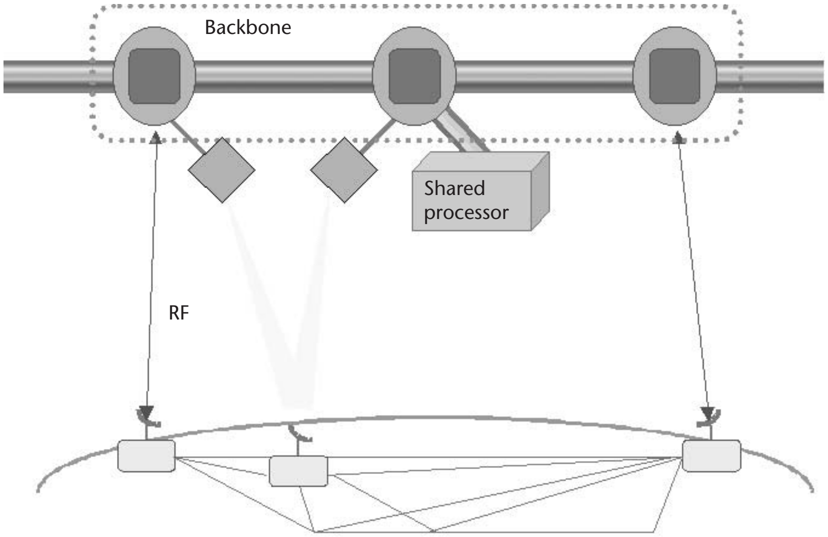

- Long baseline interferometer increases sensitivity
- Provide high data rates to small users
- Significant frequency reuse
- Spaceborne processing substantially reduces D/L data rate

Figure 5.19 Coherent distributed satellite communications for enhanced capability.

or costs to the end users. Examples that come to mind are the invention of the router that led to connectionless packet service and the Internet. All-optical WDM fiber networks, wireless terrestrial, and a new generation of satellite communications will likely be classified as such transforming technologies if their architectural implications are fully exploited. Not only will the globally connected network become economically viable, its ubiquitous deployment and the extraordinary services its can offer are capable of radically transforming network usages and supporting many new applications to come. The opportunity is now to use imagination and creativity to bring home this new breakthrough.

CHAPTER 6

Standards for Optical Communications and Sensing

G. W. Day
National Institute of Standards and Technology
Boulder, Colorado

As we look toward future ubiquitous IT services, standards are among the enabling technologies that can accelerate technical and market development and affect competition. Standards are most effective when they are developed early in the emergence of a technology, their technical basis has been thoroughly established, and they are supported by a wide consensus among stakeholders.

In any discussion of the need for future standards in IT services or any other field, we are challenged not only by the science involved, but by the breadth and diversity of the requirements. In this chapter, I have therefore chosen to look backwards, principally through the development of standards for optical communications, for lessons that may be applied more generally. But, before beginning, it is helpful to remember that the definition of the term "standards" depends strongly on context.

To a physicist, the topic of standards often relates closely to systems of units, especially the international system (SI), which consists of seven base standards: meter, kilogram, second, ampere, mole, kelvin, and candela. All of these except the kilogram are now definitions based on fundamental constants rather than physical (artifact) standards. A chemist may think of standards in the context of quantitative analysis as, for example, a calibration standard for an analytic instrument. For an engineer, interest in standards relates particularly to design standards that insure product compatibility and standards that ensure consistent specification of product characteristics.

The field of standards is like the Hindu proverb about several blind men examining an elephant. Each man touches a portion of the beast and thinks it is characteristic of the whole. In fact, few scientists and engineers who work in standards have experienced the full breadth of the field.

It is difficult to obtain a suitably comprehensive definition for a standard. Perhaps we might argue that a standard is anything that leads to a greater degree of predictability or conformity. Certainly standards include artifacts and definitions of physical quantities, almost any agreement to do things in a consistent way, specifications, conditions, sometimes regulations or rules, and requirements imposed by a government body or organization with authority. But sometimes standards are simply de facto norms—technologies evolve and standards may emerge without any accredited body behind them

In optical communications, most standards have emerged from national and international groups known as standards developing organizations (SDOs). International SDOs—the International Organization for Standardization (ISO), the International Electrotechnical Commission (IEC), and the International Telecommunication Union (ITU)—derive their authority to produce standards from treaties or other agreements. Countries are often represented on these SDOs through national organizations such as the American National Standards Institute (ANSI) in the United States, the British Standards Institute (BSI) in the United Kingdom, and other groups accredited by their national representatives. Accreditation often goes to professional societies and industry associations. Unaccredited groups, often independent groups of stakeholders commonly known as forums (e.g., the Optical Internetworking Forum and the DVD Forum) often produce standards with wide acceptance. National measurement institutes (NMIs)—for example, the National Institute of Standards and Technology (NIST) in the United States and the National Institute of Advanced Industrial Science and Technology (AIST) in Japan, provide technical support for standardization.

The large number of groups involved and the attendant investments reflect the enormous technical and economic significance of standards in the marketplace. The existence or absence of standards can dramatically accelerate or stall the development and acceptance of a technology, and issues of standards, especially competing standards, are increasingly important to consumers.

Important, but less obvious, are economic issues of standards in manufacturing. For example, product characterization associated with performance specifications often accounts for 10% to 30% of the cost of manufacturing, and may depend substantially on the standards underlying the specifications.

The development of standards for the specification of lasers is an example of a need for standards that led to a revolution in a field of measurement science. In the 1960s, when many types of lasers were developed, there were no reliable methods of measuring their output. Radiometric standards then in use, based on “standard sources,” and “calibrated detectors,” could not survive the high peak power of the pulses from a ruby or Nd:YAG laser or the continuous power of many gas lasers. And, even if they could, they were not sufficiently linear to provide accurate measurements over the broad range of power levels for which measurements were needed. These problems, and other complicating properties of laser radiation, including high coherence, complex and dynamic irradiance (beam profile) properties, and dynamic polarization effects, made it very difficult to adapt existing technology.

Research on laser radiometry thus shifted toward devices in which absorbed laser power or energy could be accurately compared to dissipated electrical power or energy. One of the first such laser calorimeters [1] is shown in Figure 6.1. In it, an intense laser pulse is absorbed in a liquid and the resulting temperature rise is compared to that produced by a measurable amount of electrical energy dissipated in the liquid by a heater. This instrument was resistant to optical damage, and since it was placed directly in the beam without additional optical elements, the effects of coherence, beam profile, and polarization were minimized. The liquid-cell calorimeter

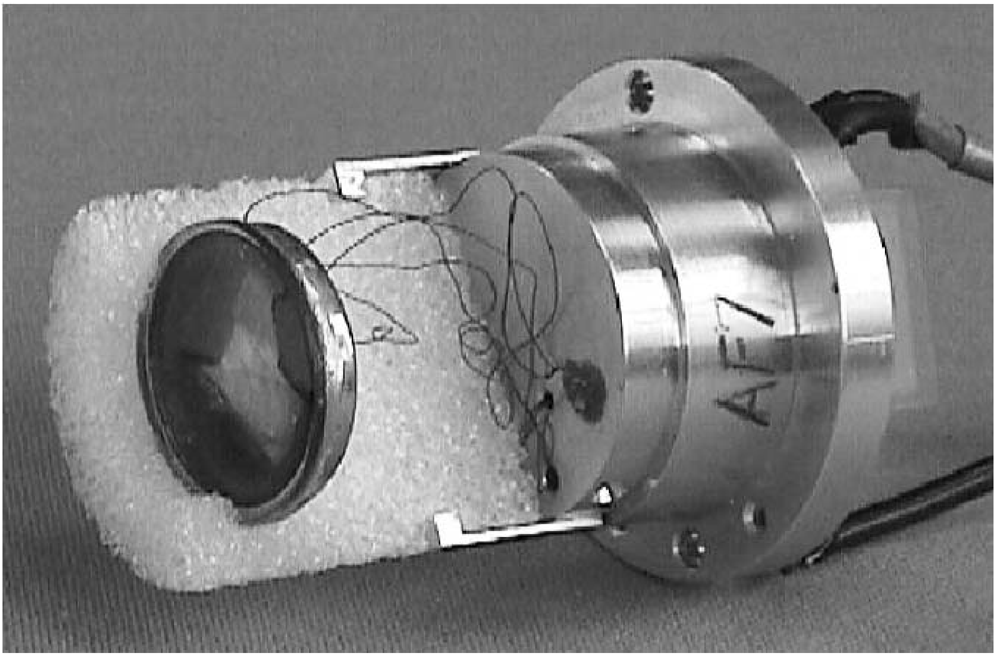

Figure 6.1 Photograph of the first primary standard for laser energy measurement, a liquid-cell calorimeter.

became the first U.S. national standard for measurement of laser energy, and was used for calibrations for several years.

Subsequent work led to more accurate “isoperibol” calorimeters [2], in which the radiation is absorbed in multiple surfaces, arranged in configurations (traps) designed to collect and absorb reflected light (Figure 6.2). Today, the NIST Optoelectronics Division maintains eight such instruments, each designed for a particular class of laser characteristics—power or energy level, pulsed or cw emission, and wavelength. The most accurate is a helium-cooled instrument, known as a cryogenic radiometer, which provides calibration of cw instruments at low levels (~100 μW) with uncertainties in the range of 0.05 %. The largest is a water-cooled instrument designed to measure 100 kW or more of power.

Though the comparison of optical and electrical energy, as a radiometric technique, had been used long before the development of lasers, it was the requirements of laser metrology that stimulated its full development. Today, it is used in almost all areas of radiometry.

But laser metrology also provides a good example of how the existence of good primary standards does not always assure good procedures for product characterization. Standard procedures developed for the characterization of radiation from laser diodes, which, without additional optical components, typically have a large divergence angle, may not be compatible or consistent with procedures for characterizing well collimated gas or solid-state lasers. In part, this situation has resulted from the fact that the procedures were developed independently by different SDOs, demonstrating the need for coordination and communication.

Standards for the development of optical fiber provide many illustrations that may be useful in the development of future IT services. In the late 1970s, when opti-

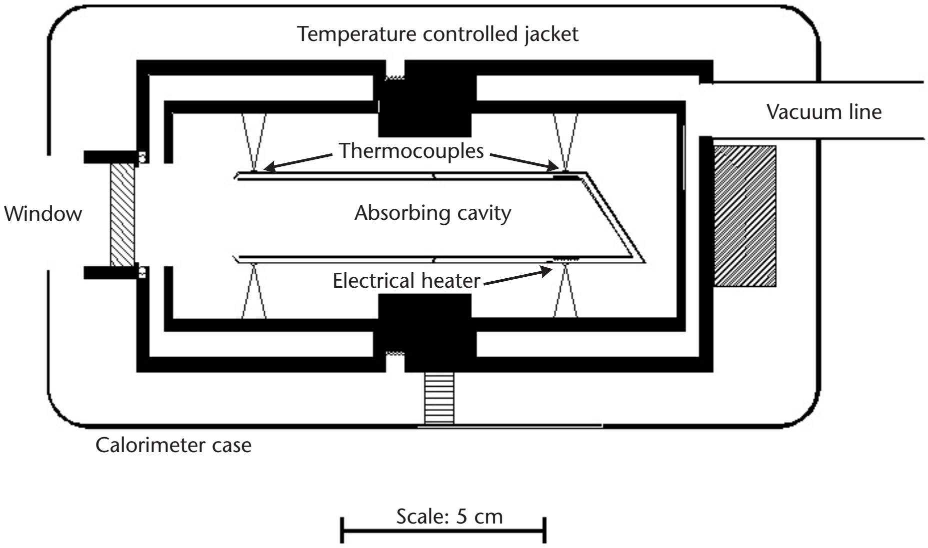

Figure 6.2 Diagram of the first isoperibol calorimeter used for traceable laser power and energy measurements.

cal fiber first became a commercial product and there were many more companies in the field than there are today, it quickly became apparent that a lack of standards for product characterization meant that products produced by different manufacturers could not be usefully compared. Companies responded to that problem quickly and as a group, and, largely for those reasons, the optical communications industry has an extensive infrastructure of standards today.

Good standard procedures can lead to significant improvements in the uncertainties of measurements used for product specification. The data in Figure 6.3 shows improvements in the measurement of fiber attenuation (in one company) during the development of attenuation measurement standards.

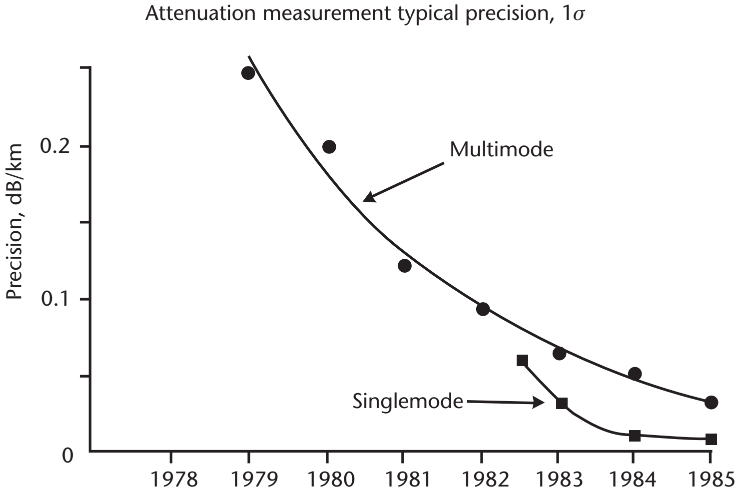

Figure 6.3 History of improvement in the precision of fiber attenuation in one company during the development of standard procedures.

A lack of standards can impede the development of a technology and/or precipitate product improvements. Standards for the determination of the bandwidth of multimode fiber provide examples of both effects.

In even the best early multimode fibers, differences in the group velocity among modes limited bandwidth. Worse, measured bandwidth depended on the distribution of power among the modes. And because of differences in attenuation, the length dependence of fiber bandwidth could not be predicted reliably. This measurement problem was not solved, but became less important as high-speed communications began to be designed to use single-mode fiber, while lower-speed, short-distance applications of multimode fiber generally used LED sources that excited all modes of the fiber.

A decade or more later, when interest arose in updating Ethernet standards to data rates of 1 Gbps, lasers were needed to provide the required modulation bandwidth. But lasers generally excited only a limited set of the modes of a fiber, and as was previously known, bandwidth could not be reliably predicted under that circumstance. Measurements such as those shown in Figure 6.4 demonstrated the magnitude of the problem [3]. In a typical fiber, the group velocity varied not only with mode, but the variation with mode changed along the length of the fiber.

Choosing launching conditions wisely permitted the establishment of the Gigibit Ethernet Standard, but the longer-term solution was the development of multimode fiber with much lower differential group velocity. Such fibers, commonly known as "laser fibers," now exist, and have enabled the development of an Ethernet standard at 10 Gbps.

Several examples in the development of optical fiber standards have illustrated the importance of technical verification of standards. One is the development of a standard procedure for specifying the mode-field diameter of a single-mode fiber. The proposed procedure involved a far-field measurement of the distribution of light emerging from a fiber, and the transformation of the far-field pattern back to

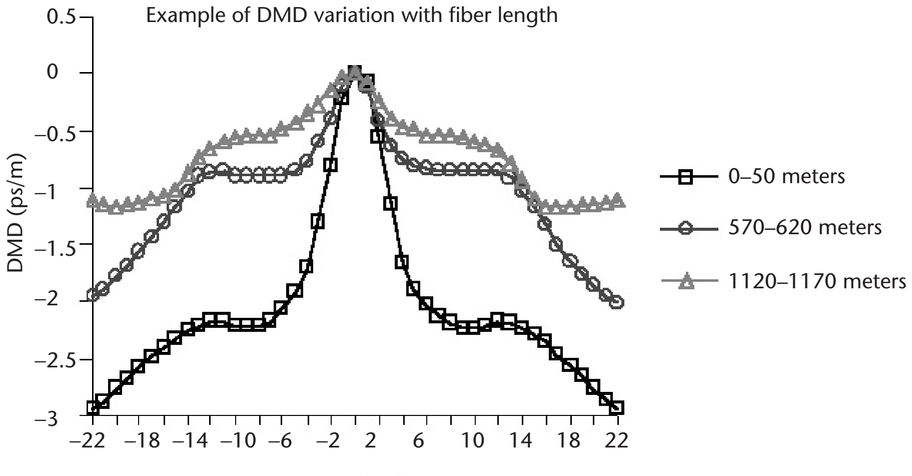

Figure 6.4 Differential mode (group velocity) delay at three positions along the length of a multimode optical fiber. In more recent fibers developed for high-speed Ethernet systems, the DMD is much reduced.

the near field. When the procedure was tested in several laboratories the agreement was fairly good, as shown in Figure 6.5(a), but there were significant systematic variations between the laboratories [4]. Further analysis and experimentation showed that the results depended on the dynamic range of the detector used for measurements. Detectors with less dynamic range smoothed deep minima in the far-field pattern [Figure 6.5(b)] and led to lower values of mode field diameter.

Another example of insufficient technical validation is the standard for specification of transmitters for Fibre Channel systems. The standard required that transmitters be tested using a receiver with a specified frequency response, and meet a certain eye-diagram requirement. The frequency response of the receiver was specified to match, within tolerances, a particular analytic function at frequencies up to 1.5 GHz. However, subsequent testing showed that differences in the frequency response of receivers well above 1.5 GHz could determine whether a transmitter passed or failed the specification [5] (Figure 6.6).

Sometimes standards can be too complex for practical implementation in industry. After the meter was redefined in 1982 in terms of the speed of light, national standards laboratories implemented the new definition by interferometric

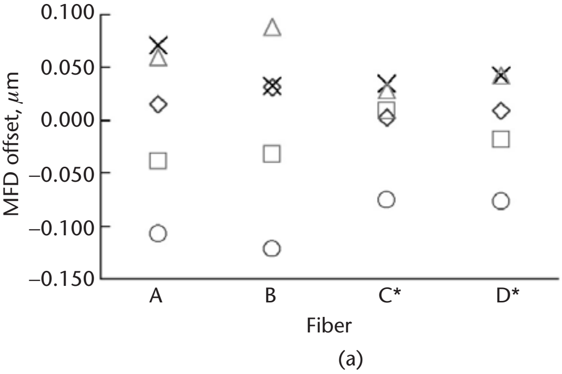

(a)

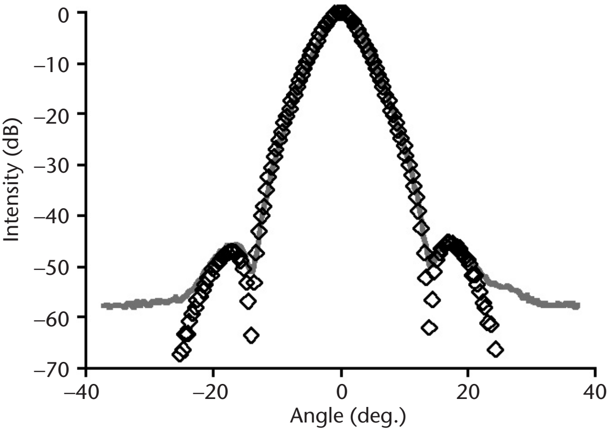

(b)

Figure 6.5 (a) Results of comparative measurements of the mode-field diameter of four single mode fibers by five laboratories showing small systematic differences between the laboratories, each represented by a different symbol. (b) The explanation for the systematic differences in the data of (a) was found to be in the degree to which detectors could detect deep nulls in the far-field pattern.

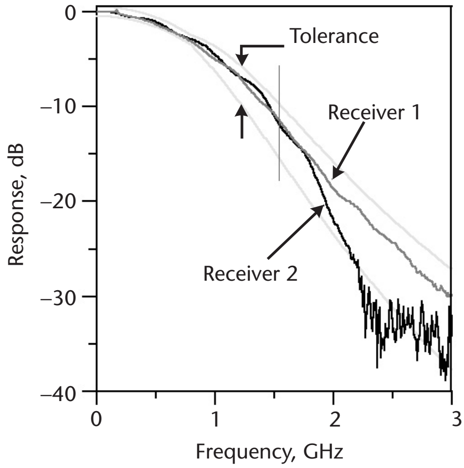

Figure 6.6 Frequency response of reference receivers used in Fibre Channel transmitter testing. Properties at frequencies above the specification (1.5 GHz) were found to be important.

comparison with frequency-stabilized laser lines that had been measured using frequency standards [6]. Though this approach provided high accuracy, it was not well suited to the calibration of optical spectrum analyzers or other instrumentation used in optical communications. Meeting calibration needs related to wavelength-division-multiplexed optical communications systems required the development of simple standards, the most successful of which are molecular gas absorption cells (Figure 6.7) [7].

The development of standards can sometimes require solving difficult technical problems. When optical fiber companies wanted to reduce the uncertainty in their specification of fiber diameter, they needed a way of measuring the diameter to an uncertainty of about 0.1 μm. Noncontact measurement methods were not sufficiently accurate, and contact methods distorted the fiber by amounts that were significant in comparison to the desired uncertainty. Ultimately, a solution involving measurement of the apparent diameter versus contact force was developed, and well-developed calibrations standards were made available to the industry [8, 9].

That fiber diameter standard also provides a good illustration of how the development of new standards can provide a competitive advantage. After diameter stan-

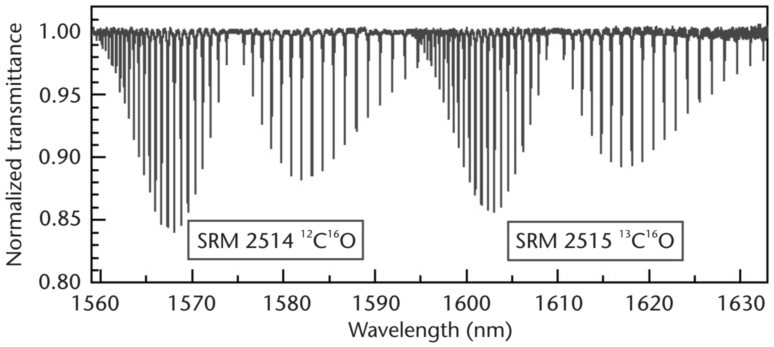

Figure 6.7 Spectral absorption of carbon monoxide (two isotopes of carbon) used in wavelength standards for optical communications.

dards became available, but before they were universally used, a study of fiber diameter measurements was conducted involving 25 participants from throughout most of the world. The results are shown in Figure 6.8, where the solid symbols are results from participants whose data were traceable to an artifact standard [5].

Existing standards can sometimes impede the development of new technology. That has been a particular problem in the development of optical sensors, which will likely play an important role in future IT systems. Optical sensors offer many advantages over electrical sensors, often including better performance and freedom from interference, as well as the possibility of distributed sensing and high degrees of multiplexing. However, optical sensors often do not naturally provide output signals that conform to previous standards. Sensors developed for use in the electrical power industry are a good example. Figure 6.9 shows an optical current and voltage measurement instrument designed to replace current and voltage transformers used in high-voltage distribution systems.[1] The measurement system contains electronics to convert the inherently low-voltage, low-current signals from the optical sensors to the nominal 1A, 120V output required by existing systems. Requirements such as these are an obvious impediment to the full exploitation of optical sensing technology.

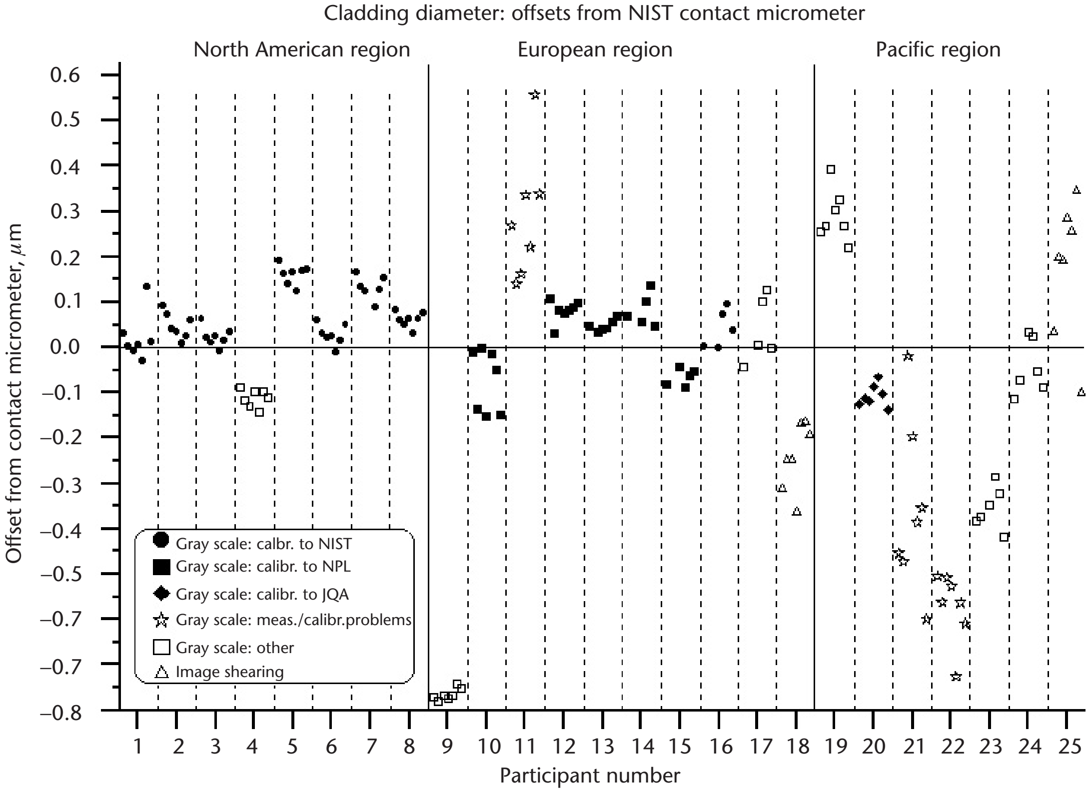

Figure 6.8 Data from a comparison of measurement of optical fiber diameter by 25 laboratories. Solid symbols are from participants whose measurements were traceable to national standards.

---

[1] The instrument shown is produced by ABB; see http://www.abb.com/. The discussion of this product as an illustration of an issue in standardization does not imply an endorsement or recommendation of the product by NIST.

Figure 6.9 A commercially available optical current and voltage sensor. To meet existing standards, the optical outputs are converted to provide nominal outputs of 1A and 120V.

In summary, experience in the optical communications and sensing industries provides many reminders that standards are technological enablers, with important economic impacts in development, production, and competition. These are good reasons to address them early in the development of a technology, being mindful of the cost and complexity. Consensus standards, developed with broad industry participation and validated analytically and experimentally, are generally most effective. Some needs for standards will pose difficult technical problems, but they can also be opportunities for, and ways to drive, technological innovation.

References

[1] Jennings, D. A., "Calorimetric Measurement of Pulsed Laser Output Energy," *IEEE Trans. Instrum. Meas.,* Vol. IM-15, 1966, pp. 161–164.

[2] West, E. D., and K. L. Churney, "Theory of Isoperibol Calorimetry for Laser Power and Energy Measurements," *J. Appl. Phys.* Vol. 41, 1970, pp. 2705–2712.

[3] Schlager, J. B., and D. L. Franzen, "Differential Mode Delay Measurements on Multimode Fibers in the Time and Frequency Domains," *Technical Digest*, *Symp. on Optical Fiber Meas.*, NIST SP 930, 1998, pp. 127–130.

[4] Young, M., "Mode-Field Diameter of Single-Mode Optical Fiber by Far-Field Scanning," *Appl. Opt.* Vol. 37, 1998, pp. 5605–5619; T. J. Drapela, "Effective Area and Nonlinear Coefficient Measurements of Single-Mode Fibers: Recent Interlaboratory Comparisons," *Proc. SPIE*, Vol. 4087, 2000, pp. 293–297.

[5] Hale, P. D., NIST, unpublished.

[6] Quinn, T. J., "Practical Realization of the Definition of the Metre (1997)," *Metrologia*, Vol. 36, 1999, pp. 211–244.

[7] Swann, W. C., and S. L. Gilbert, "Pressure-Induced Shift and Broadening of 1510-1540 μm Acetylene Wavelength Calibration Lines," *J. Opt. Soc. Am. B*, Vol. 17, 2000, pp. 1263–1270.

[8] Young, M., P. D. Hale, and S. E. Mechels, "Optical Fiber Geometry: Accurate Measurement of Cladding Diameter," *NIST J. Research*, Vol. 98, 1993, pp. 203–216

[9] Drapela, T. J., D. L. Franzen, and M. Young, "Optical Fiber, Fiber Coating, and Connector Ferrule Geometry: Results of Interlaboratory Measurement Comparisons," *NIST Technical Note 1378,* 1995.

CHAPTER 7

Physics and Applications of Nanophotonics

Motoichi Ohtsu
The University of Tokyo

Introduction

We first present three possible technical problems faced by the future optical industry in order to explain the motivation behind the work reviewed here [1]. (1) Optical fiber transmission systems require increased integration of photonic devices if data transmission rates are to reach as high as 10 Tbps by 2015. To support this increase, it is estimated that the size of photonic matrix switching devices should be reduced to a subwavelength scale, to integrate more than 1,0001,000 input and output channels on a substrate. Since conventional photonic devices (e.g., diode lasers and optical waveguides) have to confine the lightwave within their cavities and core layers, respectively, their minimum sizes are limited by the diffraction of light. Therefore, they cannot meet this requirement, because the required size is beyond this diffraction limit. (2) Progress in DRAM technology requires improved photolithography. It is anticipated that it should be possible to fabricate patterns narrower than 50 nm by 2010. Although several methods using special light sources (e.g., an extreme ultraviolet light source and a synchrotron radiation light source) have been developed, they require linewidth that far exceeds the diffraction limit of visible light. (3) It has been estimated that optical memory systems will require a recording density as high as 1 Tbit/in^2 by 2010, which is more than 100 times higher than that of a DVD. Since the mark length for 1 Tbit/in^2 is as short as 25 nm, recording such small marks far exceeds the diffraction limit of light.

From these three points, it can be readily understood that a novel optical nanotechnology that goes beyond the diffraction limit is required in order to support the optical science and technology of the twenty-first century. To meet this requirement, I have proposed a novel technology, named nanophotonics [2]. Nanophotonics is defined as a technology that utilizes local electromagnetic interactions between a small nanometric element and an optical near field. Since an optical near field is free from the diffraction of light due to its size-dependent localization and size-dependent resonance features, nanophotonics enables the fabrication, operation, and integration of nanometric devices. The primary advantage of nanophotonics is its capacity to realize novel functions based on local electromagnetic interactions. It should be noted that some of the conventional concepts of wave-optics, such as interference, are no longer essential in nanophotonics. Instead, concepts of surface elementary excitation and nanofabrication technology are essential.

To solve the first technical problem requires an advanced photonic integrated circuit (IC). The degree of integration must greatly exceed that of a conventional diffraction-limited photonic IC. Quantum dot lasers and photonic crystals, composed of many nanometric elements, cannot meet this requirement because they use conventional lightwaves as a carrier for signal transmission. Instead, it is indispensable to use a localized optical near field as the carrier, and transmit it from one nanometric element to another. Figure 7.1 schematically explains the basic structure

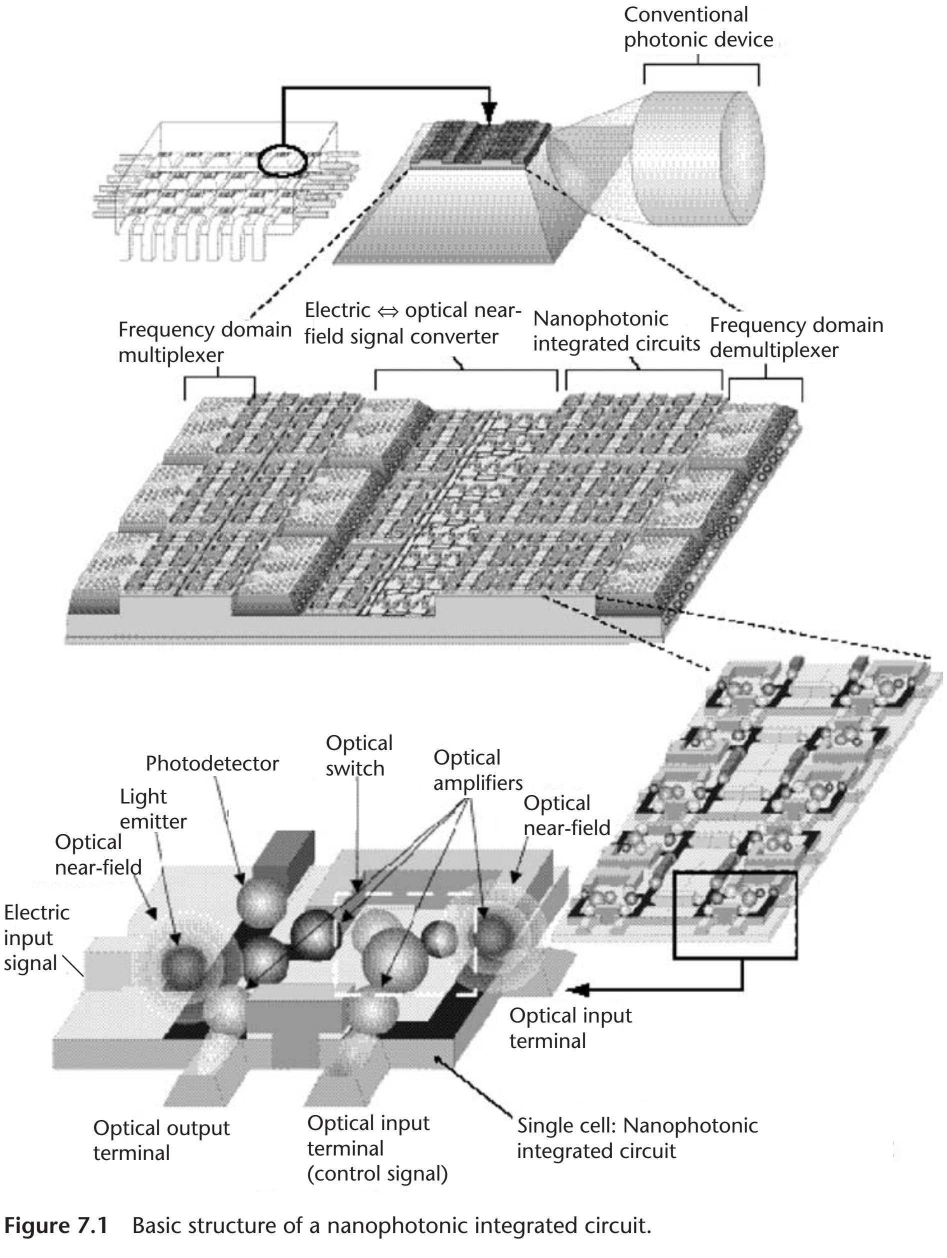

Figure 7.1 Basic structure of a nanophotonic integrated circuit.

of such an IC, called a nanophotonic IC, proposed in [3]. The light emitters, optical switches, input/output terminals, and photodetectors in this IC all consist of nanometric dots and wires. The optical near field generated at one quantum dot is transferred to an adjacent dot in order to transmit the signal. A switching device is used to modulate the optical near-field energy. To connect this IC with external conventional photonic devices, narrow waveguides are used as input/output terminals. Here, it should be noted that the nanometric size of each device and the high degree of integration are no more than a secondary advantage of this IC. The primary advantage is that novel functions and operations are realized based on the local electromagnetic interactions in a nanometric system buried in a macroscopic heat bath, as will be demonstrated in the following sections.

The next section outlines the theory of the nanophotonic switch, which is a key device in the nanophotonic IC. Its function is based on a unique optical near-field energy transfer, which is allowed between nanometric elements by the exchange of near-field photons. Experimental verification of this transfer is described in the section entitled "Observation of a Dipole Forbidden Energy Transfer for a Nanophotonic Switch." To fabricate nanophotonic devices and ICs requires a high degree of control and reproducibility of the size and position of the fabricated nanostructures, which should be as high as several nanometers. The section entitled "Nonresonant Near-Field Optical Chemical Vapor Deposition of Zn" reviews the chemical vapor deposition process developed to meet this requirement, using an optical near field. An advantage of this method is that it allows the selective growth of various materials (i.e., metals, insulators, and semiconductors) by the choice of light source. Note that this deposition method also solves problem 2 above. Further, as described in this section, an essential feature is that it allows nonresonant dissociation, which is an intrinsic phenomenon induced by an optical near field. The section entitled "Observation of Size-Dependent Features in the Photoluminescence of ZnO Nanocrystallites" reviews the quantum size effect of nanometric ZnO to demonstrate the capability of using it as a light emitter in a nanophotonic IC. The section entitled "Plasmon Waveguide for Optical Far/Near Field Conversion" reviews a novel plasmon waveguide to be used as an input/output terminal of the nanophotonic IC. For work in nanophotonics, a key device is a probe to generate/detect optical near fields with high efficiency and high resolution. The section entitled "A Key Device for Generation/Detection of Optical Near Field" reviews the progress in the development of this device. Finally, to solve problem 3, the section entitled "Application to High-Density and High-Speed Optical Memory" reviews a high-density, high-speed optical memory system that uses an optical near field. The final section summarizes the main points discussed in this chapter.

Theoretical Study of a Nanophotonic Switch

Principle of a Nanophotonic Switch

Optical near-field energy transfer between semiconductor quantum dots (QDs) can be used to design a nanophotonic switch, which is the most essential device in the nanophotonic IC of Figure 7.1. As an example, we employ cubic CuCl QDs in a NaCl matrix to describe the principle of this switch. It has been well known that translational motion of the exciton center of mass is quantized due to the small exciton Bohr radius for CuCl QDs [4–6]. The potential barrier of CuCl QDs in a NaCl crystal can be regarded as infinitely high, and the energy eigenvalues for the quantized Z_3 exciton energy level (n_x, n_y, n_z) in a cubic CuCl QD with the side length of L is given by

$$E_{n_x,n_y,n_z} = E_B + \frac{\hbar^2 \pi^2}{2M(L-a_B)^2}\left(n_x^2 + n_y^2 + n_z^2\right) \tag{7.1}$$

where E_B is the bulk Z_3 exciton energy, M is the translational mass of exciton, a_B is its Bohr radius, n_x, n_y, and n_z are quantum numbers (n_x, n_y, $n_z = 1, 2, 3,\ldots$), and $a = L - a_B$ corresponds to an effective side length found through consideration of the dead layer correction [4]. The exciton energy levels with even quantum numbers are dipole-forbidden states, that is, they are optically forbidden [7]. However, the optical near-field interaction is allowed for such energy levels [8].

Figure 7.2(a) illustrates the different-sized cubic CuCl QDs (I and O) and confined-exciton Z_3 energy levels. According to (7.1), there exists a resonance between the quantized exciton energy level of quantum number (1,1,1) for the QD-I with effective side length a and that of quantum number (2,1,1) for the QD-O with

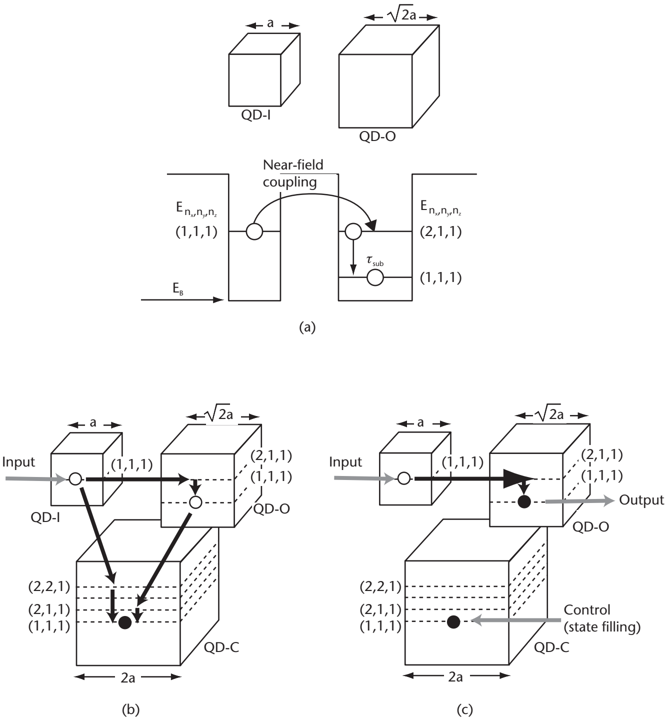

Figure 7.2 Schematic explanation of a nanophotonic switch. (a) Upper: Schematic drawings of closely located cubic CuCl QDs I and O with the effective side lengths of $a(=(L-a_B))$ and, $\sqrt{2}a$, respectively, where L and a_B are the side lengths of QDs and the exciton Bohr radius, respectively. Lower: Their exciton energy levels. n_x, n_y, and n_z represent quantum numbers of an exciton. E_B is the exciton energy level in a bulk crystal. (b) OFF state. (c) ON state.

effective side length $\sqrt{2}a$. Under this type of resonant condition, the coupling energy of the optical near-field interaction is given by the following Yukawa function [8, 9] (refer to the section entitled "Optical Near-Field Interaction Between Quantum Dots"):

$$V(r) = A\frac{\exp(-\mu r)}{r} \tag{7.2}$$

Here, r is the separation between two QDs, A is the coupling coefficient, and μ is the effective mass of the Yukawa function given by

$$\mu = \frac{\sqrt{2E_{n_x,n_y,n_z}\left(E_{NaCl} + E_{n_x,n_y,n_z}\right)}}{\hbar c} \tag{7.3}$$

where E_{NaCl} is the exciton energy of a NaCl matrix. Since the value of the coupling coefficient A depends on experimental conditions, we estimate it from the result of the previous work on the interaction between a Rb atom and the optical near-field probe-tip [8]. As a result, the value of A for a 5-nm cubic CuCl QD is found to be more than 10 times larger than that for the Rb-atom case, since the coupling coefficient A is proportional to the oscillator strength and square of the photon energy [8, 10]. Assuming that the separation r between two QDs is 10 nm, the coupling energy $V(r)$ is in the order of 10^{-4} eV, which corresponds to a transition time of 40 ps, and is much shorter than the exciton lifetime of a few nanoseconds. Further, an intersublevel transition time τ_{sub}, from higher exciton energy levels to the lowest one, is generally less than a few picoseconds and is much shorter than the transition time due to optical near-field coupling [11]. Therefore, most of the energy of the exciton in a CuCl QD-I transfer to the lowest exciton energy level in the neighboring QD-O and recombine radiatively in the lowest level.

Figure 7.2(b, c) illustrates the OFF and ON states of the proposed nanophotonic switch using three QDs including two QDs of Figure 7.2(a). The QD-I, O, and C are used as the input, output, and control ports of the switch, respectively. The quantized energy sublevels (1,1,1) in QD-I, (2,1,1) in QD-O, and (2,2,2) in QD-C resonate with each other. Additionally, the energy sublevels (1,1,1) in QD-O and (2,1,1) in QD-C also resonate. As described above, almost all the energy of the excitation in the QD-I transfer to the energy sublevels (1,1,1) in the neighboring QD-O, and finally, it transfers to the energy sublevels (1,1,1) in the QD-C. In the OFF state [Figure 7.2(b)], the input energy escapes to the QD-C, and then the output signal is obstructed. In the ON state [Figure 7.2(c)], the escape passes to the QD-C are blocked by the excitation of the QD-C, and thus the input energy goes through the QD-O giving an output signal. This switching operation is studied theoretically in the next section.

Energy Transfer Induced by Optical Near-Field Interaction

We will discuss the physical principles and phenomena behind the nanophotonic switch of Figure 7.2 (i.e., energy transfer phenomena induced by optical near field between two resonant energy levels in a QD and its adjacent QD) [12]. Optical near-field interaction (coupling) between QDs as an origin of the energy transfer will be derived microscopically within the quantum theoretical framework. As an example, a typical coupling strength and time scale of the process will be given for cubic CuCl QDs. We will also formulate a QD-heat bath system interacting with optical near field to clarify critical parameters for the proposed device, and examine the dynamics of the system numerically in order to simulate the switching behavior of the device.

A typical optical near-field system is a microscopic system (consisting of QDs and optical near field), which is coupled by a macroscopic matter system (consisting of a substrate, incident photons, and so on). It is convenient to treat this system in two steps: (1) Photons and the macroscopic matter system are described in terms of a so-called polariton basis where photons are dressed by macroscopic matter excitations, not free photons, and (2) The interaction between the microscopic and macroscopic systems is expressed by using the polariton basis.

We have developed a systematic formulation by using the projection operator method, in which photons and macroscopic matter excitations are described on an equal footing in terms of an elementary excitation mode like exciton-polaritons, and then the effects of both macroscopic matter system and photons are renormalized into an effective two-body interaction between nanometric objects in the microscopic system [8, 13–16]. Here we call this effective interaction as optical near-field interaction. On the basis of the formulation, we first illustrate interdot energy transfer phenomena, with QDs as nanometric objects, and then derive an explicit form of the optical near-field interaction. As an example, we give a typical time scale for the energy transfer process in cubic CuCl QDs.

Interdot Energy Transfer Via Optical Near Field

Let us first consider a two-QD system interacting with optical near field, as schematically depicted in Figure 7.3, in order to illustrate how excitation energy is transferred between the QDs. The QD1 and QD2 correspond to the QD-I and QD-O in Figure 7.2, respectively. The model Hamiltonian of the system is written as

$$\begin{aligned}
\hat{H} &= \hat{H}_0 + \hat{V} \\
\hat{H}_0 &= E_1 \hat{A}^\dagger \hat{A} + E_1 \hat{B}^\dagger \hat{B} + \sum_{\vec{k}} E(k) \hat{\xi}^\dagger_{\vec{k}} \hat{\xi}_{\vec{k}} \\
\hat{V} &= -\sum_{\alpha=A}^{B} \hat{\vec{\mu}}_\alpha \cdot \hat{\vec{D}}(\vec{r}_\alpha)
\end{aligned} \tag{7.4}$$

where $(\hat{A}^\dagger, \hat{A})$ and $(\hat{B}^\dagger, \hat{B})$ represent the excitation creation and annihilation operators in QD1 and QD2, respectively, and with E_1 being the excitation energy. The optical near field is modeled as exciton-polariton field, and the creation and annihilation operators and the eigenenergy for exciton-polariton [17–21] are denoted as $(\hat{\xi}^\dagger_{\vec{k}}, \hat{\xi}_{\vec{k}})$ and $E(k)$, respectively. The interaction $\hat{V}$ between the QD system and the optical near field expressed by exciton-polariton, is given by the multipolar QED Hamiltonian in the dipole approximation [22, 23], with $\hat{\vec{\mu}}_\alpha$ and $\hat{\vec{D}}(\vec{r}_\alpha)$ representing the dipole operator and the electric displacement vector at position $\vec{r}_\alpha$. As mentioned above, $\hat{\vec{D}}(\vec{r}_\alpha)$ is expressed in terms of the exciton-polariton operators as

$$\begin{aligned}
&\hat{\vec{\mu}}_A = \vec{\mu}_A\left(\hat{A}+\hat{A}^\dagger\right),\ \hat{\vec{\mu}}_B = \vec{\mu}_B\left(\hat{B}+\hat{B}^\dagger\right),\\
&\hat{\vec{D}}(\vec{r}_\alpha) = i\sqrt{\frac{2\pi\hbar}{V}}\sum_{\vec{k}\lambda}\vec{e}_{\vec{k}\lambda} f(k)\left(\hat{\xi}_{\vec{k}} e^{i\vec{k}\cdot\vec{r}_\alpha} - \hat{\xi}^\dagger_{\vec{k}} e^{-i\vec{k}\cdot\vec{r}_\alpha}\right),\\
&f(k) = \frac{\hbar ck}{\sqrt{\hbar E(k)}}\sqrt{\frac{E^2(k)-E_m^2}{2E^2(k)-E_m^2-\hbar^2c^2k^2}}
\end{aligned} \tag{7.5}$$

where $f(k)$ is the coupling coefficient between photons and the macroscopic matter system, and E_m designates the excitation energy of the macroscopic matter system [8, 14, 16]. The vector $\vec{e}_{\vec{k}\lambda}$ is the unit vector normal to the exciton-polariton wave vector $\vec{k}$, and $\hbar$ and c are the Planck constant divided by 2π and the velocity of light in a vacuum, respectively.

Dynamics of the system, including energy transfer, is now governed by the following Liouville equation

$$\dot{\hat{\rho}}_{\text{total}}(t) = -\frac{i}{\hbar}\left[\hat{H},\hat{\rho}_{\text{total}}(t)\right] \tag{7.6}$$

with the density operator $\hat{\rho}_{\text{total}}(t)$ [24–27]. Tracing out the exciton-polariton degrees of freedom from both sides of (7.6), we obtain an equation of motion for the density operator $\hat{\rho}(t)$ in mean-field approximation [27] as

$$\begin{aligned}
&\dot{\hat{\rho}}(t) = -\frac{i}{\hbar}\left[\hat{V}_{\text{dot}},\hat{\rho}(t)\right]\\
&\hat{\rho}(t) = \text{Tr}_{\text{pol}}\left[\hat{\rho}_{\text{total}}(t)\right],\ \hat{V}_{\text{dot}} = \text{Tr}_{\text{pol}}\left[\hat{V}\right]
\end{aligned} \tag{7.7}$$

Here the notation Tr_{pol} means to take a trace of the subsequent operator regarding the exciton-polariton degrees of freedom. Note that we have obtained (7.7) in the interaction representation. We then prepare two states $\left|\Phi_1\right\rangle = \left|A^*\right\rangle\left|B\right\rangle$ for the excited state in QD1 and $\left|\Phi_2\right\rangle = \left|A\right\rangle\left|B^*\right\rangle$ for the excited state in QD2, in order to construct the matrix elements of $\hat{\rho}(t)$ and to express (7.7) in the matrix form. It should be noted that the nonzero matrix elements of the interaction operator $\hat{V}_{\text{dot}}$ are the off-diagonal parts only as

$$\hbar U \equiv \left\langle\Phi_2\left|\hat{V}_{\text{dot}}\right|\Phi_1\right\rangle = \left\langle\Phi_1\left|\hat{V}_{\text{dot}}\right|\Phi_2\right\rangle \tag{7.8}$$

and thus

$$\left\langle\Phi_1\left|\hat{V}_{\text{dot}}\right|\Phi_1\right\rangle = \left\langle\Phi_2\left|\hat{V}_{\text{dot}}\right|\Phi_2\right\rangle = 0 \tag{7.9}$$

Under the initial condition of $\left\langle\Phi_1\left|\hat{\rho}(0)\right|\Phi_1\right\rangle = 1$, the matrix elements of the density operator can be exactly solved, and population probability of staying in the excited state for QD1 or QD2 is given by the diagonal part of the density matrix as

$$\begin{aligned} \langle \Phi_1 | \hat{\rho}(t) | \Phi_1 \rangle &= \cos^2(Ut), \\ \langle \Phi_2 | \hat{\rho}(t) | \Phi_2 \rangle &= \sin^2(Ut) \end{aligned} \tag{7.10}$$

Equation (7.10) shows, as is well known, that the time evolution of the population goes and returns between both QDs (i.e., nutation occurs with the Rabi flopping frequency U [25, 27]). In this way, the matter excitation energy is transferred from one QD to another neighboring QD due to the interaction $\hat{V}$ as a coupling between the QDs and the exciton-polariton field (optical near field).

Optical Near-Field Interaction Between Quantum Dots

From the preceding subsection, it follows that $\hbar U$ in (7.8) is a key parameter of the interdot energy transfer process. According to our previous studies [8, 13–16], we show how to obtain $\hat{V}_{\text{dot}}$ in a systematic and consistent way, depending on the choice of $|\Phi_1\rangle$ and $|\Phi_2\rangle$. In other words, we outline a derivation of the optical near-field interaction between QDs.

First, exact eigenstates $|\Psi_\lambda\rangle$ of the total Hamiltonian $\hat{H}$ are divided into two groups. One contains relevant states in P-space $|\Psi_\lambda^P\rangle = P|\Psi_\lambda\rangle$ and the other contains irrelevant states in Q-space $|\Psi_\lambda^Q\rangle = Q|\Psi_\lambda\rangle$, where P and Q represent the projection operators with the properties $P + Q = 1$, $P^2 = P(Q^2 = Q)$, and $P^\dagger = P(Q^\dagger = Q)$ [8, 13, 14, 28–32]. Referring to Figure 7.3, for example, P-space can be constructed from the eigenstates of $\hat{H}_0$ (i.e., a combination of two energy levels for each QD and the exciton-polariton vacuum state). Q-space is complementary to P-space and the exciton-polariton states are not vacant. Then the exact states $|\Psi_\lambda\rangle$ can be formally expressed by using the states only in P-space as [8, 13, 14, 28]

$$\begin{aligned} |\Psi_\lambda\rangle &= \hat{J}P\left(P\hat{J}^\dagger \hat{J}P\right)^{-1/2} |\Psi_\lambda^P\rangle \\ \hat{J} &= \left[1 - (E_\lambda - H_0)^{-1} Q\hat{V}\right]^{-1} \end{aligned} \tag{7.11}$$

where E_λ denotes the eigenenergy for $\hat{H}|\Psi_\lambda\rangle = E_\lambda|\Psi_\lambda\rangle$. Using (7.11), we can thus obtain the effective interaction $\hat{V}_{\text{eff}}$ that corresponds to $\hbar U$ or $\hat{V}_{\text{dot}}$ in (7.8) as

$$\begin{aligned} \langle \Psi_f | \hat{V} | \Psi_i \rangle &= \langle \Psi_f^P | \hat{V}_{\text{eff}} | \Psi_i^P \rangle, \\ \hat{V}_{\text{eff}} &\equiv \left(P\hat{J}^\dagger \hat{J}P\right)^{-1/2} P\hat{J}^\dagger \hat{V}\hat{J}P\left(P\hat{J}^\dagger \hat{J}P\right)^{-1/2} \end{aligned} \tag{7.12}$$

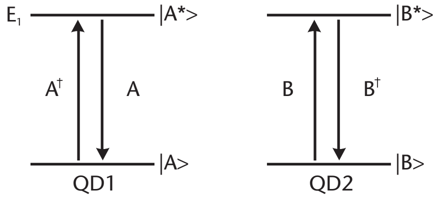

Figure 7.3 Two-level QD system coupled by the optical near field.

For further evaluation of (7.12), we need to know the explicit form of the operator $\hat{J}$ as well as the eigenvalue E_λ. If we expand the operator $\hat{J}$ in the order of $\hat{V}$, and approximate the eigenvalue E_λ as an unperturbed value, then we have the perturbative solution of $\hat{J}$ as $\hat{J} = 1 + \left(E_0^P - E_0^Q\right)^{-1}\hat{V} + \ldots$. Since it is easy to show $\left\langle \Psi_f^P \left| P\hat{V}P \right| \Psi_i^P \right\rangle = 0$, (7.12) can be rewritten within the second order as

$$\left\langle \Psi_f^P \left| \hat{V}_{\text{eff}} \right| \Psi_i^P \right\rangle = \sum_m \left\langle \Psi_f^P \left| \hat{V} \right| m^Q \right\rangle \left\langle m^Q \left| \hat{V} \right| \Psi_i^P \right\rangle \left(\frac{1}{E_{0i}^P - E_0^Q} + \frac{1}{E_{0f}^P - E_0^Q} \right) \tag{7.13}$$

where E_{0i}^P, E_{0f}^P, and E_0^Q stand for the eigenenergies of unperturbed Hamiltonian $\hat{H}_0$ for the initial and final states in P-space, and the intermediate state $\left| m^Q \right\rangle$ in Q-space, respectively.

Since we are primarily interested in the interdot interaction part of (7.13), we set the relevant initial and final states in P-space as $\left| \Psi_i^P \right\rangle = |A\rangle \left| B^* \right\rangle |0\rangle$ and $\left| \Psi_f^P \right\rangle = \left| A^* \right\rangle |B\rangle |0\rangle$. Then it is easily shown that only two states in Q-space, $\left| m^Q \right\rangle = |A\rangle |B\rangle \left| \vec{k} \right\rangle$ and $\left| A^* \right\rangle \left| B^* \right\rangle \left| \vec{k} \right\rangle$ with one exciton-polariton state $\left| \vec{k} \right\rangle$, can provide nonzero contributions. Through the above procedure, we can eliminate the explicit exciton-polariton (optical near field) degrees of freedom, and have an effective two-body interaction; that is, optical near-field interaction between QDs as

$$\begin{aligned} U(\vec{r}) &\equiv \frac{1}{\hbar} \left\langle \Psi_f^P \left| \hat{V}_{\text{eff}} \right| \Psi_i^P \right\rangle \\ &= -\frac{\mu_A \mu_B}{6\pi^2} \int_0^\infty d^3k f(k) \\ &\times \left\{ \left[\frac{1}{E(k) + E_A} + \frac{1}{E(k) + E_B} \right] e^{i\vec{k}\cdot\vec{r}} + \left[\frac{1}{E(k) - E_A} + \frac{1}{E(k) - E_B} \right] e^{-i\vec{k}\cdot\vec{r}} \right\} \end{aligned} \tag{7.14}$$

where $\vec{r} = \vec{r}_A - \vec{r}_B$ is the relative distance vector, and $\mu_{A(B)}$ is the transition dipole moment of QD1 (7.2). Approximating the energy dispersion $E(k)$ of exciton-polaritons with effective mass m_p as

$$E(k) = \frac{\hbar^2 k^2}{2m_p} + E_m \tag{7.15}$$

and substituting (7.15) into (7.14), we can finally obtain the optical near-field interaction potential as a sum of the Yukawa functions:

$$U(r) = \frac{\mu_A \mu_B}{3(\hbar c)^2} \sum_{\alpha=A}^{B} \left[W_{\alpha+} Y(\Delta_{\alpha+} r) + W_{\alpha-} Y(\Delta_{\alpha-} r) \right] \tag{7.16}$$

Here $W_{\alpha\pm}$ designates the weight factor of each Yukawa function that is defined as

$$Y(\Delta_{\alpha\pm} r) = \frac{e^{-\Delta_{\alpha\pm} r}}{r}, \qquad (7.17)$$
$$\Delta_{\alpha\pm} = \frac{1}{\hbar c}\sqrt{2E_p(E_m \pm E_\alpha)}$$

with the exciton-polariton effective mass rewritten as $E_p = m_p c^2$, and the relative distance $r = |\vec{r}_A - \vec{r}_B|$. The factor $\Delta_{\alpha-}$ becomes either real or pure imaginary depending on the magnitude of E_m and E_α, which means that this component behaves as either a localized or a propagation mode. To be precise, (7.16) includes additional two terms that are independent of the parameters of the microscopic system (i.e., the QDs), but those terms are neglected in (7.16) as a far-field contribution.

We can now, as an example, estimate the strength of the effective interaction between two cubic CuCl QDs induced by optical near field (i.e., the optical near-field interaction). We choose two-level exciton states as the microscopic matter states in P-space. The excitation energy of an exciton in a cubic QD is represented by (7.1). In Figure 7.4, the interaction potential is plotted as a function of the distance d between the closest edges of the cubic QDs. The effective side length a $(= L - a_B)$ of the cubic QDs are set as $a = 5$ and 7.1 nm whose ratio is $1 : \sqrt{2}$, and $M = 2.3m_e$ and $E_B = 3.20$ eV are used [4]. We estimated the transition dipole moments of the QDs from the experimental value of the QD oscillator strength $f_{\text{dot}} = 5$ [10] and the theoretical conversion formula [33], which are $\mu_A = \mu_B = 0.29(\text{eV}\cdot\text{nm}^3)^{1/2}$ and $\mu_A = 0.29, \mu_B = 0.49(\text{eV}\cdot\text{nm}^3)^{1/2}$ for $a = 5$ and 7.1 nm, respectively. When we choose the distance $d = 10$ nm, we find from Figure 7.4 that the interaction potential is about 60 μeV. Thus it follows from (7.10) that half of an oscillation period, π/U, is about 30 ps, which corresponds to the time for the initial population of a QD to be transferred to its neighbor. This is a very high speed and suitable for a nanophotonic device.

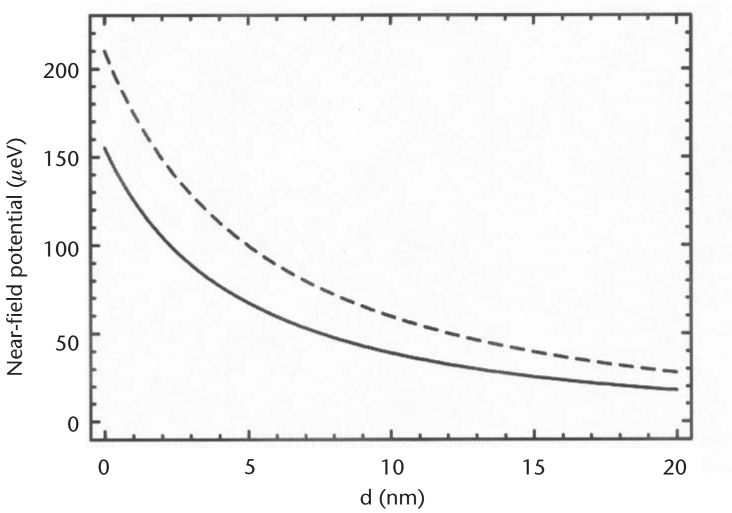

Figure 7.4 Optical near-field interaction potential for two cubic CuCl QDs. The solid and dashed curves represent the results for the cubic QD pairs with the same sizes a, and with the size ratio a: $\sqrt{2}a$ (a = 5 nm), respectively.

Dynamics of a Quantum Dot–Heat Bath Coupling System

From the discussion of the previous subsection, the population between two resonant levels of QDs undergoes nutation induced by the optical near-field interaction, and thus we have to include some mechanisms to guarantee the one-directional or irreversible energy transfer on which a nanophotonic device relies. One way is to allow intrasublevel transitions due to a phonon coupling. We therefore examine a two-QD system coupled to a phonon (heat) bath system, illustrated in Figure 7.5. The Hamiltonian of such a system is modeled as

$$\begin{aligned}
\hat{H} &= \hat{H}_0 + \hat{H}_{\text{int}} + \hat{H}_{SR} \\
\hat{H}_0 &= E_1 \hat{A}^\dagger \hat{A} + E_2 \hat{B}^\dagger \hat{B} + (E_1 - E_2)\hat{C}^\dagger \hat{C} + \sum_n \varepsilon_n \hat{b}_n^\dagger \hat{b}_n \\
\hat{H}_{\text{int}} &= \hbar U(r)\left(\hat{A}^\dagger \hat{B}\hat{C} + \hat{A}\hat{B}^\dagger \hat{C}^\dagger\right) \\
\hat{H}_{SR} &= \hbar \sum_n \left(\hat{g}_n \hat{b}_n^\dagger \hat{C} + \hat{g}_n^* \hat{b}_n \hat{C}^\dagger\right)
\end{aligned} \tag{7.18}$$

where $(\hat{A}^\dagger, \hat{A})$ and $(\hat{B}^\dagger, \hat{B})$ are fermionic operators for the creation and annihilation of an exciton in QD1 and in the lower energy level of QD2, respectively. Fermionic operators $(\hat{C}^\dagger, \hat{C})$ and bosonic operators $(\hat{b}_n^\dagger, \hat{b}_n)$ are for the E_2-E_1 levels of QD2 and for the heat bath system, respectively. The heat bath system is assumed to be a collection of many harmonic oscillators labeled n. From (7.6) the equation of motion for the total system can be written as

$$\begin{aligned}
\dot{\hat{\rho}}^I(t) &= -\frac{i}{\hbar}\left[\hat{H}_{\text{int}} + \hat{H}_{SR}^I(t), \rho^I(0)\right] \\
&-\frac{1}{\hbar^2}\int_0^t dt' \left[\hat{H}_{\text{int}} + \hat{H}_{SR}^I(t), \left[\hat{H}_{\text{int}} + \hat{H}_{SR}^I(t'), \hat{\rho}^I(t')\right]\right]
\end{aligned} \tag{7.19}$$

where the suffix I means the interaction picture, and the relation $\hat{H}_{\text{int}}^I(t) = \hat{H}_{\text{int}}$ is used [26]. In order to express the second-order temporal correlation clearly, the formal solution $\hat{\rho}^I(t)$ of (7.6) in the integral form is substituted again into the right-hand side of (7.6). Since we are mainly interested in exciton dynamics in the two-QD system, we take a trace with respect to the degrees of freedom of the heat bath system as $\hat{\rho}_S^I(t) = \text{Tr}_R[\hat{\rho}^I(t)]$. Here the density operator is assumed to be a

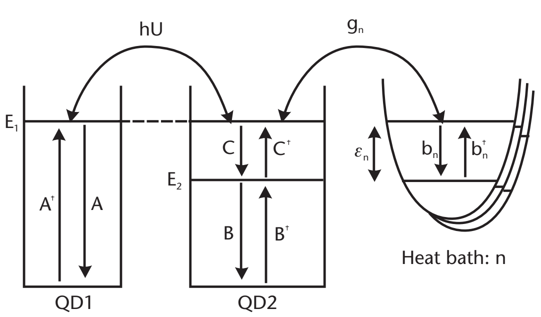

Figure 7.5 Two-QD system. Dot 1 and 2 are resonantly coupled due to the optical near-field interaction, and the sublevels in Dot 2 are coupled with the lattice vibration.

direct product of the QDs system part $\hat{\rho}_S^I(t)$ and the reservoir (heat-bath) system part $\hat{\rho}_R^I(t)$. If the reservoir system has a large volume or many degrees of freedom, the deviation from the initial value can be neglected, and the density operator can be approximated as (Born approximation)

$$\hat{\rho}^I(t) = \hat{\rho}_S^I(t)\hat{\rho}_R^I(t) \approx \hat{\rho}_S^I(t)\hat{\rho}_R^I(0) \tag{7.20}$$

Taking a trace of both sides of (7.19) about the reservoir operator, we obtain

$$\begin{aligned}\dot{\hat{\rho}}_S^I(t) &= -iU(r)\left[\hat{A}^\dagger\hat{B}\hat{C} + \hat{C}^\dagger\hat{B}^\dagger\hat{A}, \hat{\rho}_S^I(t)\right]\\ &-\sum_n n(\omega_n,T)\begin{bmatrix}\left(\left\{\hat{C}\hat{C}^\dagger, \hat{\rho}_S^I(t)\right\} - 2\hat{C}^\dagger\hat{\rho}_S^I(t)\hat{C}\right)\otimes\gamma_n^r(t)\\ -i\left[\hat{C}\hat{C}^\dagger, \hat{\rho}_S^I(t)\right]\otimes\gamma_n^i(t)\end{bmatrix}\\ &-\sum_n\left[1+n(\omega_n,T)\right]\begin{bmatrix}\left(\left\{\hat{C}^\dagger\hat{C}, \hat{\rho}_S^I(t)\right\} - 2\hat{C}\hat{\rho}_S^I(t)\hat{C}\right)\otimes\gamma_n^r(t)\\ +i\left[\hat{C}^\dagger\hat{C}, \hat{\rho}_S^I(t)\right]\otimes\gamma_n^i(t)\end{bmatrix}\end{aligned} \tag{7.21}$$

where the curly brackets $\{\cdot\}$ stands for the anticommutator, and the notation $\otimes$ designates the convolution integral. Since we assume the reservoir system to be in an equilibrium state, the terms including $\mathrm{Tr}_R\,[\hat{b}_n^\dagger\hat{\rho}_R^I(0)]$ and $\mathrm{Tr}_R\,[\hat{b}_n\hat{\rho}_R^I(0)]$ do not appear in (7.21). The number of phonons in the equilibrium state is written as $n(\omega_n,T) = \mathrm{Tr}_R\,[\hat{b}_n^\dagger\hat{b}_n\hat{\rho}_R(0)]$ to follow the Bose-Einstein statistics as [25–27]

$$n(\omega_n,T) = \frac{1}{e^{\hbar\omega_n/k_BT}-1} \tag{7.22}$$

The real and imaginary parts of the function

$$\gamma_n(t) = \left|g_n\right|^2 e^{i(\Delta\omega-\omega)t} \tag{7.23}$$

with $\hbar\Delta\omega = E_1 - E_2$ are represented as $\gamma_n^r(t)$ and $\gamma_n^i(t)$, which are related to a relaxation (real part) and energy shift (imaginary part) from the energy level in QD2 because of coupling to the heat bath system. The convolution in (7.21) expresses the effect of time delay for the transition between sublevels because of the coupling to the phonon (heat) bath system. However, if the dynamics of the reservoir (heat bath) system are much faster than that of the two-QD system, we can approximate the density operator of the two-QD system as $\hat{\rho}_S^I(t-t') = \hat{\rho}_S^I(t)$ (Markov approximation). Using this approximation, and rewriting the summation as $\sum_n = \int_0^\infty d\omega D(\omega)$, with $D(\omega)$ being the density of states for each phonon, we can express the convolution analytically as

$$\begin{aligned}\sum_n n(\omega_n,T)\hat{\rho}_S^I(t)\otimes\gamma_n(t) &= \hat{\rho}_S^I(t)\int_0^\infty d\omega\, n(\omega,T)D(\omega)\left|g(\omega)\right|^2\int_0^t dt' e^{i(\Delta\omega-\omega)t'}\\ &\approx \hat{\rho}_S^I(t)\left[\pi n(\Delta\omega,T)D(\Delta\omega)\left|g(\Delta\omega)\right|^2 + iP\int_0^\infty d\omega\frac{n(\omega,T)D(\omega)\left|g(\omega)\right|^2}{\Delta\omega-\omega}\right]\end{aligned} \tag{7.24}$$

Here we extend the upper limit of the time integration to infinity. The density operator is finally reduced to

$$\begin{aligned}\hat{\rho}_S^I(t) = -iU\left[\hat{A}^\dagger \hat{B}\hat{C} + \hat{A}\hat{B}^\dagger \hat{C}^\dagger, \hat{\rho}_S^I(t)\right] - n\gamma\left(\left\{\hat{C}\hat{C}^\dagger, \hat{\rho}_S^I(t)\right\} - 2\hat{C}^\dagger\, \hat{\rho}_S^I(t)\hat{C}\right) \\ -(1+n)\gamma\left(\left\{\hat{C}^\dagger \hat{C}, \hat{\rho}_S^I(t)\right\} - 2\hat{C}\hat{\rho}_S^I(t)\hat{C}^\dagger\right)\end{aligned} \tag{7.25}$$

where $n \equiv n(\Delta\omega, T)$ and $\gamma = \pi|g(\Delta\omega)|^2 D(\Delta\omega)$. The terms indicating the energy shift are neglected in (7.25) because it is small in the weaker system-bath coupling $\hat{H}_{SR}$.

Let us now discuss one-exciton dynamics or energy transfer in the system based on (7.25), using the three bases illustrated in Figure 7.6. The equations of motion for the matrix elements are read in the Schrödinger picture as

$$\begin{aligned}&\dot{\rho}_{11}(t) = iU(r)[\rho_{12}(t) - \rho_{21}(t)] \\ &\dot{\rho}_{12}(t) - \dot{\rho}_{21}(t) = 2iU(r)[\rho_{11}(t) - \rho_{22}(t)] - (1+n)\gamma[\rho_{12}(t) - \rho_{21}(t)] \\ &\dot{\rho}_{22}(t) = iU(r)[\rho_{12}(t) - \rho_{21}(t)] - 2(1+n)\gamma\rho_{22}(t) + 2n\gamma\rho_{33}(t) \\ &\dot{\rho}_{33}(t) = 2(1+n)\gamma\rho_{22}(t) - 2n\gamma\rho_{33}(t)\end{aligned} \tag{7.26}$$

When the temperature T is equal to zero ($n = 0$), (7.26) can be analytically solved. The diagonal parts representing the population probability for each energy level in QD1 and QD2 as well as the off-diagonal parts representing quantum coherence are given as

$$\begin{aligned}&\rho_{11}(t) = \frac{1}{Z^2}e^{-\gamma t}\left[\frac{\gamma}{2}\sinh(Zt) + Z\cosh(Zt)\right]^2 \\ &\rho_{22}(t) = \frac{U^2}{Z^2}e^{-\gamma t}\sinh^2(Zt) \\ &\rho_{33}(t) = 1 - [\rho_{11}(t) + \rho_{22}(t)] \\ &\rho_{12}(t) = -\rho_{21}(t) = i\frac{U}{Z^2}e^{-\gamma t}\sinh(Zt)\left[\frac{\gamma}{2}\sinh(Zt) + Z\cosh(Zt)\right]\end{aligned} \tag{7.27}$$

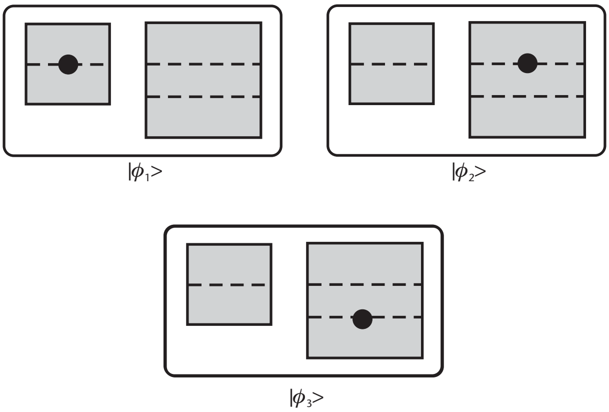

Figure 7.6 Three bases of single-exciton states in a two-QD system.

where $Z = \sqrt{(\gamma/2)^2 - U^2}$ and $\rho_{11}(0) = 1$ are used. We define the state-filling time τ_s as $\rho_{33}(\tau_s) = 1 - e^{-1}$, which corresponds to the time for excitation energy transfer from QD1 to the lower energy level in QD2. From (7.27), it follows that time evolution of the population drastically changes when the condition for the coupling strength is varied from $U < \gamma/2$ to $U > \gamma/2$. Although (7.27) seems to be undefined at $U = \gamma/2$ ($Z = 0$), we have a definite solution regardless of whether $Z \to +0$ or -0 are taken. In Figure 7.7, the state-filling time τ_s is plotted as a function of the ratio of $\gamma/2$ to U. For $U > \gamma/2$, the population $\rho_{22}(t)$ shows damped oscillation with an envelope function $e^{-\gamma t}$, and thus τ_s is determined by the relaxation constant γ (i.e., $\tau_s \tilde{} \gamma^{-1}$). On the other hand, for $U < \gamma/2$, $\rho_{22}(t)$ decays monotonically. At first glance, as $\gamma/2$ increases, we expect τ_s to become shorter (i.e., the population seems to flow into the lower level more quickly), but on the contrary the time τ_s becomes long, as shown in Figure 7.7. The reason is that the upper energy level becomes effectively broad and results in a decrease of the resonant energy transfer between the QDs. When the ratio $\gamma/2U$ is enough large, τ_s increases linearly from Figure 7.7. Therefore, the state-filling time is determined not only by the optical near-field interaction strength between two QDs, but also by the coupling strength to the heat bath (phonon bath) system. It follows from Figure 7.7 that the fastest energy transfer time τ_s is obtained when the condition $\gamma/2 \sim U$ is satisfied, and that τ_s is proportional to $\gamma/2U^2$ as $\gamma/(2U)$ becomes large.

The last term $2\gamma n \rho_{33}(t)$ on the right-hand side of the third equation in (7.26) indicates that the temperature effect due to the finite number of phonons ($n \neq 0$) induces back transfer of the excitation energy from the heat bath to the two-QD system. Within the Born approximation adopted in (7.20), this term incoherently increases the population $\rho_{22}(t)$. As the population $\rho_{33}(t)$ increases, the back transfer becomes large, and gives nonnegligible contributions to the upper-level populations $\rho_{11}(t)$ and $\rho_{22}(t)$.

Numerical Results

We present numerical calculation results for the population dynamics, using (7.26) and (7.27) for finite and zero temperature in order to verify the above theoretical considerations and to estimate the state-filling time for some practical cases. Here we assume that the system consists of two cubic CuCl QDs embedded in NaCl

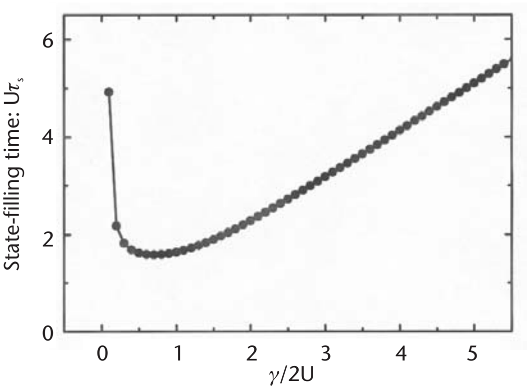

Figure 7.7 State-filling time τ_s against the ratio of exciton-phonon (heat) bath coupling strength $\gamma/2$ to intradot optical near-field coupling strength U.

matrix [12]. The effective side length of the cubes is set as $a{:}\sqrt{2}a$ ($a = 5$ nm) so that the (1,1,1) level of QD1 is resonant with the (2,1,1) level of QD2. The variable parameters are the interaction strength U or the intercube spacing, the relaxation constant g, and the temperature of the heat bath system.

In Figure 7.8, the E_1 and E_2-level populations $\rho_{22}(t)$ and $\rho_{33}(t)$ in QD2 are plotted in the cases of the intercube spacing $d = 5$, 10, and 15 nm ($U = 1.51 \times 10^{-1}$, 0.90×10^{-1}, and 0.60×10^{-1} (ps)$^{-1}$), , and $T = 0$K. The relaxation time γ^{-1} is set as 1 ps based on another experiment [34]. The populations for all three cases in Figure 7.8(a) show monotonic decays as we expected because the condition $U < \gamma/2$ is satisfied. From Figure 7.8(b), the state-filling time τ_s is estimated for the distance $d = 5$, 10, and 15 nm as 22, 60, and 140 ps, respectively. This indicates that energy transfer time of less than 100 ps can be realized when the two QDs are located within a distance of 10 nm.

Figure 7.9 gives the result for $\gamma^{-1} = 10$ ps, corresponding to a weaker coupling between an exciton and the heat bath system. Damped oscillations due to nutation between two resonant levels are clearly seen for $d = 5$ nm in Figure 7.9(a), where the condition $U > \gamma/2$ is satisfied. Although in the cases of $d = 10$ and 15 nm, the condition $U > \gamma/2$ also satisfied, we cannot observe the oscillation because of the small amplitude. From Figure 7.9(b), the state-filling times τ_s for the three cases are esti-

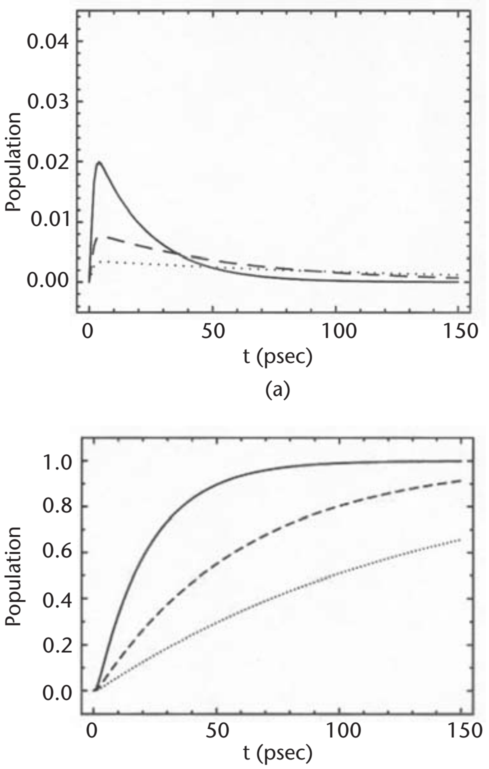

(a)

(b)

Figure 7.8 Time-evolution of (a) E_1-level population ρ_{22} (t) and (b) E_2-level population ρ_{33} (t), where the relaxation time γ^{-1} is set as 1 ps, and the temperature is set as 0K. The solid, dashed, and dotted curves represent the cases of interdot spacing $d = 5$, 10, and 15 nm, respectively.

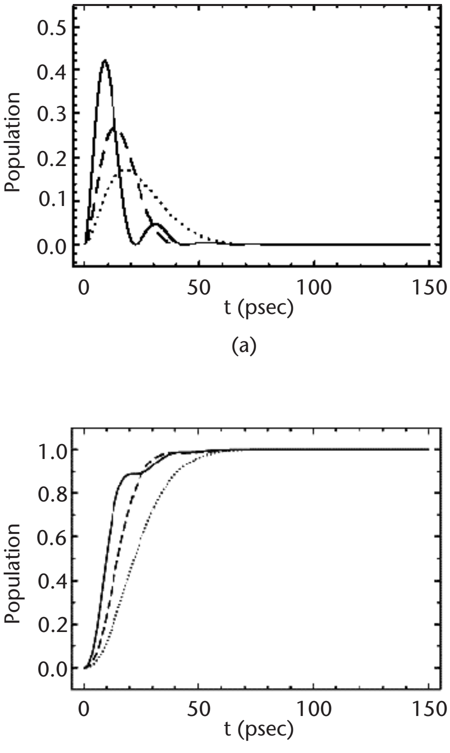

Figure 7.9 Time-evolution of (a) E_1-level population $\rho_{22}(t)$ and (b) E_2-level population $\rho_{33}(t)$, where the relaxation time γ^{-1} is set as 10 ps, and the temperature is 0K. The solid, dashed, and dotted curves represent the cases of interdot spacing $d = 5$, 10, and 15 nm, respectively.

mated as 12, 18, and 25 ps. Compared with Figure 7.8(b), the state-filling speed becomes faster in Figure 7.9(b) in spite of the increase in γ^{-1} because U is nearly equal to $\gamma/2$. These two graphs indicate that the interdot spacing should be adjusted so that the optical near-field coupling is of the same order as the exciton-phonon coupling in order to obtain the fastest energy transfer in the system.

Figure 7.10 shows the temperature dependence of the population $\rho_{22}(t)$ and $\rho_{33}(t)$. The temperature is set as either $T = 50$K or 100K. These results are obtained by using a Laplace transform, where the singular points are derived numerically for the given numerical parameters. As mentioned in the previous section, the finite temperature induces incoherent back transfer of energy, and this results in residual populations in the upper energy levels in both QDs. Figure 7.10(a) shows that there are finite convergent values depending on the temperature. However, we find from Figure 7.10(b) that the state-filling time does not change so drastically.

The results and discussions described above might be valid within the Born-Markov approximation. Even if the Born approximation is allowed because of the large volume of the heat bath system, the Markov approximation may not be guaranteed at low temperatures, as assumed in the transformation in (7.24). Therefore, we might deal with it more carefully, since it is said that non-Markov behavior manifests itself at low temperatures [26, 35]. The effects of non-Markov behavior on the dynamics are now under investigation. We have focused our attention on the energy transfer process in the nanometric regime, or signal transfer in a nanopho-

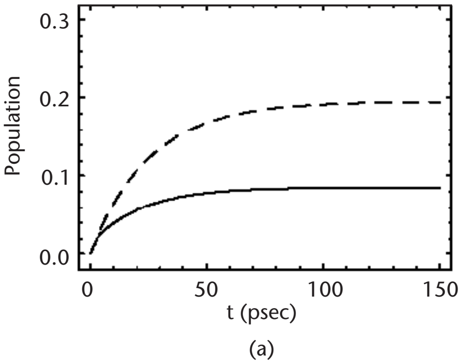

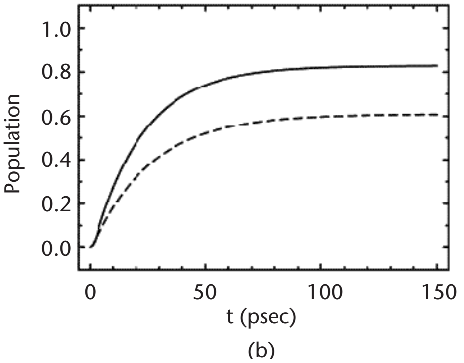

Figure 7.10 Temperature dependence of (a) E_1-level population $\rho_{22}(t)$ and (b) E_2-level population $\rho_{33}(t)$ when $d = 5$ nm and γ^{-1} are fixed. The solid and dashed curves represent the cases of the temperature $T = 50$K and 100K, respectively.

tonic switch, but it is quite important to investigate the control of signals in such a system.

Observation of a Dipole-Forbidden Energy Transfer for a Nanophotonic Switch

This section reviews our experimental studies on optical near-field interaction between QDs described earlier [12]. Recently, Mukai et al. reported ultrafast "optically forbidden" energy transfer from an outer ring of loosely packed bacteriochlorophyll molecules, called B800, to an inner ring of closely packed bacteriochlorophyll molecules, called B850, in the light-harvesting antenna complex of photosynthetic purple bacteria [36]. They theoretically showed that this transfer is possible when the point transition dipole approximation is violated due to the size effect of B800 and B850. From our viewpoint, this energy transfer is due to the optical near-field interaction between B800 and B850. Similarly, the energy can be transferred from one QD to another by the optical near-field interaction in the QDs system, even though it is a dipole-forbidden transfer.

Cubic CuCl QDs embedded in NaCl is a promising candidate for an optical near-field coupling system that exhibits this optically forbidden energy transfer. This is because, for this system, other possibility of energy transfer, such as carrier tunneling, Coulomb coupling, and so on, can be neglected. This is also because carrier wave function is localized in QDs due to a deep potential depth of more than 4 eV and the Coulomb interaction is weak due to small exciton Bohr radius of 0.68 nm. Conventional optical energy transfer is also negligible, since the energy levels of nearly perfect cubic CuCl QDs are optically forbidden, and are confined to the energy levels of exciton with an even principal quantum number [7]. However, Sakakura et al. observed the optically forbidden transition in a hole-burning experiment using CuCl QDs [4]. Although they attributed the transition to an imperfect cubic shape, the experimental and simulation results did not show such imperfection. We believe that the transition was due to the energy transfer between the CuCl QDs, via the optical near-field interaction similar to the optically forbidden energy transfer between B800 and B850 in the above-mentioned photosynthetic system. However, this type of energy transfer has not yet been directly observed. This section describes the direct observation of energy transfer from the exciton state in a CuCl QD to the optically forbidden exciton state in another CuCl QD by near-field optical spectroscopy.

We fabricated cubic CuCl QDs embedded in a NaCl matrix by the Bridgman method and successive annealing, and found the average size of the QDs to be 4.3 nm. The sample was cleaved just before the near-field optical spectroscopy experiment in order to keep the clean sample surface. The cleaved surface of the sample with 100-μm thickness was sufficiently flat for the experiment (i.e., its roughness was less than 50 nm at least within a few micrometer squares). A 325-nm He-Cd laser was used as a light source. A double-tapered UV fiber probe was fabricated by chemical etching and a 150-nm-thick gold film was coated. A 50-nm-diameter aperture was fabricated by the pounding method [37].

The curve in Figure 7.11(a) shows a far-field photoluminescence (PL) spectrum of the sample that was recorded with a probe-sample separation of 3 μm in the collection-mode operation [9] of the cryogenic near-field optical spectrometer at 15K. It represents the collective PL intensity from several CuCl QDs, and is inhomogeneously broadened owing to the size distribution of the QDs. The curve in Figure 7.11(b) represents the differential spectrum, which is the difference between the PL intensities measured with probe-sample separations of 3 μm and of less than 10 nm. This curve consists of many fine structures, which are attributed to the contribution of the QDs near the apex of the probe because of the drastic increase in the measured PL intensity for a probe-sample separation less than 10 nm. Since the average density of the QDs is 10^{17} cm^{-3}, average separation between the QDs is less than 30 nm. Therefore, the spectral peaks in Figure 7.11(b) originate from several QDs of different sizes. Among these, the peaks X and Y correspond to the confined Z_3-exciton energy levels of quantum number (1,1,1) for the QDs with side lengths (L) of 4.6 and 6.3 nm, respectively. Their effective side lengths a are 3.9 and 5.6 nm, whose size ratio is close to $1{:}\sqrt{2}$, and thus the (1,1,1) and (2,1,1) quantized exciton levels of these QDs are resonant with each other to be responsible for optical near-field energy transfer. It means that these QDs can be used as the input and output ports of the nano-photonic switch of Figure 7.1.

Figure 7.12(a, b) shows the spatial distributions of the PL intensity (i.e., near-field optical microscope images) for peaks X and Y of Figure 7.11(b), respectively. The spatial resolution, which depends on the aperture diameter of the fiber probe,

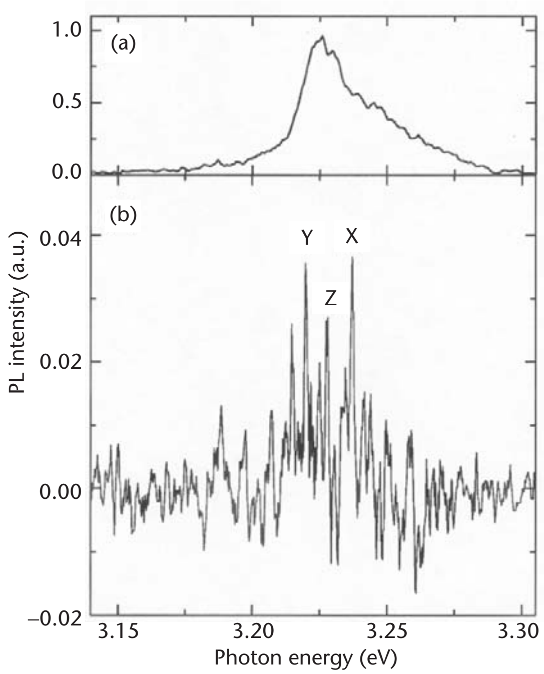

Figure 7.11 (a) Far-field PL spectrum of a sample recorded with probe-sample separation of 3 μm for the collection-mode operation at 15K. (b) The differential PL spectrum, which is the intensity difference between PL measured with the probe-sample separations of 3 μm and of less than 10 nm. The spectral peaks X, Y, and Z correspond to the wavelengths of lowest exciton state in cubic QDs with the side lengths of 4.6, 6.3, and 5.3 nm, respectively.

was smaller than 50 nm. These images clearly establish anticorrelation features in their intensity distributions, as manifested by the dark and bright regions surrounded by white broken curves. Figure 7.12(c) shows the spatial distribution of the PL intensity of peak Z in Figure 7.12(b), which corresponds to the QDs with side length of 5.3 nm. Their sizes do not satisfy the resonant condition given by (7.1), and thus, this figure does not show any anticorrelation features. In Figure 7.12(d), the anticorrelation features of the PL intensity of X and Y are demonstrated by

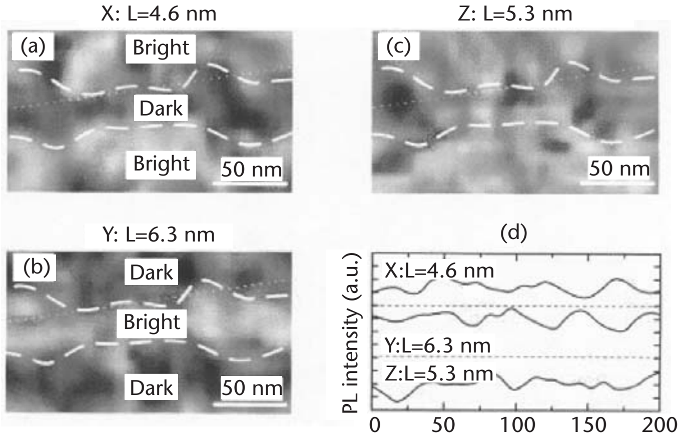

Figure 7.12 (a), (b), and (c) Spatial distributions of the near-field PL intensity for peaks X, Y, and Z in Figure 7.11(b), respectively. (d) Cross-sectional profiles along the dotted lines in (a), (b), and (c).

cross-sectional profiles taken along the dotted lines in Figure 7.12(a, b), respectively. This figure also shows the cross-sectional profile of Z [Figure 7.12(c)], which does not shows anticorrelation features with X and Y.

In order to confirm the anticorrelation feature more quantitatively, Figure 7.13 shows the values of the cross-correlation coefficient C between the spatial distribution of the intensity of the PL emitted from the (n_x, n_y, n_z) level of exciton in a QD with 6.3-nm side length and that from the (1,1,1) level in a QD with a different side length L. They have been normalized to that of the autocorrelation coefficient of the PL intensity from the (1,1,1) level in a 6.3-nm QD, which is identified by an arrow (1) in Figure 7.13. To calculate the values of C, spatial Fourier transform was performed on the series of PL intensity values in the chain of pixels inside the region surrounded by the broken white curves in Figure 7.12. The large negative value of C identified by an arrow (2) clearly shows the anticorrelation feature between Figure 7.12(a, b); that is, between the (2,1,1) level in a 6.3-nm QD and the (1,1,1) level in a 4.6-nm QD. This anticorrelation feature can be understood by noting that these spatial distributions in PL intensity represent not only the spatial distributions of the QDs but also some kind of resonant interaction between the QDs. This interaction induces energy transfer from 4.6-nm QDs to 6.3-nm QDs. Interpreting this, most of 4.6-nm QDs "accidentally" located close to 6.3-nm QDs cannot emit light, but instead transfer the energy to the 6.3-nm QDs. As a result, in the region containing embedded 6.3-nm QDs, the PL intensity in Figure 7.12(a) from 4.6-nm QDs is low, while the corresponding position in Figure 7.12(b) is high. As mentioned above, it is reasonable to attribute the origin of the interaction to the optical near-field energy transfer. For reference, we note the dark area outside the broken curves in Figure 7.12(b). This occurs because there are very few 6.3-nm QDs. From the absorption spectra of the sample, it is estimated that the

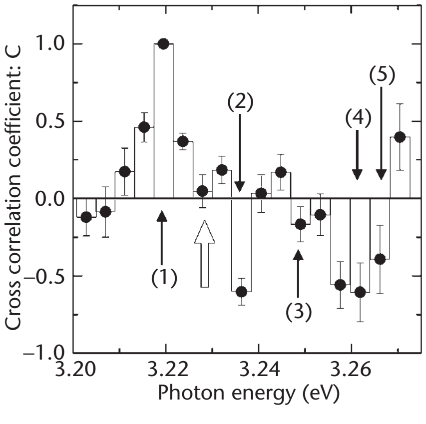

Figure 7.13 Values of the cross-correlation coefficient C between the spatial distributions of the PL intensity emitted from the (n_x, n_y, n_z) level of exciton in a cubic QD with 6.3-nm side length and that from the (1,1,1) level in a cubic QD with the different side length L. They have been normalized to that of the autocorrelation coefficient of the PL intensity from the (1,1,1) level in a 6.3-nm QD, which is identified by an arrow (1). Other four arrows (2)–(5) represent the cross-correlation coefficient C between higher levels in a 6.3-nm QD and other sized QDs. They are between (2) the (2,1,1) level in a 6.3-nm QD and the (1,1,1) level in a 3.9-nm QD; (3) the (2,2,1) level in a 6.3-nm QD and the (1,1,1) level in a 3.9-nm QD; (4) the (3,1,1) level in a 6.3-nm QD and the (1,1,1) level in a 3.6-nm QD; and (5) the (2,2,2) level in a 6.3-nm QD and the (1,1,1) level in a 3.5-nm QD. For reference, a white arrow represents the value of C between the (2,1,1) level in a 6.3-nm QD and the nonresonant (1,1,1) level in a 5.3-nm QD.

population of 6.3-nm QDs is one-tenth the population of 4.6-nm QDs. As a result, the corresponding area in Figure 7.12(a) is bright due to absence of the energy transfer. On the other hand, the spatial distributions of the PL intensities from other QDs do not show any anticorrelation features. This is confirmed by comparing Figure 7.12(a–c). The white arrow in Figure 7.13 indicates the relationship between Figure 7.12(b, c). The negligibly small value of *C* identified by this arrow proves the absence of the anticorrelation feature between the exciton energy levels in a 6.3-nm QD and the (1,1,1) level in a 5.3-nm QD due to their nonresonant condition.

Furthermore, arrows (3)–(5) also represent large negative values of C, which means the existence of the anticorrelation feature between higher levels in 6.3-nm QD and other sized QDs due to the resonant optical near-field energy transfer. They are (3) the (2,2,1) level in a 6.3-nm QD and the (1,1,1) level in a 3.9-nm QD; (4) the (3,1,1) level in a 6.3-nm QD and the (1,1,1) level in a 3.6-nm QD; and (5) the (2,2,2) level in a 6.3-nm QD and the (1,1,1) level in a 3.5-nm QD. The large anticorrelation coefficients C, identified by arrows (4) and (5) in Figure 7.13 can be attributed also to multiple energy transfer: Since the (1,1,1) levels in 3.6-nm and 3.5-nm QDs resonate or nearly resonate to the (2,1,1) level in a 4.6-nm QD, there is another route of energy transfer in addition to direct transfer from the 3.5- and 3.6-nm QDs to 6.3-nm QDs (i.e., the transfer via the 4.6-nm QDs).

The anticorrelation features appear for every pair of QDs if the resonant conditions of the confinement exciton energy levels are satisfied. Figure 7.14 shows 2D plots of cross correlation coefficient *C* between two QDs. White solid lines indicate the QDs pairs with resonant energy levels of (2,1,1)-(1,1,1), (2,2,1)-(1,1,1), (3,1,1)-(1,1,1), and (2,2,2)-(1,1,1), respectively. Large negative *C* appears along the solid lines due to optical near-field energy transfer between QDs.

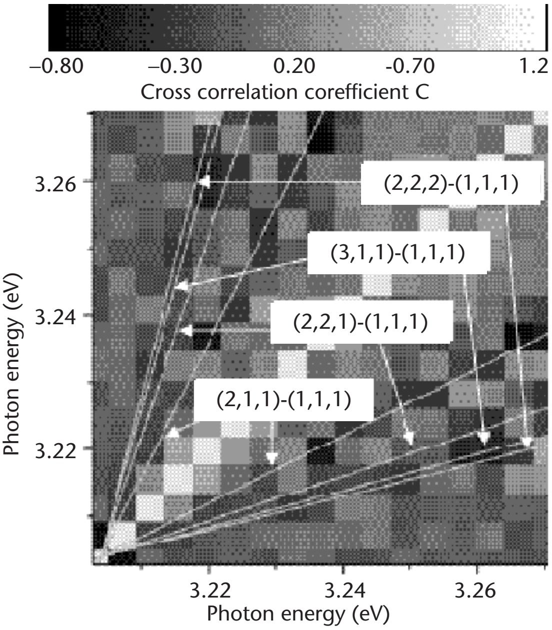

Figure 7.14 2D plots of cross correlation coefficient *C* between two cubic QDs. White solid lines show the QDs pairs with resonant energy levels of (2,1,1)-(1,1,1), (2,2,1)-(1,1,1), (3,1,1)-(1,1,1), and (2,2,2)-(1,1,1), respectively.

Fabrication and Characterization of Nanopatterns by Optical Near Field

Nonresonant Near-Field Optical Chemical Vapor Deposition of Zn

To realize the proposed nanophotonic switch and nanophotonic IC in Figure 7.1, an advanced nanofabrication technique is required that realizes high spatial resolution, high precision in controlling size and position, and is applicable to various materials. Self-organized growth has been employed for nanofabrication [38]; however, its spatial precision is not sufficiently high to meet this requirement. To improve the precision, an e-beam [39], STM [40], and surface modification [41] are used for site-control of the substrate. In-situ patterning of nanoscale structures using a scanning probe microscope such as STM [42] has also been investigated; however, it has a fatal disadvantage in that it limits the materials that can be deposited, because it cannot deal with insulators. By the conventional optical chemical vapor deposition (CVD), vapors of organometallic molecules are dissociated by the photochemical reaction with the far-filed light; however, it is difficult to deposit subwavelength-sized materials due to the diffraction limit of light.

Figure 7.15 shows the principle of near-field optical CVD (NFO-CVD), which has been proposed by the authors in order to solve these problems by utilizing high spatial resolution capability of the optical near field. Nanometric Zn, Al, and ZnO dots and loops have been successfully deposited by this method [37, 43–45]. As an example, Figure 7.16 shows the shear-force topographic images of the deposited Zn and Al dots whose sizes are less than 50 nm. It has been confirmed from these results that the precision of the deposited position was as high as about 1 nm [44]. As an outstanding advantage, we recently found that the photodissociation can take place even in nonresonant conditions, which is due to the inherent properties of the optical near field [46].

This subsection discusses nonresonant NFO-CVD of nanometric Zn dots (i.e., the possible mechanisms of diethylzinc (DEZn) dissociation by the nonresonant optical near field). Figure 7.17 shows potential curves of an electron in the DEZn molecular orbitals drawn as a function of the internuclear distance of a C-Zn bond, which are involved in photodissociation [47]. The relevant energy levels of the molecular vibration modes are also represented by horizontal lines on each potential curve. When a conventional far-field light is used, photoabsorption dissociates DEZn, as is indicated by a white arrow in this figure [48]. In contrast, there are four possible mechanisms of photodissociation when a nonresonant optical near field is used. They are: (1) *Two-photon absorption process, as indicated by the two arrows*

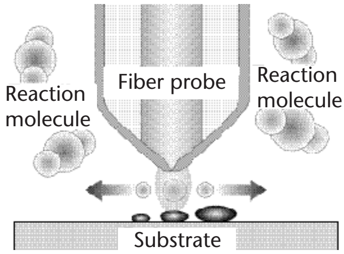

Figure 7.15 Principle of the near-field optical chemical vapor deposition(NFO-CVD). Vapors of the organometallic molecules are dissociated by the photochemical reaction with the optical near-field on the probe tip.

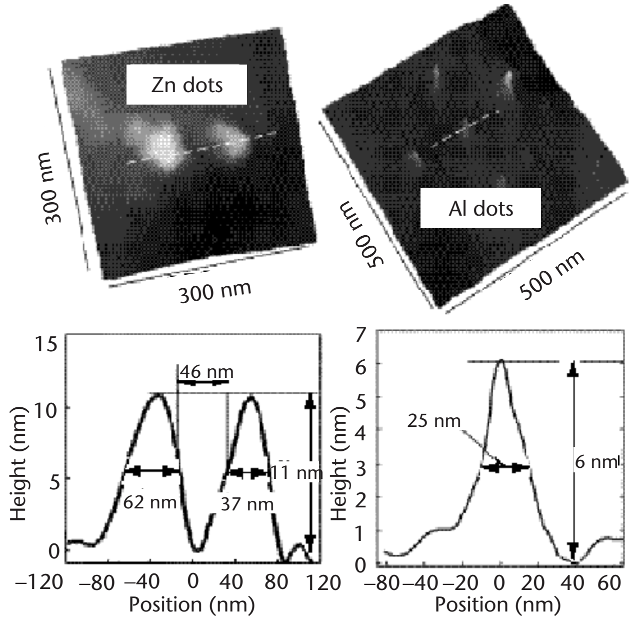

Figure 7.16 Top: Shear-force topographic images of Zn dots and Al dots deposited by NFO-CVD. Bottom: Cross-sectional profiles of the deposited Zn and Al patterns along the broken

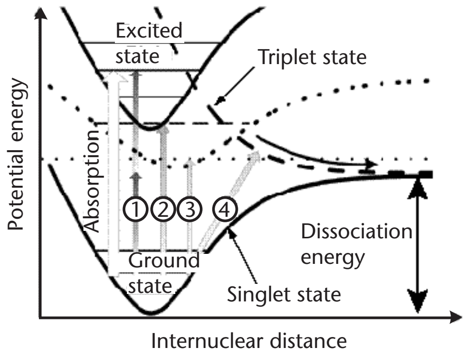

Figure 7.17 Potential curves of an electron in DEZn molecular orbitals. Solid and broken curves correspond to singlet and triplet states of DEZn molecule, respectively. The relevant energy levels of the molecular vibration modes are also represented by horizontal lines.

①. It is possible due to the high energy density of the optical near field at the apex of the high throughput fiber probe. (2) *The transition, shown by an arrow ②, to the intermediate energy level (a broken line on the dotted curve) induced by the fiber probe and successive relaxation to the dissociative triplet state.* This induced intermediate level is created for several reasons, such as the energy shift of the excitation level in the molecule due to the interaction between molecules and the fiber probe, activation of the optically forbidden energy levels to the allowed levels for the optical near field, and so on. Similar activation of the optically forbidden energy levels has been observed in dye molecules and coupled QDs [12, 36]. (3) *The transition to an excited state of a molecular vibration mode whose energy is higher than the dissociation energy (2.26 eV), as indicated by the dotted line and an arrow ③.* Although this transition is prohibited by the wavenumber conservation law for conventional far-field light, it is allowed in the present case because of the large uncertainty in the wavenumber of the subwavelength-sized optical near field. (4) *Direct transition from the singlet ground state to the dissociative triplet state is represented by arrow* ④. A spatially homogeneous far-field light cannot interact with the polarization of a DEZn molecule, as is easily understood by referring to the Frank-Condon principle. Thus, the far-field light interacts only with electrons. However, since the optical near field has a very large spatial gradient with a nanometric decay length, it can interact with the polarization of the molecule. As a result of this interaction, atoms in the molecule can be translated directly, as indicated by arrow ④.

Figure 7.18 shows the experimental setup used to confirm the NFO-CVD under nonresonant condition. An atomic smooth sapphire (0001) was used as a substrate for deposition [49]. Ultrahigh purity argon (Ar) was used as a buffer gas and DEZn as a reacting molecular gas source. The second harmonic ($\lambda = 244$ nm) of an Ar^+ laser was used as a light source that resonates the absorption band of DEZn [47]. The fundamental frequencies of Ar^+ ($\lambda = 488$ nm) and He-Ne ($\lambda = 633$ nm) lasers were used as nonresonant light sources. In order to investigate simultaneously the deposition effect of far-field light, a bare fiber probe (i.e., a fiber probe without the metal coating) was used for CVD. This fiber probe was fabricated by pulling and etching a pure silica core fiber. Therefore, the far-field light leaked through the circumference of the fiber probe, while the optical near field was generated at the apex. The laser output power from the fiber probe was measured with a photodiode placed behind the sapphire substrate. Topographic profiles of the deposited Zn dots were measured using a shear-force microscope. During deposition, the partial pressure of DEZn was 100 mTorr and the total pressure in the chamber was 3 Torr. Note that the deposition of Zn on the fiber probe and the resultant decrease in the efficiency of optical near-field generation were negligible because the deposition time was sufficiently short, as has been confirmed by the previous works [44, 50].

Figure 7.19 shows the shear-force topographic images before and after NFO-CVD on the sapphire substrate with atomic-level steps for $\lambda = 244$ (a), 488 (b), and 633 nm (c). For Figure 7.19(a) ($\lambda = 244$ nm), the laser power was 1.6 μW and the

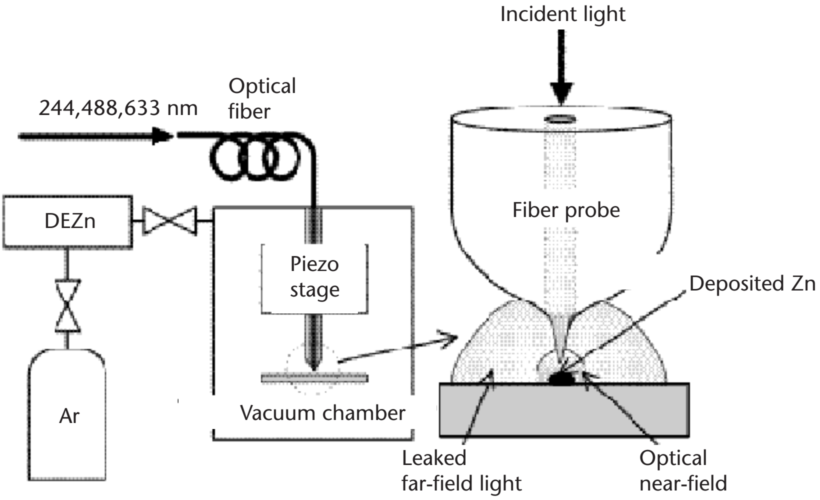

Figure 7.18 Experimental setup for NFO-CVD under nonresonant condition. An atomic smooth sapphire was used as a substrate for deposition.

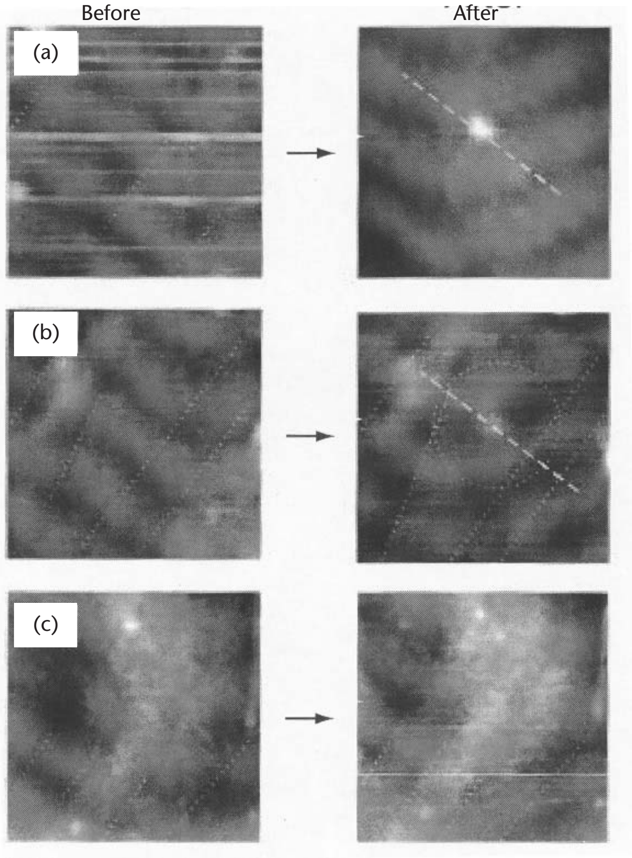

Figure 7.19 Shear-force topographic images before and after NFO-CVD at wavelengths of λ = 244 (a), 488 (b), and 633 (c) nm. The image sizes are 300 × 300 nm. The observed laser output power and the irradiation time for deposition were 1.6 μW and 60 seconds (a), 150 μW and 75 seconds (b), and 240 μW and 300 seconds (c).

irradiation time was 60 seconds. A white circle at the center of the right figure represents a Zn dot deposited by an optical near field. However, since the bare fiber probe also leaked strong far-field light, a Zn film was deposited around the dot, which covered the atomic-step structures on a substrate. For Figure 7.19(b), the laser power was 150 μW and the irradiation time was 75 seconds. The photon energy at this wavelength (λ = 488 nm) is higher than the dissociation energy of DEZn, but it is still lower than the absorption edge of DEZn [47]. Under this condition, it is amazing to find a Zn dot less than 50 nm in diameter at the center of the broken circle on the right figure. For Figure 7.19(c) (λ = 633 nm), the laser power was 240 μW and the irradiation time was 300 seconds. Despite the higher power and longer irradiation time, there was no Zn deposition, which means that the thermal effect of laser irradiation is negligible for Zn deposition.

In Figure 7.20, the broken curve represents the cross-sectional profile of the Zn pattern deposited at λ = 244 nm, taken along the broken line in Figure 7.19(a). The solid curve is a cross sectional profile of the Zn pattern deposited at 488 nm along the broken line in Figure 7.19(b). These curves confirm that Zn dots with a full width at a half maximum of 30 nm were deposited in the region where the optical near field is dominant. The broken curve has tails of 4-nm height on both sides of

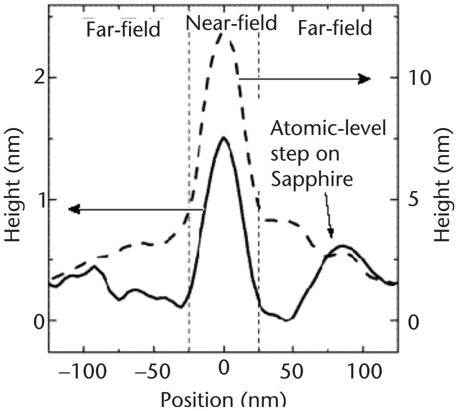

Figure 7.20 Cross-sectional profiles of the deposited Zn patterns. Broken and solid curves represent cross-sectional profiles along the broken lines on the right figure of Figure 7.19(a, b), respectively.

the peak, which correspond to the film deposited by the leaked far-field light. In contrast to this, the solid curve has no tails. Thus, it is clear that the leaked 488-nm far-field light did not deposit a Zn film. This result agrees with previous work using conventional optical CVD for Zn deposition with a far-field light with $\lambda = 300$ nm [51]. Therefore, it is confirmed that a Zn dot of Figure 7.19(b) was deposited under a nonresonant condition, despite the presence of leaked far-field light.

Although more studies are required to identify the mechanism of this nonresonant deposition among the four possible candidates given above, the experimental results and the suggested mechanisms described here show numerous potential advantages. As an example, this technique makes it possible to use various light sources and gas sources that have never been used in conventional far-field optical CVD. Thus, it can be claimed that the nonresonant NFO-CVD is a powerful nanofabrication technique.

Observation of Size-Dependent Features in the Photoluminescence of ZnO Nanocrystallites

As an application of NFO-CVD, nanometric ZnO has been produced by oxidizing the deposited Zn [45]. Since free-excitons in ZnO can emit an UV light, it is possible to use a nanometric ZnO dot as a light emitter in the nanophotonic IC of Figure 7.1. In order to confirm this possibility, this subsection evaluates its PL characteristics of ZnO nanocrystallites, especially its size-dependent features by using an optical near-field technique [52, 53]. ZnO has a wide band gap of 3.37 eV and a larger exciton binding energy (60 meV) than those of GaN (28 meV) or ZnSe (19 meV). Recently, several groups have reported room-temperature UV lasing [54, 55].

For quantitative evaluation of the size-dependent features, ZnO nanocrystallites were prepared by conventional optical CVD, not by NFO-CVD. This method is composed of two steps: (1) 200-nm-thick Zn nanocrystallites were grown on a sapphire (0001) substrate at room temperature by optical CVD. DEZn was used as a gas source. The partial pressures of DEZn and the Ar buffer gas were 10mTorr and 200 mTorr, respectively. The second harmonic (SH) light of an Ar^+ laser ($\lambda = 244$ nm) was used as the light source for the photodissociation of DEZn [56], whose power and spot size were 10 mW and 600 μm, respectively. (2) The deposited Zn nuclei were thermally oxidized in ambient oxygen at 1 atm and 750°C for 30 min [55]. This method is applicable to NFO-CVD [57] in order to deposit nanometric ZnO dots with high precision in the size and position because depositing Zn at room temperature in step (1) avoids thermal drift of the substrate and the probe.

Figure 7.21 shows a shear-force topographic image of oxidized Zn, obtained using a sharpened fiber probe with an apex diameter of 100 nm. Hexagonal (A_1, A_2, and A_3) and square (B_1, B_2, and B_3) nanocrystallites can be seen, which proves that oxidized Zn is composed of many nanocrystallites with various orientations. The grain sizes were in the range of 30 to 160 nm.

Figure 7.22 shows a far-field PL spectrum at room temperature, measured by using a He-Cd laser (λ = 325 nm) as a light source. The emission peak energy was close to the reported value of 3.26 eV (λ = 380 nm), which corresponds to spontaneous emission from the free exciton in high-quality ZnO nanocrystallites [54]. The full width at half maximum (FWHM) of the PL spectrum was about 118 meV, which is comparable with the 117 meV of molecular beam epitaxy grown ZnO nanocrystallites at room temperature [58]. These results imply that the oxidized Zn is composed of high-quality ZnO nanocrystallites. Furthermore, since ZnO has a

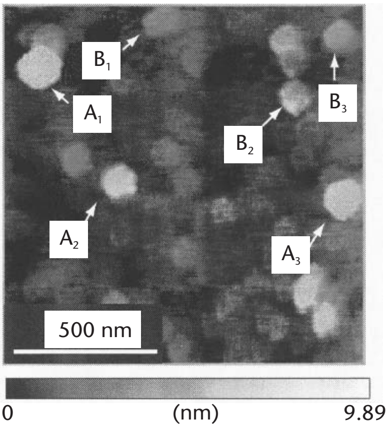

Figure 7.21 Shear-force topographic image of polycrystalline ZnO.

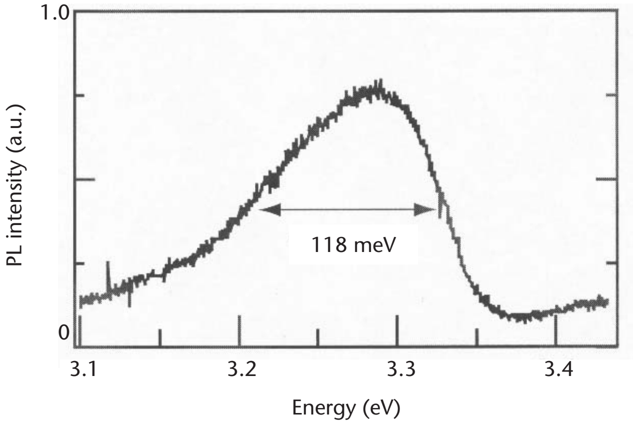

Figure 7.22 Far-field PL spectrum of polycrystalline ZnO at room temperature.

wurtzite structure, the hexagonal and square nanocrystallites shown in Figure 7.21 represent nanocrystallites oriented along the c-axis [54] and in other directions, respectively. These results imply that fabricated ZnO nanocrystallites are polycrystalline.

Using a collection-mode near-field optical spectrometer, we measured spatially and spectrally resolved PL spectra, for which a UV fiber probe with an 80-nm aperture diameter was used. Figures 7.23(a) and (b) show monochromatic PL images, in which the detection wavelengths were 370 ± 2.5 nm and 380 ± 2.5 nm, respectively. The closed and open circles in Figure 7.23(c) represent cross-sectional profiles along the broken lines through spots s_{1a} and s_{1b} in Figures 7.23(a) and (b), respectively. Those in Figure 7.23(d) are for spots s_{2a} and s_{2b} in Figure 7.23(a, b). Note that the FWHM of spots s_{1a} and s_{2a} was 155 and 55 nm, respectively, which is comparable to the grain sizes of ZnO nanocrystallites. This indicates that each emission spot originated from an individual ZnO nanocrystallite.

One technical problem was that the sensitivity of near-field optical spectrometer was not sufficiently high in order to evaluate precisely the spectral profile of individual ZnO nanocrystallites. To solve this problem, we defined the relative PL intensity RI_{PL} by (PL intensity at a detection wavelength of 370 ± 2.5 nm) / (PL intensity at a detection wavelength of 380 ± 2.5 nm). This parameter RI_{PL} can be used to evaluate the magnitude of the blue-shift of the PL spectral peak because it increases with decreasing the spectral peak wavelength. Figure 7.24 shows the measured relation between the value of RI_{PL} and the PL spot size of ZnO nanocrystallites, where the spot sizes were estimated from the FWHM of Figure 7.23. An outstanding feature of this figure is that the RI_{PL} is larger for a smaller spot size. It means that the smaller ZnO nanocrystallites have shorter wavelength at its PL spectral peak, which is

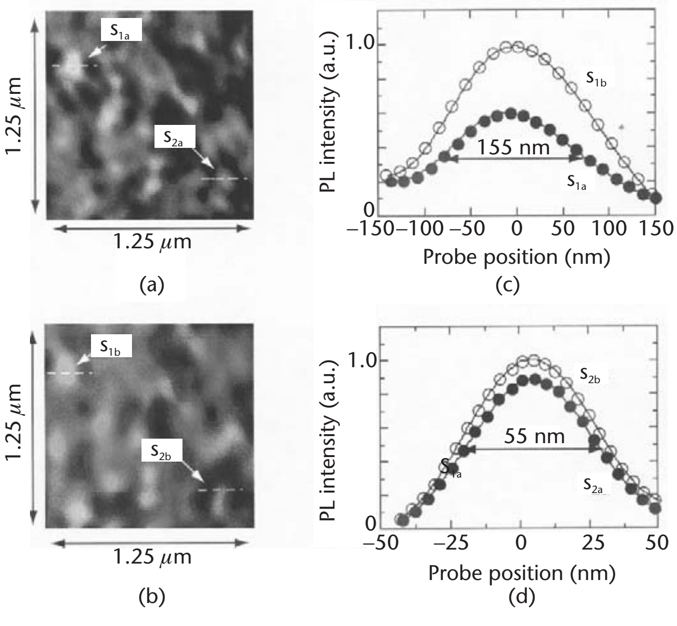

Figure 7.23 Monochromatic PL images of polycrystalline ZnO obtained at wavelengths of (a) 370 and (b) 380 nm. (c) Closed and open circles represent cross-sectional profiles along the broken lines through spots s_{1a} and s_{1b}, respectively. (d) Closed and open circles represent cross-sectional profiles along the broken lines through spots s_{2a} and s_{2b}, respectively.

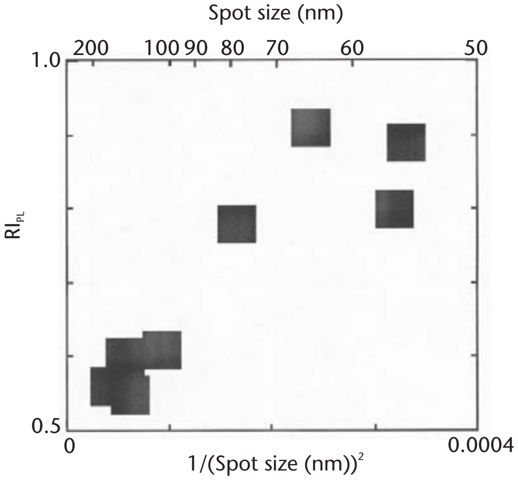

Figure 7.24 Relative PL intensity RI_{PL} [= (PL intensity at 370 ± 2.5 nm)/(PL intensity at 380 ± 2.5 nm)] of ZnO nanocrystallites as a function of spot size.

attributed to the quantum size effect in ZnO nanocrystallites. Although this size-dependent feature of the PL intensity has ever been evaluated for an ensemble of nanocrystallites using a conventional diffraction-limited optical method [55], the present results are the first to evaluate individual nanocrystallites using a spatially resolved optical near-field method.

Since Zn dots less than 50 nm in size have been fabricated by the NFO-CVD [57], fabrication and integration of nanophotonic devices are expected by assembling high-quality ZnO nanocrystallites by optical near-field method.

Plasmon Waveguide for Optical Far/Near-Field Conversion

Principle of a Plasmon Waveguide

A nanometric optical waveguide is required for far/near-field conversion in order to connect the nanophotonic IC with external conventional diffraction-limited photonic devices, as is schematically explained by Figure 7.25(a). Performances required for this waveguide include: (a) high conversion efficiency, (b) a sub-100-nm width of a guided beam for efficient coupling of the converted optical near field to nanometric dots, and (c) a superwavelength propagation length to avoid direct coupling of the propagating far-field light to the nanometric dots.

A cylindrical metal core waveguide is a promising candidate to realize a sub-100-nm beam width, through which the TM plasmon mode propagates [59]. However, the TM plasmon mode is not easily excited by far-field light due to mode mismatching. To overcome this difficulty, we employed a metal-coated silicon wedge structure [Figure 7.25(b)] [60]. The main part consists of a silicon wedge, which is coated with a thin metal film. An incoming far-field light, which is polarized parallel to the y-axis, is first transformed into the two-dimensional (2-D) surface plasmon mode on the surface F1 [Figure 7.25(c)]. Next, the 2-D surface plasmon mode is converted into the 1-D TM plasmon mode at the edge between F1 and the plateau. This conversion occurs because of the scattering coupling at the edge [61]. Finally,

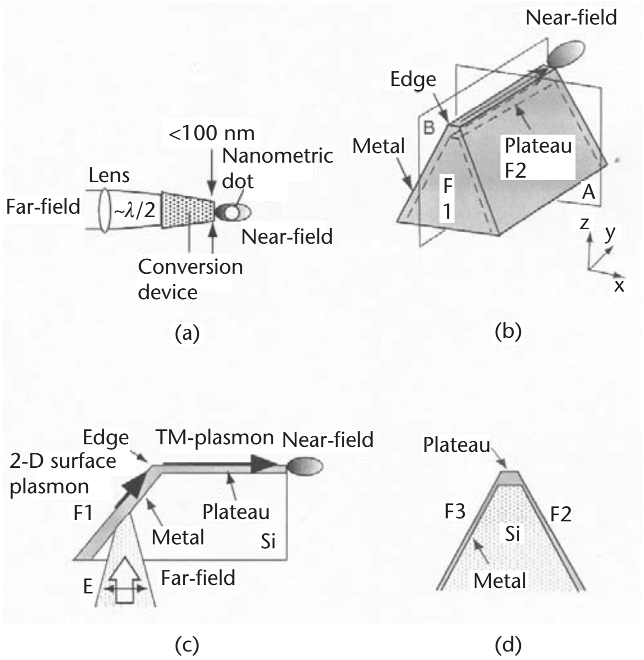

Figure 7.25 Optical far/near-field conversion device. (a) Schematic explanation of operation. (b) Bird's-eye view of a plasmon waveguide. The *x*- and *y*-axes are perpendicular and parallel to the plateau axis, respectively. (c) Cross-section along the plane B (yz-plane) in (b). (d) Cross-section along the plane A (xz-plane) in (b).

the TM plasmon mode propagates along the plateau in a manner similar to an edge mode in a tetrahedral tip [62]. Since the metal film deposited on the plateau is sufficiently thicker than on the other surfaces (F1, F2, and F3) due to the normal evaporation process, the plateau acts as a metal core waveguide (Figure 7.25(d)). Finally, the TM plasmon mode at the outlet of the waveguide is converted to the optical near field.

Advantages of this plasmon waveguide are: (a) High conversion efficiency from the 2-D surface plasmon mode to the 1-D TM plasmon mode due to the scattering coupling, which meets the requirement (A) [61, 63]. (b) The beamwidth decreases to as narrow as 1 nm with decreasing the core diameter, since this waveguide does not have a cutoff [59]. It meets the requirement (B). (c) The propagation length of the TM-plasmon mode is sufficiently long. As an example, the propagation length is 2.5 μm (at $\lambda = 830$ nm) for the TM plasmon with a gold core (diameter $D = 40$ nm) insulated by air [59]. It meets the requirement (C).

The plasmon waveguide was fabricated in four steps: (1) A (100)-oriented silicon wafer was bonded to the glass substrate by anodic bonding [Figure 7.26(a)] [64]. (2) In order to avoid any deformation of the convex corners [65], the patterned rectangular mask was tilted 30° with respect to the <110> crystal orientation of silicon [Figure 7.26(b)]. (3) The silicon wedge was fabricated by anisotropic etching (40 g KOH + 60 g H_2O + 40 g isopropyl alcohol, 80°C). By maintaining the silicon wedge height lower than 10 μm, its propagation loss can be kept sufficiently low [Figure 7.26(c)]. (4) After removing the SiO_2 layer, the silicon wedge was coated with a 50-nm-thick gold layer [Figure 7.26(d)]. SEM images of the fabricated waveguide are shown by Figure 7.26(e, f).

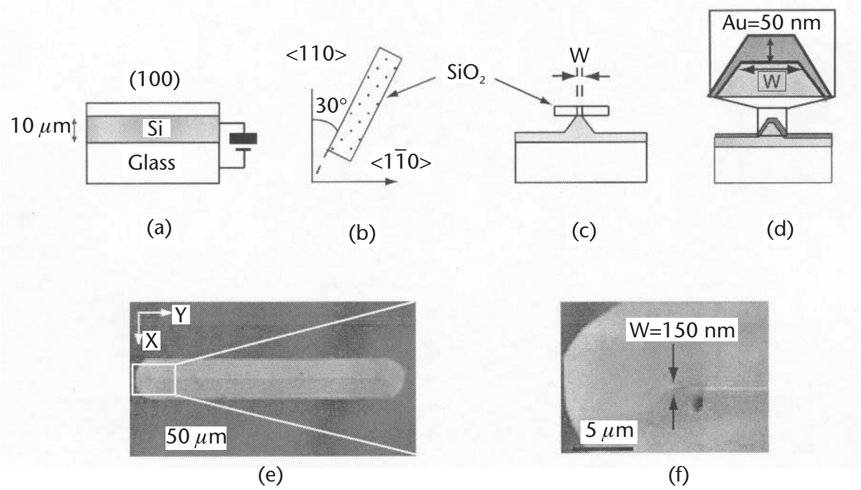

Figure 7.26 Fabrication processes for a plasmon waveguide. (a) Anodic bonding; (b) mask alignment; (c) anisotropic etching for fabrication of the silicon wedge, *W:* plateau width; (d) metal coating, (e) and (f) SEM images of the metal-coated silicon wedge, $W = 150$ nm.

Excitation and Observation of 1-D Plasmon Mode

The spatial distribution of the electric-field energy on the plateau of a metallized silicon wedge was measured by scanning a fiber probe with an aperture diameter D_a of 60 nm. In order to excite the plasmon mode, linearly polarized light ($\lambda = 830$ nm) was focused onto the surface F1. Figure 7.27(a, b) shows a bird's-eye views of the observed electric-field energy distributions on the wedges with plateau width $W = 1$

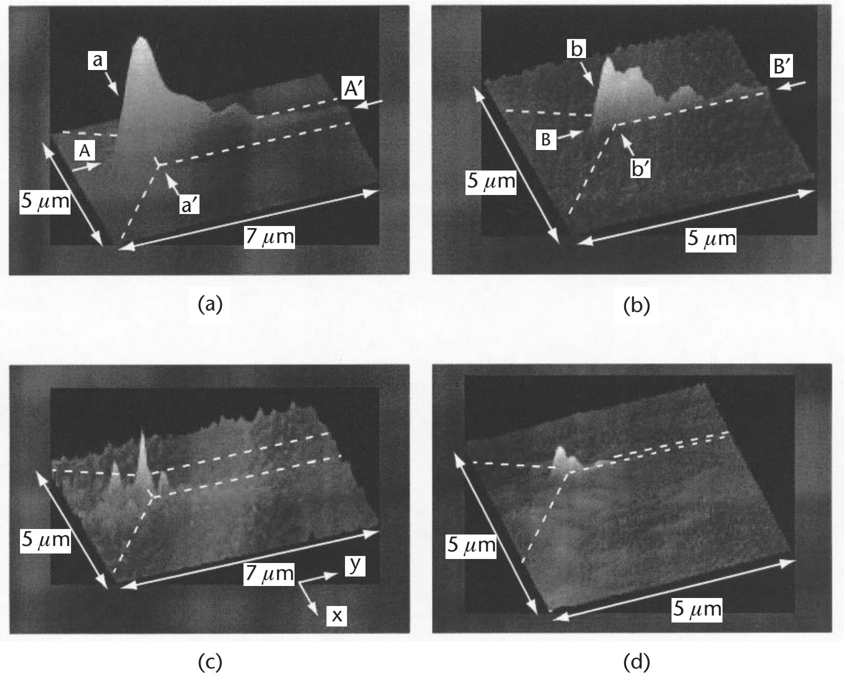

Figure 7.27 Bird's eye views of the electric-field energy distribution $\lambda = 830$ nm on the silicon wedge plateau. (a) TM polarization: $W = 1$ μm. (b) TM polarization: W = 150 nm. (c) TE polarization: $W = 1$ μm. (d) TE polarization: $W = 150$ nm.

μm and 150 nm for TM polarization (the incident light polarization is parallel to the y-axis), respectively. Figure 7.27(c, d) is for TE polarization (parallel to the x-axis). Comparing Figure 7.27(a, c) [or Figure 7.27(b, d)], it is confirmed that the propagating mode was excited efficiently only by TM polarized incident light. Closed and open circles in Figure 7.28(a, b) show the cross-sectional profiles along the lines in Figures 7.27(a) ($A - A'$ and $a - a'$) and 7.27(b) ($B - B'$ and $b - b'$), respectively. In these figures, transmission was defined as the ratio of the light power detected by the fiber probe to the input light power. From the dotted exponential curve in Figure 7.28(a) fitted to the open circles, the propagation length is estimated as 2.5 μm for the 150-nm wedge. This value is comparable to the theoretical value for TM plasmon mode in a cylindrical metal core waveguide with $D = 40$ nm, which is consisted of a gold core and air cladding ($\lambda = 830$ nm) [59]. From the solid exponential curve in Figure 7.28(a) fitted to the closed circles, the propagation length for $W = 1.0$ μm is estimated as 4.0 μm, which is longer than that for $W = 150$ nm. This is because, as W increases, the effective refractive index approaches that of surface plasmon at the planar boundary between gold and air [59]. These experimental results confirm that the observed excitation along the plateau was the TM plasmon mode.

Figure 7.28(b) shows that FWHM of the cross-sectional profiles was 150 nm for $W = 150$ nm, which can be decreased by minor improvements of the waveguide design in order to meet the requirement (B). Further, note that the transmission was 5.0×10^{-3} for $W = 150$ nm, which is 10 times higher than that of a fiber probe with

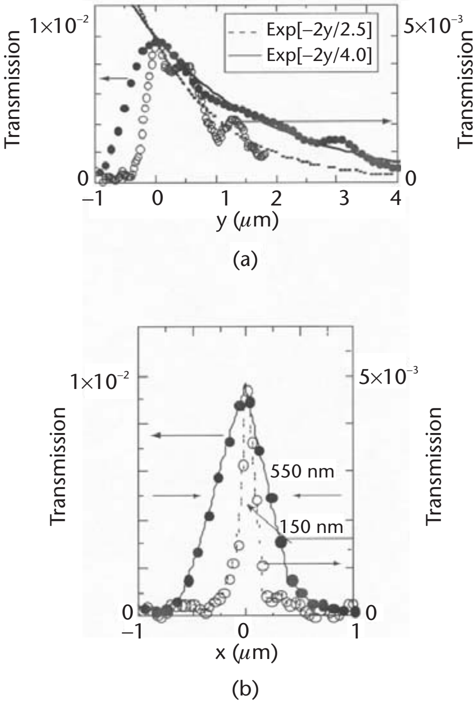

Figure 7.28 (a) Cross-sectional profiles along *A-A′* (closed circles) and *B-B′* (open circles) in Figure 7.27(a, b), respectively. Solid and dotted exponential curves were fitted to the experimental values of closed and open circles, respectively. (b) Cross-sectional profiles along *a-a′* (closed circles) and *b-b′* (open circles) in Figure 7.27(a, b), respectively.

$D_a = 150$ nm [66]. This efficient excitation of the TM plasmon mode is attributed to the scattering coupling at the edge between F1 and the plateau in Figure 7.25(b) [61, 63], and thus, it meets the requirement (A). Finally, the propagation length estimated above is longer than the incident light wavelength, which meets the requirement (C).

In the case when this waveguide is used in the UV region to excite nanometric ZnO, CuCl, and so on, higher coupling efficiency could be expected by introducing a grating coupler in order to convert the propagating far-field light to the 2-D plasmon mode.

A Key Device for Generation/Detection of Optical Near Field

Metallized Pyramidal Silicon Probe

A key device for nanophotonics is the one generating or detecting optical near field. Such a device (a fiber probe) has been fabricated by selective chemical etching, which was developed by the authors of [67]. Recently, several groups have reported cantilevered probes based on micromachining [68–71]. High throughput and small spot size are expected due to high refractive indices of their cores; however, they have not yet been realized for applications to nanophotonics. This section reviews the successful fabrication of a probe with extremely high throughput, introducing a pyramidal silicon structure and localized surface plasmon resonance at the metallized probe tip.

In order to realize a nanometric spot size at the probe tip, a metallic probe is a promising candidate, through which the surface plasmon mode propagates. Since a metallic core waveguide does not have a cutoff, the spot size of the propagating mode decreases with decreasing the core diameter [59]. However, the plasmon mode is not easily excited by the propagating mode inside the dielectric core due to mode mismatching. In order to overcome this difficulty, we employed a pyramidal silicon probe that is entirely coated with a thin metal film, as is schematically explained by Figure 7.29. Due to the high refractive indices of the core and the thin metal film, light propagates inside the silicon core and is converted into the surface plasmon mode at the metallic tip.

To find the optimum tip parameters, numerical calculations were carried out for the geometry shown in Figure 7.30(a, b) by using the finite-difference time-domain (FDTD) method [72]. Figure 7.30(a) is for the probe-to-probe method used to measure the spatial distribution of the optical near-field energy on the pyramidal silicon probe [66]. The model consisted of $180 \times 180 \times 150$ cells with the cell size of $10 \times 10 \times 10$ nm. As shown in Figure 7.30(b), the pyramidal silicon probe (refractive index $n = 3.67$ at $\lambda = 830$ nm) was coated with aluminum film ($n = 2.74 – i\ 8.3$) [73], and the four sidewalls resulted from (111) silicon crystal planes. A scanning probe with a glass core ($n = 1.53$) was used to detect the optical near-field energy on the probe tip. The scanning probe with a cone angle of 30° was coated with a 1-μm-thick gold ($n = 0.19 – i\ 5.4$) layer, and had an aperture with a diameter D_a of 50 nm. Separation between the probes was fixed to 10 nm. The pyramidal silicon probe was illuminated with a linearly polarized light ($\lambda = 830$ nm).

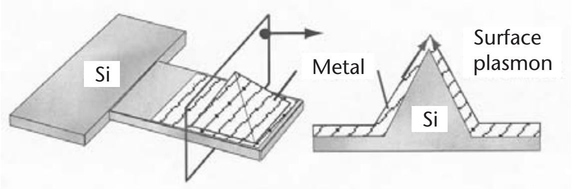

Figure 7.29 Structure of a metallized pyramidal silicon probe.

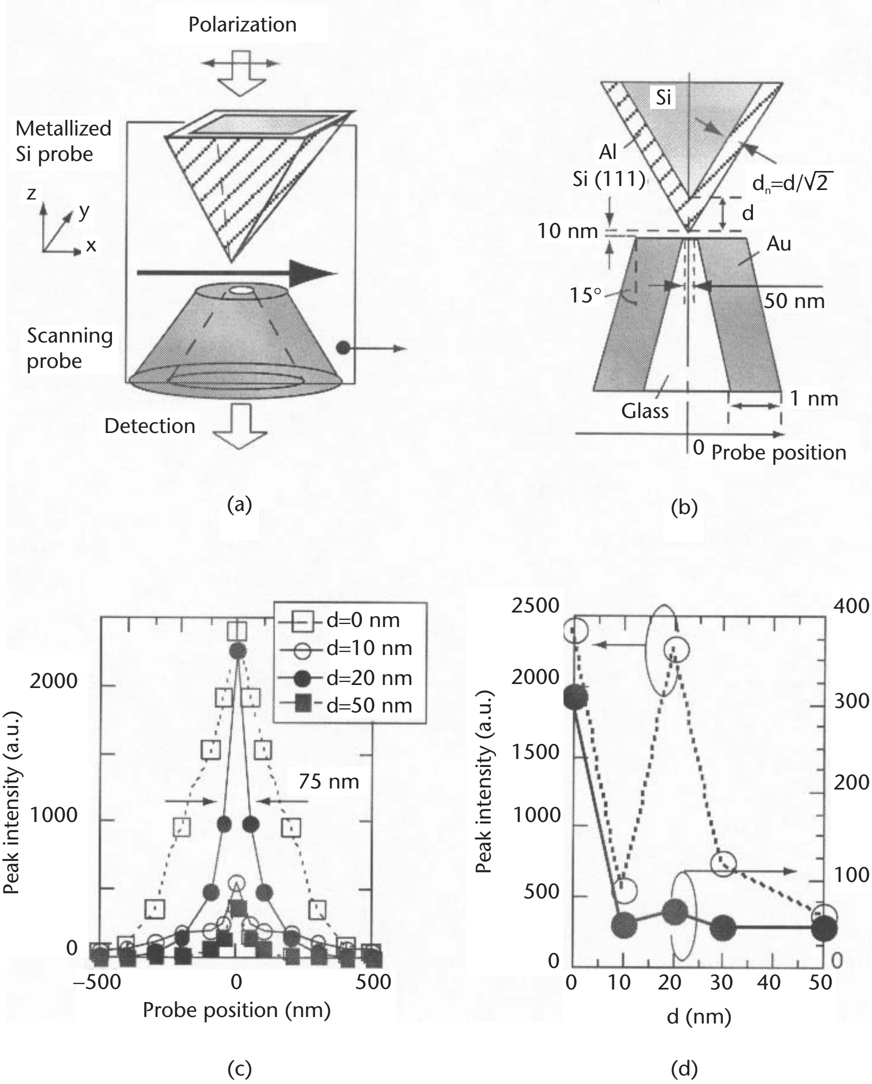

Figure 7.30 (a) FDTD geometry of the probe-to-probe method. (b) Cross-section along the xz-plane in (a). d = aluminum thickness. (c) Thickness dependence of the calculated distributions. (d) Thickness dependence of peak intensity and FWHM of the profiles in (c).

Figure 7.30(c) shows the thickness dependence of the calculated cross-sectional profiles of the detected optical near-field energy, which represents that the peak energy for the metallized silicon probe (metal thickness $d = 20$ nm) is as high as that of the bare silicon tip ($d = 0$ nm) and the FWHM is 75 nm. The thickness dependence of the peak energy and FWHM is illustrated in Figure 7.30(d), which indicates that the metallized silicon structure produced a spot size as small as 50 nm ($< \lambda/10$). Since efficient excitation of the surface plasmon is obtained with a 15-nm-thick aluminum coating ($\approx d/\sqrt{2}$) on silicon in the Kretschmann configuration [74], these size-dependent features are attributed to localized surface plasmon resonance [75]. As a result of these numerical calculations, the optimum Al thickness was found to be 20 nm.

Fabrication of a Metallized Pyramidal Silicon Probe and Observation of Localized Plasmon Resonance

Based on the optimization in the above section, a pyramidal silicon probe was fabricated in three steps: (1) A (100)-oriented silicon wafer was bonded to a glass substrate by anodic bonding [Figure 7.31(a)] [64]. (2) The probe was fabricated by anisotropic etching [Figure 7.31(b)]. By maintaining the silicon probe height at less than 10 μm, the propagation loss is kept sufficiently low. (3) After removing the SiO_2 layer, the probe was coated with an Al layer ($d = 20$ nm). Figure 7.31(c, d) shows SEM images of our sharpened (mesa length $L_m < 10$ nm) pyramidal silicon probe with an Al layer.

Spatial distribution of the optical near-field energy on the pyramidal silicon probe was measured using the probe-to-probe method (i.e., it was scanned with an apertured probe with $D_a = 50$ nm with a cone angle of 30°). The separation between the probes was kept within 10 nm using the shear-force feedback technique. For comparison, we also measured the optical near-field energy of a triple-tapered fiber

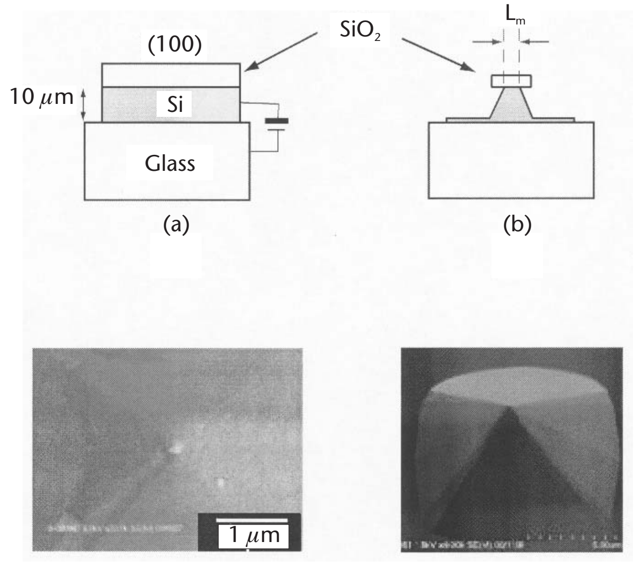

(a) (b)

(c) (d)

Figure 7.31 Fabrication processes for a pyramidal silicon probe. (a) Anodic bonding. (b) Anisotropic etching for fabrication of the silicon wedge. L_m: mesa length. (c) SEM image of the fabricated pyramidal silicon probe. (d) Magnified image of (c).

probe with $D_a = 60$ nm. The throughput of this triple-tapered fiber probe has been calibrated to be 1.5×10^{-3} [66], which is the highest among existing fiber probes due to the interference characteristics of the guided modes [66].

Figure 7.32(a–c) shows the observed spatial distributions of the optical near-field energy for the metallized pyramidal silicon probe ($d = 20$ nm), the bare pyramidal silicon probe ($d = 0$ nm), and the triple-tapered fiber probe with $D_a = 60$ nm, respectively. Curves A, B, and C in Figure 7.32(d) are cross-sectional profiles along the dashed white lines in Figures 7.32(a–c), respectively. Note that the FWHM of the metallized pyramidal silicon probe is 85 nm ($\sim\lambda/10$)(curve B), which is in good agreement with the value in Figure 7.30(c). Further, the peak energy of the metallized pyramidal silicon probe is 5 and 15 times larger than those of the bare pyramidal silicon and the triple-tapered probes, respectively. Such effective excitation of the optical near field by the metallized silicon probe is attributed to localized surface plasmon resonance. These results indicate that the metallized pyramidal silicon structure resulted in high throughput (2.3%) and small spot size (85 nm) simultaneously.

Considering the aperture diameter ($D_a = 50$ nm) of the fiber probe used for detection, the spot size of the metallized pyramidal silicon probe ($d = 20$ nm) should have the capability of higher resolution (e.g., 50 nm or higher should be possible). Higher throughput is expected by combining the pyramidal silicon probe tip and the microfabricated solid immersion lens [76]. Further, by using the transparent material with high refractive index in the UV region, such as Si_3N_4, GaP, GaN, and so on, the plasmon resonance effect described here can be applicable also to the blue-violet region.

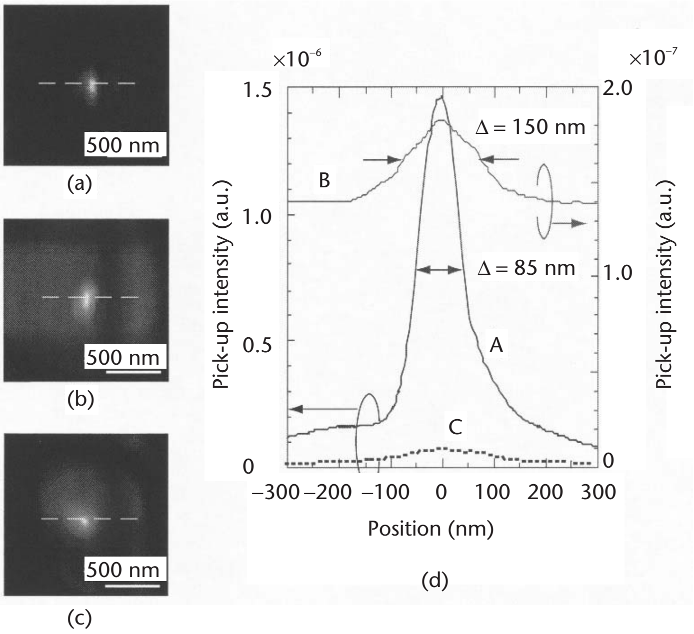

Figure 7.32 Observed spatial distributions of the optical near-field energy of (a) the metallized pyramidal silicon probe ($d = 20$ nm), (b) bare pyramidal silicon probe ($d = 0$ nm), and (c) triple-tapered probe with $D_a = 60$ nm. (d) Curves A, B, and C are the cross-sectional profiles along the dashed white lines in (a), (b), and (c), respectively.

Application to High-Density and High-Speed Optical Memory

Optical Near-Field Slider

Nanophotonics can be applied to a next-generation optical storage system with 1Tbit/in^2 recording density and 1-Gbps data transmission rate. A superresolution near-field structure [77] and a planar probe mounted on an optical slider [78] were proposed recently for this application. Though these methods do not require shear-force feedback, the optical near-field energies on the subwavelength apertures are too low because the incident light is focused by a conventional lens. We review here an advanced system using a contact slider as a more promising candidate to realize high recording density on a phase-change recording medium and fast data transmission rate. Our metallized pyramidal silicon probe technology of the previous section is applied to this system.

Structures of the system and the slider are illustrated in Figure 7.33 [79]. A metallized pyramidal silicon probe array is arranged on a surface of the slider. The probes in the array are designed by utilizing the results of the previous section. Advantages of such a slider are (1) the probe array with sub-10-μm heights has high durability because it is bonded to a thick glass substrate, (2) since the height of the probe tips and the pads are determined by the uniformity of the thickness of silicon wafer, ultrahigh homogeneity in the heights of the probes and pads can be obtained, (3) use of a probe array with many probe tips increases the total data transmission rate by parallel readout [80–82]. For this readout, the incident light is spatially

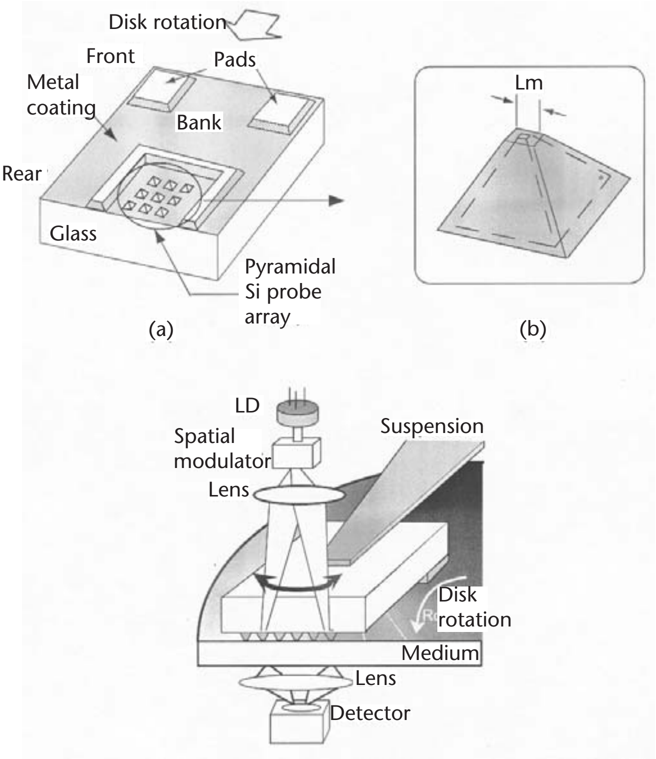

Figure 7.33 (a) Contact slider with a pyramidal silicon probe array. (b) Pyramidal silicon probe, L_m: mesa length. (c) Data storage system with the slider.

modulated by an electro-optics method, and the scattered light from each probe is detected as a time-sequential signal.

Fabrication of Optical Near-Field Slider and Recording-Readout Experiments

Since the key issue in realizing a pyramidal silicon probe array is high homogeneity in the heights of the probes, the probe array is fabricated from a (100)-oriented silicon-on-insulator (SOI) wafer in four steps: (1) A 10-μm SOI wafer is bonded to the glass substrate by anodic bonding [Figure 7.34(a)] [64]. (2) After removal of the silicon substrate from the SOI wafer by wet etching, the probe array, the bank, and the pads are fabricated by anisotropic etching (40g KOH + 60g H_2O + 40g isopropyl alcohol, 80°C) [Figure 7.34(b)]. Note that the height homogeneity is maintained by the remaining the SiO_2 layer [see Figure 7.34(c)]. (3) The slider is quarried with a dicing saw. (4) After removal of the SiO_2 layer, the slider is coated with 30-nm-thick aluminum.

Figure 7.34(d, e) shows an optical image of the contact slider and a SEM image of the pyramidal silicon probe array fabricated on the slider, respectively. The height dispersions of the probes and pads are decreased to less than 10 nm due to the uniformity of thickness of the SOI wafer. The slider is designed by use of the design criteria [83] for a contact-type hard-disk head so that its jumping height over the phase-change recording medium is maintained to be less than 10 nm. Furthermore, since the phase-change recording medium is fragile, we designed the bank so that the contact stress becomes 100 times lower than the yield stress of the magnetic disk at a constant linear velocity (v_{CL}) of 0.3 m/s, corresponding to a data transmission rate of 10 Mbps for a data density of 1 Tbit/in^2. To increase the data transmission rate 100 times (i.e., to realize a 1-Gbps data transmission rate for recording density of 1 Tbit/in^2), we fabricated 100 probe elements on the inner part of the bank for parallel readout.

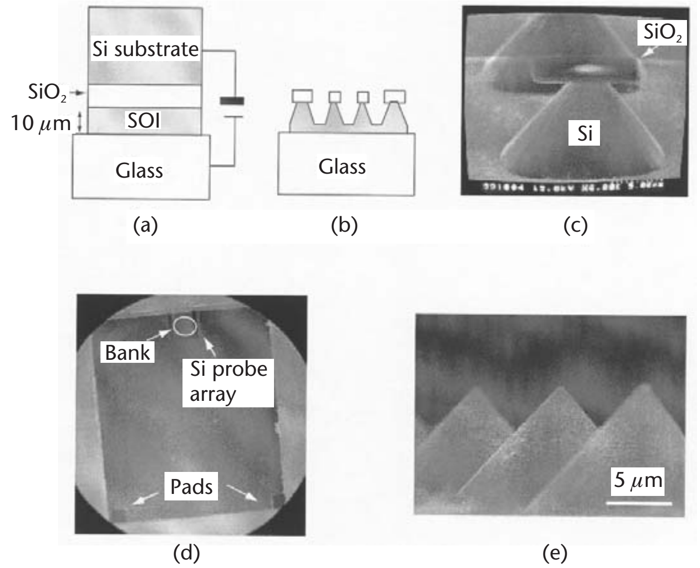

Figure 7.34 Fabrication processes of a contact slider with a pyramidal silicon probe array. (a) Anodic bonding. (b) Anisotropic etching for fabrication the probe array, the bank, and the pads. (c) SEM image as the result of step (2). (d) Optical image as the result of step (4). (e) Magnified SEM image of the fabricated pyramidal silicon probe array.

In recording and readout experiments (see Figure 7.35), an as-deposited AgInSbTe film was used as a phase-change recording medium. We compared the signal transmitted through phase-changed marks recorded with a single element of the probe array and that with a focused propagating light ($\lambda = 830$ nm). The slider was in contact with a phase-change recording medium coated with a thin lubricant film. The frequency of the rectangularly modulated signal with 50% duty was changed from 0.16 to 2.0 MHz at $\nu_{CL} = 0.43$ m/s. The recording optical powers for a pyramidal silicon probe with a mesa length L_m of 150 nm (see the SEM image in Figure 7.35) and a focused propagating light with an object lens (N.A., 0.4) were 200 and 15 mW, respectively. Readout was carried out at $\nu_{CL} = 0.43$ m/s. The reading optical powers for the pyramidal silicon probe and the focused propagating light were 20 and 3.6 mW, respectively. The resolution bandwidth was 30 kHz.

Measured dependences of the carrier-to-noise ratio (CNR) on the mark length are shown in Figure 7.36. In comparison with the closed circles, open circles indicate that shorter crystalline phase-changed marks beyond the diffraction limit were recorded and read out by an optical near field on the pyramidal silicon probe. The shortest mark length was 110 nm at $\nu_{CL} = 0.43$ m/s, corresponding to a data transmission rate of 2.0 Mbps. This is the first phase-change recording-readout with a contact slider. The constant CNR of the pyramidal silicon probe shown by the open circles in this figure is due to the small spot size of the optical near field for recording-readout and the narrow recorded mark width, which are as small as L_m of the pyramidal silicon probe. These results indicate that further increases in CNR and decreases in mark length are possible by means of tracking during readout.

The data transmission rate of 2.0 Mbps can be increased to 200 Mbps by parallel readout with all elements of the probe array. Further, it is expected that the recording density can be increased to as high as 1 Tbit/in^2 by further improvements in the plasmon resonance effect at the pyramidal silicon probe tip.

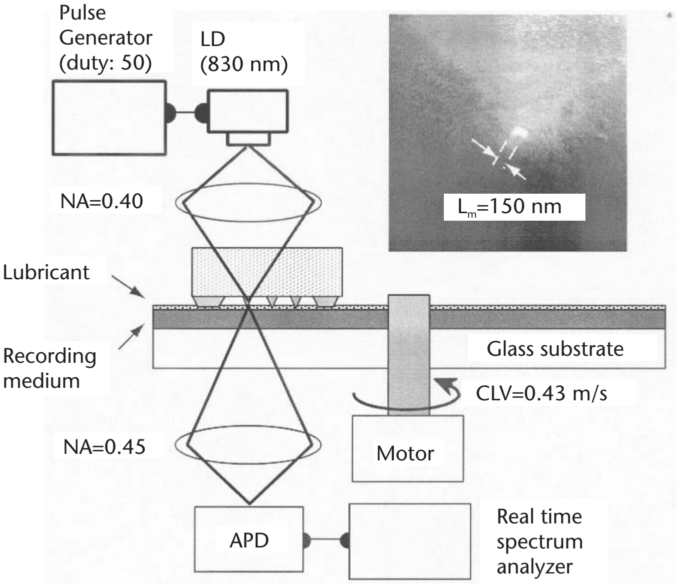

Figure 7.35 Experimental setup for phase-change recording-reading by the contact slider. Inset: SEM image of the pyramidal silicon probe tip used for optical near-field recording-reading.

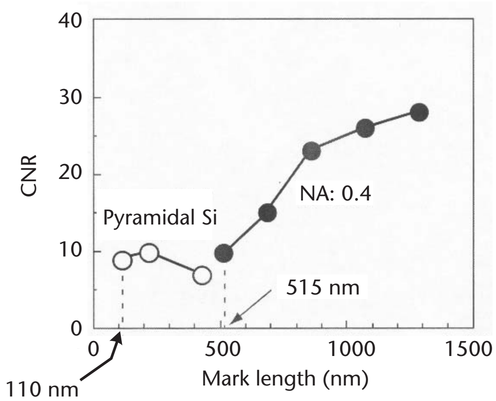

Figure 7.36 Dependence of the CNR on mark length by an optical near field with the pyramidal silicon probe (open circles), and by a propagating light focused with an object lens (closed circles).

Summary

This chapter reviewed nanophotonics, a novel optical nanotechnology utilizing local electromagnetic interactions between a small number of nanometric elements and an optical near field. Its potential for high integration beyond the diffraction limit of light can solve the technical problems of the future optical industry. A prototype nanophotonic integrated circuit was presented. All the devices in this circuit involve nanometric dots and wires, and an optical near field is used as a carrier to transmit the signal. As a key device, we proposed a nanophotonic switch based on optical near-field energy transfer between QDs.

Using a density matrix formulation, we theoretically showed that the optical near-field interaction is expressed as the sum of the Yukawa function, and estimated that the oscillation period of the nutation for cubic CuCl QDs is less than 100 psec at a 10-nm inter-QD distance, which is sufficiently short for the switching operation. In order to guarantee one-directional (i.e., irreversible) energy transfer between two resonant levels of QDs, we examined intrasublevel transitions due to phonon coupling, by considering a simple two-QD plus phonon heat-bath system, and formulated the population dynamics of the system. As a result, we found that the state-filling time strongly depended on both the strength of the optical near-field interaction and the relaxation rate due to phonon coupling. To numerically evaluate CuCl QDs, the state-filling time was estimated as 22 ps, which is sufficiently short for the switching operation. Our analysis also showed that the state-filling time was almost independent of the temperature within the Born-Markov approximation. However, the finite temperature results in a residual population in the upper energy levels, which might degrade the aspect ratio of the ON/OFF signals of the switch. The optical near-field energy transfer to be used for the nanophotonic switch was experimentally studied using cubic CuCl QDs in a NaCl matrix as a test sample. Using near-field optical spectroscopy with a spatial resolution smaller than 50 nm in the near-UV region at 15K, we observed the optical near-field energy transfer occurring from the lowest state of excitons in 4.6-nm QDs to the first dipole-forbidden excited state of excitons in 6.3-nm QDs.

To fabricate nanophotonic devices and ICs, we developed a new technique of chemical vapor deposition that uses an optical near field. Reviewing the experimental results of depositing nanometric Zn and Al patterns, we confirmed that this technique was sufficiently precise in controlling the size and position of the deposited material. Furthermore, we demonstrated a novel deposition scheme under nonresonant conditions and discussed its origin. In order to confirm the possibility of using a nanometric ZnO dot as a light emitter in a nanophotonic IC, we performed spatially and spectrally resolved PL imaging of individual ZnO nanocrystallites with a spatial resolution as high as 55 nm using a UV fiber probe. We observed the quantum size effect in ZnO nanocrystallites (i.e., the intensities of higher energy components of the PL spectrum increased as the spot size decreased).

To connect the nanophotonic IC with external photonic devices, we developed a nanometer-scale waveguide using a metal-coated silicon wedge structure. Propagation of the TM plasmon mode was observed using a near-field optical microscope. Illumination ($\lambda = 830$ nm) of the metal-coated silicon wedge ($W = 150$ nm) caused a TM plasmon mode with beam width of 150 nm and propagation length of 2.5 μm.

To improve the performance of a key device for nanophotonics, we realized an optical near-field probe with an extremely high throughput by introducing a pyramidal silicon structure and localized surface plasmon resonance at the metallized probe tip. Throughput as high as 2.5% was achieved for a spot size of 85 nm.

To apply nanophotonics to a high-density, high-speed optical memory system, we proposed and fabricated a novel contact slider with a pyramidal silicon probe array, with high homogeneity in the heights of the probes. We carried out phase-change recording/reading using this slider. Illuminating one element of the silicon probe array with a laser beam ($\lambda = 830$ nm), we demonstrated mark lengths as short as 110 nm.

Acknowledgments

The author gratefully acknowledges fruitful discussion with Professors H. Hori, N. Onishi, and I. Banno (Yamanashi University), Professor K. Kitahara (International Christian University), Dr. H. Nejo (National Institute for Materials Science), Professor H. Ito and Dr. M. Kourogi (Tokyo Institute of Technology), and Professor Y. Masumoto and his coworkers (Tsukuba University). He is also grateful to Dr. S. Mitsugi and Professor K. Goto (Tokai University) for their help with the numerical calculations. Further, he would like to thank Drs. K. Kobayashi, T. Kawazoe, S. Sangu, T. Yatsui, T.W. Kim, and A. Shojiguchi (ERATO, Japan Science and Technology Corporation) for their collaboration.

References

[1] Ohtsu, M., "Overview," in *Near-Field Optics: Principles and Applications,* X. Zhu and M. Ohtsu, (eds.), Singapore: World Scientific, 2000, pp. 1–8.

[2] Ohtsu, M., "Near-Field Nano-Optics toward Nano/Atom Deposition," *Technical Digest of the 18th Congress of the International Commission for Optics, SPIE,* Vol. 3749, 1999, pp. 478–479.

[3] Ohtsu, M., "Nanotechnology and Nano/Atom Photonics by Optical Near Field," *Proc. SPIE,* Vol. 4416, 2001, pp. 1–13.

[4] Sakakura, N., and Y. Masumoto, “Persistent Spectral-Hole-Burning Spectroscopy of Cucl Quantum Cubes,” *Phys. Rev. B,* Vol. 56, August 1997, pp. 4051–4055.

[5] Ekimov, A. I., A. L. Eflos, and A. A. Onushchenko, “Quantum Size Effect in Semiconductor Microcrystals,” *Solid State Commun.,* Vol. 56, 1985, pp. 921–924.

[6] Itoh, T., et al., “Interface Effect on the Properties of Confined Excitons in CuCl Microcrystals,” *J. Lumin.,* Vol. 60&61, 1994, pp. 396–399.

[7] Tang, Z. K., et al., “Optical Selection Rule and Oscillator Strength of Confined Exciton System in CuCl Thin Films,” *Phys. Rev. Lett.,* Vol. 71, August 1993, pp. 1431–1434.

[8] Kobayashi, K., et al., “Near-Field Potential for a Neutral Atom,” *Phys. Rev. A,* Vol. 63, January 2001, pp. 013806-1–9.

[9] Ohtsu, M., (ed.), *Near-Field Nano/Atom Optics and Technology,* New York: Springer-Verlag, 1998, Ch. 9.

[10] Kataoka, T., T. Tokizaki, and A. Nakamura, “Mesoscopic Enhancement of Optical Nonlinearity in CuCl Quantum Dots: Giant-Oscillator Strength Effect on Confined Excitons,” *Phys. Rev. B,* Vol. 48, July 1993, pp. 2815–2818.

[11] Suzuki, T., et al., “Observation of Ultrafast All-Optical Modulation Based on Intersubband Transition in N-Doped Quantum Wells by Using Free Electron Laser,” *Appl. Phys. Lett.,* Vol. 69, December 1996, pp. 4136–4138.

[12] Kawazoe, T., et al., “Direct Observation of Optically Forbidden Energy Transfer between CuCl Quantum Cubes Via Near-Field Optical Spectroscopy,” *Phys. Rev. Lett.,* Vol. 88, No. 6, 2002, pp. 067404–1-4.

[13] Kobayashi, K., and M. Ohtsu, “Quantum Theoretical Approach to a Near-Field Optical System,’’ *J. Microsc.,* Vol. 194, May/June 1999, pp. 249–254.

[14] Kobayashi, K., and M. Ohtsu, “Quantum Theory and Virtual Photon Model of Near Field Optics,” *Proc. SPIE,* Vol. 3791, 1999, pp. 10–20.

[15] Kobayashi, K., et al., “Effective Probe—Sample Interaction: Toward Atom Deflection and Manipulation,” in *Near-Field Optics: Principles and Applications,* X. Zhu and M. Ohtsu, (eds.), Singapore: World Scientific, 2000, pp. 82–88.

[16] Sangu, S., K. Kobayashi, and M. Ohtsu, “Optical Near Fields as Photon—Matter Interacting Systems,” *J. Microsc.,* Vol. 202, May 2001, pp. 278–285.

[17] Hopfield, J. J., “Theory of the contribution of Excitons to the Complex Dielectric Constant of Crystals,” *Phys. Rev.,* Vol. 112, December 1958, pp. 1555–1567.

[18] Orrit, M., C. Aslangul, and P. Kottis, “Quantum-Mechanical-Model Calculations of Radiative Properties of a Molecular Crystal, I. Polaritons and Abnormal Decays of Excitons in One- and Two-Dimensional Systems,” *Phys. Rev. B,* Vol. 25, June 1982, pp. 7263–7280.

[19] Knoester, J., and S. Mukamel, “Intermolecular Forces, Spontaneous Emission, and Superradiance in a Dielectric Medium: Polariton-Mediated Interactions,” *Phys. Rev. A,* Vol. 40, December 1989, pp. 7065–7080.

[20] Huttner, B., and S. M. Barnett, “Quantization of the Electromagnetic Field in Dielectrics,” *Phys. Rev. A,* Vol. 46, October 1992, pp. 4306–4322.

[21] Juzeliunas, G., and D. L. Andrews, “Quantum Electrodynamics of Resonant Energy Transfer in Condensed Matter,” *Phys. Rev. B,* Vol. 49, April 1994, pp. 8751–8763.

[22] Cohen-Tannoudji, C., J. Dupont-Roc, and G. Grynberg, *Photons and Atoms,* New York: John Wiley & Sons, 1989.

[23] Craig, D. P., and T. Thirunamachandran, *Molecular Quantum Electrodynamics,* London, England: Academic Press, 1984.

[24] Harken, H., *Light, Vol. 1,* Amsterdam, Netherlands: North-Holland, 1986.

[25] Mandel, L., and E. Wolf, *Optical Coherence and Quantum Optics,* Cambridge, England: Cambridge University Press, 1995.

[26] Carmichael, H. J., *Statistical Methods in Quantum Optics 1,* Berlin, Germany: Springer-Verlag, 1999.

[27] May, V., and O. Kühn, *Charge and Energy Transfer Dynamics in Molecular Systems,* Berlin, Germany: Wiley-VCH, 2000.

[28] Hyuga, H., and H. Ohtsubo, "Breakdown of the Siegert Theorem and the Many-Body Charge Density Operators," *Nucl. Phys. A,* Vol. 294, 1978, pp. 348–356.

[29] Zwanzig, R., "On the Identity of Three Generalized Master Equations," *Physica,* Vol. 30, 1964, pp. 1109–1123.

[30] Mori, H., "Transport, Collective Motion, and Brownian Motion," *Prog. Theor. Phys.,* Vol. 33, 1965, pp. 423–455.

[31] Willis, C. R., and R. H. Picard, "Time-Dependent Projection-Operator Approach to Master Equations for Coupled Systems," *Phys. Rev. A,* Vol. 9, March 1974, pp. 1343–1358.

[32] Fulde, P., *Electron Correlations in Molecules and Solids,* 3rd ed., Berlin, Germany: Springer-Verlag, 1995.

[33] Hanamura, E., "Very Large Optical Nonlinearity of Semiconductor Microcrystallites," *Phys. Rev. B,* Vol. 37, January 1988, pp. 1273–1279.

[34] Masumoto, Y., et al., "Homogeneous Width of Confined Excitons in Quantum Dots at Very Low Temperatures," *Phys. Stat. Sol. (b),* Vol. 224, No.3, 2001, pp. 613–619.

[35] Lindenberg, K., and B. West, "Statistical Properties of Quantum Systems: The Linear Oscillator," *Phys. Rev. A,* Vol. 30, July 1984, pp. 568–582.

[36] Mukai, K., S. Abe, and H. Sumi, "Theory of Rapid Excitation-Energy Transfer from B800 to Optically-Forbidden Exciton State of B850 in the Antenna System LH2 of Photosynthetic Purple Bacteria," *J. Phys. Chem. B,* Vol. 103, March 1999, pp. 6096–6102.

[37] Polonski, V. V., et al., "Nanometric Patterning of Zinc by Optical Near-Field Photochemical Vapor Deposition," *J. Microsc.,* Vol. 194, May/June 1999, pp. 545–551.

[38] Leonard, D., et al., "Direct Formation of Quantum-Sized Dots from Uniform Coherent Islands of InGaAs on GaAs Surfaces," *Appl. Phys. Lett.,* Vol. 63, December 1993, pp. 3203–3205.

[39] Tsutsui, T., et al., "Site Controlled Metal and Semiconductor Quantum Dots on Epitaxial Fluoride Films," *Microelectronics Engineering,* Vol. 47, June 1999, pp. 135–137.

[40] Kohmoto, S., et al., "Site-Controlled Self-Organization of Individual InAs Quantum Dots by Scanning Tunneling Probe-Assisted Nanolithography," *Appl. Phys. Lett.,* Vol. 75, November 1999, pp. 3488–3490.

[41] Kuramochi, E., et al., "Perfect Spatial Ordering of Self-Organized InGaAs/AlGaAs Box-Like Structure Array on GaAs (311)B Substrate with Silicon Nitride Dot Array," *Appl. Phys. Lett.* Vol. 71, September 1997, pp. 1655–1657.

[42] Wiesendanger, R., "Fabrication of Nanometer Structures Using STM," *Appl. Surf. Sci.,* Vol. 54, January 1992, pp. 271–277.

[43] Polonski, V. V., et al., "Vacuum Shear-Force Microscopy Application to High Resolution Work," *Jpn. J. Appl. Phys,* Part 2, Vol. 38, July 1999, pp. L826–L829.

[44] Yamamoto, Y., et al., "Fabrication of Nanometric Zinc Pattern with Photodissociated Gas-Phase Diethylzinc by Optical Near-Field," *Appl. Phys. Lett.,* Vol. 76, April 2000, pp. 2173–2175.

[45] Lee, G. H., et al., "Fabrication of ZnO Nanostructure Using Near-Field Optical Technique," *Proc. SPIE,* Vol. 3791, 1999, pp. 132–139.

[46] Kawazoe, T., Y. Yamamoto, and M. Ohtsu, "Fabrication of a Nanometric Zn Dot by Nonresonant Near-Field Optical Chemical Vapor Deposition," *Appl. Phys. Lett.,* Vol. 79, August 2001, pp. 1184–1186.

[47] Jacson, R. L., "Vibrational Energy of the Monoalkyl Zinc Product Formed in the Photodissociation of Dimethyl Zinc, Diethyl Zinc, and Dipropyl Zinc," *J. Chem. Phys.,* Vol. 96, April 1992, pp. 5938–5951.

[48] Okabe, H., *Photochemistry,* New York: John Wiley & Sons, 1978.

[49] Yoshimoto, M., et al., “Atomic-Scale Formation of Ultrasmooth Surfaces on Sapphire Substrates for High-Quality Thin Film Fabrication,” *Appl. Phys. Lett.,* Vol. 67, November 1995, pp. 2615–2617.

[50] Ohtsu, M., et al., “Nanofabrication and Atom Manipulation by Optical Near-Field and Relevant Quantum Optical Theory,” *Proc. IEEE,* Vol. 88, September 2000, pp. 1499–1518.

[51] M. Shimizu, et al., ”Low Temperature Growth of ZnO Film by Photo-MOCVD,” *J. Crystal Growth,* Vol. 89, 1988, pp. 365–370.

[52] Yatsui, T., et al., “Near-Field Ultraviolet Photoluminescence Spectroscopy for Evaluating the Crystallinity of Polycrystalline Zinc Oxide,” *Appl. Phys. Lett.,* Vol. 79, No. 15, 2001, pp. 2369–2371.

[53] Yatsui, T., et al., “Observation of Size-Dependent Features in the Photoluminescence of Zinc Oxide Nanocrystallites by Near-Field Ultraviolet Spectroscopy,” *Appl. Phys. Lett.,* Vol. 80, No. 8, 2002, pp. 1444–1446.

[54] Tang, Z. K., et al., “Room-Temperature Ultraviolet Laser Emission from Self-Assembled ZnO Microcrystallite Thin Films,” *Appl. Phys. Lett.,* Vol. 72, No. 25, 1998, pp. 3270–3272.

[55] Cho, S., et al., “Photoluminescence and Ultraviolet Lasing of Polycrystalline ZnO Thin Films Prepared by the Oxidation of the Metallic Zn,” *Appl. Phys. Lett.,* Vol. 75, No. 18, 1999, pp. 2761–2763.

[56] Krchnavek, R. R., et al., “Photodeposition Rates of Metal from Metal Alkyls,” *J. Vac. Sci. Technol. B,* Vol. 5, 1987, pp. 20–26.

[57] Yamamoto, Y., et al., “In-Situ Lateral Fabrication of Zinc and Aluminum Nanodots by Near Field Optical Chemical Vapor Depostion,” *Tech. Digest Pacific Rim Conference on Lasers and Electro-Optics,* Vol. 4, 2001, pp. I520–I521.

[58] Chen, Y., et al., “Plasma Assisted Molecular Beam Epitaxy of ZnO on C-Plane Sapphire: Growth and Characterization,” *J. Appl. Phys.,* Vol. 87, 1998, pp. 3912–3918.

[59] Takahara, J., et al., “Guiding of a One-Dimensional Optical Beam with Nanometer Diameter,” *Opt. Lett.,* Vol. 22, No. 7, 1997, pp. 475–477.

[60] Yatsui, T., M. Kourogi, and M. Ohtsu, “Plasmon Waveguide for Optical Far/Near-Field Conversion,” *Appl. Phys. Lett.,* Vol. 79, No. 27, 2001, pp. 4583–4585.

[61] Marcuse, D., *Light Transmission Optics,* New York: Van Nostrand, 1972, Ch. IV.

[62] Fischer, U. C., J. Koglin, and H. Fuchs, “The Tetrahedral Tip as a Probe gor Scanning Near-Field Optical Microscopy At 30 nm Resolution,” *J. Microsc.,* Vol. 176, 1994, pp. 231–237.

[63] Yatsui, T., M. Kourogi, and M. Ohtsu, “Highly Efficient Excitation of Optical Near-Field on an Apertured Fiber Probe with an Asymmetric Structure,” *Appl. Phys. Lett.,* Vol. 71, No. 13, 1997, pp. 1756–1758.

[64] Anthony, T. R., “Dielectric Isolation of Silicon by Anodic Bonding,” *J. Appl. Phys.,* Vol. 58, 1998, pp. 1240–1247.

[65] Puers, B., and W. Sansen, “Compensation Structures for Convex Corner Micromachining in Silicon,” *Sens. and Actuators,* Vol. A21–A23, 1990, pp. 1036–1041.

[66] Yatsui, T., M. Kourogi, and M. Ohtsu, “Increasing Throughput of a Near-Field Optical Fiber Probe over 1000 Times by the Use of a Triple-Tapered Structure,” *Appl. Phys. Lett.,* Vol. 73, No. 15, 1998, pp. 2090–2092.

[67] Ohtsu, M., (ed.), *Near-Field Nano/Atom Optics and Technology,* New York: Springer-Verlag, 1998, Ch. 3.

[68] Noell, W., et al., “Micromachined Aperture Probe Tip for Multifunctional Scanning Probe Microscopy,” *Appl. Phys. Lett.,* Vol. 70, No. 10, 1997, pp. 1236–1238.

[69] Heisig, S., et al., “Monolithic gallium Arsenide Cantilever for Scanning Near-Field Microscopy,” *Ultramicroscopy,* Vol. 71, No. 1, 1998, pp. 99–105.

[70] Danzebrink, H.-U., et al., "Transmission Scanning Near-Field Optical Microscopy with Uncoated Silicon Tips," *Ultramicroscopy,* Vol. 71, No. 1, 1998, pp. 371–377.

[71] Eckert, R., et al., "Near-Field Fluorescence Imaging with 32 nm Resolution Based on Microfabricated Cantilevered Probes," *Appl. Phys. Lett.,* Vol. 77, No. 23, 2000, pp. 3695–3697.

[72] Mitsugi, S., Y. J. Kim, and K. Goto, "Finite-Difference-Time-Domain Analysis for Electro-Magnetic Field Distribution on Near-Field Optical Recording Probe Head," *Opt. Rev.,* Vol. 8, 2001, pp. 120–125.

[73] Palik, E. D., (ed.), *Handbook of Optical Constants of Solids,* New York: Academic, 1985.

[74] Raether, H., (ed.), *Surface Plasmons,* New York: Springer, 1988.

[75] Boyd, G. T., et al., "Local-Field Enhancement on Rough Surfaces of Metals, Semimetals, and Semiconductors with the Use of Optical Second-Harmonic Generation," *Phys. Rev. B,* Vol. 30, July 1984, pp. 519–526.

[76] Fletcher, D. A., et al., "Near-Field Infrared Imaging with a Microfabricated Solid Immersion Lens," *Appl. Phys. Lett.,* Vol. 77, No. 14, 2000, pp. 2109–2111.

[77] Tominaga, J., T. Nakano, and N. Atoda, "An Approach for Recording and Readout Beyond the Diffraction Limit with an Sb Thin Film," *Appl. Phys. Lett.,* Vol. 73, No. 15, 1998, pp. 2078–2080.

[78] Yoshikawa, H., et al., "7.5-MHz Data-Transfer Rate with a Planar Aperture Mounted upon a Near-Field Optical Slider," *Opt. Lett.,* Vol. 25, No. 1, 2000, pp. 67–69.

[79] Yatsui, T., et al., "High Density/Speed Optical Near Field Recording/Reading with a Pyramidal Silicon Probe on a Contact Slider," *Opt. Lett.,* Vol. 25, No. 17, 2000, pp. 1279–1281.

[80] Kim, Y. J., et al., "Fabrication of Micro-Pyramidal Probe Array with Aperture for Near-Field Optical Memory Applications," *Jpn. J. Appl. Phys.,* Vol. 39, No. 3B, 2000, pp. 1538–1541.

[81] Yatsui, T., et al., "Subwavelength-Sized Phase-Change Recording with a Silicon Planar Apertured Probe," *Proc. SPIE,* Vol. 3791, 1999, pp. 76–84.

[82] Pohl, D. W., "Some Thoughts About Scanning Probe Microscopy, Micromechanics, and Storage," *IBM J. Res. Dev.,* Vol. 39, 1995, pp. 701–711.

[83] Bhatia, C. S., and A. K. Menon, (eds.), *Tribology of Contact/Near-Contact Recording for Ultra High Density Magnetic Storage, TRIB-Vol. 6,* New York: American Society of Mechanical Engineers, 1996.

CHAPTER 8

Optical Coherence Tomography and the Related Techniques for Biomedical Applications

Masamitsu Haruna
Department of Allied Health Sciences
Graduate School of Medicine
Osaka University
Osaka, Japan

This chapter describes optical coherence tomography and related techniques for biomedical applications. Optical coherence tomography (OCT) was demonstrated for the first time by Dr. Fujimoto's group at MIT in 1991 [1]. Only 5 years later, a practical OCT imaging system became commercially available for ophthalmology applications [2]. This technique marks a new epoch in both optics and optoelectronics.

Japanese researchers also contributed greatly to the development of OCT before its first demonstration by Dr. Fujimoto. In 1987, Dr. K. Takada of Nippon Telephone Telegraph (NTT) reported fault detection in an optical waveguide using a low coherence interferometer [3]. Then in 1990, Professor Tanno of Yamagata University obtained a Japanese patent for cross-sectional imaging using optical waves [4]. Very recently, OCT research activity has increased greatly in Japan and more than 10 research groups, including some private companies, are undertaking experiments to develop future OCT technologies.

I will briefly describe the imaging principle of OCT, its basic properties, and its application to clinical diagnosis. The existing OCT technique has certain problems that must be solved, and I will discuss consequential technical improvements. I will also describe the application of OCT to biophysics and brain science [5, 6].

Figure 8.1 shows the imaging principle of OCT, in which the light source is a superluminescent diode (SLD), operating at a wavelength of 0.8 μm, and whose coherence length is typically 15 to 20 μm. The SLD output is divided into two parts, a reference arm and a signal arm. The signal-arm light is incident on the sample, as shown in Figure 8.1, and then many lights are reflected from the tissue sample. Ballistic photons are detected selectively from the reflected light by using this sort of low coherence interferometer. In the basic interferometer the position of the reference mirror corresponds to each reflection point inside the sample. The reference mirror is scanned at a constant speed along the optical axis in synchronization with

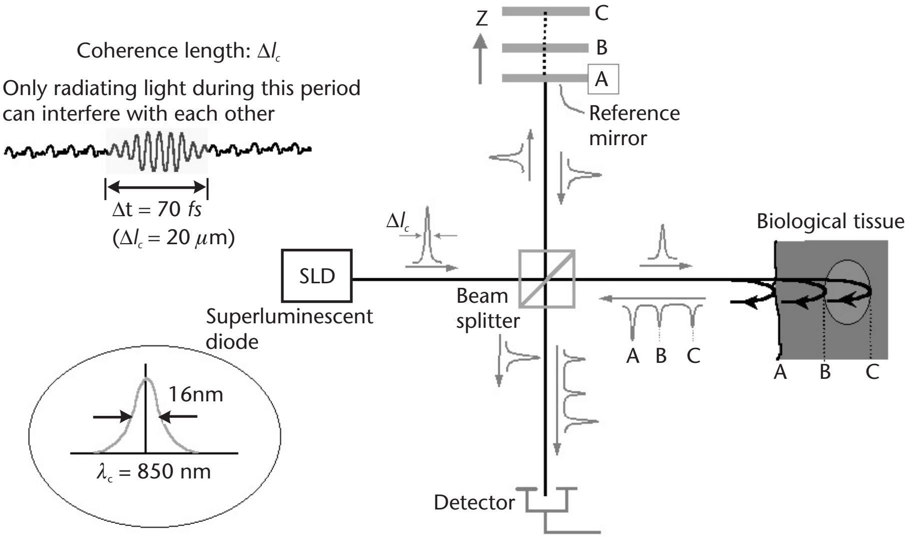

Figure 8.1 Imaging principle 1 of OCT: Optical echo using the low-coherence interferometer.

the movement of the tissue sample normal to the optical axis. Therefore, we can obtain cross-sectional imaging, namely the OCT image, parallel to the screen.

Figure 8.2 shows how the OCT image is constructed. The process is extremely simple. The raster-scan signal is detected repeatedly and then the signals are displayed on the monitor. The great advantage of OCT is that any image reconstruction and processing techniques are unnecessary, unlike conventional X-ray computed tomography.

Very often a fiber-optic Michelson interferometer, such as that shown in Figure 8.3, is used for OCT imaging because the fiber optics are very simple and compact. Figure 8.4 shows a photograph of the OCT imaging system we built at our laboratory. The complete imaging optics are placed on a very small optical bench 50 × 50 cm in size; consequently, the other advantage of OCT is that the imaging system is

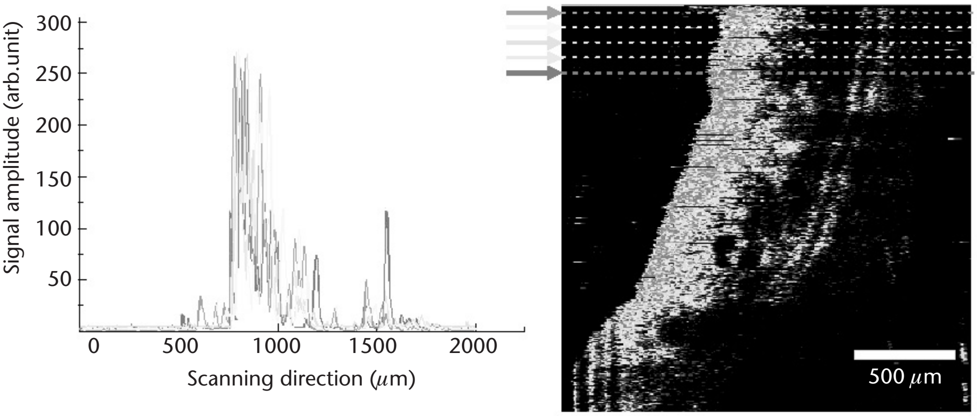

2 × 2 mm 5μm/step

Figure 8.2 Imaging principle 2 of OCT: Formation of cross-sectional images.

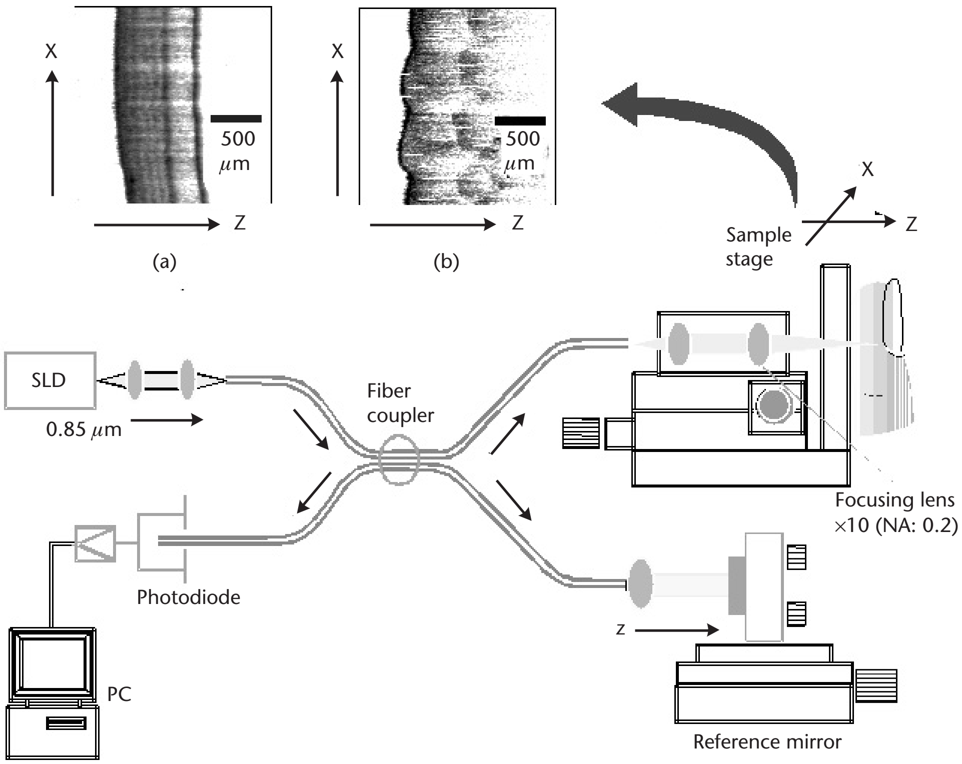

Figure 8.3 Fiber-optic interferometer for OCT.

very simple. Figure 8.5 is an OCT image of tissue beneath the skin of a human forearm. The image clearly shows the boundary between the epidermis and dermis. This is because a great deal of light is scattered in the epidermis, while in dermis there are many capillary vessels and lymphatic glands.

The light transmission of the dermis is relatively high compared with that of the epidermis. The important factor with respect to OCT is the light penetration depth, which can be estimated by the raster-scan signal as shown in the figure. Therefore, for a wavelength of 0.8 μm, the light penetration depth is only 0.7 mm. But the depth can be improved greatly by using a wavelength of 1.3 μm, as shown in Figure 8.6. This is because the scattering-induced attenuation for a wavelength of 1.3 μm is almost half that, at a wavelength of 0.8 μm. Figure 8.6 shows the OCT of an earlobe of a nude mouse. Figure 8.7 compares two OCT images obtained at wavelengths of 0.8 and 1.3 μm. Obviously, the light penetration depth for 1.3 μm is much better than for 0.8 μm [7].

Another important factor is the spatial resolution of OCT. Figure 8.8 shows a very strange OCT image, namely an image of a human scalp hair. A hair has a very simple structure that consists of a cuticle, a cortex, and a medulla. The diameter of the medulla is only 20 or 30 μm. The OCT image in the figure clearly shows the medulla in the center part of a scalp hair. This result shows that the spatial resolution of OCT is approximately 10 μm.

In terms of the clinical application of OCT, the main target is to employ it for the diagnosis of early stage malignant cancerous tumors. Figure 8.9 is an OCT

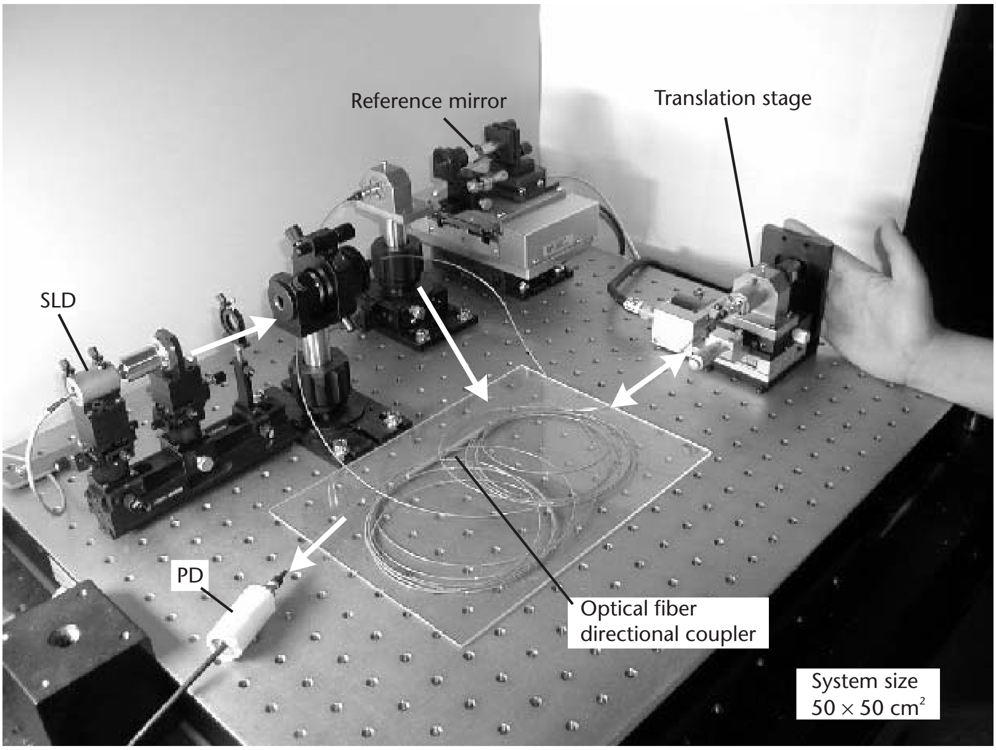

Figure 8.4 Fiber-optic OCT system.

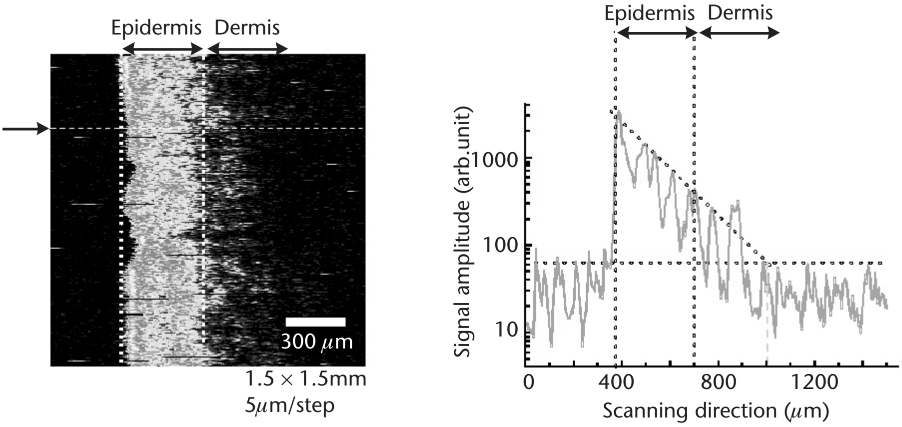

Figure 8.5 Possible imaging depth of 0.8-μm OCT inside the skin of a human forearm.

image of an epithelial tumor. In our experiment, the epithelial tumor (or to be precise, fibrosarcoma tumor cells) was introduced into the back of a nude mouse. Then after 1 week, the tumor cells grew and completely destroyed the layered structure of the skin surface. Therefore, in this OCT we can recognize that there is a lot of scattering underneath the skin surface. In contrast, the left-hand side of Figure 8.9 is an OCT image of a control (normal) mouse. It clearly shows the layered structure of the

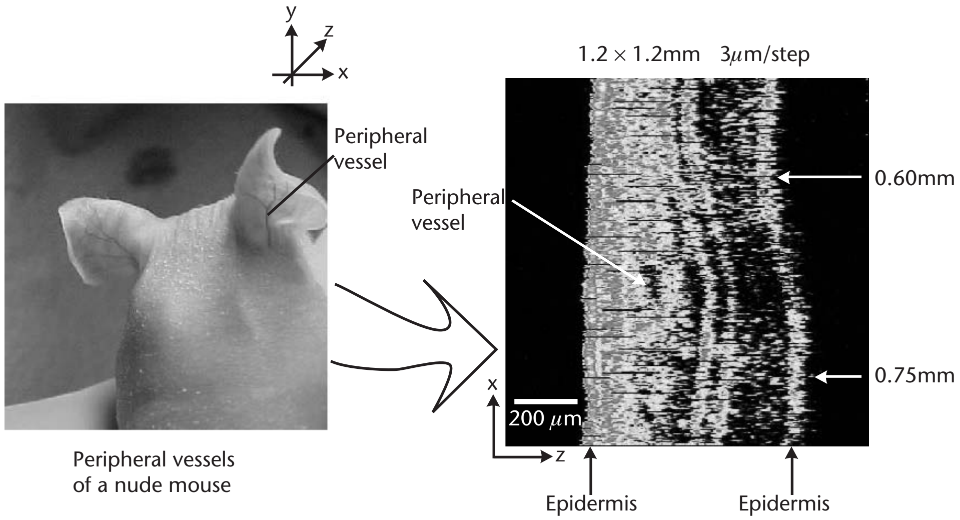

Figure 8.6 OCT of an earlobe of a nude mouse ($\lambda = 1.3\ \mu$m).

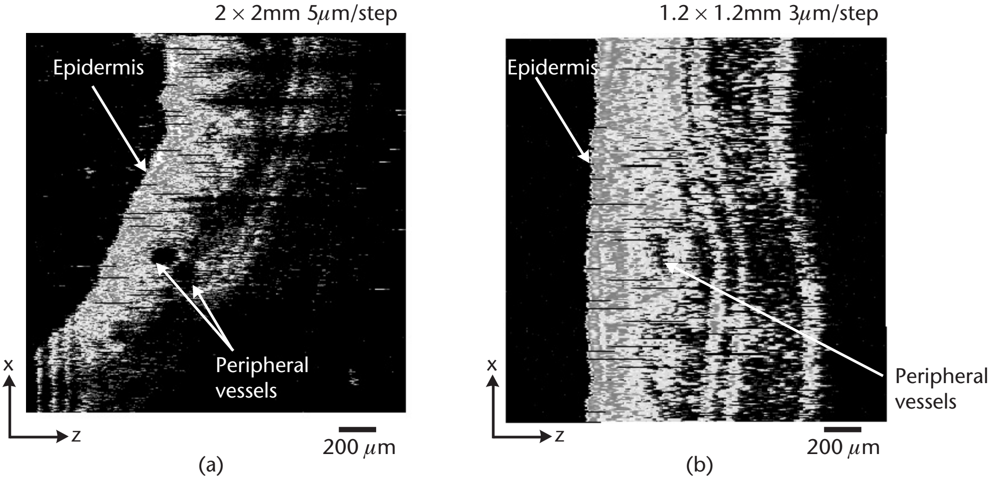

(a) (b)

Figure 8.7 Comparison of OCT images of a mouse earlobe for: (a) 0.8- and (b) 1.3-μm wavelengths.

skin surface, thus revealing an obvious difference. This experimental result will be useful for diagnosing the early stages of cancer in the near future.

Next, I will briefly describe the application of OCT to clinical diagnosis. As I mentioned above, in 1996 a practical OCT measurement system became commercially available for use in ophthalmology. Since then, OCT has been a powerful tool for the diagnosis of eye diseases. Medical doctors find OCT an extremely useful technique for the discrimination of the various tissues inside the human eye, with a resolution of 10 μm as shown in Figure 8.10 [8]. OCT is particularly useful for the diagnosis of diseases of the retina, such as macular edema and the removal of the retina, as shown in the OCT images in Figure 8.11.

For other clinical applications besides ophthalmology and dermatology, OCT should be combined with a fiber catheter and an endoscope [9]. Figure 8.12 shows

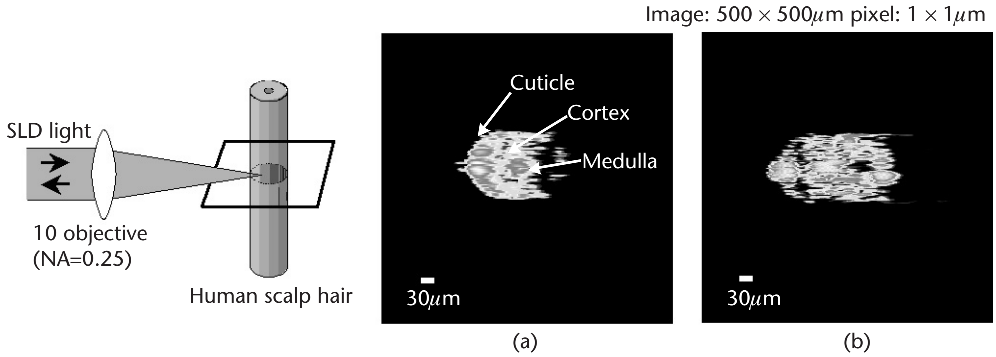

Figure 8.8 OCT of human scalp hair using: (a) 0.8-μm SLD, and (b) 1.3-μm SLD.

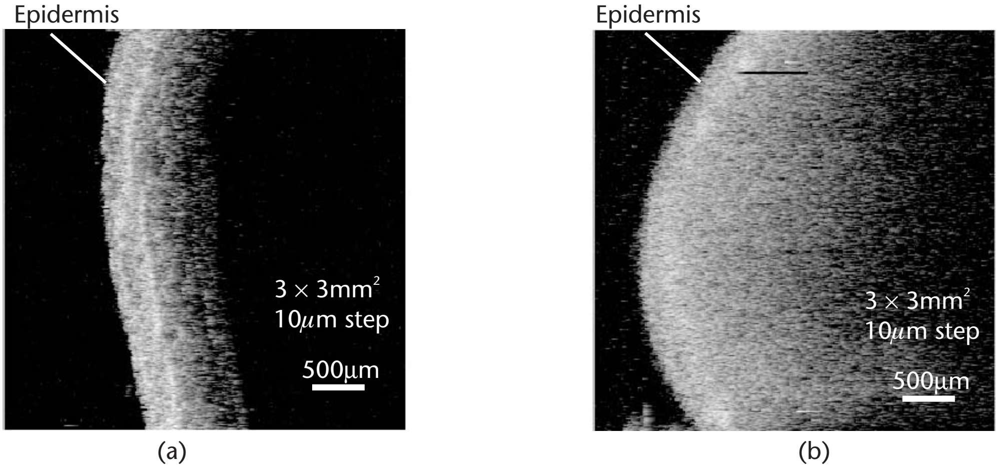

Figure 8.9 OCT of a nude mouse: (a) Normal tissue and (b) epithelial tumor.

the OCT catheter developed by Dr. Fujimoto's group for use in intramuscular imaging. A microprism is attached at the top of the fiber and an OCT image can be obtained by rotating it. This provides the kind of OCT image seen on the right of the figure, which is an image of a vessel wall where the light penetration depth was around 500 μm.

OCT diagnosis has been discussed experimentally in relation to many clinical fields, including gastroenterology, in which the main target is the diagnosis of cancer of the esophagus and stomach wall, as shown in Figure 8.13 [10]. In the field of dermatology an important target is the diagnosis of malignant melanoma, or skin cancer. Skin cancer is a more serious problem in the United States and Australia than it is in Japan. Figure 8.14 is an OCT image of a malignant tumor. The tumor cells have completely destroyed the layered structure beneath the skin's surface [9].

As listed in Figure 8.15, the conventional OCT technique has certain problems that must be solved. The first problem is that the OCT image does not reflect the real tissue structure because it has a dimension of optical thickness, which means the index times the thickness along the optical axis. In contrast, actual clinical diagnosis

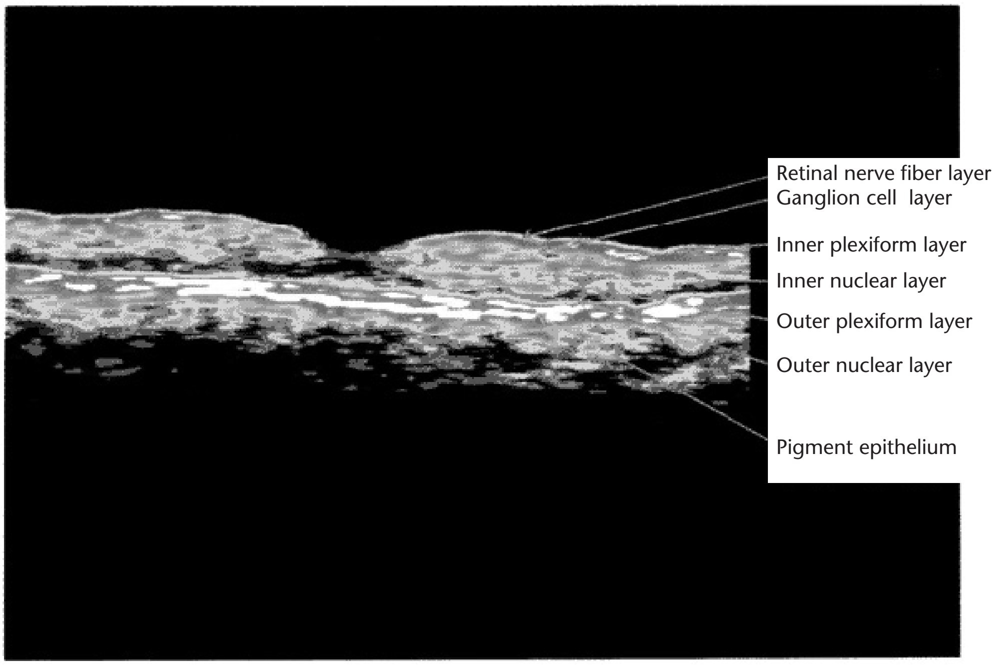

Figure 8.10 In vivo OCT image of macula retinae [8].

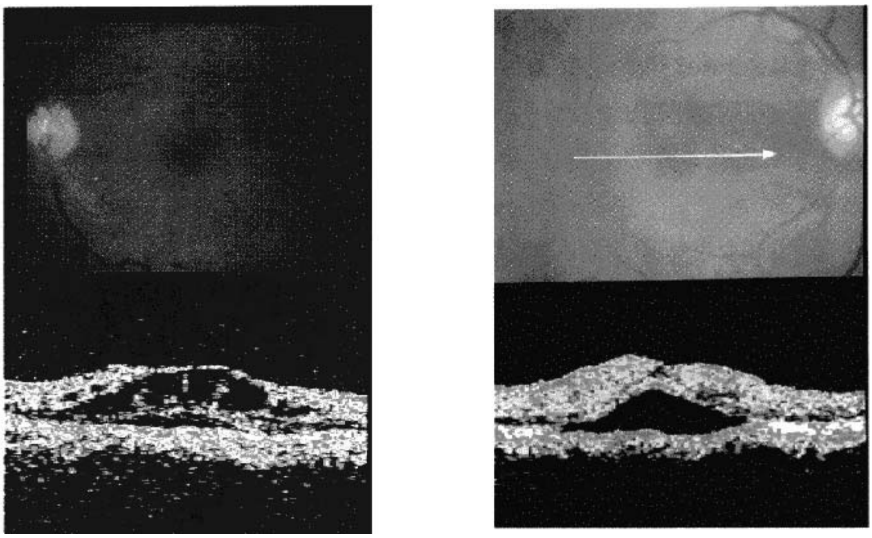

(a) (b)

Figure 8.11 Examples of OCT diagnoses for ophthalmology: (a) Diabetic macular edema, and (b) macula retinodialysis [8].

requires optical tomography with the geometrical thickness [11, 12]. This is a key point. The second problem with conventional OCT is that the illumination light is focused at a certain point on a tissue sample. This means a precisely focused image is obtained only near the focal point of the object; in other words, the remaining parts

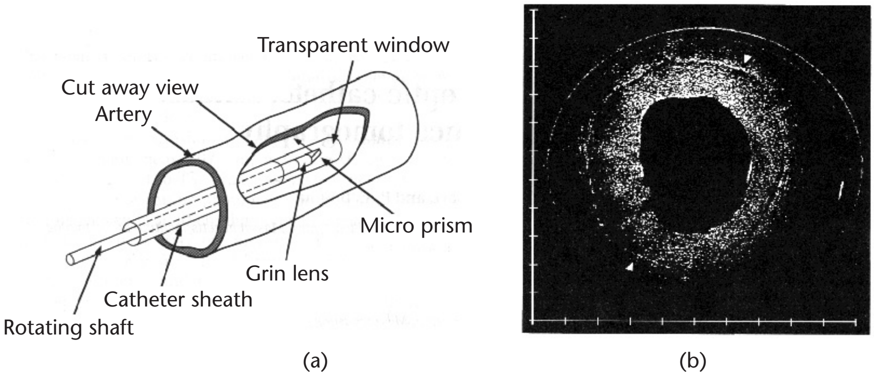

Figure 8.12 OCT catheter: (a) OCT catheter-endoscope, and (b) OCT image of in vitro saphenous vein (~500 mm) acquired with the catheter-endoscope [9].

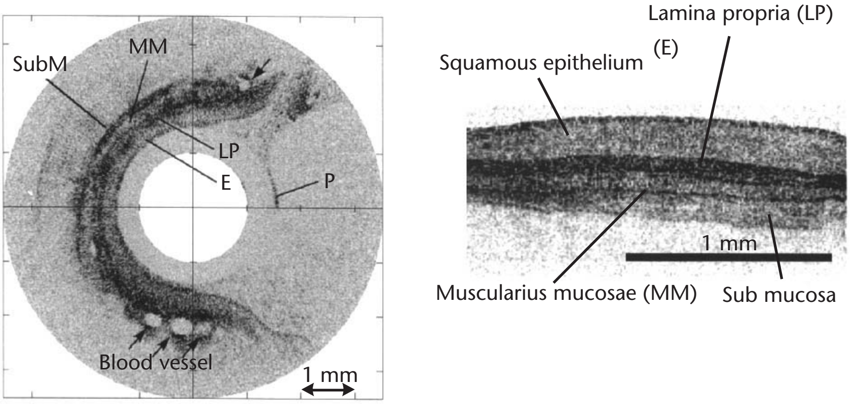

Figure 8.13 OCT of normal human esophagus [10].

of the OCT image are out of focus. For actual clinical diagnosis we need a precisely focused image of the entire cross-sectional area of interest. We call this "in-focus OCT" [13].

The third problem is that OCT is very often compared with histology. Histology involves obtaining a microscope photograph of tissue. The spatial resolution for histology must be 1 μm or better. Therefore, the spatial resolution of OCT should also be 1 μm or better because the spatial resolution of the two techniques should be comparable. Our goal is to realize this level of resolution with OCT for future OCT-based clinical diagnosis. Moreover, stereographic or three-dimensional OCT is more convenient for clinical diagnosis, as with X-ray computer tomography.

First, I would like to discuss the early stage diagnosis of advanced stomach cancer using in-focus OCT. With stomach cancer, a malignant tumor grows and penetrates from the mucosa to the submucosa, as shown in Figure 8.16. The efficacy of a surgical operation depends critically upon whether this malignant tumor has penetrated the muscularis mucosa. The muscularis mucosa is the boundary tissue between the mucosa and submucosa and is a film-like tissue with a typical thickness of 30 to 80 μm. The key to this kind of diagnosis is to obtain a clear image of the muscularis mucosa.

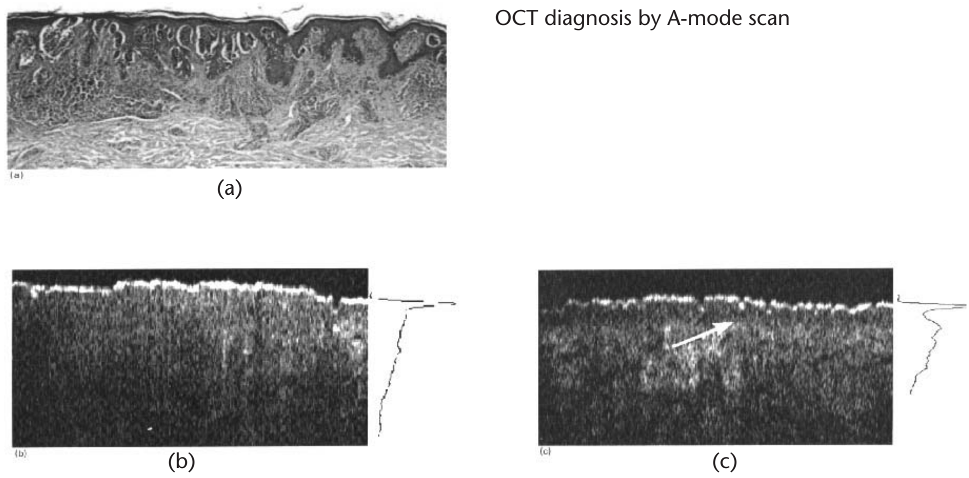

OCT diagnosis by A-mode scan

(a)

(b)

(c)

Figure 8.14 OCT of a malignant melanoma on a shoulder: (a) Histology, (b), OCT, and (c) healthy skin [9].

(1) OCT does not reflect a real tissue structure because it has the dimension of optical thickness (n x t).

⟶ Optical tomography along the geometrical thickness

(2) Out-of-focus imaging in OCT

⟶ Quasi in-focus OCT or in-focus OCT

(3) OCT corresponding to histology

⟶ High-resolution OCT (mm-order resolution)

(4) 3-D OCT

⟶ Stack of en-face OCT

Figure 8.15 Technical improvements of OCT: Problems, requirements, and solutions.

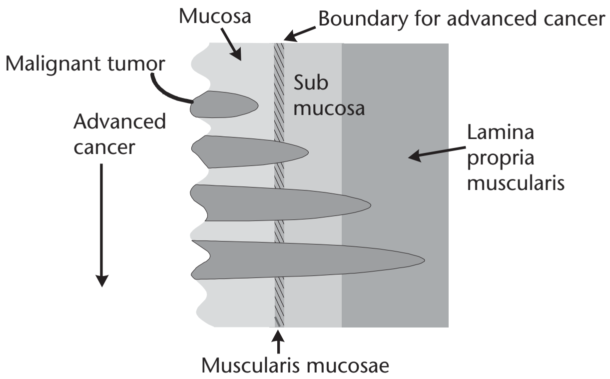

Figure 8.16 Early-stage diagnosis of advanced cancer in stomach.

Figure 8.17 shows a tissue sample of a human stomach wall, supplied by a university hospital. Figure 8.18 shows a usual OCT image of the stomach wall where

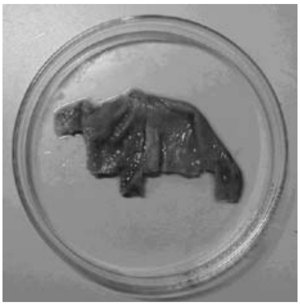

Figure 8.17 Sample of human stomach wall.

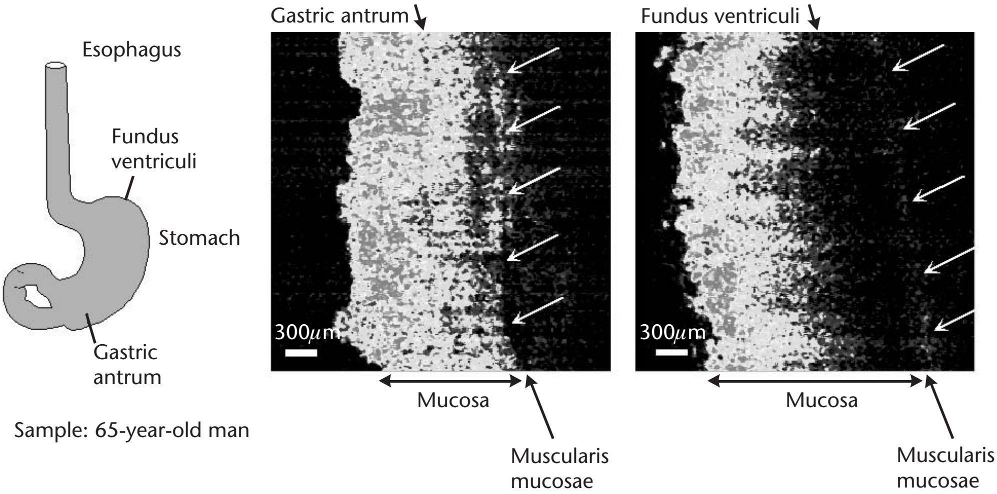

Figure 8.18 In vitro OCT of human stomach wall ($\lambda = 1.3\ \mu$m).

the muscularis mucosa is indicated by the arrows. Unfortunately the image of the muscularis mucosa is not very clear because it is out of focus. In our experiment several OCT images were made by shifting the focal point of the objective a distance of 200 μm, as shown in Figure 8.19, thus collecting a series of OCT images. As a result, we realize quasi in-focus OCT through which an almost perfectly focused image can be obtained for almost the entire cross-section of interest, as shown in Figure 8.20 [13]. This method allows us to see the muscularis mucosa clearly. The thickness is about 30 to 80 μm and sometimes 100 μm. In this quasi in-focus OCT, however, the reference mirror must be scanned many times. This in turn means that it takes a long time to obtain the quasi in-focus OCT images.

Very recently we demonstrated another method in which a single scanning of the reference mirror can be used to obtain in-focus OCT. The details of the operating principle of this method will be published. The resulting in-focus OCT agrees well with the corresponding histology, that is, a microscope photograph of biological tissue.

The major difference between the in-focus OCT and histology is the spatial resolution of the two images. With OCT, the resolution is approximately 10 μm, and for histology, it is better than 1 μm.

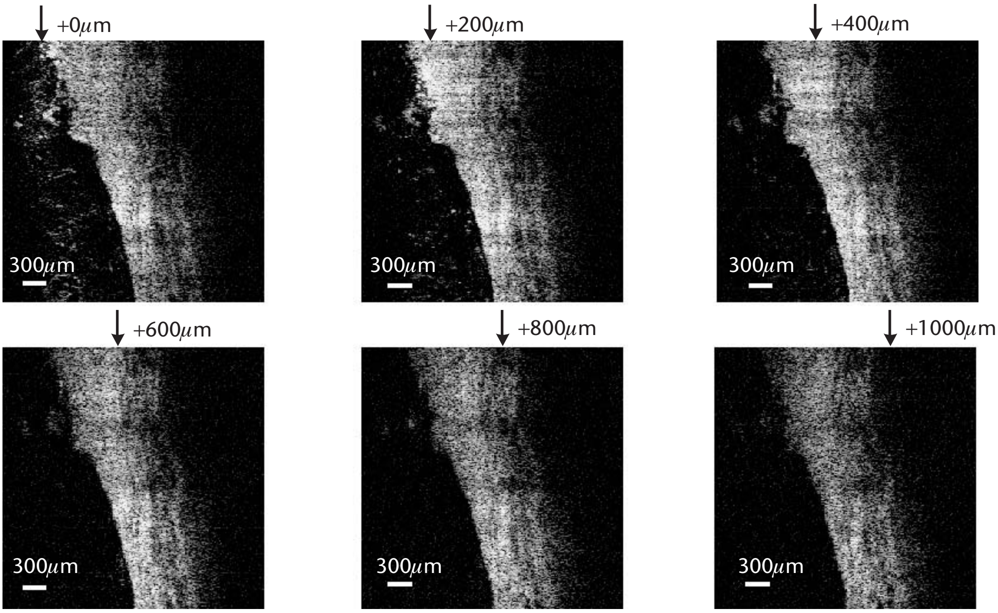

×10 objective(NA=0.25) image: 3×3mm pixel: 10×10μm

Figure 8.19 Multiple OCT with shift of the focal plane for human stomach wall (gastric antrum).

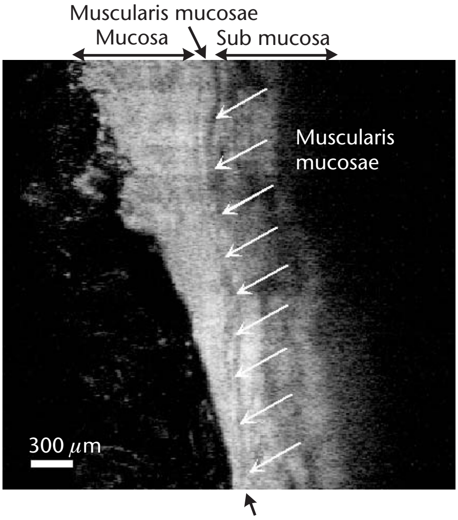

×10 objective (NA=0.25)
Image: 3×3mm
Pixel: 10×10μm
Sample: 65-year-old man

Figure 8.20 Quasi in-focus OCT of human stomach wall (gastric antrum).

The spatial resolution of OCT can be improved by broadening the wavelength bandwidth of the light source, as shown in Figure 8.21. For example, a 10-fs laser pulse can provide the required coherence length. The coherence length is the resolution of the OCT and is 3 μm, as described below. Moreover, a submicron coherence length can be obtained by using a super continuum light, (SC light), in which the photonic crystal fiber is excited by a mode-locked Ti: sapphire laser [14]. Another light source candidate for the high resolution OCT is thermal light. Thermal light

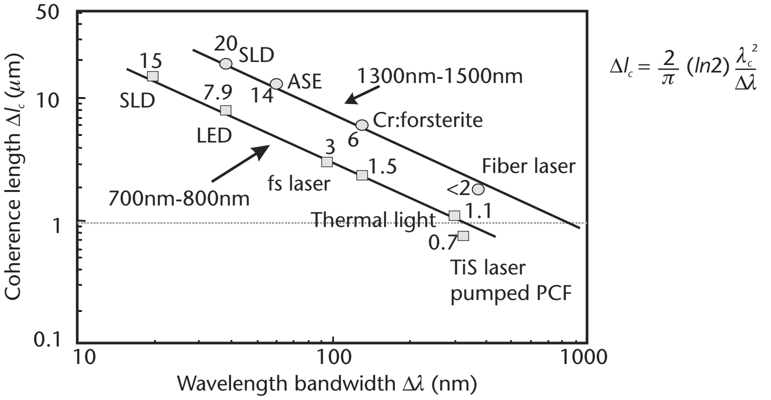

Figure 8.21 Possible light sources for high-resolution OCT.

means, for example, a halogen or tungsten lamp. These thermal lights can provide a coherence length as short as 1.1 μm.

Figure 8.22 is the measured interference fringe of a 10-fs laser pulse showing a coherence length of 3.1 μm. Figure 8.23 compares OCT images of an onion obtained with SLD and a 10-fs laser pulse; the difference between them is obvious. With the OCT image obtained using the 10-fs laser pulse, the cell structure just beneath the onion surface is very clear.

Figure 8.24 shows an in vivo high-resolution OCT image of a human forearm showing the very thin tissue structure of the stratum corneum layer, whose thickness is typically 20 μm.

Figure 8.25 shows another example obtained using high resolution OCT. In this case the coherence length is as short as 1.5 μm. By using a special mode-locked Ti: sapphire laser, Dr. Fujimoto's group obtained images of the cell structures of an African frog tadpole as shown in the figure [15].

Another candidate for high-resolution OCT is the thermal light interferometer shown in Figure 8.26. Here, a halogen lamp is used as a light source, and its output is fed into graded index (GI) fiber for collimation and spatial filtering. Using this thermal light interferometer we obtained a coherence length of only 1.1 μm, as shown in Figure 8.27. Figure 8.28 shows OCT images of a transparent film with a thickness of nearly 10 μm, obtained using the halogen lamp as a light source. As

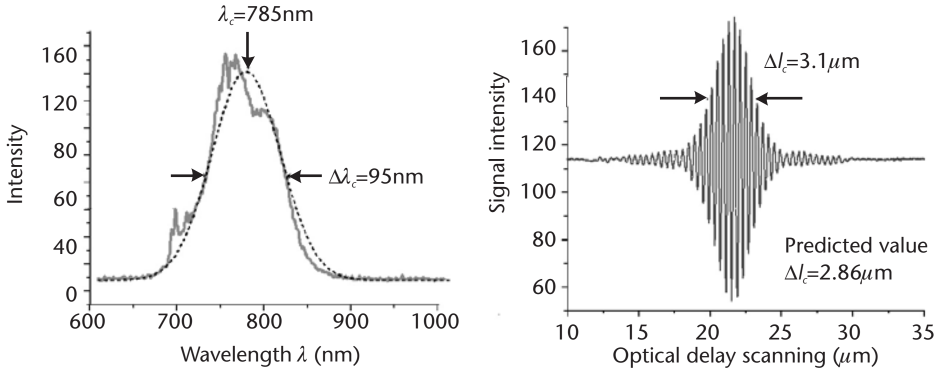

Figure 8.22 Interference fringe of the femtosecond laser.

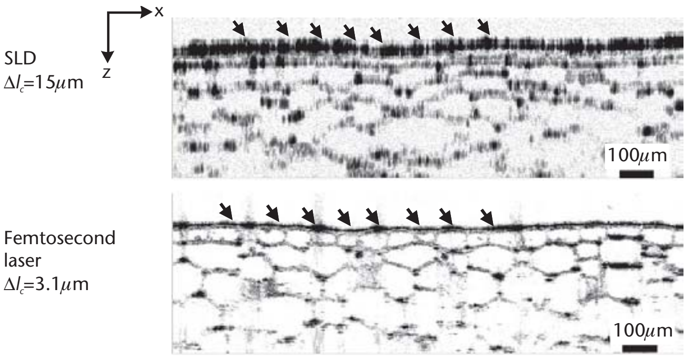

Figure 8.23 Comparison of OCT images from SLD and the femtosecond laser.

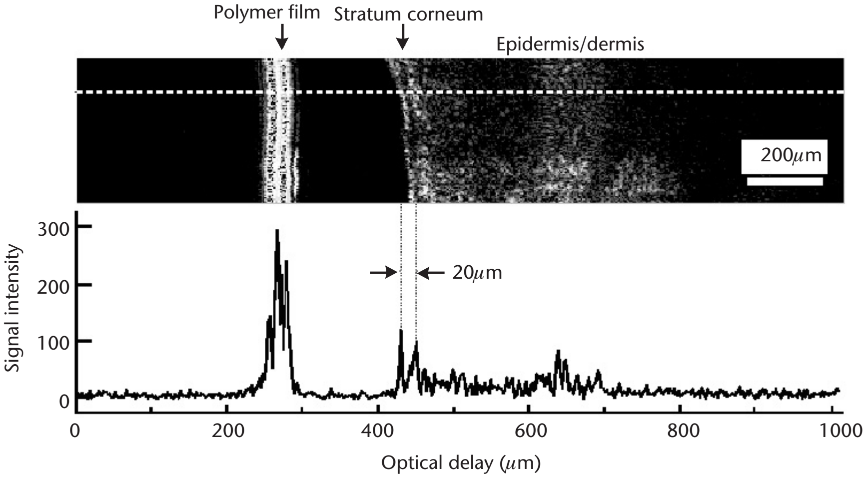

Figure 8.24 In vivo high-resolution OCT of human forearm.

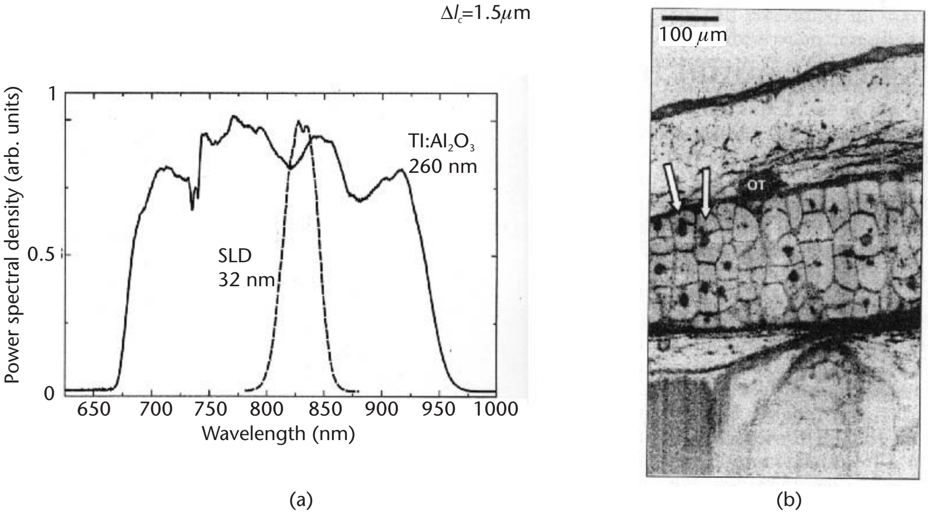

Figure 8.25 High-resolution OCT using a Kerr-lens mode-locked Ti-sapphire laser: (a) Spectrum, and (b) in vivo subcellular-level resolution tomography of an African frog tadpole [15].

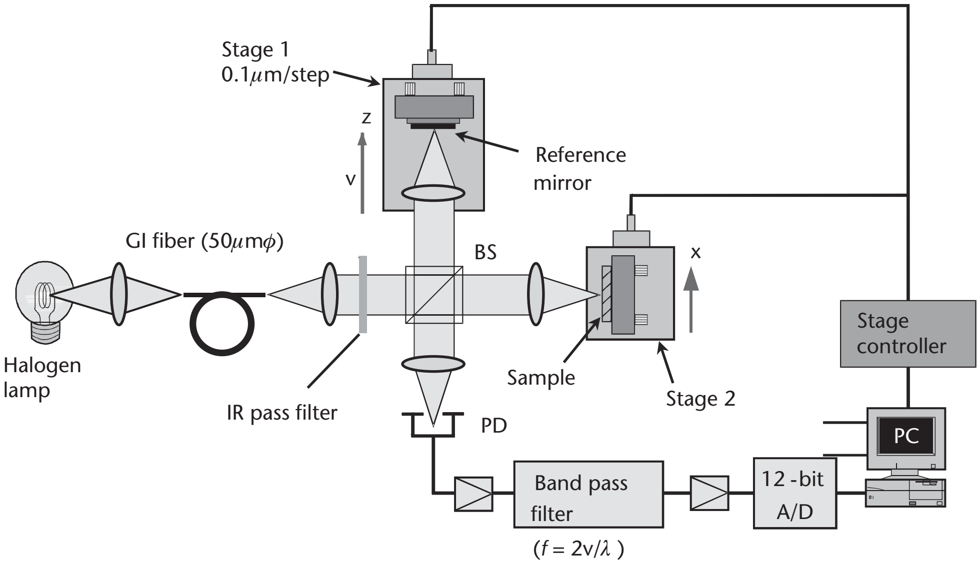

Figure 8.26 Thermal-light interferometer.

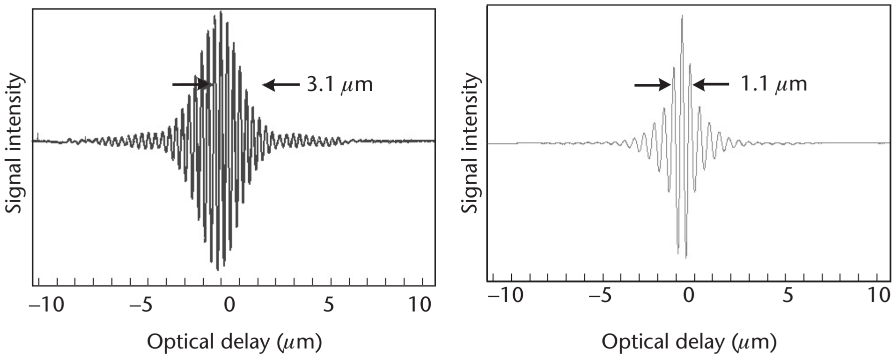

(a)

(b)

Figure 8.27 Measurement of the coherence length: (a) Femtosecond laser, and (b) halogen lamp.

shown in Figure 8.28 the front and rear surfaces can be distinguished very clearly using the halogen lamp [16].

Another key issue for future OCT technology relates to three-dimensional OCT images. As shown in Figure 8.29 [17], the three-dimensional OCT images can be constructed by stacking two-dimensional OCT images [17]. The two-dimensional OCT is an en-face or C-scan OCT image. In this experiment the sample was a plant leaf and it was also the en-face. Two-dimensional OCT images were obtained using a CCD camera. More than 100 OCT images were obtained with a depth interval of 6 μm. Then, all the OCT images were stacked to obtain the three-dimensional OCT.

An identical configuration for three-dimensional OCT is now being developed in a private company in Japan, according to [18]. In this configuration, the two-dimensional image is obtained with OCT or a scanning laser ophthalmoscope (SLO). These OCT or SLO images are stacked to construct three-dimensional OCT

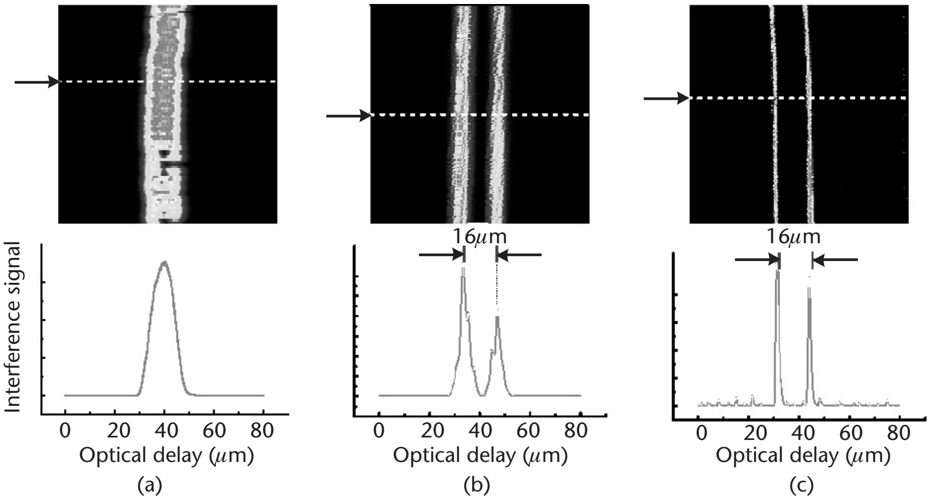

Figure 8.28 OCT images of transparent film of nearly 10-μm thickness, using (a) SLD, (b) LED, and (c) a halogen lamp.

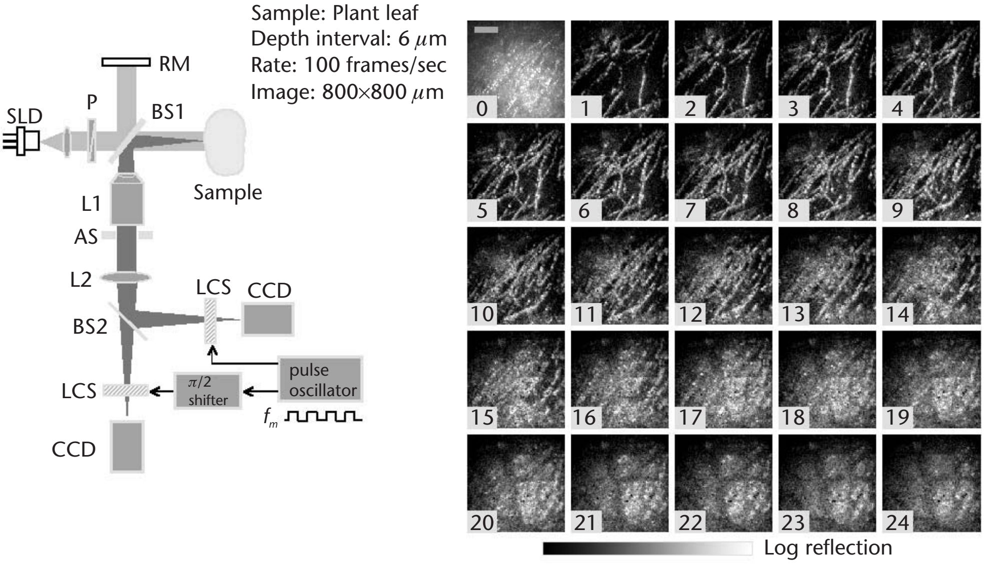

Figure 8.29 En-face OCT by two-dimensional heterodyne detection [17]. (*Courtesy of*: Professor Chan.)

images. The SLO image can be obtained by using confocal optics, thus making its spatial resolution much better than that of C-scan OCT. In this configuration the SLO images are stacked to obtain three-dimensional OCT images. I believe this kind of three-dimensional OCT will be commercially available within 1 year.

Finally, I will describe the application of OCT to biophysics and brain science. The first application in biophysics relates to biological membranes. Cell membranes are important tissues in terms of maintaining life functions. In general, a biological membrane mainly consists of phospholipid bilayers, as shown in Figure 8.30. Thus, the various functions of a biological membrane depend critically on the phase transition of these phospholipid bilayers. The existing method for the detection of the

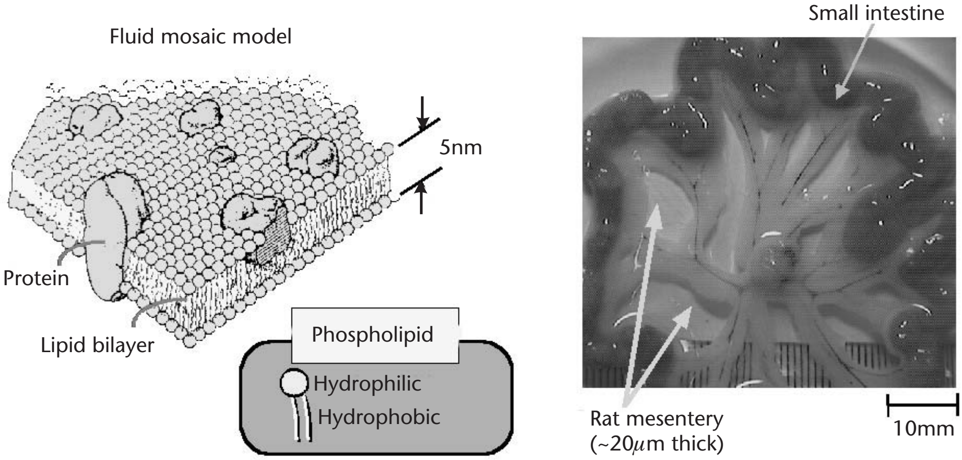

Figure 8.30 Biological membrane.

phase transition of the membrane is the differential scanning calorimetric, (DSC) method, as shown in Figure 8.31. Unfortunately, the DSC method is a destructive method, so as a result, we recently demonstrated the nondestructive optical probing method for detecting the phase transition of a membrane based on the OCT technique (i.e., based on a low coherence interferometer). Figure 8.32 is an example of our experimental results, which shows the abrupt changes in the refractive index and the transmission of a membrane cell in both the subtransition and main transition areas [19]. This optical probe method is nondestructive and will be applied to the in vivo analysis of biological membranes in the near future.

The second topic is the functional OCT of a cat's visual cortex. This method was proposed, developed, and demonstrated by Dr. Tanifuji at the Institute of Physical and Chemical Research (Riken). In this experiment, the signal arm light of the interferometer is incident on the cortex of the cat's brain, as shown in Figure 8.33 [6, 20]. A visual stimulus is then applied to the cat using horizontal or vertical bar patterns.

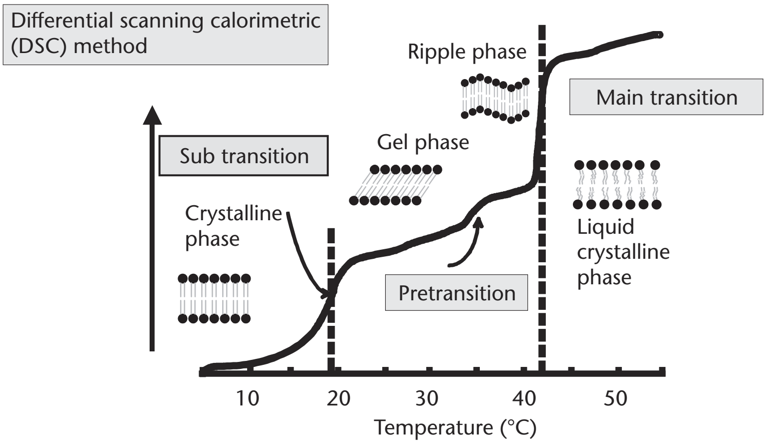

Removal of impurities by a centrifugal (destructive) method

Figure 8.31 The existing method for phase transition of a membrane.

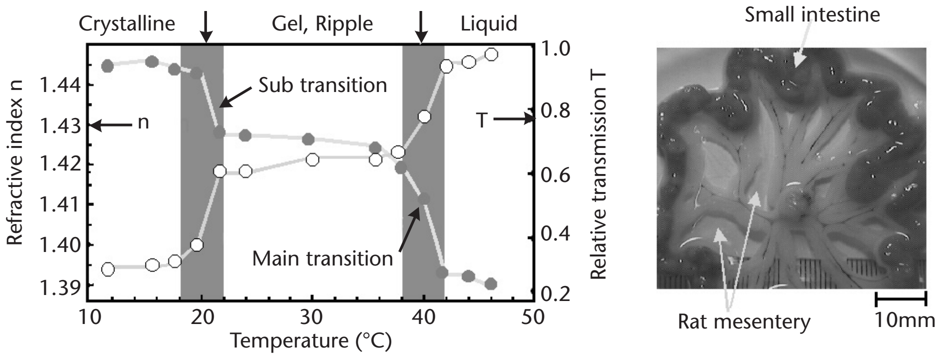

Figure 8.32 Nondestructive detection of phase transition of a rat membrane using OCT (A-mode scan).

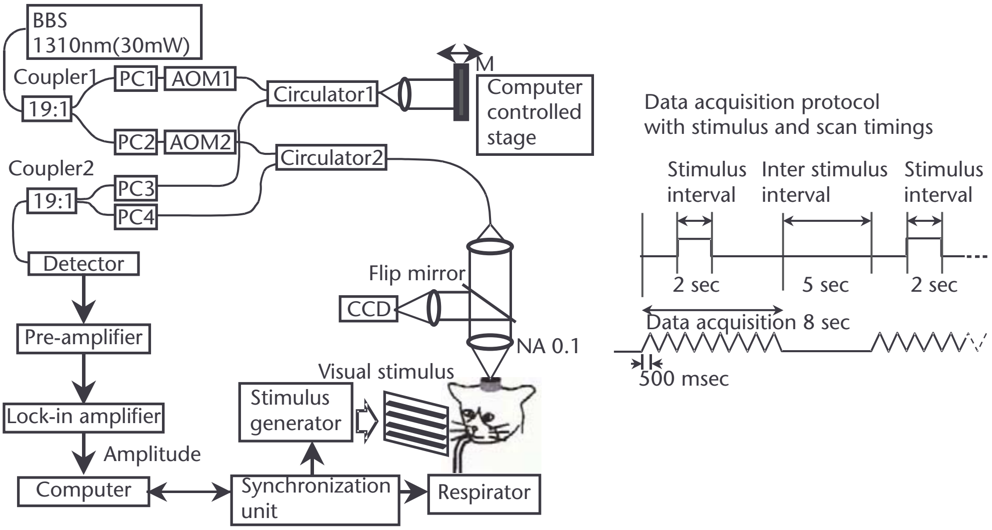

Figure 8.33 Functional OCT of a cat's visual cortex [6].

Figure 8.34 shows an example of the experimental data. It shows raster-scan signals along the cortex depth, and these signals correspond to the neural response of the cortex of the cat's brain. I think this function of OCT can be compared with the conventional functional MRI or positron emission tomography (PET). Functional OCT is a very interesting technique for the future application of OCT.

What are the prospects for the future? Will OCT become a popular diagnostic tool in clinical medicine in the same way that conventional ultrasonic echo imaging has? The answer depends greatly upon whether or not the light penetration depth is improved. A penetration depth of 1 or 2 mm is insufficient for actual clinical diagnosis, with the exception of ophthalmology. We need to achieve a light penetration depth of more than 10 mm.

We anticipate the development of a breakthrough technology to improve the light penetration depth. But at the present stage it is unclear how this will be achieved. In summary, OCT is really a very interesting and useful technique for medical applications. It is also useful for nonmedical applications including, for

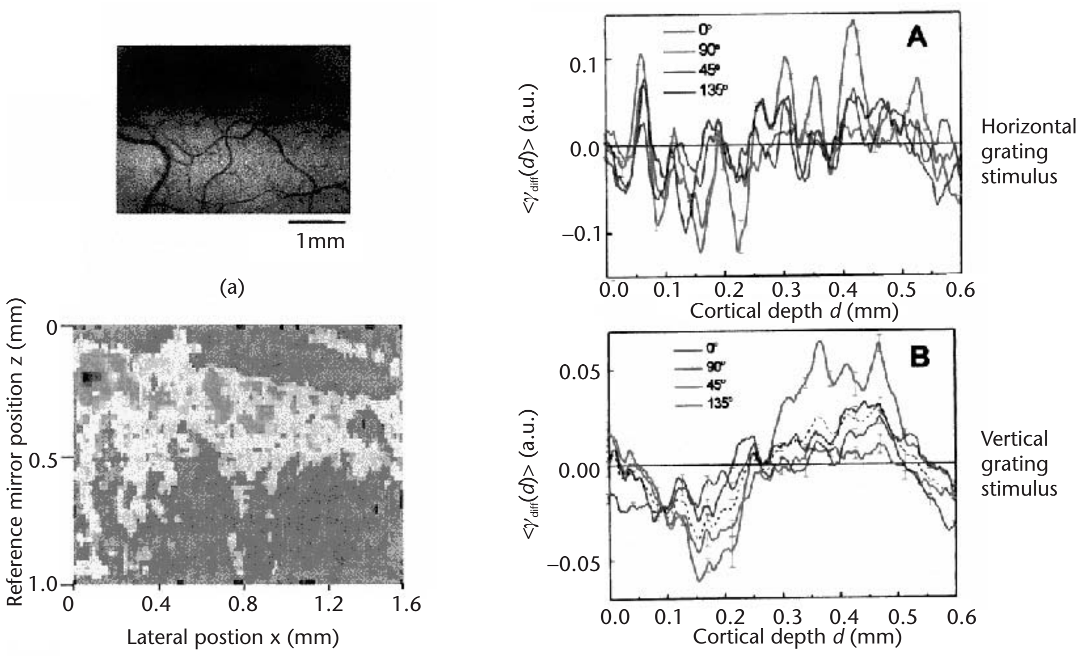

(b)

Figure 8.34 Anode signals and OCT image of a cat's visual cortex [20].

example, precise surface profile measurement and the simultaneous measurement of the refractive index of a certain thickness [21, 22].

References

[1] Huang, D., et al., "Optical Coherence Tomography," *Science,* Vol. 254, 1991, p. 1178.

[2] Humphery Instru. Inc., Humphery OCT scanner, OCT2000, 1996.

[3] Takada, K., et al., *Appl. Opt.,* Vol. 26, 1987, p. 1603.

[4] Tanno, N., T. Ichimura, and A. Saeki, Japanese Patent No. 2010042, issued 1990.

[5] Haruna, M., and M. Ohmi, *Proc. 3rd Asian Pacific Laser Symp.*, Osaka, 2002, (The Laser Society of Japan, 2003), p. 165.

[6] Maheswari, R. Uma, et al., *Opt. Commun.,* Vol. 202, 2002, p. 47.

[7] Ohmi, M, T. Kurata, and M. Haruna, *Proc. 8th Microoptics Conf.,* Osaka, 2001 (The Group of Microoptics, *Opt. Soc. Japan*, Tokyo, 2001), p. 88.

[8] Kishi, S., *Kohgaku,* Vol. 38, 1999, p. 126 (in Japanese).

[9] Bouma, B. E., and G. J. Tearney, (eds.), *Handbook of Optical Coherence Tomography,* New York: Marcel Dekker, 2002.

[10] Izatt, J. A., et al., *IEEE J. Selected Topics in Quatum Electron.,* Vol. 2, 1996, p. 1017.

[11] Haruna, M., et al., *Tech. Dig. Biomed. Topical Meet.*, Miami Beach, FL, 2000 (*Opt. Soc. Am.,* Washington, D.C., 2000), p. 194.

[12] Yoden, K., et al., *Opt. Rev.,* Vol. 7, 2000, p. 402.

[13] Haruna, M., M. Ohmi, and T. Kurata, *Proc. Asian Symp. Biomed. Opt. and Photomed. (BOPM), MB1-1,* Hokkaido, 2002 (Biomed. Opt. Group in *Opt. Soc. Japan*, 2001), p. 114.

[14] Hartl, I., et al., *Opt. Lett.*, Vol. 26, 2001, p. 608.

[15] Bouma, B. E., et al., *Opt. Lett.,* Vol. 20, 1995, p. 1486.
[16] Ohmi, M., and M. Haruna, *Opt. Rev.,* Vol. 10, 2003, p. 478.
[17] Akiba, M., K. P. Chan, and N. Tanno, *Opt. Lett.*, Vol. 28, 2003, p. 816.
[18] Podoleanu, A. G., et al., *Opt. Express,* Vol. 7, 2000, p. 292.
[19] Haruna, M., et al., *Proc. SPIE,* Vol. 3915, 2000, p. 188.
[20] Maheswari, R. Uma, and M. Tanifuji, *Rev. Laser Eng.,* Vol. 30, 2002, p. 648.
[21] Haruna, M., et al., *Opt. Lett.,* Vol. 23, 1998, p. 966.
[22] Maruyama, H., et al., *Appl. Opt.,* Vol. 41, 2002, p. 1315.

CHAPTER 9

Optical Fiber Sensors for Smart Materials/Structures and Optical Communications

Kazuo Hotate
Department of Electronic Engineering
School of Engineering
The University of Tokyo

Introduction

This chapter describes optical fiber sensors for smart materials, structures, and optical communications. The purpose of the research in our group is shown schematically in Figure 9.1. We are currently making fiber-optic nerve systems. Human nerves enable us to sense damage to our bodies, but we are applying this function to materials and structures.

For example, by equipping an airplane wing with an optical fiber sensor, we hope to determine both the location and degree of any damage in order to maintain the health of the wing material. Moreover, we can detect the strain applied to a material by installing fiber on its surface. Materials that have a self-diagnosis function are sometimes called smart materials. By using similar technology we can obtain a smart structure. Another possible application is a security system that can detect a potential burglary. In our laboratory we are also trying to apply these fiber-optic nerve systems to the subscriber optical fiber network, namely to fiber-to-the-home (FTTH) systems.

We have developed an original technique to obtain distributed data along a fiber, and realized a high spatial resolution, a fast measurement speed, and random access function to the damaged points, which were difficult to obtain with conventional ways.

Distributed and Multiplexed Fiber-Optic Sensing

To obtain such nerve systems we need to use a distributed fiber-optic sensing scheme or a multiplexed fiber-optic sensing scheme, which are shown in Figure 9.2. The fiber Bragg grating has been developed, mainly for communication applications, for filters, or for dispersion compensation. However, those working in the

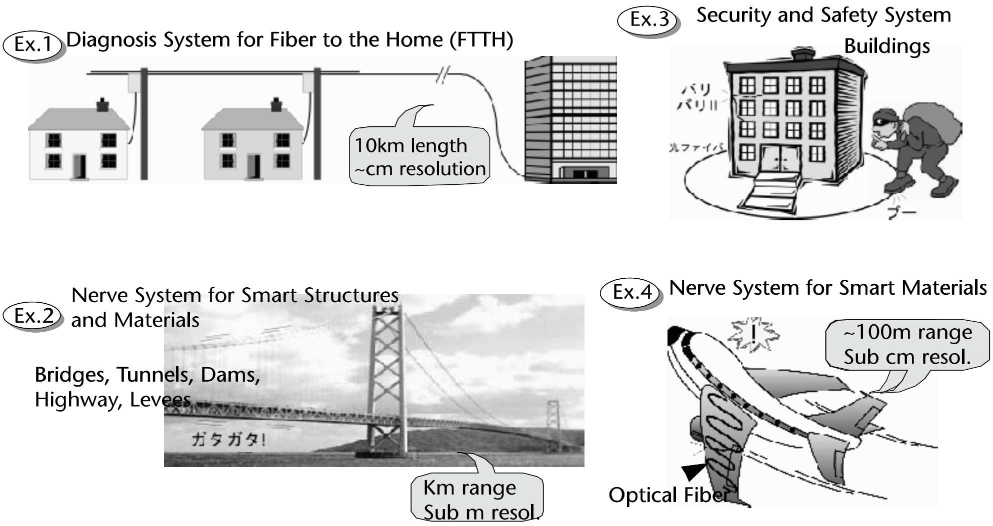

Figure 9.1 Fiber-optic nerve systems for smart materials, smart structures, and optical communications.

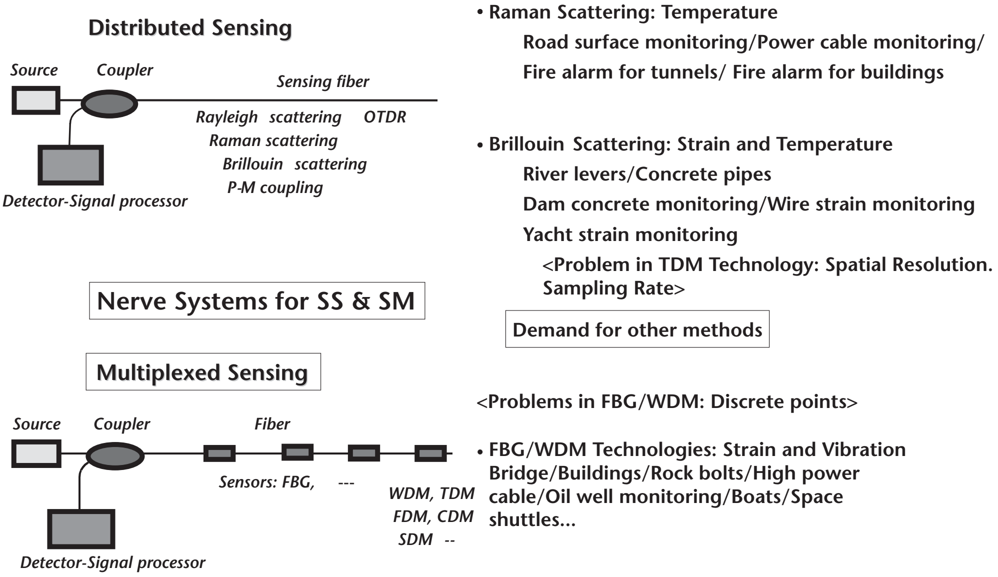

Figure 9.2 Distributed and multiplexed fiber-optic sensing schemes: Technologies and problems.

sensor field have also used the fiber Bragg grating (FBG) because it performs well as a strain gauge or a temperature sensor. With one light source and one detector we can obtain a large amount of information along a fiber. This kind of approach is called the multiplexed sensing technique [1]. However, this method has a drawback because the damage may occur in a place where we cannot detect it. Therefore, our aim is to realize fully distributed sensing schemes. To achieve this we must use the characteristics of the fiber itself, for example, Raman scattering, Brillouin scattering, or polarization mode coupling.

This kind of technology has already been developed for fiber-optic nerve systems, but they mainly employ optical time domain reflectometry (OTDR) [2]. This approach imposes limits regarding, spatial resolution, for example. By using Brillouin scattering, for example, we can obtain strain distribution information. However, if we use OTDR technology the spatial resolution is limited to approximately 1m. One meter is insufficient for damage detection; for the surface of an airplane wing, we need a spatial resolution of 1 cm.

In addition to the lack in spatial resolution, time domain technology also has an inadequate sampling rate because we need to detect very small amounts of backscattering induced by a pulsed lightwave; the amount of the power we obtain is very small. Therefore, in order to obtain a sufficient S/N ratio we must employ a very large number of pulses. This in turn means that we require a long time to obtain the distribution information. Typically, the time needed for distribution sensing is just 1 or 2 minutes. By using time-domain technology, we only obtain the static distribution of the strain or temperature. We cannot measure the dynamic strain. This has led to the desire to create other new methods, which must have higher spatial resolution and a dynamic measurement capability.

Synthesis of Optical Coherence Function

In order to realize these functions, we are using continuous wave technology rather than time domain technology. In our laboratory, we use an interferometer. As shown in Figure 9.3, the interferometer has a light source that provides a reference light and a sensing light. There is an interference fringe whose amplitude is a function of the propagation time difference between the reference and sensing lightwaves. This is called the optical coherence function and is easily calculated by the Fourier transformation of the power spectrum shape of the light source. Therefore, when we use a given light source, the coherence function shape is decided automatically.

In our work we use a highly coherent light source, which means a narrow spectrum light source. We then change the lasing spectrum in the time domain as shown in right side of Figure 9.3. This means we synthesize the shape of the power spectrum. In addition, we employ a phase modulator (PM) that is driven synchronously with the frequency modulation waveform shown in the figure. We found that we were able to synthesize optical coherence functions with arbitrary shapes. The figure shows an optical coherence function with a triangular shape. We can synthesize a coherence function with any shape including rectangular, Gaussian, and delta function-like shapes. We are currently trying to expand the applications of this technique for synthesizing the optical coherence function [3–6]. These are described next.

Brillouin Optical Correlation Domain Analysis

Brillouin Scattering

In this section, I will describe a nerve system developed in our laboratory, where we used Brillouin scattering to obtain the strain distribution along a fiber. The goal of

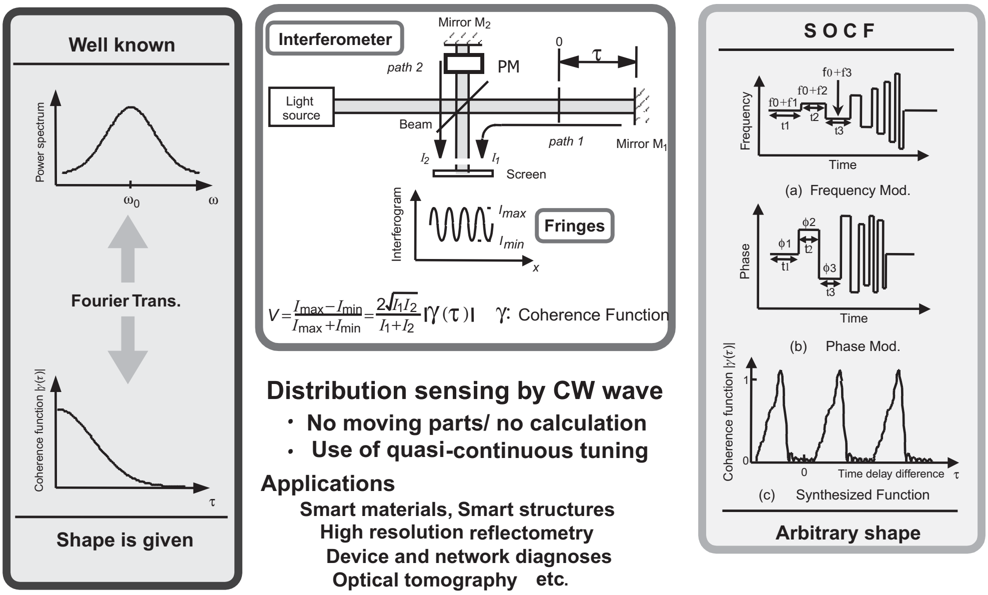

Figure 9.3 Original seed technology: synthesis of optical coherence function [3–6].

this work is to realize a nerve system for smart materials. As I mentioned earlier, if we use time domain technology, we cannot realize a 1-cm spatial resolution. The resolution is limited to just 1m and the sampling rate is several minutes. To overcome these problems we employed a synthesis of optical coherence function technology.

Figure 9.4 illustrates Brillouin scattering. The fiber we used is made of SiO_2, and SiO_2 vibrates thermally as shown in the figure. A thermal vibration frequency of 11 GHz causes a sound in the fiber, which has a period of exactly half the wavelength of the 1.5-μm lightwave. This 11-GHz sound acts as a Bragg reflector for the input 1.5-μm lightwave. The lightwave is then back reflected and this is called Brillouin backscattering. As shown in Figure 9.4, the sound moves in a way that results in a Doppler shift, and then the Brillouin backscattering has a downshifted frequency of 11 GHz. This frequency is given by the speed of the sound in the fiber. Therefore, if we apply strain, the speed of the sound should change, meaning the value of 11 GHz should change. Therefore, by measuring the downshifted frequency of the Brillouin scattering we can obtain information on the applied strain.

We need a scheme to obtain the distributed information—one method is to use a pulse lightwave. However, if we use a shorter pulse, its spectrum widens, as shown in Figure 9.5. On the contrary, Brillouin scattering has only a 30-MHz bandwidth.

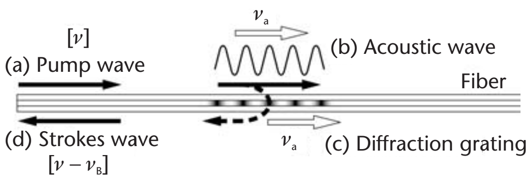

Figure 9.4 Brillouin scattering: (a) pump wave, (b) acoustic wave, (c) diffraction grating, and (d) Stokes wave.

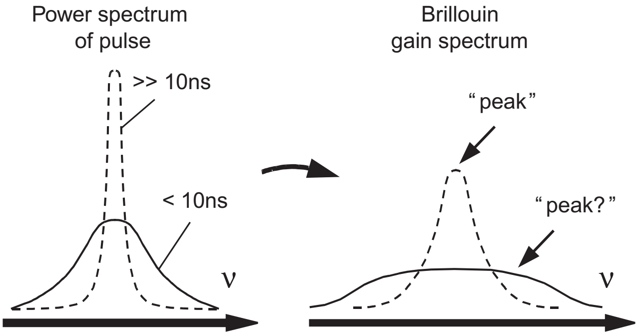

Figure 9.5 Limitation in time-domain techniques.

In order to obtain the center frequency precisely, we must maintain a narrow Brillouin spectrum. However, if we employ a 1-m pulse, it has a 200-MHz bandwidth. This means we cannot obtain the peak of the Brillouin spectrum precisely. Therefore, we will lack spatial resolution if we use time domain technology. This shows us that a 1-m spatial resolution limitation is inherent when we use time domain technology [2, 7, 8] .We must, therefore, find another approach that does not use time domain technology.

A Brillouin-based distributed strain-sensing system, in which the time domain scheme is used [2], has already been available commercially. For example, fiber is installed on the surface of a pipe and a force is exerted. The approach successfully obtained the strain distribution along the surface of the pipe. However, the pipe was 3m in diameter, so the perimeter was approximately 10m. This shows that we can obtain the strain distribution for this kind of large structure, but the spatial resolution was only 1m. Therefore, we cannot employ this technique for airplane health monitoring.

BOCDA Technique

Several years ago we proposed the system shown in Figure 9.6. The system is called Brillouin optical correlation domain analysis (BOCDA) and was developed by synthesis of optical coherence function technology [9–18]. This system employs a tunable distributed feedback laser (DFB) with three electrodes. As shown in the figure, there is a probe lightwave and a pump lightwave. In the fiber under test we have two lightwaves counterpropagating in opposite directions. By using an intensity modulator we generate the downshifted frequency component by 11 GHz in the probe lightwave. We then have two lightwaves with an 11-GHz discrepancy and they induce stimulated Brillouin scattering. Therefore, we can obtain stimulated Brillouin scattering by using a photodetector.

However, we cannot obtain position information under these circumstances. Therefore, we additionally imposed frequency modulation on the laser diode. There is a pump and a probe and they both experience frequency modulation. The lightwave frequency then fluctuates beyond 30 MHz, so we cannot obtain any Brillouin scattering. However, at a specific portion of the fiber, shown as the correlation point in Figure 9.6, the two lightwaves exhibited frequency modulation but were

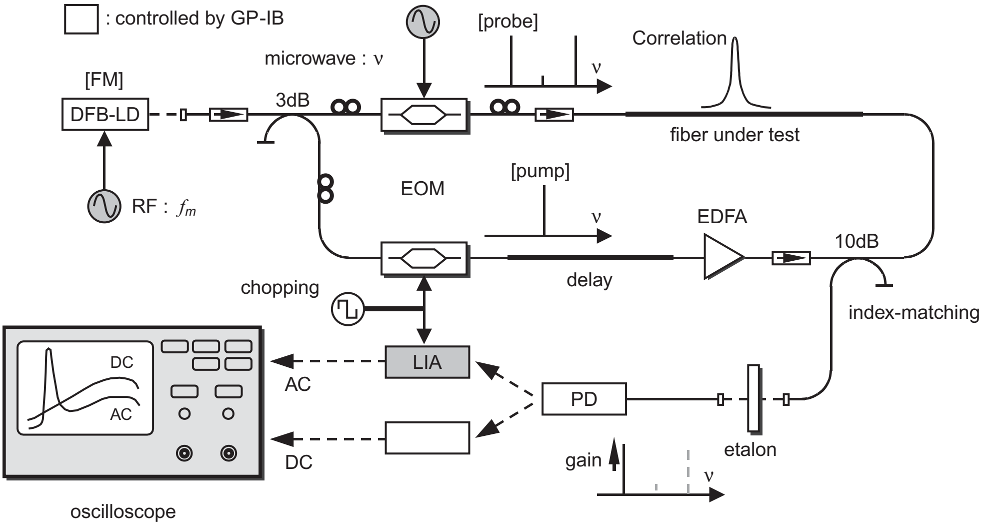

Figure 9.6 Brillouin optical correlation domain analysis: BOCDA [9–18].

synchronized. This means that there is an 11-GHz frequency discrepancy and we can obtain stimulated Brillouin scattering.

In the scheme shown in Figure 9.6, we use a continuous lightwave but we only excite the stimulated Brillouin scattering at a specific portion. The correlation width can be restricted to centimeter order, providing us with a high spatial resolution distributed sensing technique.

As shown in Figure 9.7, there is, therefore, a correlation peak along the fiber. At the correlation peak position, which is induced by the frequency modulation on the laser diode, we have clearly obtained a Brillouin spectrum shape with a 30-MHz width. On the other portion we have no clear spectrum. Therefore, at the end of the fiber we have a kind of small mountain structure with a tower at its top and the peak frequency at this point gives us information on the strain applied to this correlation portion. The correlation position can be easily swept by changing the modulation frequency of the laser. This means we can obtain the distributed strain information. The spatial resolution is inversely proportional to the frequency and the amplitude of the frequency modulation, and this provides us with a spatial resolution of one centimeter.

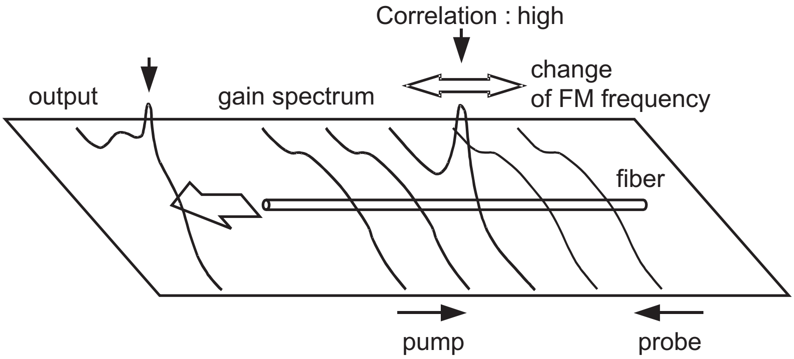

Figure 9.7 A correlation peak generated along the fiber.

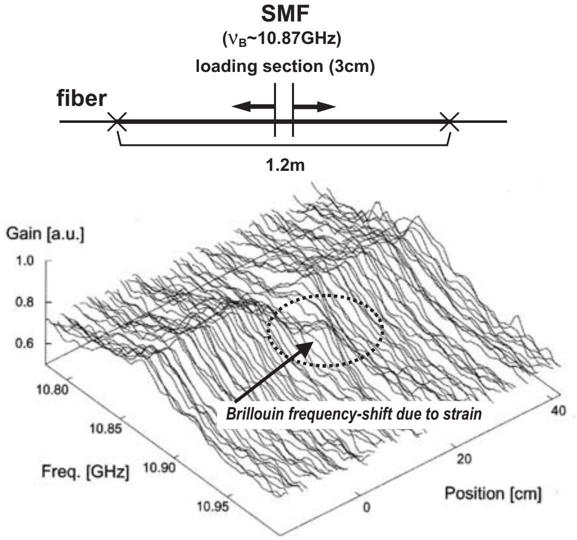

Figure 9.8 Demonstration of a spatial resolution of 3 cm [13, 17, 18].

High Spatial Resolution Distributed Strain Measurement

The following section describes our experimental data. The axis at the bottom of Figure 9.8 shows the position along the fiber in centimeter units [13, 17, 18]. The figure also shows the spectrum and the Brillouin frequency peak. The peak frequency provides us with information on the strain, and a 1% strain corresponds to a 500-MHz frequency shift. As seen in the figure, there is constant strain, then some strain change, and then constant strain again. In this sample fiber we applied strain to just a 3-cm section and the figure shows the strain distribution along the fiber obtained with our method. The fact that we can clearly observe the 3-cm section means that we have achieved a spatial resolution that is 30 times higher than that provided by conventional time domain technology.

So I asked my student, “Why can’t you obtain a 1-cm spatial resolution?” The next day the student brought me the 1-cm spatial resolution data shown in Figure 9.9 [13, 17, 18]. This is 100 times higher than is possible with time domain technology.

However, a synthesized coherence function characteristically has an iterative or periodic shape. This means that the correlation peaks are arranged periodically along the fiber. As a result, the measured range is restricted to a typical length of only 5m. Therefore, we must extend the measurement range. One easy way to achieve this is to apply multiple frequency modulation to the laser diode frequency modulation [15, 17]. In the example shown in Figure 9.10, we applied $2f_0$ and $3f_0$, and after a number of correlation steps we realized an excellent overall correlation. This enabled us to expand the measurement range. With this easy technique we have already obtained a 20-m measurement range. The fiber shown in Figure 9.11 is 20m long and we can clearly obtain four strain-applied portions [15, 17]. Now we apply time domain technology in which we use, for example, a 5- or 10-m-wide pulse, and in this pulse we synthesize the correlation peak with a 1-cm spatial resolution. By changing the pulse delay along the fiber we can realize a larger and larger measurement range [19].

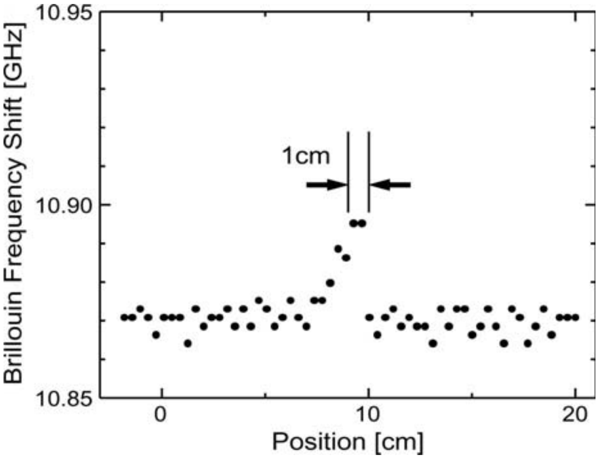

Figure 9.9 Demonstration of a spatial resolution of 1 cm [13, 17, 18].

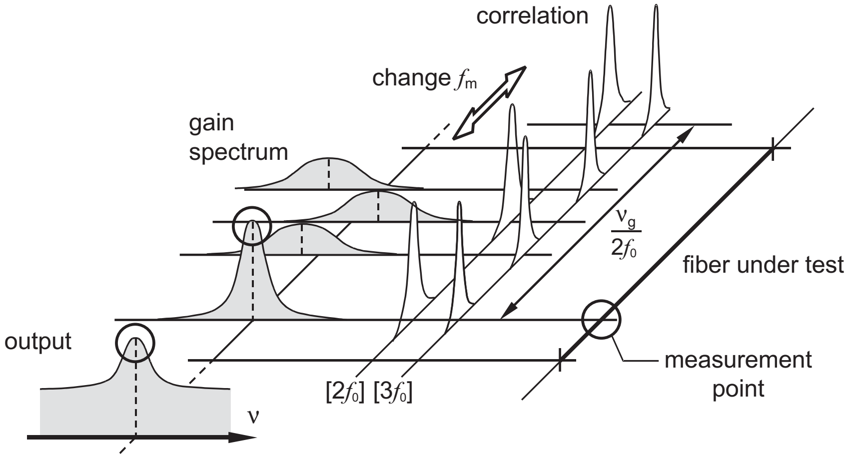

Figure 9.10 Simultaneous modulation to enlarge the measurement range [15, 17].

The spatial resolution had now reached only 1 cm and we used this technique to obtain a smart material with a higher spatial resolution. The sample we used in this experiment is the acryl ring with a 15-cm diameter shown in Figure 9.12 [20]. We coiled fiber around the 50-cm perimeter of the ring. We employed our method and obtained the strain distribution along surface of the ring with a spatial resolution of 1 cm. The spatial resolution would have been only 1m had we used time-domain technology. Moreover, the perimeter was only 50 cm, so time-domain technology could not have been employed in this case. Figure 9.13 shows the strain distribution obtained along the ring surface [20].

Dynamic Strain Measurement

Next we attempted a dynamic strain measurement using our technology, namely, continuous wave (CW) technology, which gave us a lot of power. If we used a pulse, the power would have been very small so we had to accumulate a number of pulses.

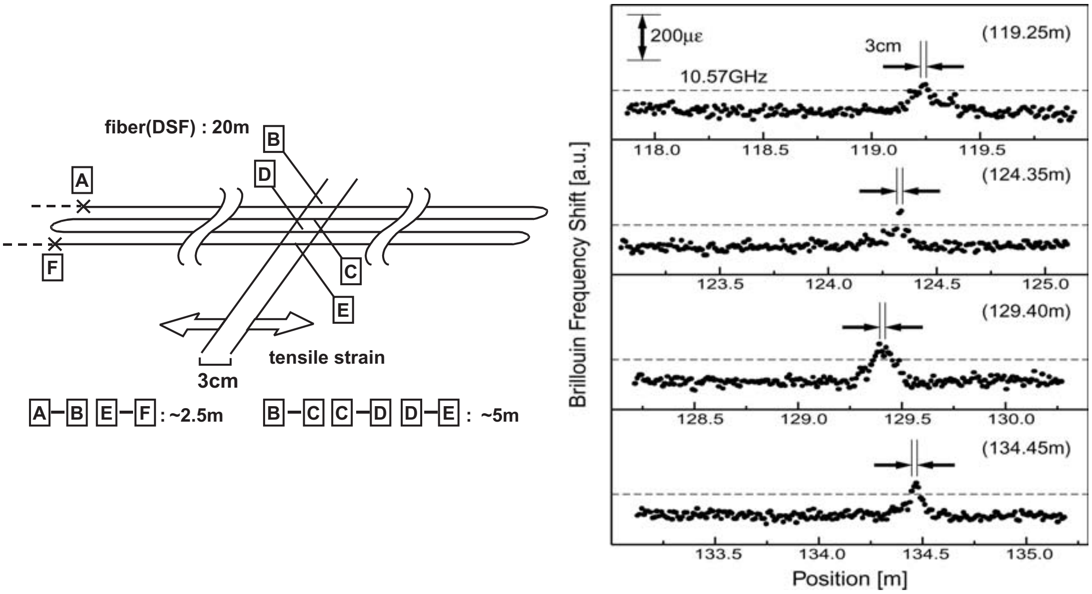

Figure 9.11 Measurement range enhancement [15, 17].

It took 1 or 2 minutes to obtain the required information, which means that time domain technology did not work for dynamic strain measurement, though we were able to use a CW technique.

By using a piezoelectric actuator and pulling and pushing the fiber dynamically, we obtained the Brillouin spectrum shape over time, as shown in Figure 9.14 [21, 22]. The peak frequency gave us information on the strain. When we vibrated the fiber with the piezoelectric devices there was sinusoidal vibration in the time domain. This frequency gave us information on the portion at which we applied the strain. The vibration frequency was 0.1 Hz, and the sampling rate was 2 Hz. Currently, we are using equipment with a sampling rate of 55 Hz, which is 10^4 higher than with conventional time domain technology [23].

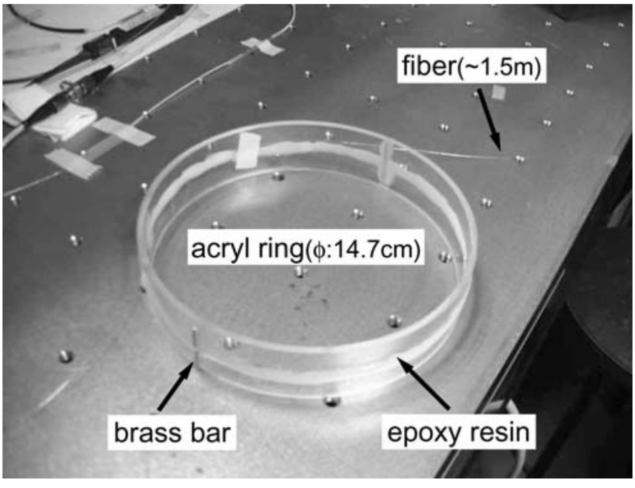

Figure 9.12 Application to smart materials [20].

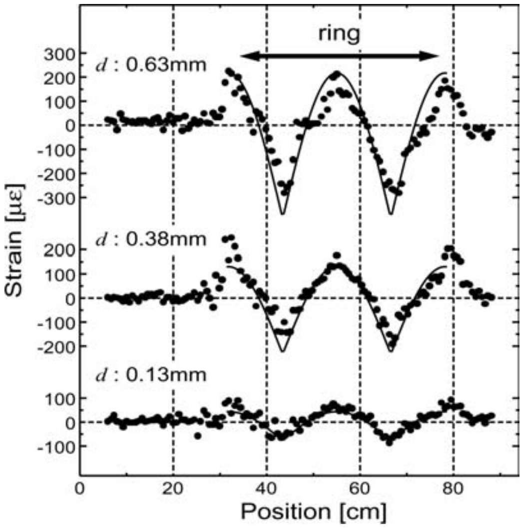

Figure 9.13 Strain distribution measurement along the surface of a ring structure [20].

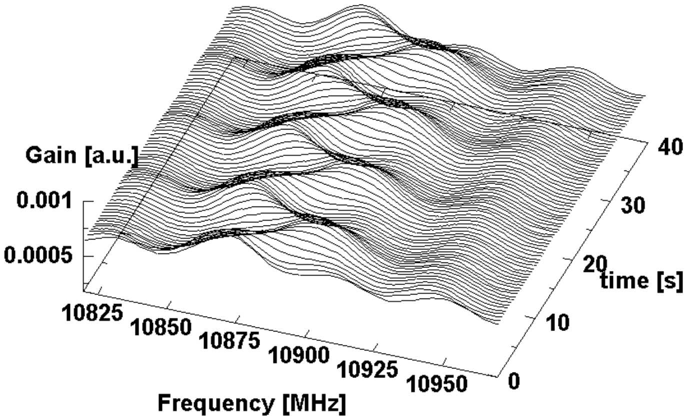

Figure 9.14 Dynamic strain measurement by BOCDA [21, 22].

We now have a rather high sampling rate, and this technique has a random access function along the fiber. In the experiment shown in Figure 9.15, we demonstrated three point multiplexed dynamic strain sensing [24]. With a sampling rate of around 30 Hz, we applied 10 Hz to three points and we found that there was dynamic vibration at a particular portion of the fiber, as shown in Figure 9.15 (right). We then employed a rather high sampling rate, namely 15 Hz, for the vibrating portion, as shown in Figure 9.15 (left). Such changes can be easily made because we are using dynamic random access function technology.

We obtained a very good S/N ratio and we can expect to have an increasingly higher sampling rate, which we tried to demonstrate. We realized the full measurement capability; that is, we measured the full spectrum and obtained the peak frequency. However, we do not need to have the full spectrum shape to obtain the

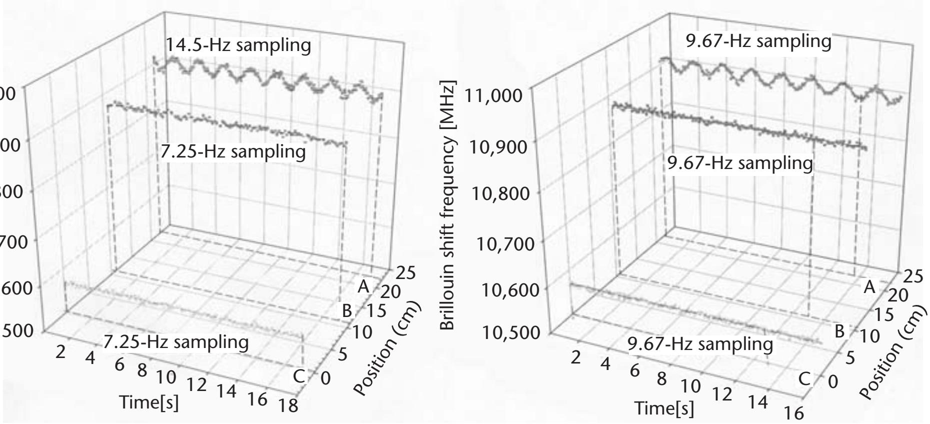

Figure 9.15 Multipoint random access measurement [24].

vibration itself. In the example shown in Figure 9.16, we fixed the frequency, and the amplitude of the Brillouin scattering is obtained. This easy mode is sufficient to obtain the vibration of the fiber. We applied this measurement method and obtained a 2-KHz sampling rate [21, 22]. However, even with the 2-kHz sampling rate we clearly had a signal and no additional noise. I, therefore, believe that the inherent limitation of the sampling rate is beyond 10 kHz.

Demonstration of Smart Materials and Smart Structures

Figure 9.17 shows an application of our higher spatial resolution distributed strain measurement [25]. This work was undertaken with the Shimizu Corporation. We used steel reinforced concrete and we created a weak plane by adding a further layer of concrete. Finally, we applied a force so that the block would crack. To detect the

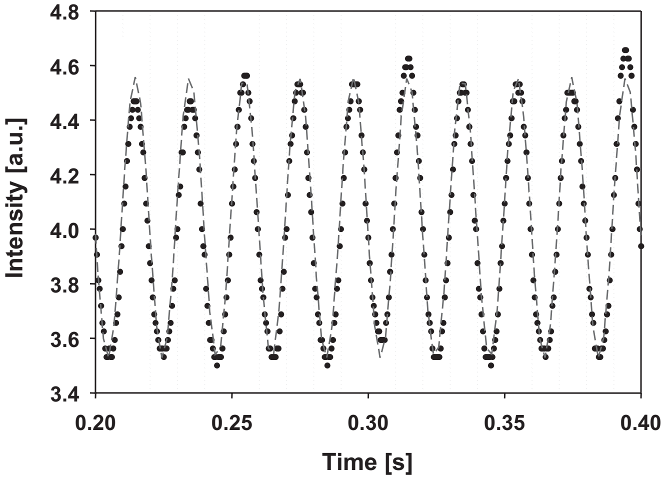

Figure 9.16 Measurement of Brillouin intensity at 2-kHz sampling rate [21, 22].

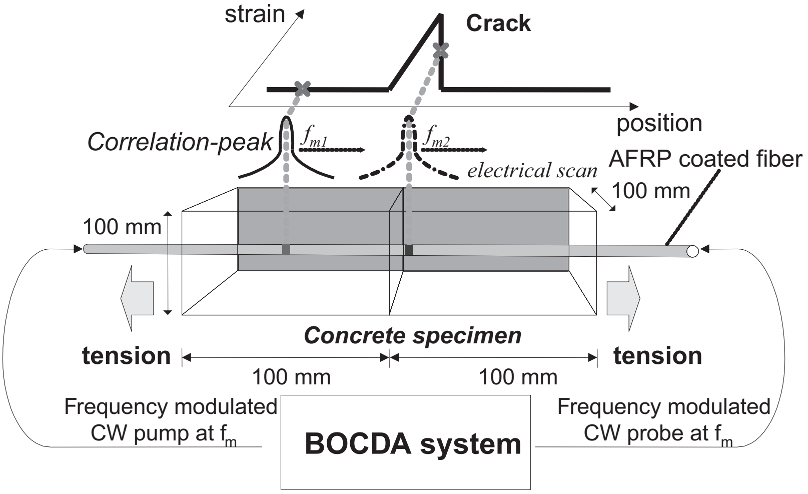

Figure 9.17 Crack detection in concrete [25].

crack we installed a fiber and employed our BOCDA system. Figure 9.18 shows the data we obtained [25]. When we pulled on the two portions of concrete a crack appeared. As the crack grew, the distributed strain also grew. We clearly detected the crack location with a spatial resolution of approximately 1.5 cm. Time domain technology could not supply this kind of data.

By the integration of the strain along the fiber portion, we can obtain the crack width. Figure 9.19 shows the crack width measured with another scheme and the

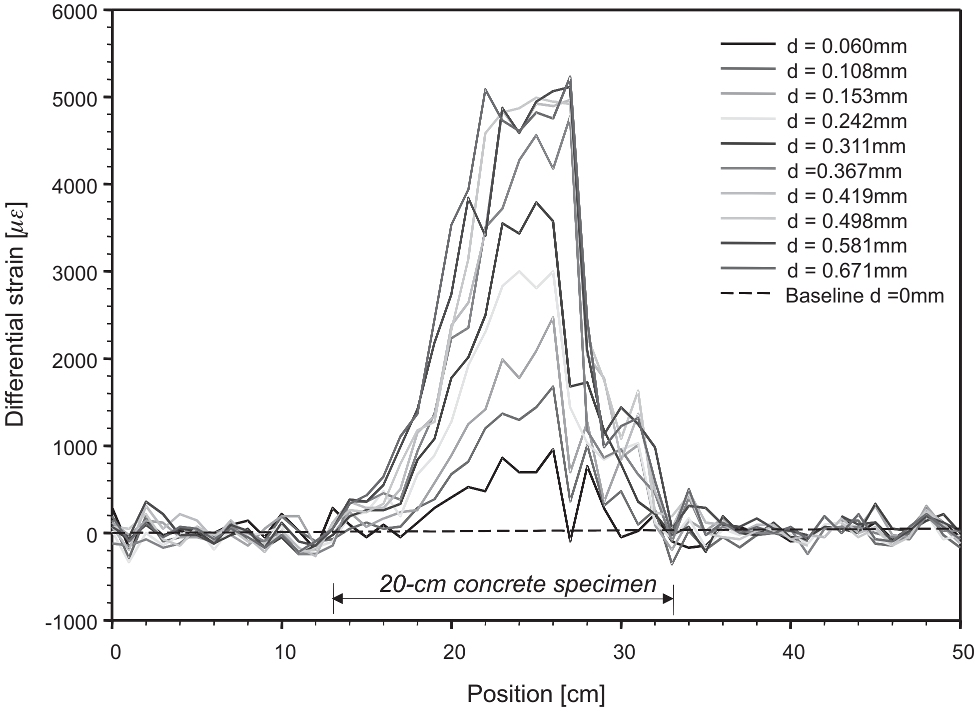

Figure 9.18 Distributed strain profile along a crack induced in concrete [25].

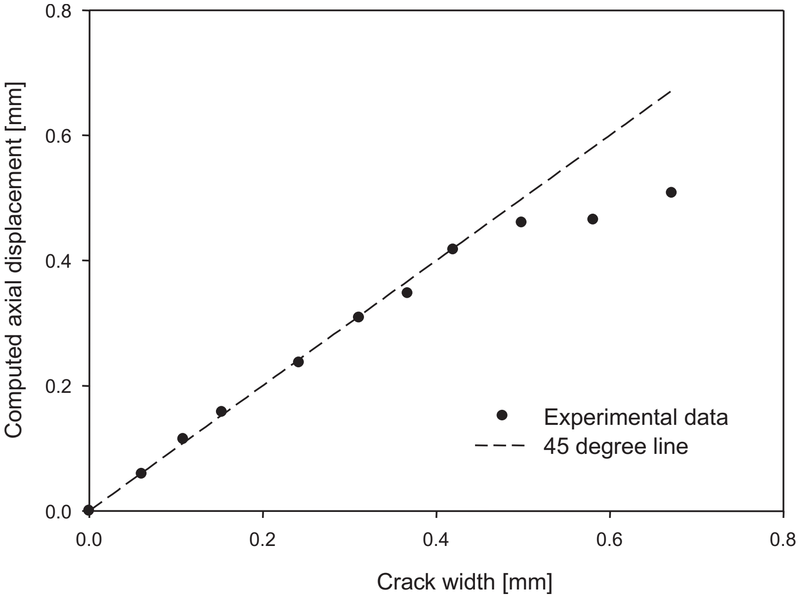

Figure 9.19 Crack width measured using BOCDA [25].

integration of this result with the previous data [25]. The figure also shows their linear relationship.

Civil engineers have stated that if we have a 0.3-mm wide crack, rainwater can penetrate the concrete and distort the steel, leading to a dangerous situation. It was therefore important to determine whether or not we could detect a 0.3-mm wide crack. Because our system can obtain such information, this technique could be applied to the health monitoring of concrete structures.

We then applied dynamic strain measurement to the small building-type structure shown in Figure 9.20 [26]. This experiment was undertaken with the Kajima Corporation. The height of the structure was just 50 cm and it was equipped with sensing fiber. Figure 9.21 shows the static strain distribution along the fiber [26]. There was not a steep change in the strain distribution. This was not due to the lack of spatial resolution, but rather, to the toughness of the materials at the joint and edge portions. Next, we applied the vibration to the small building. We employed the shape of the Hakuta earthquake, which was loaded in our computer and then used to shake the vibration machine. At the bottom of Figure 9.20, we have the vibration machine. Large buildings have an Eigen vibration frequency and a high building has a typical value of 1 or 2 Hz. The fundamental vibration frequency of this model is just 1.5 Hz and the second vibration is 3 Hz.

Figure 9.22 shows data of the dynamic strain measurement [26]. The data in black dots were obtained by using optical fiber technology; the data in dashed-wave were obtained with an electronic strain gauge. The two sets of data are in good agreement. The figure also shows that the dominant vibration frequency is 3 Hz. The Hakuta earthquake did not have a 1.5-Hz fundamental component. Nevertheless, the results obtained with the strain gauge and our optical way were in agreement.

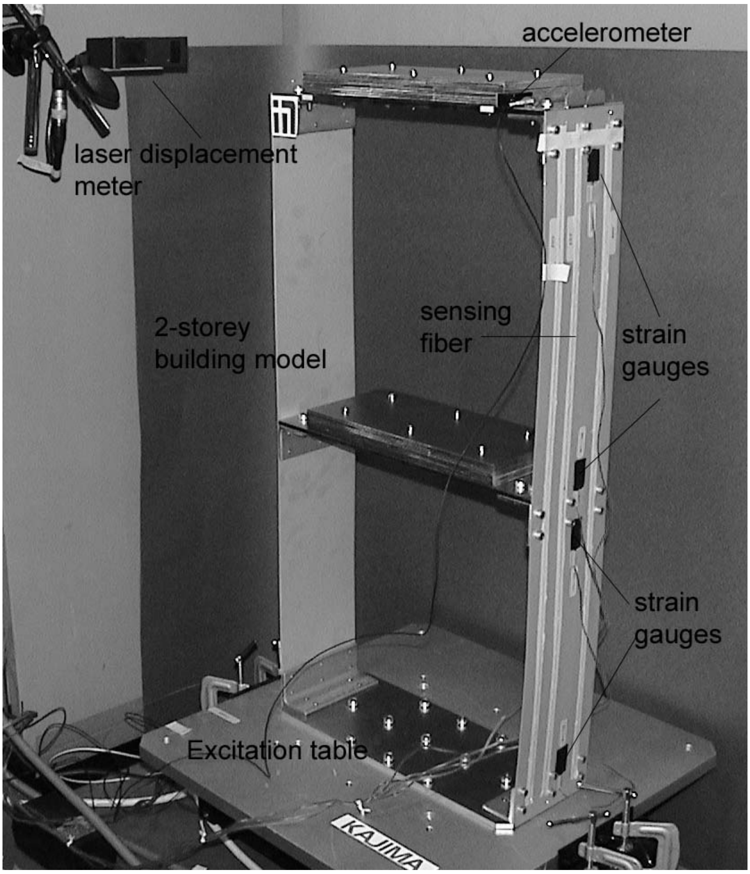

Figure 9.20 Dynamic strain measurement of a building model [26].

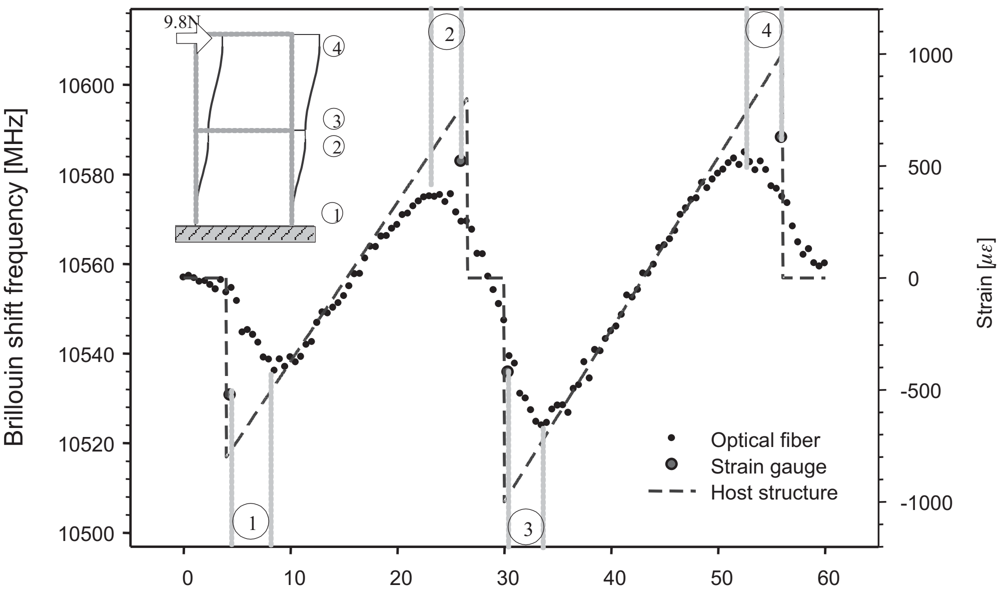

Figure 9.21 Static strain measurement along the building model [26].

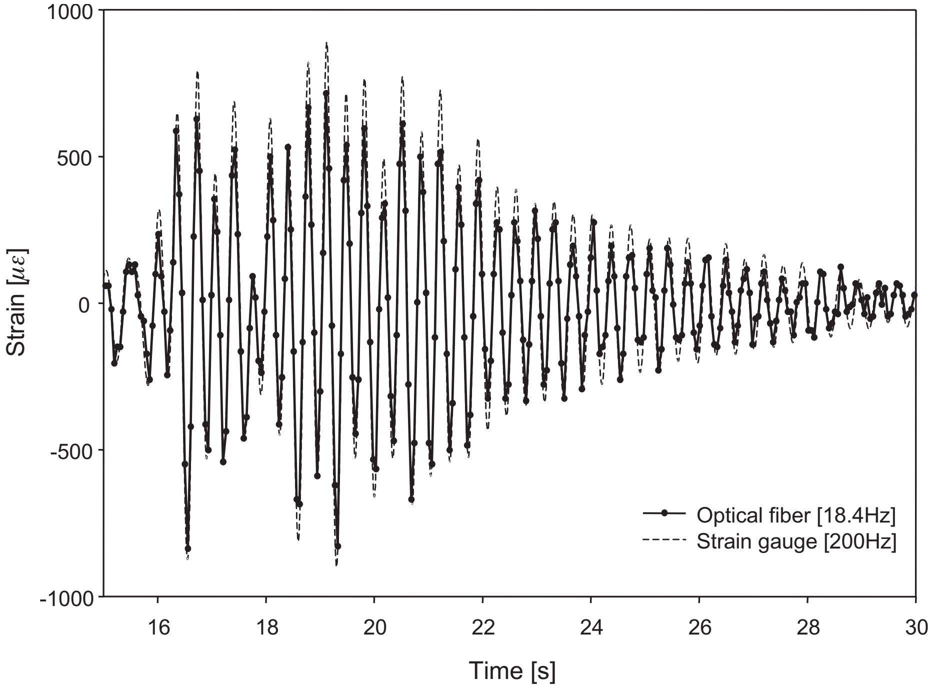

Figure 9.22 Dynamic strain measurement under the Hakuta earthquake vibration [26].

Distributed Fiber-Optic Force Sensing

By employing the synthesis of optical coherence function technology (CW technology) to obtain the distributed measurement function, we have created another way in which we can determine the force distribution along a fiber [27–30]. We then applied the technique to polarization maintaining fiber, and one polarization lightwave is excited at the end of the fiber, as shown in Figure 9.23. If there is stress at some point we have orthogonal polarization. The two orthogonal polarization modes have different propagation speeds. Then, at the end of the fiber, these two polarization components will have a propagation length difference. Therefore, by synthesizing the optical coherence function we can determine the strain location. For example, we can obtain the data shown in top of the figure by creating a delta function-like coherence peak and scanning it. This figure shows a 1-km length of fiber and stress was applied to several portions [27]. This approach can be used to measure the lateral force distribution. However, in this case the spatial resolution was only 9m. To improve this we must strengthen the tunability of the light source. Therefore, a wide tunable light source is needed to obtain a higher spatial resolution [28].

NTT collaborated with us in this endeavor and kindly lent me a super structure grating distributed Bragg reflector (SSG DBR) laser diode. This has 5-THz tunability. However, the tunability was not continuous but step-by-step. Nevertheless, this was sufficient for our application, because with the synthesis of optical coherence function technology we can use either continuous frequency tuning or discrete step-by-step frequency tuning. By using this technique, we have already realized a spatial resolution of 20 cm, as shown in Figure 9.24 [31]. This corresponded to a spatial

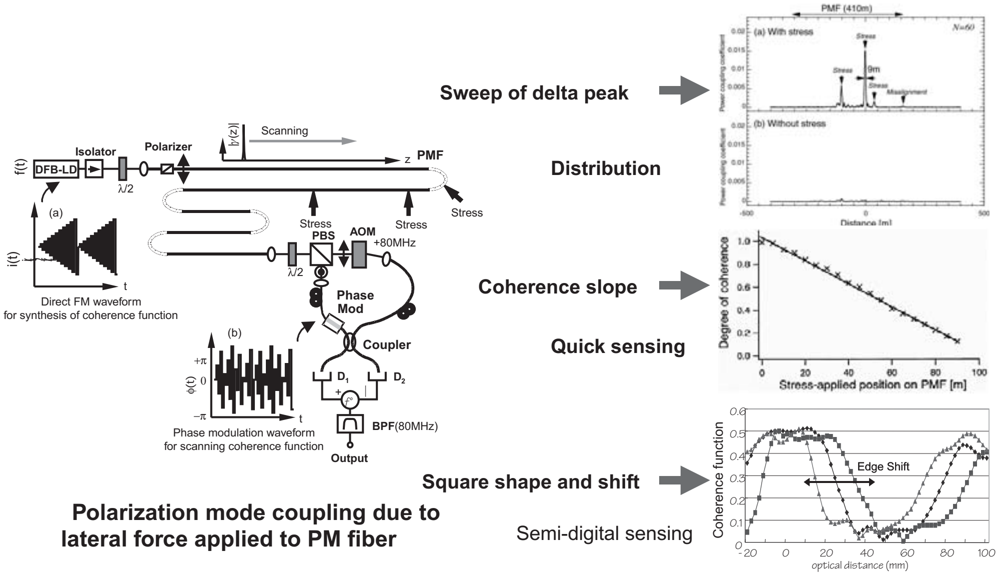

Flexible/ random access/ zooming/ variable resolution, etc.

Figure 9.23 Distributed force sensing by synthesis of optical coherence function [27–30].

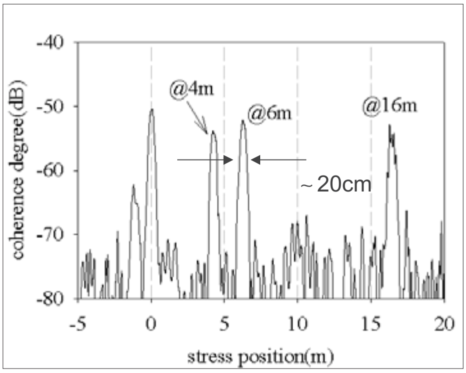

Figure 9.24 High-resolution PMF sensing results [31].

resolution of around 30 μm in the simple reflectometry. The propagation speed difference between the two modes is less than only 0.1%. This means the spatial resolution is decreased by a factor of 10^3.

We have already obtained a spatial resolution of 20 cm. This is a good value because the length of a burglar's foot is about 20 cm, which means that we can apply the system for security purposes.

Reflectometry for FTTH

In addition, we have already developed the reflectometry for FTTH technology [32–35]. In the FTTH network we have a discrepancy of around 5 to 10 km from an

NTT office to an individual home. It is important to know the reflectivity distribution at the fiber end to monitor the health of the FTTH network. This would require a spatial resolution of several centimeters. Time domain technology is not the answer because its spatial resolution is insufficiently high. We therefore applied our synthesis of optical coherence function technology and have already obtained a 6-cm spatial resolution over a 5-km fiber, as shown in Figure 9.25 [32, 33].

FBG Multiplexed Sensing

Finally, I will describe another technique in which we use the fiber Bragg grating—this is called the multiplexed technique. Bragg grating multiplex sensing technology may sometimes be used, but to reduce the cost we would like to use exactly the same fiber Bragg grating. However, wavelength division multiplexing has been used. We can obtain position information on the wavelength division multiplexing technology. However, in such cases various kinds of FBGs are required, which makes the cost high. For this reason, we would like to use exactly the same FBG. However, in such cases we cannot use wavelength division multiplexing, so here we also apply the synthesis of optical coherence function technology.

Figure 9.26 shows the interferometer [36, 37]. The lightwaves reflected at FBG's have interfered with the reference lightwave. By modulating the lightwave frequency in an appropriate waveform, we can synthesize a delta-function-like coherence peak. In such a case, only the reflected lightwave from one FBG interferes with the reference. Therefore, we can select only one strain gauge by the synthesis of optical coherence function technology.

We then change the center frequency of the laser diode and obtain the back reflection spectrum of the fiber Bragg grating as shown in Figure 9.27 [36]. The peak frequency gives us information on the applied strain in the fiber Bragg grating. If we apply strain to the fiber Bragg grating, the center frequency shifts as shown in

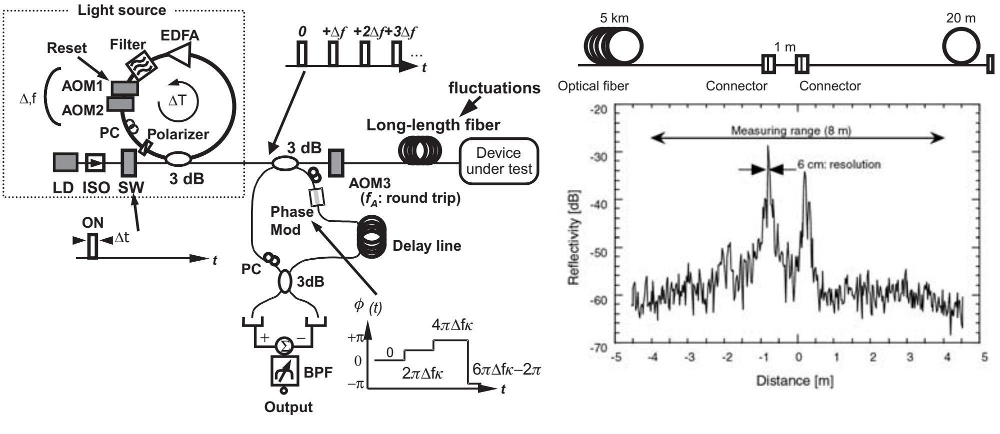

(a) Synthesis Configuration

(b) 6 cm resolution at 5km distance

Figure 9.25 Reflectometry for fiber subscriber networks with cm resolution: (a) system configuration, and (b) 6-cm resolution at 5-km distance [32, 33].

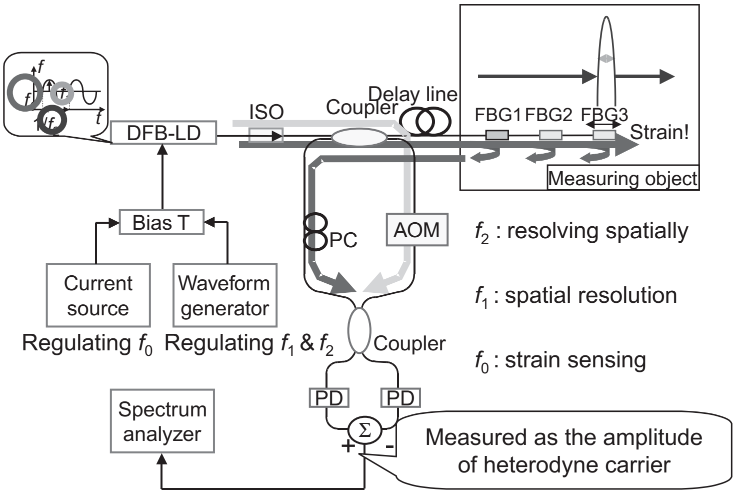

Figure 9.26 Multiplexing technique of FBG sensors with the same Bragg wavelength by SOCF [36, 37].

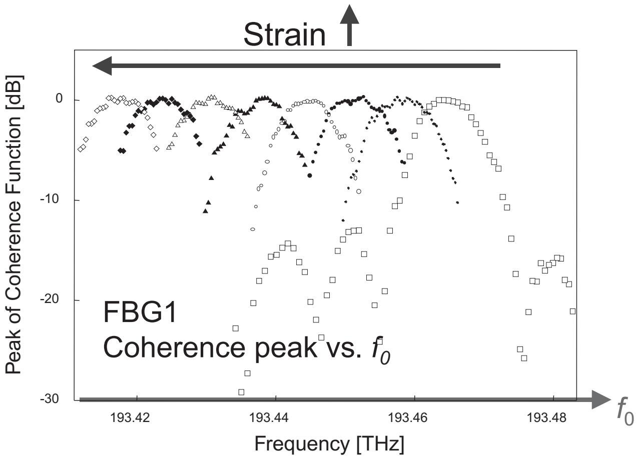

Figure 9.27 Strain sensing [36].

the figure. The strain and the wavelength shift have a linear relationship and we can obtain a 6-μm strain resolution.

Conclusion

In summary, our goal is to construct fiber-optic nerve systems with higher spatial resolution and a faster sampling rate. We have already obtained a spatial resolution of 1 cm and a sampling rate of 55 Hz, and these values are 100 times and 10^4 times higher than the conventional values, respectively. We obtained this function by using the continuous wave technique rather than the pulse-lightwave technique. Recently, we have started to create simplified systems to reduce the cost with keeping the performance [38].

This researche has been conducted under the support of the Grant-in-Aid for Specially Promoted Research from the Ministry of Education, Culture, Sports, Science and Technology in Japan, and is a theme in the 21st Century COE Program, also assigned by the ministry.

References

[1] Kersey, A., "Multiplexing Techniques for Fiber-Optic Sensors," in *Optical Fiber Sensors Vol. IV*, Dakin, J., and B. Culshaw, (eds.), Norwood, MA: Artech House, 1997, pp. 369–407.

[2] Horiguchi, T., et al., "Distributed Sensors: Recent Developments," in *Optical Fiber Sensors Vol. IV*, Dakin, J., and B. Culshaw, (eds.), Norwood, MA: Artech House, 1997, pp. 309–368.

[3] Hotate, K., "Fiber Sensor Technology Today," *Optical Fiber Technology*, Academic Press, March 1998, pp. 356–402.

[4] Hotate, K., T. Saida, and Z -Y. He, "Distribution Sensing by Synthesis of the Optical Coherence Function," *Intel. Conf. on Applied Optical Metrology,* Balatonfured, Hungary, June 1998, pp. 366–373.

[5] Hotate, K., Z -Y. He, and T. Saida, "Synthesis of Optical Coherence Function and Its Applications in Photonics Sensing," *Interferometry IX: Techniques and Analysis*, *SPIE Annual Meeting*, San Diego, CA, July 1998, pp. 254–265.

[6] Hotate, K., "Application of Synthesized Coherence Function to Distributed Optical Sensing," *IOP Measurement Science and Technol.,* Vol. 13, No. 11, November 2002, pp. 1746–1755.

[7] Thévenaz, L., "Distributed Deformation Sensors," in *Trends in Optical Non-Destructive Testing and Inspection*, P. Rastogi and D. Inaudi, (eds.), New York: Elsevier, 2000, pp. 447–458.

[8] Bao, X., et al., "Tensile and Compressive Strain Measurement in the Lab and Field with the Distributed Brillouin Scattering Sensor," *J. of Lightwave Technology*, Vol. 19, No. 11, November 2001, pp. 1698–1704.

[9] Hotate, K., and T. Hasegawa, "Measurement of Brillouin Gain Spectrum Distribution Along an Optical Fiber with a High Spatial Resolution Using a Novel Correlation-Based Technique—Demonstration of 45cm Spatial Resolution," *Proc. Intern. Conf. on Optical Fiber Sensors (OFS-13)*, Kyongju, Korea, April 1999, pp. 337–340.

[10] Hotate, K., and T. Hasegawa, "Measurement of Brillouin Gain Spectrum Distribution along an Optical Fiber Using a Correlation-Based Technique—Proposal, Experiment and Simulation," *IEICE Trans. on Electron.,* Vol. E83-C, No. 3, March 2000, pp. 405–412.

[11] Hasegawa, T., and K. Hotate, "Measurement of Brillouin Gain Spectrum Distribution along an Optical Fiber by Direct Frequency Modulation of a Laser Diode," *Proc. SPIE Fiber Optic and Laser Sensors and Applications*, Vol. 3860-44, Boston, MA, September 1999, pp. 306–316.

[12] Hotate, K., and T. Hasegawa, "A Correlation-Based Continuous-Wave Technique for Measuring Brillouin Gain Spectrum Distribution along an Optical Fiber with Centimeter-Order Spatial Resolution," *Proc. Intern. Conf. on Optical Fiber Sensors (OFS-14)*, Venice, Italy, Vol. Fr2-1 (part II), October 2000, pp. 651–661.

[13] Hotate, K., and M. Tanaka, "Distributed Fiber Brillouin Strain Sensing with 1 cm Spatial Resolution by Correlation-Based Continuous Wave Technique," *Proc. Intern. OFS-14,* Venice, Italy, Vol. Fr2-1 (part I), October 2000, pp. 647–650.

[14] Hotate, K., and M. Tanaka, "High-Resolution Distributed Fiber Brillouin Strain Sensing," in *Proc OECC/IOOC 2001 Conf.*, Sydney, July 2001, pp. 271–274.

[15] Hotate, K., and M. Tanaka, "Correlation-Based Continuous Wave Technique for Fiber Brillouin Distributed Strain Sensing for Smart Materials with cm Order Spatial Resolution," *Proc. CLEO/Pacific Rim 2001,* Chiba, Japan, Vol. TuG4-1, July 2001, pp. I-496–497.

[16] Hotate, K., and M. Tanaka, "Correlation-Based Continuous-Wave Techniques for Distributed Fiber Optic Sensing with a High Spatial Resolution," *Proc. SPIE OE Magazine*, Vol. 11, November 2001, pp. 36–40.

[17] Hotate, K., and M. Tanaka, "Correlation-Based Continuous-Wave Technique for Optical Fiber Distributed Strain Measurement Using Brillouin Scattering with cm-Order Spatial Resolution—Applications to Smart Materials," *IEICE Trans. on Electronics*, Vol. E84-C, No. 12, December 2001, pp.1823–1828.

[18] Hotate, K., and M. Tanaka, "Distribution Fiber Brillouin Strain Sensing with 1 cm Spatial Resolution by Correlation-Based Continuous-Wave Technique," *IEEE Photonic Technology Letters*, Vol. 14, No. 2, February 2002, pp. 179–181.

[19] Kannou, M., S. Adachi, and K. Hotate, "Temporal Gating Scheme for Enlargement of Measurement Range of Burillouin Optical Correlation Domain Analysis for Optical Fiber Distributed Strain Measurement," *Proc. OFS-16*, Nara, Japan, Vol. We3-1, October 2003.

[20] Tanaka, M., and K. Hotate, "Application of Correlation-Based Continuous-Wave Technique for Fiber Brillouin Sensing to Measurement of Strain Distribution on a Small Size Material," *IEEE Photon. Technol. Lett.*, Vol. 14, No. 5, May 2002, pp. 675–677.

[21] Hotate, K., and S. S. L. Ong, "Distributed Fiber Brillouin Strain Sensing by Correlation-Based Continuous-Wave Technique—cm-Order Spatial Resolution and Dynamic Strain Measurement," *Proc. SPIE Photonics Asia*, Shanghai, China, Vol. 4920-51, October 2002, pp. 299–310.

[22] Hotate, K., and S. S. L. Ong, "Distributed Dynamic Strain Measurement Using a Correlation-Based Brillouin Sensing System," *IEEE Photon. Technol. Lett.,* Vol. 15, No. 2, 2003, pp. 272–274.

[23] Ong, S. S. L., and K. Hotate, "Dynamic Strain Measurement at 50Hz Using a Brillouin Optical Correlation Domain Analysis Based Fiber Optic Sensor," *Proc. CLEO/Pacific Rim 2003*, Shanghai, China, December 2003.

[24] Ong, S. S. L., and K. Hotate, "Correlation-Based Brillouin Optical Sensor for Dynamic Strain Monitoring," *Proc. CLEO/QELS 2003*, Baltimore, MD, June 2003.

[25] Ong, S.S.L., et al., "Crack Detection in Concrete Using a Brillouin Optical Correlation Domain Analysis Based Fiber Optic Distributed Strain Sensor," *Proc. Intern. Conf. on Optical Fiber Sensors (OFS-16),* Nara, Japan, Vol. We3-3, October 2003, pp. 462–465.

[26] Ong, S. S. L., et al. "Dynamic Strain Measurement and Damage Assessment of a Building Model Using a Brillouin Optical Correlation Domain Analysis Based Distributed Strain Sensor," *Proc. OFS-16*, Nara, Japan, Vol. We3-2, October 2003, pp. 458–461.

[27] Saida, T., and K. Hotate, "Distributed Fiber Optic Stress Sensor by Synthesis of the Optical Coherence Function," *IEEE Photon. Technol. Lett.,* Vol. 9, No. 4, 1997, pp. 484–486.

[28] He, Z.-Y., and K. Hotate, "Distributed Fiber Optic Stress Sensing by Arbitrary Shaping of Optical Coherence Function," *Jour. of Lightwave Technol.*, Vol. 20, No. 9, 2002, pp. 1715–1723.

[29] Hotate, K., X. Song, and Z.-Y. He, "Stress-Location Measurement Along an Optical Fiber by Synthesis of Triangle-Shape Optical Coherence Function," *IEEE Photon. Technol. Lett.*, Vol. 13, No. 3, 2001, pp. 233–235.

[30] Hotate, K., A. Kuramoto, and Z. He, "Stress-Location Measurement Along an Optical Fiber by Synthesis of Rectangular-Shaped Optical Coherence Function," *Proc. Intern. OFS-14*, Venice, Italy, Vol. P3-29, October 2000, pp.796–799.

[31] Hotate, K., and K. Makino, "High Spatial Resolution Fiber Optic Distributed Force Sensing with Synthesis of Optical Coherence Function," *Proc. SPIE Photonics East*, Vol. 5272-23, October 2003.

[32] Saida, T., and K. Hotate, “High Spatial Resolution Reflectometry by Synthesis of Optical Coherence Function for Measuring Reflectivity Distribution at a Long Distance,” *IEEE Photon. Technol. Lett.,* Vol. 10, No. 4, 1998, pp. 573–575.

[33] Saida, T., and K. Hotate, “High Resolution Reflectometry for Measuring Optical Devices at a Long Distance by Synthesis of Optical Coherence Function Using Optical Loop with Frequency Shifter,” *Proc. IOOC/ECOC’97*, Edinburgh, Scotland, September 1997, pp. 283–286.

[34] Hotate, K., and M. Kashiwagi, “High Spatial Resolution Reflectometry for Optical Subscriber Networks by Synthesis of Optical Coherence Function with Measurement Range Enhancement,” *IEICE Trans. on Electron.,* Vol. E86-C, No. 2, 2003, pp. 213–217.

[35] Kashiwagi, M., and K. Hotate, “Measurement Range Elongation in a High Spatial Resolution Reflectometry for Optical Subscriber Networks by Synthesis of Optical Coherence Function,” *Proc. OFS-16,* Nara, Japan, Vol. We1-4, October 2003, pp. 270–273.

[36] Hotate, K., et al., “High Density Multiplexing Technique of Fiber Bragg Grating Sensors by Synthesis of Optical Coherence Function,” *Proc. SPIE Photonics Asia*, Shanghai, China, Vol. 4920-48, October 2002, pp. 285–294.

[37] Hotate, K., and M. Enyama, “Dynamic Strain Measurement by FBG Sensing System with Synthesis of Optical Coherence Function,” *Proc. OFS-16*, Nara, Japan, Vol. Th1-2, October 2003, pp. 522–525.

[38] Hotate, K., and T. Yamauchi, “Simplified System of Fiber Brillouin Optical Correlation Domain Analysis for Distributed Strain Sensing,” *Proc. OFS-16*, Nara, Japan, Vol. We2-3, October 2003, pp. 290–293.

CHAPTER 10

A Near-Field Sensing Transceiver for Intrabody Communications

Mitsuru Shinagawa
NTT Microsystem Integration Laboratories

Introduction

As personal digital assistants (PDAs), digital audio devices, digital cameras, and other information and communication devices become smaller and more widespread, there are increasing opportunities for people to come in contact with many small computers in their everyday lives (Figure 10.1). The process of miniaturization will continue, and we will soon see the emergence of the so-called ubiquitous computing environment, where, ideally, many computers will serve each person everywhere in the world [1]. For ubiquitous computing to be implemented in a comfortable and useful way, it is essential that we are able to share data not only among our own personal computers but also among environmental computers. Wire connections are clearly impractical because they so easily become tangled, so some sort of short-range wireless communications technology is required. A number of short-range wireless schemes have been considered, most of which are based on the Bluetooth and IEEE 802.11 standards. However, these radio-wave-based methods are susceptible to interference. One solution is intrabody communications [2], which use the human body as the transmission medium. The unique features of intrabody communications are that data can be exchanged by natural actions, such as touching or stepping, and the person is clearly aware of connection. Mobile computers can be intentionally connected with environmental devices

Some intrabody communications systems using small voltages [2–5], or currents [6] applied to and detected by the human body have been reported. Drawbacks in all recent systems are a short operating range and low speed, because the receivers detected signals using FET devices. Basically, a FET device needs an earth ground. However, the earth ground is floating in the reported intrabody communications system. As a result, the FET does not work correctly, and the detection bandwidth is degraded. In addition, the input impedance of the FET device is not very high, so the FET disturbs the electric field on the human body. As a consequence, the typical operating range is only about 30 cm and the speed is limited to about 40 Kbps.

We have been researching electric-field sensors using an electro-optic (EO) crystal and laser light, which we have applied in the development of probing systems

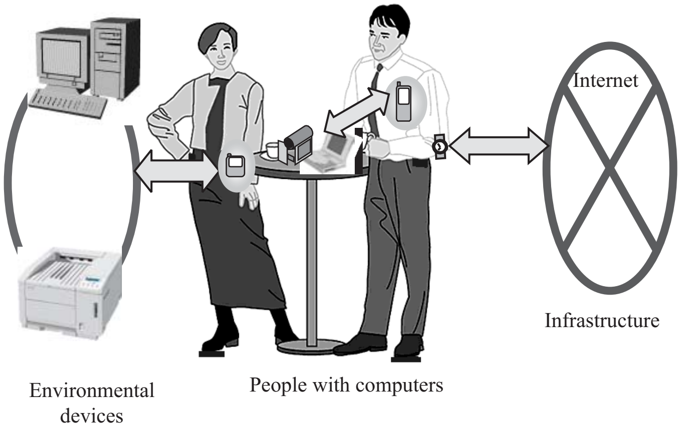

Figure 10.1 Living space with many computers.In addition, data transmitted through the human body eventually escapes through the feet into the ground, thus minimizing the chance of intercept and thereby providing secure transmissions.

[7–9] for ultrafast electronics. Because our EO sensor has extremely high input impedance and ultrawide detection bandwidth, it is especially useful for accurate detection of small and high-speed electric fields. Recently, we developed a near-field-sensing transceiver using the EO sensor for intrabody communications. We achieved the first successful 10-Mbps half-duplex communications through the human body at an operating range of about 150 cm between the hands, as stipulated by IEEE 802.3.

We also confirmed intrabody communications through clothes and interbody communications between two persons by a handshake. In this chapter, we describe the configuration of the transceiver and the electric-field sensor unit in detail and present results of a communications test.

Near-Field-Sensing Transceiver

Electric-Field Model

Typical applications of intrabody communications are illustrated in Figure 10.2. In one, a person might wear several wearable computers, such as a PDA, head-mounted display, and data storage device, and data could be exchanged among them. In another, two people could exchange personal data with a handshake, which would mean they wouldn't have to exchange business cards. In a security system, one could touch a sensor or a doorknob to transmit ID data, and the door would unlock automatically. Then there is the idea of covering a table with an electric field transmission medium. One could just put a personal computer on the table, and the computer would be connected to the network.

Figure 10.3 depicts a model of the electric near field produced by the human body [2]. The electric field, E_a, induced by a signal electrode of a transmitter passes through the human body and flows toward the ground. It is necessary to detect E_s, the electric near field around the human body, for intrabody communications. However, E_s is extremely small, because a part of it, E_a, is canceled out in the human body by electric field E_b generated from the ground electrode of the transmitter, and

Wearable computers

Exchange personal data

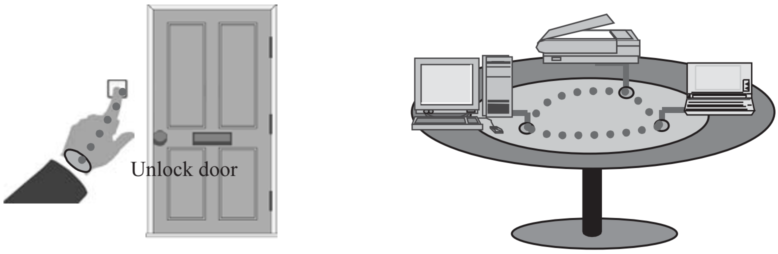

Security system

Tabletop network

Figure 10.2 Application of intrabody communications.

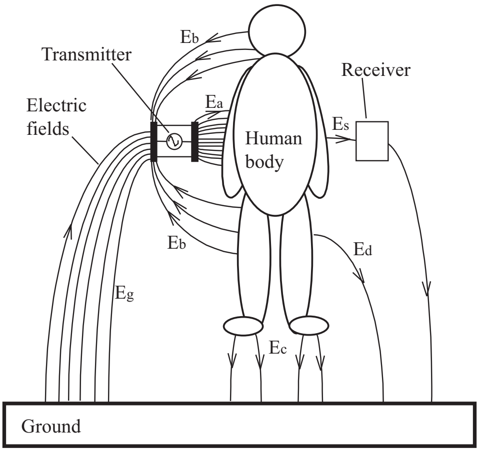

Figure 10.3 Electric field model.

because a lot of the electric field, E_c, escapes through the feet, which are in direct contact with the ground. The electric near fields would be subject to change as a result of a person's movement.

Electric-Field-Sensor Unit

The principle of the EO sensor is shown in Figure 10.4. The electric fields are coupled with the EO crystal, and the refractive index of the crystal changes. When the laser light passes through the crystal, the polarization of the laser light is changed by means of the strength of the electric fields. We have developed various EO probing

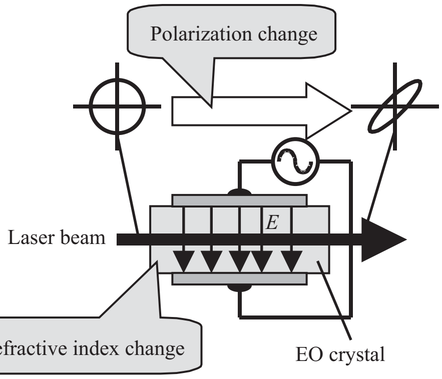

Figure 10.4 Principle of EO sensor.

systems for internal-node measurement of ICs and printed circuit board measurement. Figure 10.5(a) shows a noncontact probing system for internal-node measurement of ultrahigh speed ICs. Figure 10.5(b) shows a contact-type microprobe system for internal-node measurement of LSIs. Figure 10.5(c) is a sampling oscilloscope for measuring waveforms on high-speed printed circuit board. Figure 10.5(d) shows a real-time handy probe that can be directly connected to conventional scopes.

A schematic of the electric-field sensor unit is shown in Figure 10.6. The unit is 48 × 14 × 9 mm. The sensor employs a transverse EO crystal (KTiOPO$_4$ (KTP), LiNbO$_3$, (110)-cut CdTe, (110)-cut ZnTe, or (110)-cut GaAs) sensitive to electric fields that are perpendicular to the laser light propagation. The transverse EO crystal easily extends the interaction time between fields and laser light when we increase the length of the crystal. In addition, the strength of electric fields coupled with the crystal becomes large by narrowing the distance between the signal and ground electrode. These result in high sensitivity, which allows the receiver to detect minute electric fields.

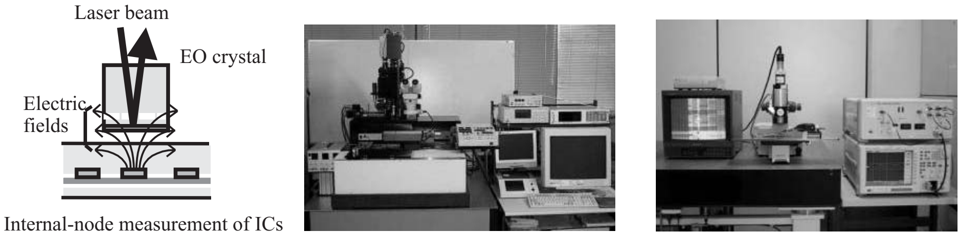

(a) Noncontact probing system

(b) Microprobe system

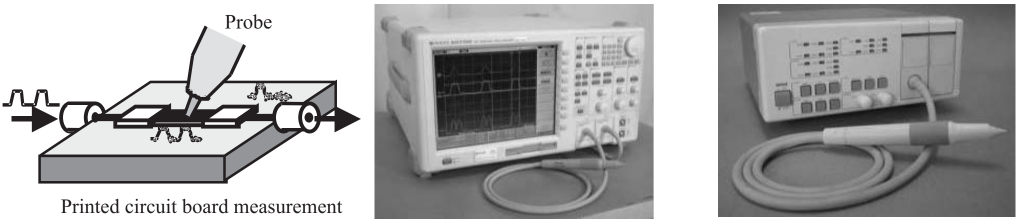

(c) Sampling oscilloscope

(d) Real-time handy probe

Figure 10.5 EO probing systems: (a) noncontact probing system; (b) microprobe system; (c) sampling oscilloscope, and (d) real-time handy probe.

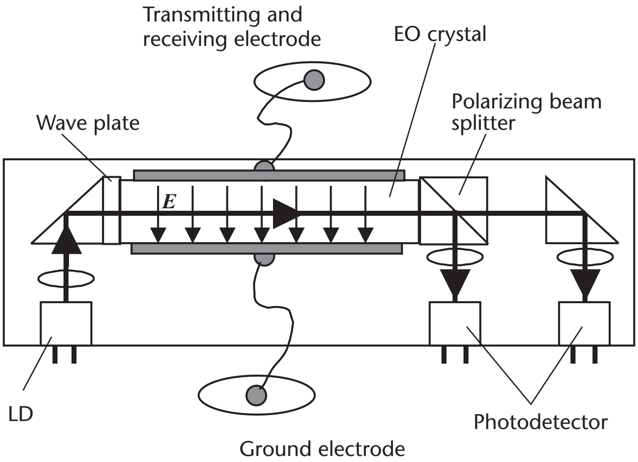

Figure 10.6 Electric-field sensor unit.

The electric fields produced by the human body are coupled with the EO crystal through the transmitting and receiving (TR) electrode, and the refractive index of the crystal changes. Then, when the laser light from a laser diode (LD) passes through the EO crystal, the polarization of the laser light is changed by means of the strength of the electric fields. The polarization change is converted into an intensity change by a polarizing beam splitter, and then converted to electric signals by two photodetectors. The EO crystal is insulated from the receiver electronics, so the sensor has an extremely high input impedance exceeding 100 MΩ [8].

Configuration of the Transceiver

The configuration of the transceiver is shown in Figure 10.7. The transmitter board consists of a transmitter circuit and a data sensing circuit. The data sensing circuit detects transmitted data and outputs the control signals needed for half-duplex communications. The receiver board consists of an amplifier, a band-pass filter, a peak-hold circuit, and two comparators. The signal from the electric-field sensor unit is amplified, and noise outside the detection bandwidth is eliminated by the band-pass filter. The output signal from the band-pass filter is divided into two signals. One is input to comparator 1 as data. The other is used as a control signal for packet extraction by the peak-hold circuit and comparator 2. Figure 10.8 shows typical waveforms of the receiver board. The center of the detected signal is analog ground level because the electric-field sensor does not respond to the low-frequency signals, including dc. The peak-hold signal is input to comparator 2, and the rectangular signal corresponding to the length of the packet is generated. The band-pass filter signal and the rectangular signal are input to comparator 1, which then generates received data.

A photograph of the inner board of the transceiver is shown in Figure 10.9. From the right, it consists of an electric-field sensor unit, a receiver board, and a transmitter board. It has a power consumption of 650 mW, and the power supply voltage is 5V. Figure 10.10 shows a photograph of the developed transceiver connected to a PDA with a network interface card. The transceiver is 15 × 55 × 80 mm.

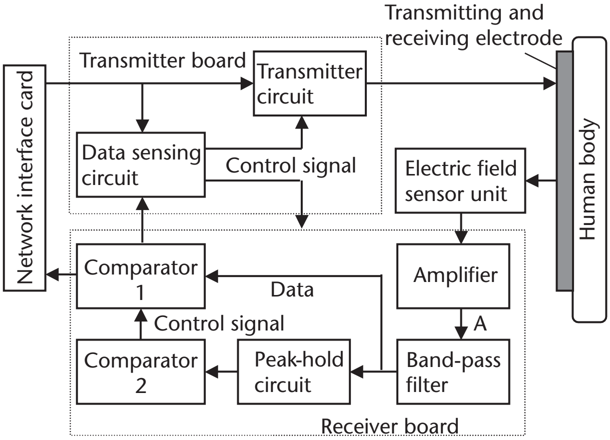

Figure 10.7 Configuration of the transceiver.

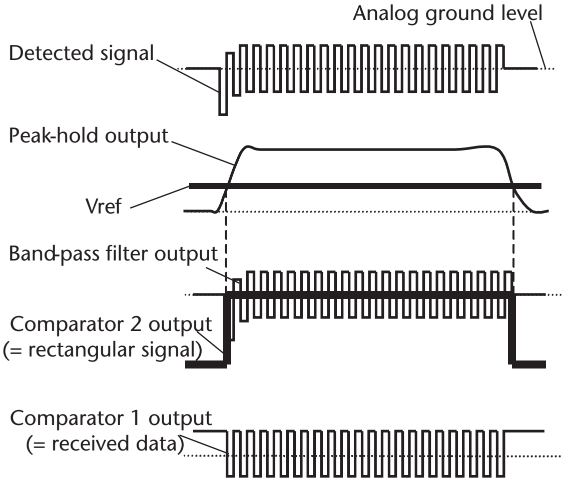

Figure 10.8 Typical waveforms of the receiver board.

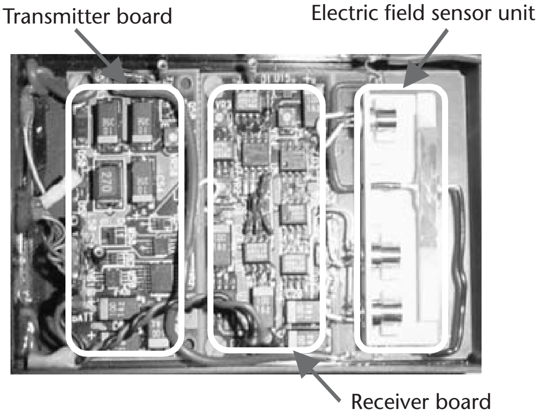

Figure 10.9 Photograph of the transceiver inner board.

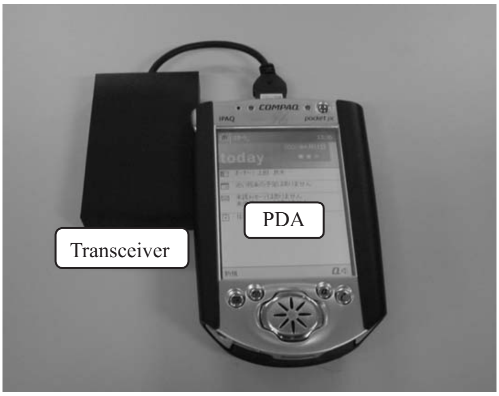

Figure 10.10 Photograph of the transceiver connected to a PDA.

Experimental Results

Waveform Estimation on Phantom Model

Before discussing the experimental results, we explain the ground issue in measurement of the transceiver. In general, an electrical high-impedance probe is widely used. If the probe and a ground wire are in contact with the receiver circuit, this creates another electrical path from the receiver circuit to the ground (Figure 10.11).

A lot of the electric field, E_p, escapes through the probe and the outlet, which is in direct contact with the ground, and E_s becomes large due to this electrical path. This produces incorrect results that could never be obtained when the transceiver would be used for a mobile device.On the other hand, the EO probe does not create such an electrical path because the probe head is insulated from the detection electronics of the scope, as mentioned before. The EO probe is therefore better for estimating the performance of such transceivers.

For the measurement, the transmitter generated signal of 10 Mbps [01010011], and the electrode of the transmitter was in contact with a phantom model. The phantom model was composed of polymeric materials to absorb water and hung in

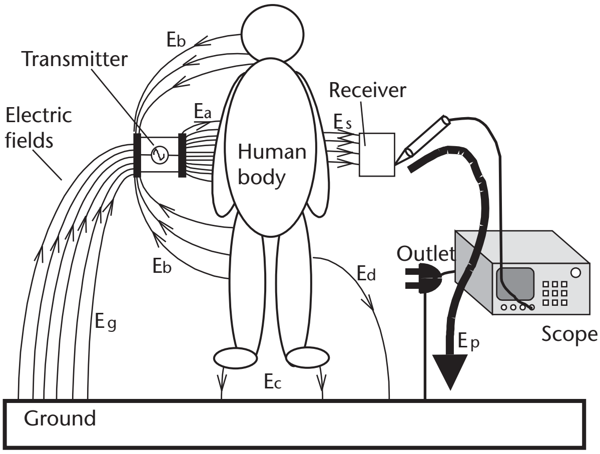

Figure 10.11 Ground issue in measurement of transceiver performance.

the air by insulated wires. It measured 150 cm × 15 cmϕ. The electrode of the receiver was about 1m from that of the transmitter. The waveform was measured at the output of the amplifier (see Figure 10.7).

To make the experiment more rigorous in consideration of transmission between two mobile computers in an actual situation, we employed battery-powered components, which were suspended in the air by insulated wires. The measured waveform is shown in Figure 10.12. When an old receiver using FET devices detected the signal, the waveform was severely distorted and 10-Mbps communications were difficult. Further, the waveform distortion varied depending on the position of the receiver electrode. Using our new receiver implemented with an EO sensor, we obtained a waveform whose quality is more than sufficient for 10-Mbps communications. It was also found that the waveform did not change very much by varying the position of the receiver electrode and that the quality of the waveform was preserved.

Intrabody Communication

The experimental setup is illustrated in Figure 10.13 (*HB1*). Each transceiver was connected to a PDA. All components were battery powered. One person touched the *TR* electrodes of the two transceivers with his right and left hand. As mentioned before, the transceivers and PDAs were suspended in the air by insulated wires. The *TR* electrode was covered with an insulating film so that the person could not touch the electrode directly. The transmitter circuit generated signal of 25V, but actually the induced voltage on the human body was less than 100 mV because the electrical load of the human body is so large that the transmitter circuit cannot drive it efficiently. We confirmed 10-Mbps (10BASE) half-duplex communications through the human body in the operating range of about 150 cm between the hands, as stipulated by IEEE 802.3. In addition, we verified intrabody communications through clothes without direct contact with the skin, and interbody communications as well by having two people shake hands while each touched the *TR* electrode of his transceiver with the free hand [Figure 10.14 (*HB2*)].

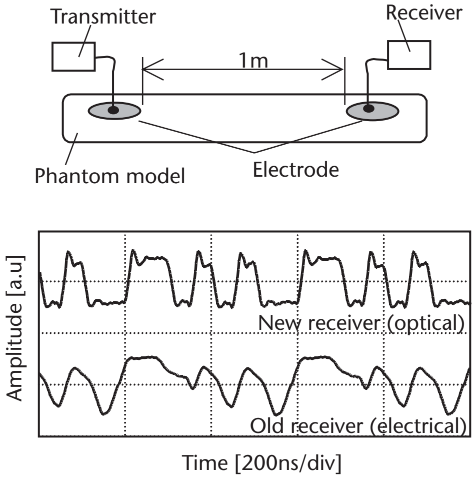

Figure 10.12 Waveform estimation of the receiver.

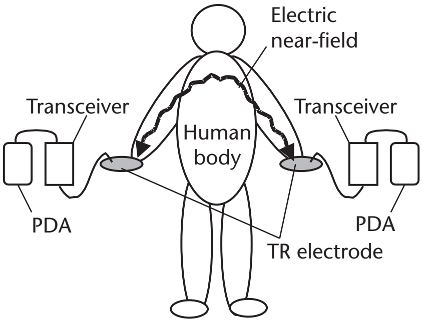

Figure 10.13 Experimental setup for intrabody communications (*HB1*).

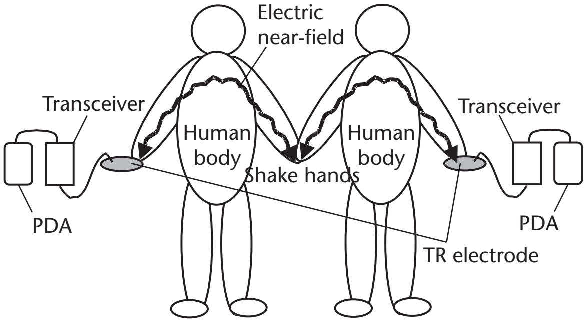

Figure 10.14 Handshake interbody communications (*HB2*).

Communications Test

The communications test was performed using three types of communications mediums: a conventional LAN cable (*UTP*), one person (see Figure 10.13, *HB1*), and two people (see Figure 10.14, *HB2*). A schematic diagram of the test packet transmission is shown in Figure 10.15. The number of packets transmitted from PDA 1 is *TP*. Error packets were generated by the noise from the transceiver circuit and by the degradation of the signal amplitude in the communication medium. Some of the packets disappeared due to error, and the remainder reached PDA 2. PDA 2 transmitted the response packet to PDA 1. In this case, some of the response packets disappeared due to error for the earlier-mentioned reason, and the remainder, *RP*, reached PDA 1.

The number of received success packets *RP* subtracted from *TP* was assumed to be the total number of error packets. The packet error rate (*PER*) is expressed as

$$PER = (TP - RP) / TP * 100 \ [\%]$$

The packet error rates are shown in Table 10.1.

The time interval of the transmitted packet was adjusted so that there were no collisions with other packets, and the *PER* of the *UTP* was 0%, which is the ideal case.

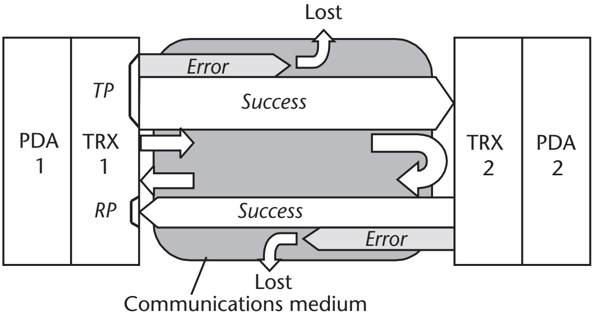

Figure 10.15 Schematic diagram of test packet transmission.

Table10.1 Packet Error Rates

Packet Size (Octets)	*UTP (%)*	*HB1 (%)*	*HB2 (%)*
560	0	0.03	3
1,070	0	0.04	3

The *PER* of *HB1* was about 0.04% or less, an excellent result. On the other hand, the *PER* of *HB2* was about 3%, indicating that it was difficult to communicate comfortably. Figure 10.16 shows the results for successful packets transmitted every second for one minute. There was no problem in *HB1*, whose results were similar to those of the *UTP*. However, *HB2* was unstable, and almost every packet was destroyed in the worst case as shown in the figure. We believe the reason for this is that the elect\ric coupling between the two people varied because of their movement.

Conclusion

We have developed a transceiver to achieve an intrabody communications system, which uses the human body as a data transmission medium. The receiver is an

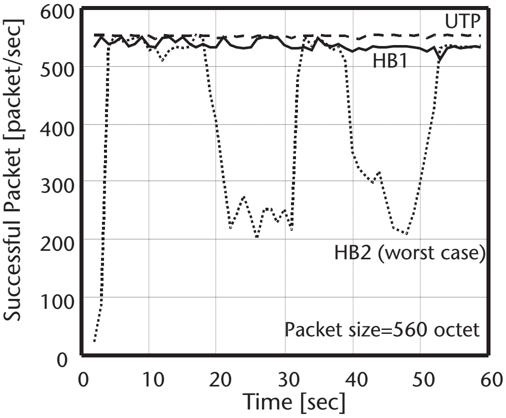

Figure 10.16 Change in the number of successful packets.

electric-field sensor implemented with an electro-optic crystal and laser light. Using this transceiver, we succeeded, for the first time, in 10BASE communications in accordance with IEEE 802.3 through the human body at an operating range of about 150 cm between the hands. The packet error rate was 0.04% in intrabody communications. Moreover, intrabody communications through clothes and interbody communications between two people by a handshake were also confirmed.

This transceiver will open the way for the incorporation of intrabody communications in a comfortable and useful ubiquitous computing environment. To improve the performance of the transceiver, we are now working to develop a high-sensitivity electric-field sensor, low-power transmitter and receiver circuits, and an efficient electric-field generating method.

Acknowledgments

The author is deeply indebted to M. Fukumoto, Y. Yanagisawa, K. Ochiai, A. Sasaki, T. Minotani, and N. Shibata for their useful discussions and comments. He greatly appreciates the assistance of T. Harada, K. Kamiyama, Y. Kato, Y. Ueda, T. Takizawa, and H. Asou for their help with the experiment. He also thanks H. Kyuragi, T. Sugimura, T. Nagatsuma, K. Machida, and S. Sudo for their useful comments.

References

[1] Weiser, M., "The Computer for the Twenty-First Century," *Scientific American*, September 1991, pp. 66–75.

[2] Zimmerman, T. G., "Personal Area Networks: Near-Field Intrabody Communication," *IBM Systems Journal*, Vol. 35, No. 3&4, 1996, pp. 609–617.

[3] Fukumoto, M., and Y. Tonomura, "Body Coupled FingeRing: Wireless Wearable Keyboard," *Proc. ACM CHI'97*, March 1997, pp. 147–154.

[4] Matsushita, N., et al., "Wearable Key: Device for Personalizing Nearby Environment," *Proc. Fourth International Symposium on Wearable Computers (ISWC'00),* 2000, pp. 119–126.

[5] Partridge, K., et al., "Empirical Measurements of Intrabody Communication Performance under Varied Physical Configurations," *Proc. ACM UIST*, 2001, pp. 183–190.

[6] Doi, K., et al., "Development of the Communication Module Used Human Body as the Transmission Line," *Proc. Human Interface Symposium 2001*, 2001, pp. 389–392 (in Japanese).

[7] Shinagawa, M., and T. Nagatsuma, "An Automated Electro-Optic Probing System for Ultra-High-Speed IC's," *IEEE Trans. Instrum. Meas.*, Vol. 43, No. 6, 1994, pp. 843–847.

[8] Shinagawa, M., and T. Nagatsuma, "A Novel High-Impedance Probe for Multi-Gigahertz Signal Measurement," *IEEE Trans. Instrum. Meas.,* Vol. 45, No. 2, 1996, pp. 575–579.

[9] Shinagawa, M., et al., "A Real-Time Electro-Optic Handy Probe Using a Continuous-Wave Laser," *IEEE Trans. Instrum. Meas.*, Vol. 50, No. 5, 2001, pp. 1076–1080.

CHAPTER 11

Millimeter-Wave Photonic Technologies for Communications and Sensor Applications

Tadao Nagatsuma
NTT Microsystem Integration Laboratories, NTT Corporation

Introduction

The recent explosive growth in communications has been brought about by optical (or fiber-optic) and wireless (or radio-wave) communications technologies. These two technologies have started to merge to create a new interdisciplinary area called microwave and millimeter-wave photonics [1, 2]. In addition, viewing the electromagnetic spectrum with wavelengths progressively decreasing to the millimeter and submillimeter-wave bands on the radio side [3, 4] and wavelengths progressively increasing to the infrared region on the optical side, we see that there is a large gap in utilization on the boundary between radio waves and light waves (i.e., the frequency band between 100 GHz and 10 THz). This untapped region represents a major resource for humankind in the twenty-first century. Millimeter-wave photonic technology aims at achieving advancement and improved functions in telecommunications systems that cannot be achieved by extension of individual technologies, mainly through the combination of radio-wave technology and photonic technology. At the same time, millimeter-wave photonic technology is also expected to open up unused frequency bands through the fusion of different fields. The opening of new application fields other than communications is also expected.

This chapter describes our research on millimeter-wave photonic technologies for communications and sensor applications. The second section provides a little background on this field, emphasizing the importance of interdisciplinary area between light waves and radio waves. The third section reviews recent progress in key-component technologies, such as ultrafast semiconductor lasers, photodiodes, and high-frequency signal generators. The fourth and fifth section cover possible applications of these components to future communications and sensors, presenting our preliminary results on ultrahigh-speed wireless links at a bit rate of over 10 Gbps and on the imaging of objects and galaxies with radio waves at frequencies of 100 GHz to 1 THz.

Light Waves and Radio Waves

Figure 11.1 shows the frequencies and wavelengths of the electromagnetic spectrum, and how they are being used. Since the epoch-making accomplishments of Marconi and Roentgen in 1895, the first successful radio-wave wireless communication and the discovery of X-rays, respectively, humankind has, over the twentieth century, become able to utilize most regions of the spectrum out to both extremes of radio waves and light waves. However, we can see that there is a large gap in the utilization at the boundary between radio waves and light waves (the frequency band between 100 GHz and 10 THz). This region is indeed a "spectral black hole." The field of study that deals with this region is also referred to as teraphotonics or terahertz optoelectronics. We believe that the combination of radio-wave and light-wave technology is essential to developing this spectral black hole.

As for the world of modern telecommunications, "optical" and "wireless" are the key words. Figure 11.2 shows how the bit rate in communications has been increasing for fiber-optic technologies, such as long-haul and Ethernet LANs, and wireless radio-wave technologies. It may be somewhat of an overstatement, but it seems as if both the fiber-optic and radio-wave communications technologies will reach the same performance target of several tens to 100 Gbps. Through ingenious intertwining of photonic technology and radio-wave technology, an infrastructure network for our information society is being established. Now, these technologies are starting to merge together through the use of high-speed photonic and radio-wave devices.

Progress in Key Component Technologies

As is well known, devices that convert optical signals to electrical signals and vice versa are the key components linking light-wave technology and radio-wave tech-

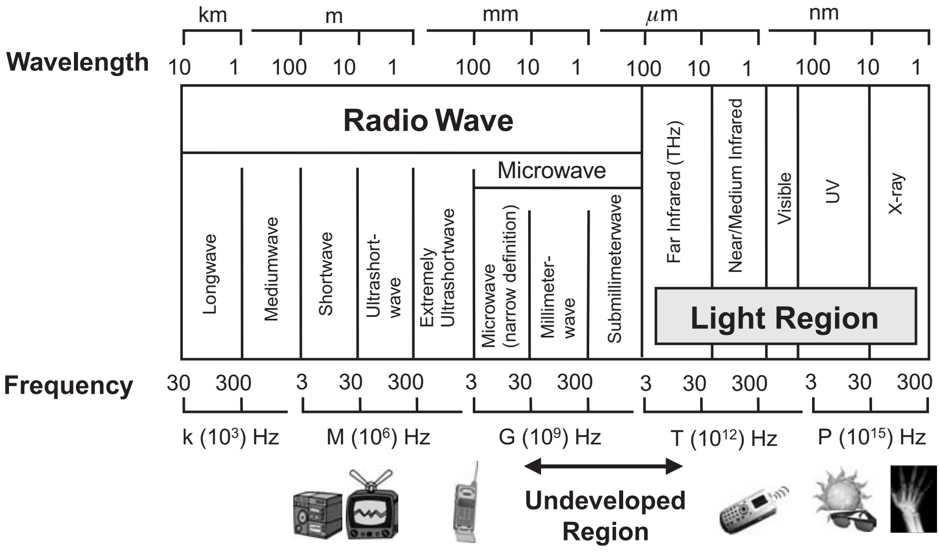

Figure 11.1 Wavelength and frequency of electromagnetic waves.

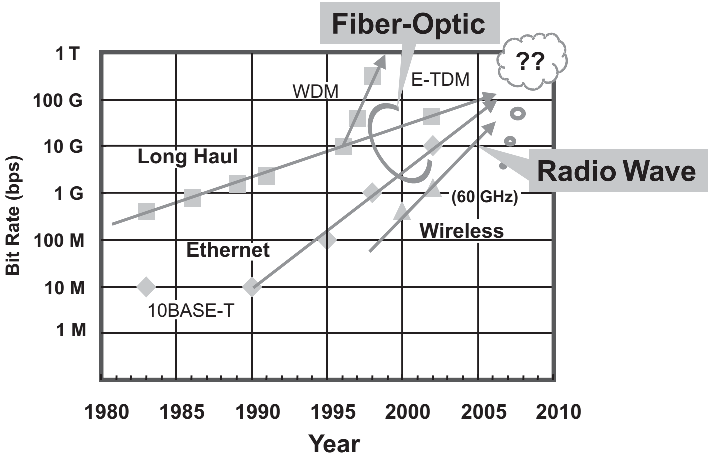

Figure 11.2 Evolution of fiber-optic and radio-wave communications.

nology, or in other words, photonics and electronics. As outlined in Figure 11.3, several physical phenomena involved in optical-electrical interactions play significant roles in realizing OE converters and optical modulators. In what follows, recent progress in device technologies is briefly reviewed.

The current research-level status of three key components, namely, lasers, modulators, and photodetectors, is summarized in Table 11.1. The optical subcarrier frequency is 30 GHz for direct modulation [5], over 100 GHz for actively mode-locked lasers, and in excess of 1 THz for passively mode-locked ones [6–9]. By means of heterodyne mixing, it's easy to generate THz optical signals, as long as we are not too concerned about stability [10–12]. As for external modulators, 50 GHz is now common for electro-optic (EO) and electroabsorption (EA) modulators [13, 14]. Two main issues for modulators are how to achieve operating frequencies of over 100 GHz [15] and how to reduce the driving voltage [16, 17]. There has also been marked progress in photodetectors [18–23]. At a wavelength of 1.55 μm, the 3-dB bandwidth now exceeds 300 GHz [22].

Optical MMW Sources

First, we the show generation of over-100-GHz optical MMW signals using semiconductor lasers. Figure 11.4 shows block diagrams of 120-GHz optical

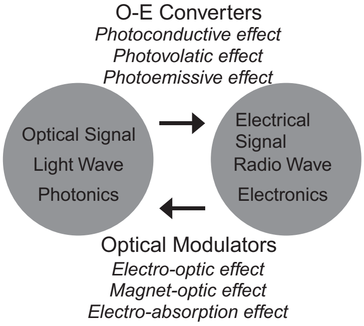

Figure 11.3 Optical-electrical interactions.

Table 11.1 Recent Photonic Component Technologies

Optical Sources: Lasers
Direct modulation: 30 GHz
Mode-locked lasers
Active: 100 GHz, passive: 1 THz
Heterodyne mixing: 1 THz
External Modulators
EO modulators
LN: 70 GHz, GaAs: 50 GHz, polymer: 110 GHz
EA modulators: 50 GHz
Photodetectors
MSM: 1 THz (short wavelength)
PIN: 300 GHz (long wavelength)

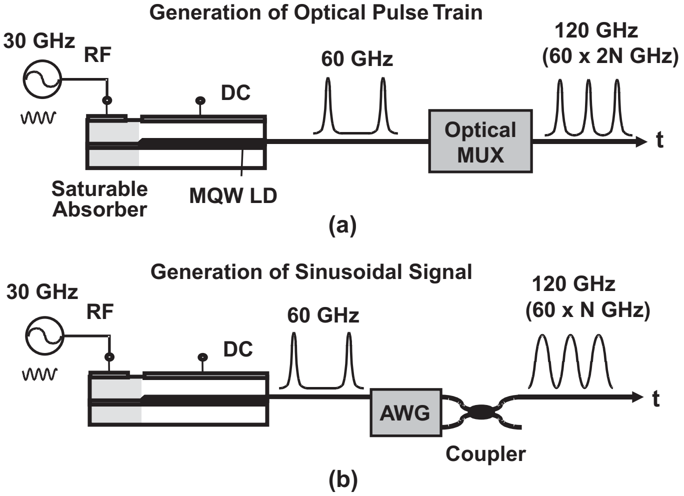

Figure 11.4 120-GHz active optical MMW sources. (a) Optical time-division multiplexing (O-MUX); (b) two-mode beat generation.

millimeter-wave sources made with actively mode-locked laser diodes. The optical signal is generated with a subharmonically mode-locked laser diode integrated with an EA modulator. The laser diode is driven at 30 GHz to generate the second harmonic at 60 GHz. To obtain 120-GHz signals, we employ two methods: optical multiplexing and two-mode beat signal generation with an arrayed waveguide grating (AWG) and a coupler. Electrical spectra of 120-GHz millimeter waves measured by converting the optical signals with the OE converter are shown in Figure 11.5. For both the optical multiplexing and two-mode beat generation, we obtained very clean, stable spectra; the RF linewidths are much smaller than 1 kHz.

Figure 11.6(a) shows another type of optical MMW source, which is a passively mode-locked laser. The relationship among the phases of a Fabry-Perot laser is not random, and subpicosecond pulses at 120 GHz are obtained when the dispersion is compensated for by using a single-mode fiber of appropriate length [24, 25]. Figure 11.6(b) shows autocorrelation traces of the laser with and without a fiber. Simply by driving the laser with a dc current source, we obtain a pulse width of 0.8 ps when the fiber is 15m long. The RF spectrum of a passive 120-GHz source is shown in Figure

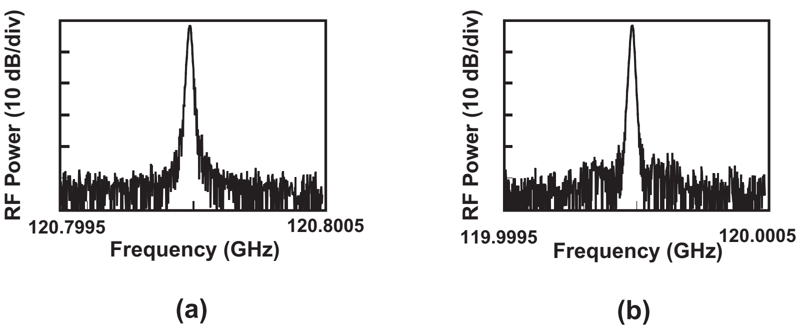

Figure 11.5 RF spectra of active 120-GHz MMW sources measured by converting optical signal to MMW with an emitter. (a) Optical multiplexing, (b) two-mode beat generation.

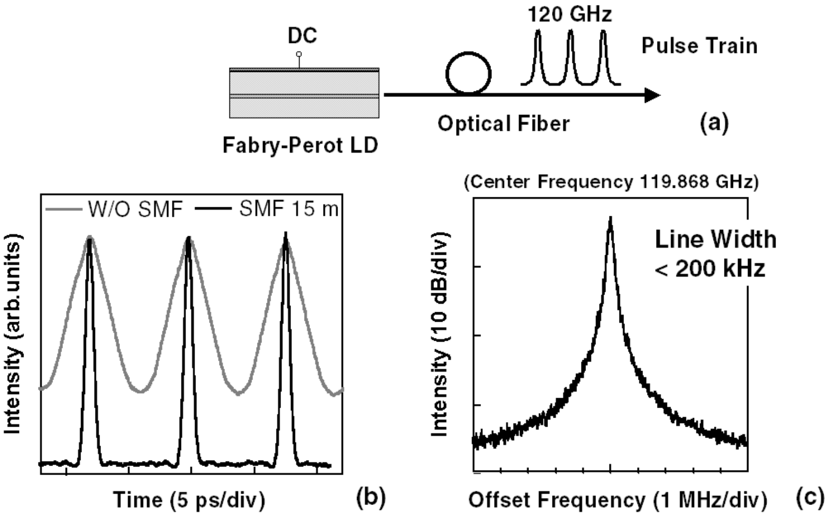

Figure 11.6 120-GHz passive optical MMW sources. (a) Configuration; (b) time-domain waveform; and (c) RF spectrum.

11.6(c). The line width of the source is less than 200 kHz without any stabilization. Also, the frequency drift of the source is less than 200 kHz over a period of one hour.

O-E Conversion Devices

Among the various types of OE conversion devices, the bandwidth and output power of p-i-n photodiodes have improved a great deal recently through the use of traveling-wave [18] and distributed structures [19] and novel carrier dynamics. An ultrafast one that has achieved the highest performance to date at a wavelength of 1.55 μm is called a unitraveling carrier photodiode, or UTC-PD [20–23].

Figure 11.7 shows a band diagram of the UTC-PD. The UTC-PD has a light absorption layer and a photocarrier collection layer. With this structure, only electrons are the active carriers. In addition, electrons exhibit velocity overshoot in the carrier collection layer, which is made of InP. Figure 11.8 shows the fastest pulse response of the UTC-PD to date [22]. The pulse width is 0.97 ps. By Fourier transforming the waveform, we obtain a corresponding 3-dB bandwidth of 310 GHz.

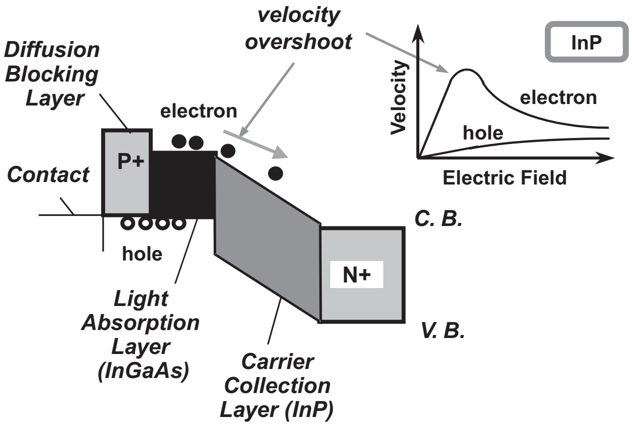

Figure 11.7 Band diagram of a unitraveling-carrier (UTC) photodiode.

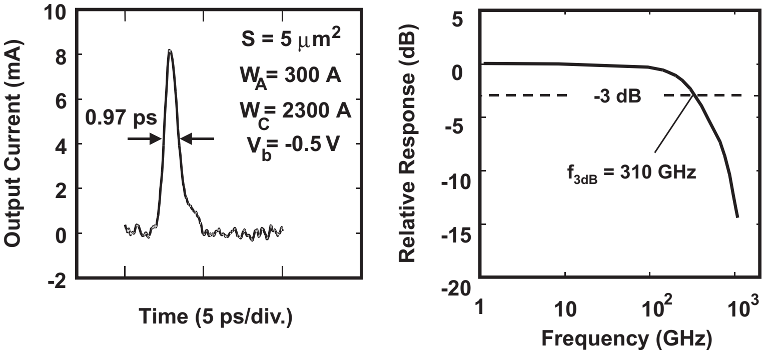

(a) (b)

Figure 11.8 Characterization of UTC-PD.(a) Time-domain waveform, (b) frequency response.

The device also exhibits a 10-dB bandwidth of 750 GHz, and a 15-dB bandwidth of 1 THz.

To achieve a higher output power at frequencies of over 100 GHz, we have designed and tested a photodiode with a resonating matching circuit [Figure 11.9(a)] [23]. This circuit overcomes the limitations imposed by the CR time constant. This device integrates a UTC-PD and a short-stub circuit consisting of a CPW and a MIM capacitor. Figure 11.9(b) shows the relationship between the millimeter-wave output power and the diode photocurrent at 100 GHz. The linearity is maintained over a wide range of up to 10 mW. A wide range like this is important for analog applications. The output power is 20.8 mW at a photocurrent of 25 mA. To our knowledge, this is the highest output power directly generated by a PD at frequencies in the millimeter-wave range.

Integrated MMW Emitter

By integrating the photodiode with a planar antenna in either a hybrid or monolithic fashion, we can make compact millimeter-wave emitters for free-space applications as schematically depicted in Figure 11.10.

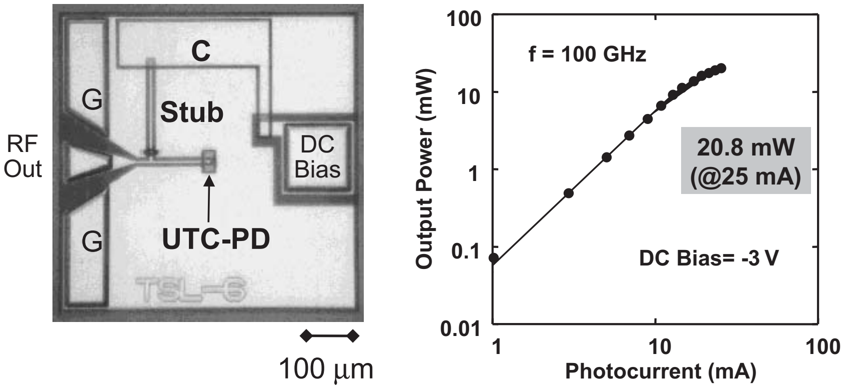

Figure 11.9 UTC-PD with matching circuit. (a) Photograph of IC chip; (b) output power against photocurrent.

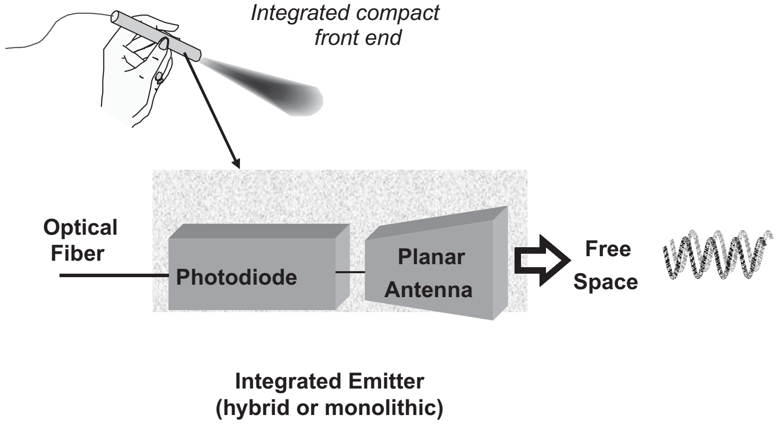

Figure 11.10 Integrated MMW emitter.

Figure 11.11 shows a millimeter-wave emitter made by hybrid integration [26]. The UTC-PD chip is a flip-chip mounted on a planar antenna, since it usually requires back-illumination. The antenna chip is bonded to a hemispherical silicon lens in order to collimate millimeter-wave signals in the direction opposite the illumination. For this emitter, we used a simple slot antenna made on a Si substrate.

We have examined the monolithic integration of an antenna and photodiode to make the MMW emitter smaller and more cost-effective. Figure 11.12(a) shows a Yagi-Uda antenna fabricated on an InP substrate [27]. This antenna radiates millimeter-waves in the direction parallel to the substrate. A patch antenna has been fabricated on a Si substrate as shown in Figure 11.12(b) [28]. Here, the UTC-PD is made on Si by a wafer-bonding process. This antenna radiates millimeter-waves in the direction perpendicular to the substrate. For a broadband emitter extending to submillimeter-wave regions, we have integrated the UTC-PD with a self-complementary log-periodic toothed planar antenna (Figure 11.13), whose teeth correspond to frequencies from 150 GHz to 2.4 THz [29]. The maximum output power from the device is 300 μW at 300 GHz.

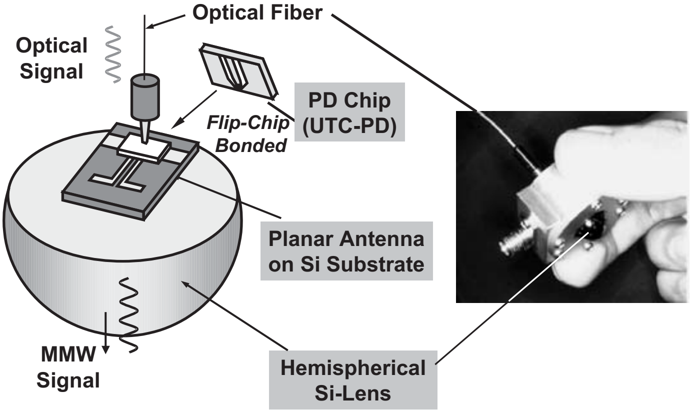

Figure 11.11 MMW emitter made by hybrid integration.

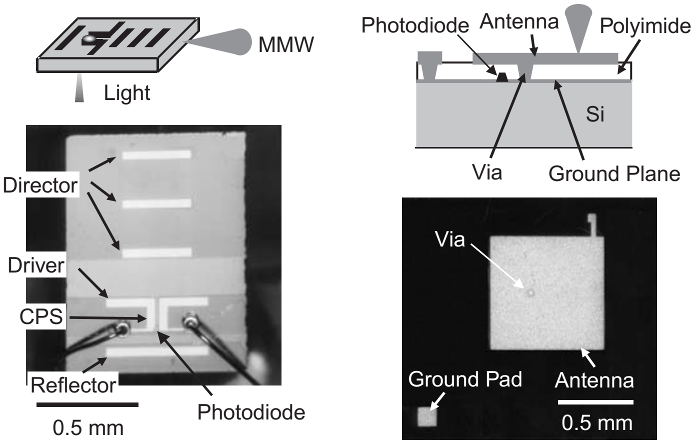

(a) (b)

Figure 11.12 MMW emitter made by monolithic integration. (a) Yagi-Uda antenna, (b) patch antenna.

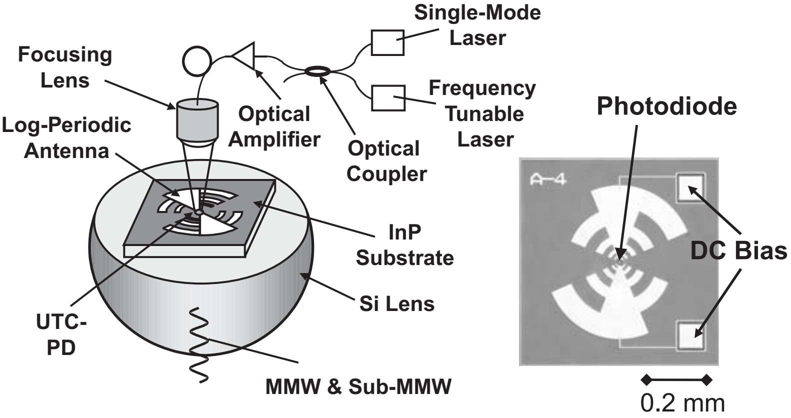

(a) (b)

Figure 11.13 Integration with log-periodic antenna. (a) Emitter configuration, (b) photograph of IC chip.

Communications Applications

In this section, we describe possible applications of these high-frequency components to a high-speed wireless link. Figure 11.14 shows the data rate of wired and wireless link systems. There is an increasing demand for higher data rates in wireless communications in order to keep up with the remarkable speed-up of LANs. The prospective data rates of wired LANs are 10 Gbps for Ethernet and 3.2 for IEEE 1394. On the other hand, currently available wireless LANs are still slow, and even for wireless 1394, the data rate will only be 1.6 Gbps.

One way to boost the wireless data rate is to use a free-space optical (FSO) link. An FSO link has already achieved a rate of 2.5 Gbps. However, it requires a bulky telescope-like positioning apparatus to align the beam. Another way is to use millimeter waves with a higher carrier frequency, and the 60-GHz band is now under intensive development. Figure 11.15 shows the attenuation of electromagnetic waves in the frequency range from 10 GHz to 1,000 THz [30]. There are several peaks of attenuation due to the absorption of water and oxygen in the millimeter-wave regions. The dashed line represents the attenuation by fog. In foggy conditions, the attenuation in the visible and near-infrared region is about two orders of magnitude higher than that in the millimeter-wave region. This indicates that FSO links are generally not very robust in foggy or hazy conditions when used outdoors.

The graph of data rate versus carrier frequency for a wireless link (Figure 11.16) shows that the rate increases with the frequency. From this empirical trend, it seems clear that one promising way of creating a 10-Gbps wireless link is to use millimeter waves at a frequency of over 100 GHz. This leads to the question: What is the best frequency band for communications from 100 GHz to 300 GHz? As shown in Figure 11.17, there are three valleys where the attenuation becomes local minimum. Also, considering frequency regulation issues in Japan, we have first chosen the band around the center frequency of 120 GHz. It is rather difficult for existing electronic techniques to handle such high frequencies. Photonic techniques are more suitable for handling over 100-GHz millimeter-wave signals than electronic techniques, because they have a larger bandwidth.

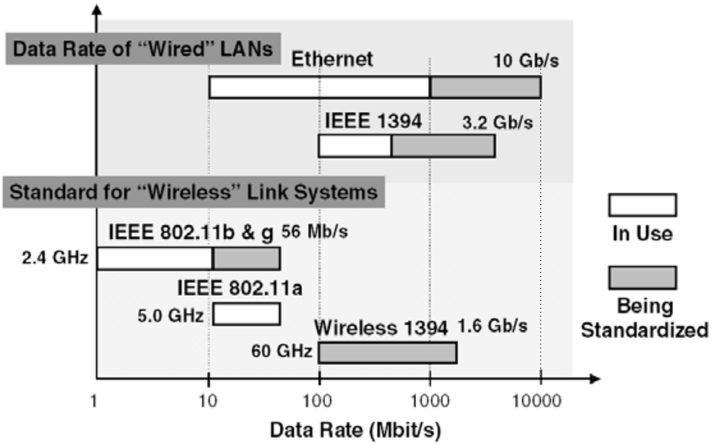

Figure 11.14 Demand for high-speed wireless LANs.

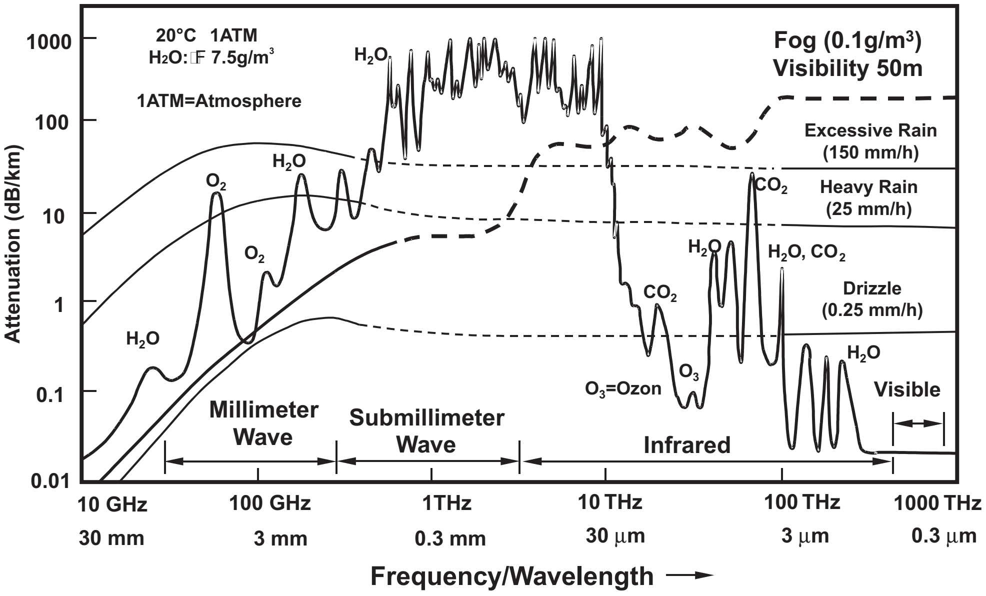

Figure 11.15 Attenuation: MMW versus NIR.

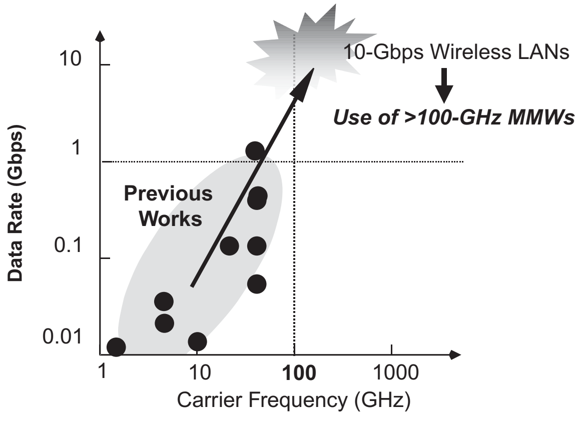

Figure 11.16 Data rate versus carrier frequency.

We have examined a 120-GHz millimeter-wave wireless link using a transmitter based on photonic techniques (Figure 11.18) [26, 31–33]. In the transmitter, optical millimeter-wave signals are generated at 120 GHz, modulated at a specific data rate, and amplified with an optical fiber amplifier. They are delivered through an optical fiber cable to an integrated emitter. As for the receiver, a millimeter-wave detector employing a Schottky-barrier diode is integrated with a planar antenna. It demodulates the signals by a simple envelope detection scheme.

Figure 11.19 is a schematic of the receiver [31]. The Schottky-barrier diode chip is flip-chip bonded on a uniplanar antenna. The antenna chip includes a slot-ring antenna and a coplanar waveguide filter. Just as for the emitter, a Si-lens is attached to the antenna chip to increase the directivity. The measured sensitivity and band-

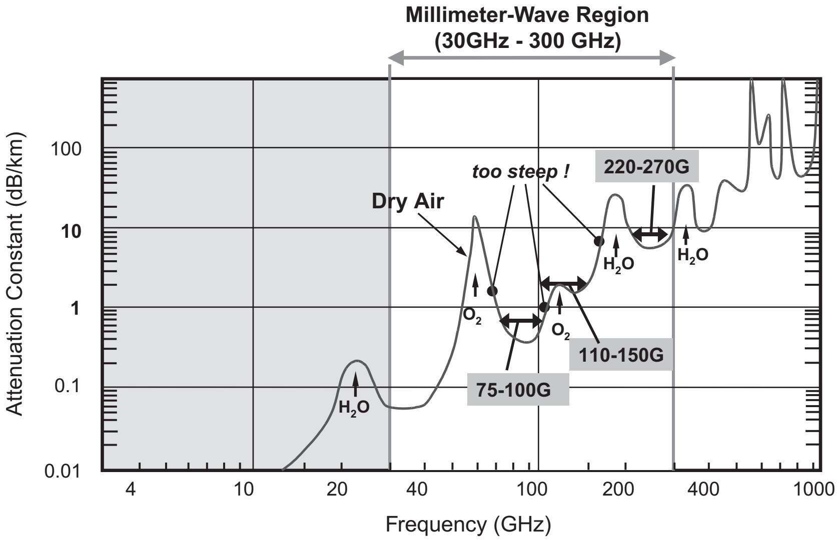

Figure 11.17 Choice of MMW bands.

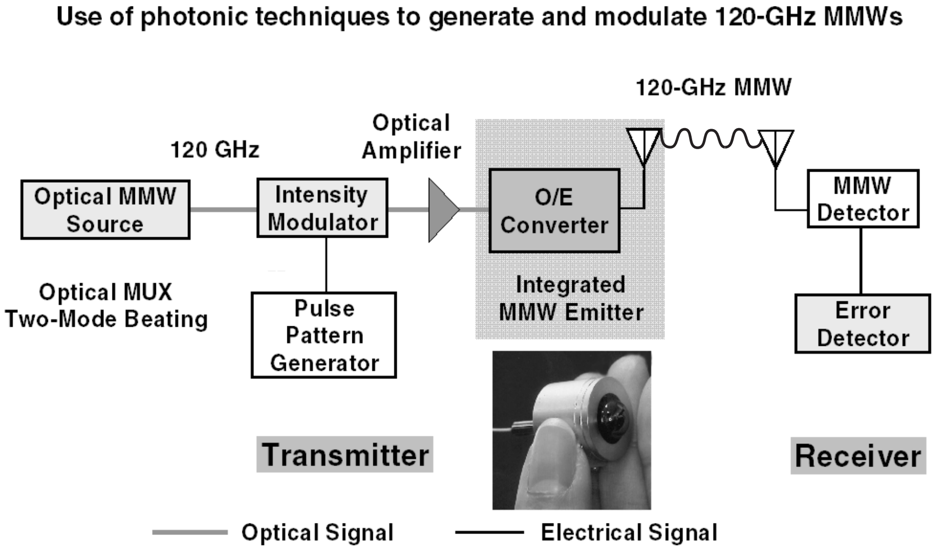

Figure 11.18 120-GHz wireless link based on photonics.

width of the receiver are shown in Figure 11.20, where the sensitivity is plotted as a function of the carrier frequency. The maximum sensitivity is about 200 V/W, and the effective occupied bandwidth is 25 GHz at the center frequency of 117 GHz. When the receiver is operated at 120 GHz, the 3-dB bandwidth is 8.5 GHz, which corresponds to a maximum bit rate of 11.3 Gbps. Figure 11.21 shows demodulated 10-Gbps pseudorandom bit stream data transmitted over the link. The eyes are clear and open. The bit error rate of the link is less than 10^{-10}. In other words, the transmission is error-free. This is the fastest transmission rate ever reported for wireless links.

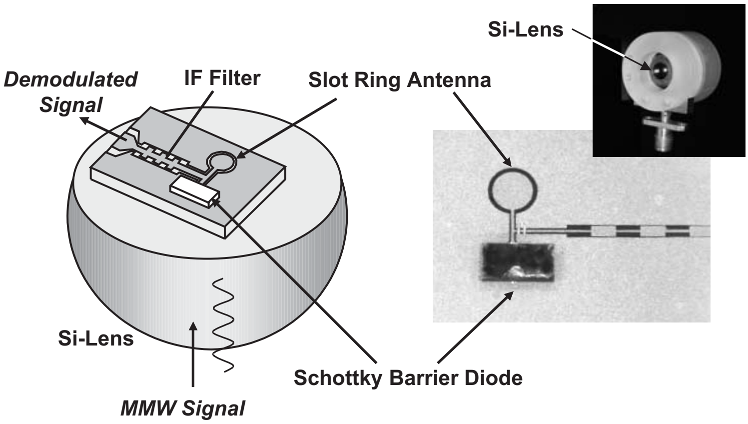

Figure 11.19 A 120-GHz integrated receiver.

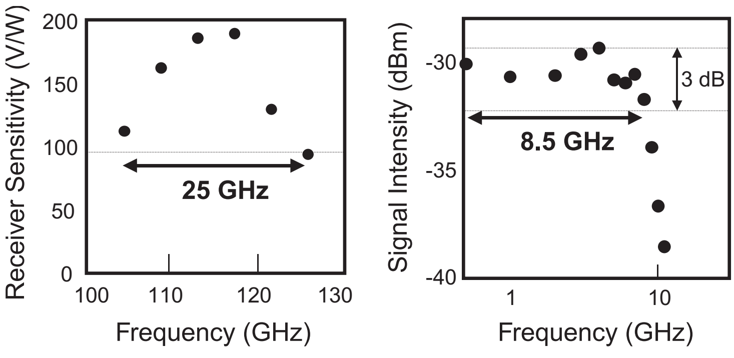

(a)

(b)

Figure 11.20 Receiver performance. (a) Receiver sensitivity; and (b) receiver bandwidth.

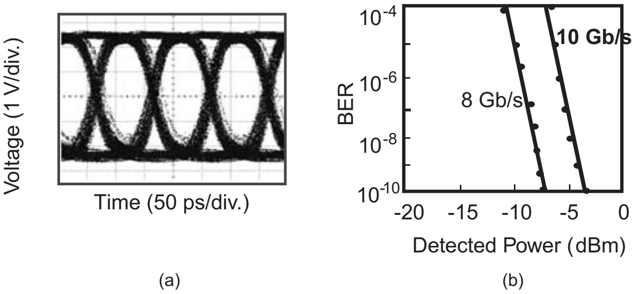

(a)

(b)

Figure 11.21 Wireless transmission experiments. (a) Eye diagram; and (b) BER characteristics.

Sensor Applications

Finally, we discuss sensor applications, focusing on the imaging of objects using high-frequency radio waves. Imaging techniques are needed in various fields, such as medicine, security, environmental measurement, and for the identification or recognition of humans and objects. Figure 11.22 shows the frequencies of the electromag-

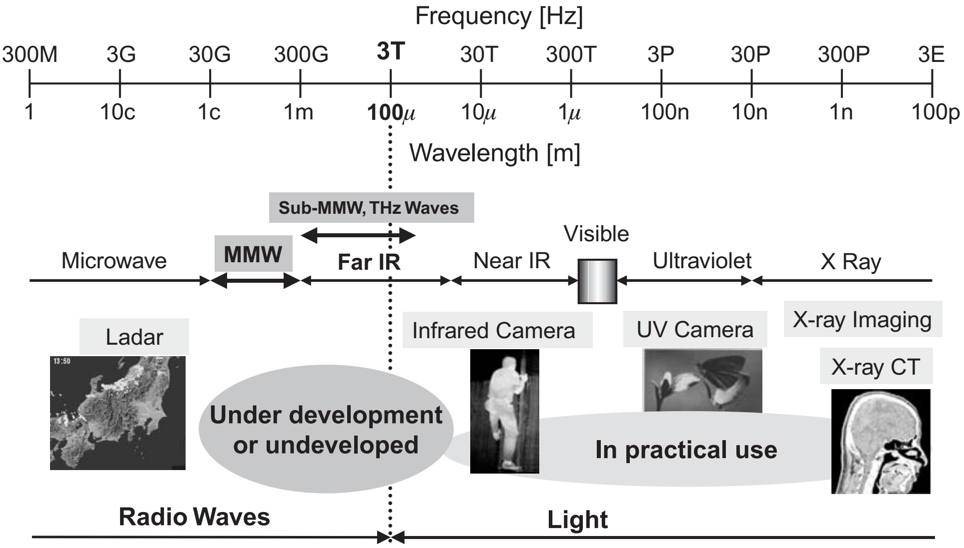

Figure 11.22 Imaging technologies and electromagnetic spectrum.

netic waves used in various imaging techniques. Imaging techniques using millimeter waves, submillimeter waves, and terahertz waves are now under intensive development.

Figure 11.23 shows a setup for imaging with millimeter waves. By using the photonic techniques described in the section entitled “Progress in Key Component Technologies,” widely tunable millimeter-wave emitters can be applied to illuminate the object. The waves transmitted through or reflected by the object are detected with an EO sensor. Possible areas of application are the inspection of materials and packages. Moreover, because electromagnetic waves in the frequency band from 100 GHz to 10 THz interact strongly with molecules and gases, there is an interest in applications in environmental measurement and medical measurement.

Figure 11.24 shows the operation principle and a photograph of the EO sensor for radio-wave signals [34, 35]. The polarization of the laser beam reflected from the bottom of an EO crystal, such as CdTe or KTP, changes with the intensity of the electric field coupled to the crystal. We have conducted some imaging experiments

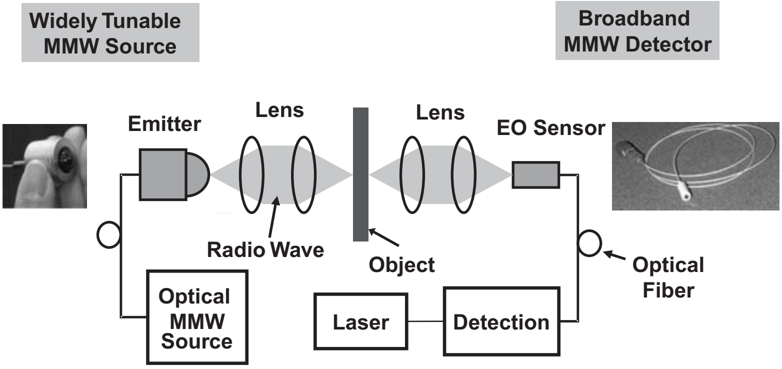

Figure 11.23 Millimeter-wave imaging.

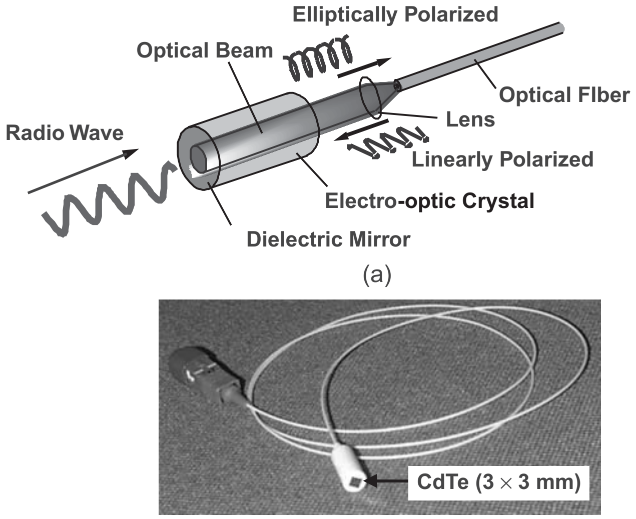

(a)

(b)

Figure 11.24 Optical detection of MMW signals. (a) Operation principle; and (b) photograph of EO sensor.

to investigate the resolution and sensitivity of the technique [36–38]. Figure 11.25 shows the 100-GHz millimeter-wave images of a floppy disk and small clippers in a purse. The technique provides a good view of these objects with a diffraction-limited resolution of about 3 mm. Figure 11.26 shows 180-GHz images of the inside of a card. With a special arrangement, we can obtain these images within 30 seconds. Further development is necessary in order to decrease the acquisition time and achieve real-time imaging.

In addition to the above active imaging, interesting results have recently been reported on passive imaging. The human body emits millimeter-wave signals as black-body radiation. Just by passively detecting these millimeter-wave signals, we can see people in a house through walls or concealed weapons through clothes [39].

The scale of radio-wave imaging is largest in radio astronomy. An ongoing international project, called ALMA (Atacama Large Millimeter/Submillimeter Array), aims to build a large millimeter and submillimeter interferometer array consisting of 64 parabolic antennas arranged over an area of 10 km^2 in northern Chile (Figure

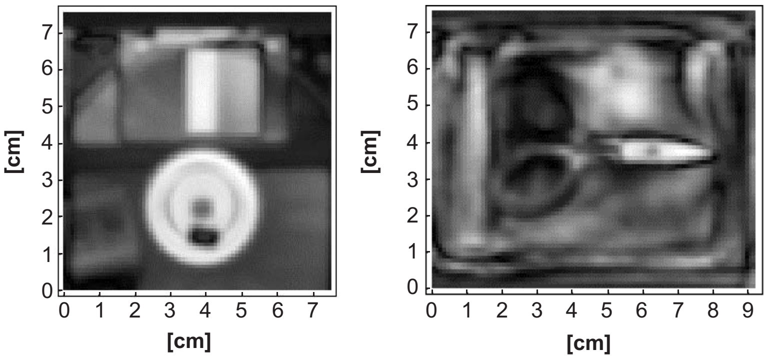

(a)

(b)

Figure 11.25 Example of MMW images. (a) Floppy disk; and (b) clippers inside a purse.

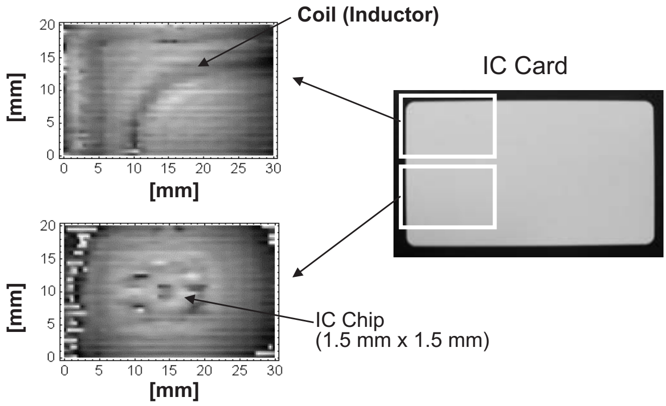

Figure 11.26 MMW images inside IC card.

11.27) [40]. From images of galaxies taken using various electromagnetic waves, such as visible, infrared, X-rays, and millimeter-wave and submillimeter-wave radio waves, we can obtain information about each stage in the evolution of stars (Figure 11.28). By using millimeter-wave and submillimeter-wave radio waves, we will be able to understand the initial stages of the formation of stars when they are still clouds of molecules and balls of gasses.

In the ALMA radio telescope, signals from the universe at frequencies from 30 to 950 GHz are detected with heterodyne receivers consisting of superconducting mixers and photonic local oscillators as shown in Figure 11.29. The 64 receivers have to be phase-locked to each other by means of local oscillator signals distributed by optical fiber cables. This requires a photodiode with an extremely large bandwidth.

We have tested our UTC-PD's ability to generate local oscillator signals for the mixer. We measured the receiver noise and compared it with that of a Gunn oscillator [41–43]. As shown in Figure 11.30, the noise temperature is almost the same for the photonic LO and Gunn LO: as low as 20 K. This indicates that the amplitude noise of photonically generated millimeter-wave signal is small enough for very highly sensitive radio astronomy applications. Most recently, we have succeeded in measuring actual signals form the universe using the photonic LO [44]. The combi-

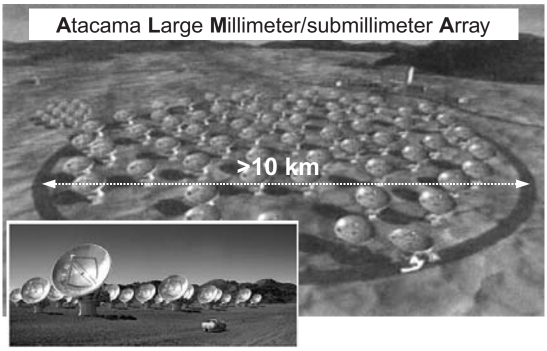

Figure 11.27 ALMA project.

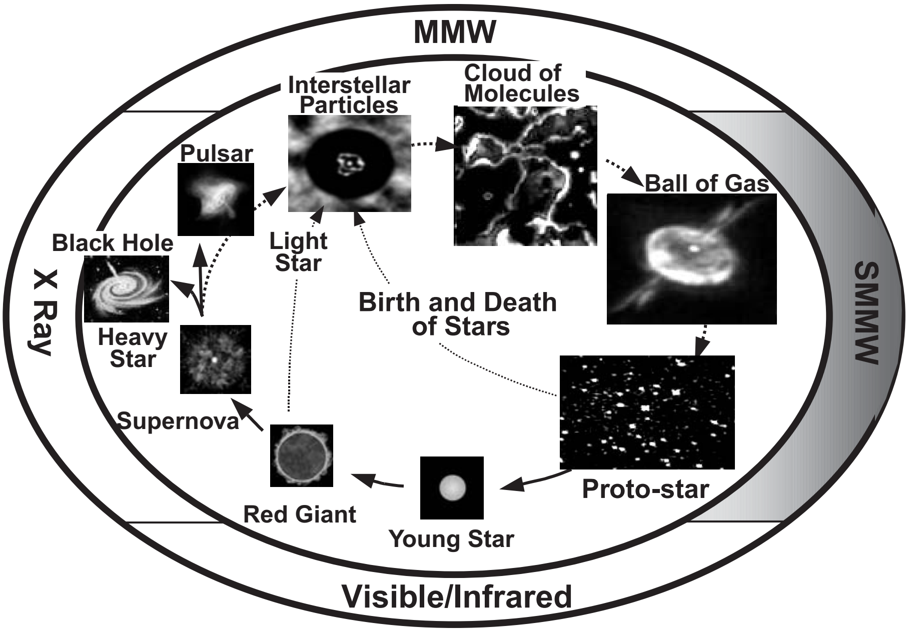

Figure 11.28 Evolution of stars.

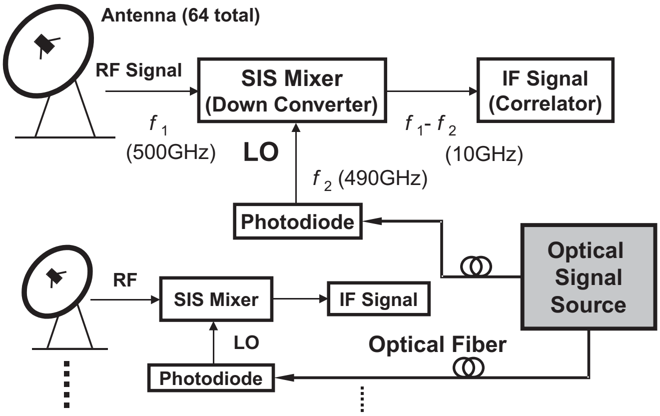

Figure 11.29 Photonically distributed local oscillator signals for superconducting receiver arrays.

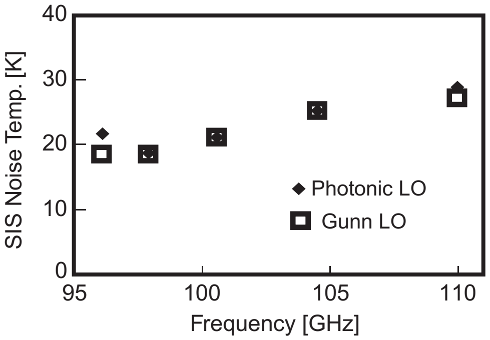

Figure 11.30 Comparison of noise temperature.

nation of millimeter-wave technologies with photonic technologies is now essential for advancing the science of the universe and Earth.

Conclusion

The fusion of “wireless” telecommunications technology and optical fiber “wired” telecommunications technology, as exemplified by radio-on-fiber [2, 45, 46], will continue to steadily advance in a form that will support the need for high speed and ubiquity in telecommunications. Technology for the optical generation and detection of radio waves will become essential for various fields of measurement, as it facilitates the handling of ultrahigh-frequency radio waves, which has been difficult with previous technology. Moreover, because electromagnetic waves in the frequency band from 100 GHz to 10 THz interact strongly with various molecules and gases, there is an interest in applications for environmental measurement and medical measurement. Millimeter-wave photonic technology is the foundation for such measurements, and will probably also serve as a tool for elucidating phenomena that involve the interaction of radio waves and matter.

In conclusion, we believe that the undeveloped frequency band, once harnessed, will lead to new technologies where, for example, antennas could be placed against the human body for medical sensing and for a kind of human interface. Millimeter-wave photonic technology is a key to realizing the dream of ubiquitous services (see Figure 11.31).

Acknowledgments

This research is a collaborative work by three laboratories at NTT, Microsystem Integration Laboratories, Photonics Laboratories, and Network Innovation Laboratories. The author would like to express his deepest appreciations to all the project members involved.

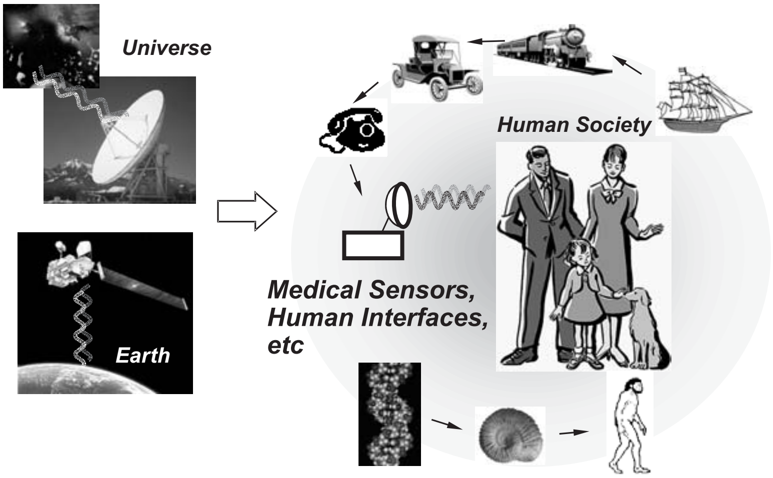

Figure 11.31 From science to human technology for ubiquitous IT services.

References

[1] *Technical Digest of International Topical Meeting on Microwave Photonics* (MWP), 1996: The first use of the term microwave photonics was at this international conference held at ATR (Kyoto) in December 1996. This MWP conference has subsequently been held yearly in the United States, Europe, and the Asian region.

[2] Seeds, A., "Microwave Photonics," *IEEE Trans. Microwave Theory and Tech.*, Vol. 50, No. 3, March 2002, pp. 877–887.

[3] Mizuno, H., "Millimeter-Wave Communication-Key Technologies and Features," *Tech. Digest of 2000 Topical Symposium on Millimeter Waves*, Yokosuka, Japan, 2000, pp. 19–22.

[4] Lawrence, A., "Millimeter-Wave ICs Open Up New Spectrum," *Compound Semiconductor*, Vol. 7, No. 4, May 2001, pp. 91–94.

[5] Sato, K., et al., "40 Gbit/s Direct Modulation of Distributed Feedback Laser for Very-Short-Reach Optical Links," *Electron. Lett.*, Vol. 38, No. 15, July 2002, pp. 816–817.

[6] Sato, K., et al., "High-Repetition Frequency Pulse Generation at 102 GHz Using Mode-Locked Lasers Integrated with Electroabsorption Modulators," *Electron. Lett.*, Vol. 34, No. 8, August 1998, pp. 790–792.

[7] Yanson, D. A., et al. "Ultrafast Harmonic Mode-Locking of Monolithic Compound-Cavity Laser Diodes Incorporating Photonic Bandgap Reflectors," *IEEE J. Quantum Electronics*, Vol. 38, No. 1, January 2002, pp. 1–11.

[8] Arahira, S., et al., "Stabilization and Timing Jitter Reduction of 160-GHz Colliding-Pulse Mode-Locked Laser Diode by Subharmonic-Frequency Optical Pulse Injection," *IEICE Trans. Electron.*, Vol. E83-C, No. 6, June 2000, pp. 966–973.

[9] Wen, Y. J., et al., "Generation of 140-GHz Optical Pulses with Suppressed Amplitude Modulation by Subharmonic Synchronous Modelocking of Fabry-Perot Semiconductor Laser," *Electron. Lett.*, Vol. 37, No. 9, April 2001, pp. 581–582.

[10] Payne, J., B. Shillue, and A. Vaccari, "Photonic Techniques for use on the Atacama Large Millimeter Array," *Tech. Dig. Microwave Photonics 1999*, Melbourne, Australia, November 1999, pp. 105–108.

[11] Swanson, E. A., et al., "100-GHz Soliton Pulse Train Generation Using Soliton Compression of Two Phase Side Bands from a Single DFB Laser," *IEEE Photon. Technol. Lett.*, Vol. 6, No. 10, October 1994, pp. 1194–1196.

[12] Gough, O. P., C. F. C. Silvia, and A. J. Seeds, "Exact Millimeter-Wave Frequency Synthesis by Injection Locked Laser Comb Line Selection," *Tech. Dig. Microwave Photonics 1999*, Melbourne, Australia, November 1999, pp. 61–64.

[13] Noguchi, K., H. Miyazawa, and O. Mitomi, "75 GHz Broadband Ti:LiNbO$_3$ Optical Modulator with Ridge Structure," *Electron. Lett.*, Vol. 30, No. 12, June 1994, pp. 949–951.

[14] Kawano, K., et al., "Polarisation-Insensitive Traveling-Wave Electrode Electroabsorption (TW-EA) Modulator with Bandwidth over 50 GHz and Driving Voltage Less Than 2 V," *Electron. Lett.*, Vol. 33, No. 18, August 1997, pp. 1580–1581.

[15] Chen, D., et al., "Demonstration of 110 GHz Electro-Optic Polymer Modulators," *Appl. Phys. Lett.*, Vol. 70, No. 25, June 1997, pp. 3335–3337.

[16] Nakazawa, T., "Low Drive Voltage and Broad-Band LiNbO3 Modulator," *Tech. Dig. Microwave Photonics 2002*, Awaji, Japan, November 2002, pp. 45–48.

[17] Toyoda, S., et al., "Low-Driving-Voltage Electro-Optic Modulator with Nobel KTN Crystal Waveguides," *Tech. Dig. 9th Microoptics Conference (MOC'03),* J3, Odaiba, Tokyo, Japan, October 2003.

[18] Stöhr, A., et al., "Ultra-Broadband Ka to W-Band 1.55-μm Travelling-Wave Photomixer," *Electron. Lett.*, Vol. 36, No. 11, May 2000, pp. 970–971.

[19] Chau, T., et al., "Generation of Millimeter Waves by Photomixing at 1.55 mm Using InGaAs-InAIAs-InP Velocity-Matched Distributed Photodetectors," *IEEE Photon. Technol. Lett.*, Vol. 12, No. 8, August 2000, pp. 1055–1057.

[20] Ishibashi, T., et al., "Uni-Travelling-Carrier Photodiodes," *Tech. Dig. Ultrafast Electron. Optoelectron.*, 1997, pp. 83–87.

[21] Ishibashi, T., et al., "InP/InGaAs Uni-Travelling-Carrier Photodiodes," *IEICE Trans. Electron.*, Vol. E83-C, No. 6, June 2000, pp. 938–949.

[22] Ito, H., et al., "InP/InGaAs Uni-Travelling-Carrier Photodiode with 310-GHz Bandwidth," *Electron. Lett.*, Vol. 36, No. 21, October 2000, pp. 1809–1810.

[23] Ito, H., et al., "High-Power Photonic Millimeter-Wave Generation at 100 GHz Using Matching-Circuit-Integrated Uni-Travelling-Carrier Photodiodes," *IEE Proc. Optoelectron.*, Vol. 150, No. 2, April 2003, pp. 138–145.

[24] Sato, K., "100GHz Optical Pulse Generation Using Fabry-Perot Laser Under Continuous Wave Operation," *Electron. Lett.*, Vol. 37, No. 12, June 2001, pp. 763–764.

[25] Hirata, A., et al., "Low-Cost Millimeter-Wave Photonic Techniques for Gigabit/s Wireless Link," *IEICE Trans. Electron.*, Vol. E86-C, No.7, July 2003, pp. 1123–1128.

[26] Hirata, A., H. Ishii, and T. Nagatsuma, "Design and Characterization of a 120-GHz Millimeter-Wave Antenna for Integrated Photonic Transmitter," *IEEE Trans. Microwave Theory and Tech.*, Vol. 49, No. 11, November 2001, pp. 2157–2162.

[27] Hirata, A., T. Furuta, and T. Nagatsuma, "Monolithically Integrated Yagi-Uda Antenna for Photonic Emitter Operating at 120GHz," *Electron. Lett.*, Vol. 37, 2001, pp. 1–2.

[28] Hirata, A., T. Minotani, and T. Nagatsuma, "A 120GHz Microstrip Antenna Monolithically Integrated with a Photodiode on Si," *Jpn. J. Appl. Phys.*, Vol. 41, No. 3A, March 2002, pp. 1390–1394.

[29] Hirata, A., et al., "Output Power Measurement of Photonic Millimetre-Wave and Sub-Millimetre-Wave Emitter at 100-800 GHz," *Electron. Lett.*, Vol. 38, No. 15, July 2002, pp. 798–800.

[30] CCIR Report 721-2, *Attenuation by Hydrometers in Particular Precipitation, and Other Atmospheric Particles,* Geneva, Switzerland, 1986.

[31] Minotani, T., A. Hirata, and T. Nagatsuma, "A Broadband 120-GHz Schottky-Diode Receiver for 10-Gbit/s Wireless Links," *IEICE Trans. Electron.*, Vol. E86-C, No. 8, August 2003, pp. 1501–1505.

[32] Hirata, A., et al., "Hight-Directivity Photonic Emitter for 10-Gbit/s Wireless Link," *Tech. Dig. Microwave Photonics 2003*, Budapest, Hungary, September 2003, pp. 35–38.

[33] Hirata, A., M. Harada, and T. Nagatsuma, "120-GHz Wireless Link Using Photonic Techniques for Generation, Modulation, and Emission of Millimeter-Wave Signals," *J. Lightwave Technology*, Vol. 21, No. 10, October 2003, pp. 2145–2153.

[34] Nagatsuma, T., "Measurement of High-Speed Devices and Integrated Circuits Using Electro-Optic Sampling Techniques," *IEICE Trans. Electron.*, Vol. E76-C, 1993, pp. 55–63.

[35] Nagatsuma, T., et al., "1.55-μm Photonic Systems for Microwave and Millimeter-Wave Measurement," *IEEE Trans. Microwave Theory and Tech.*, Vol. 49, No. 10, October 2001, pp. 1831–1839.

[36] Sasaki, A., and T. Nagatsuma, "Millimeter-Wave Imaging Using an Electrooptic Detector as a Harmonic Mixer," *IEEE J. Selected Topics Quantum Electron.*, Vol. 6, No. 5, September 2000, pp. 735–740.

[37] Sasaki, A., and T. Nagatsuma, "Reflection-Type CW-Millimeter-Wave Imaging with a High-Sensitivity Waveguide-Mounted Electro-Optic Sensor," *Jpn. J. Appl. Phys.*, Vol. 41, January 2002, pp. L83–L86.

[38] Sasaki, A., and T. Nagatsuma, "Electric-Field Scanning System Using Electro-Optic Sensor," *IEICE Trans. Electron.*, Vol. E86-C, No. 7, July 2003, pp. 1345–1351.

[39] Yujiri, L., M. Shoucri, and P. Moffa, "Passive Millimeter-Wave Imaging," *IEEE Microwave Magazine*, Vol. 4, No. 3, September 2003, pp. 39–50.

[40] Payne, J. M., and W. P. Shillue, "Photonic Techniques for Local Oscillator Generation and Distribution in Millimeter-Wave Radio Astronomy," *Tech. Dig. Microwave Photonics 2002*, W1-3, Awaji, Japan, November 2002, pp. 9–12.

[41] Ito, H., et al., "W-Band Uni-Travelling-Carrier Photodiode Module for a Photonic Local Oscillator," *Electron. Lett.*, Vol. 38, No. 22, October 2002, pp. 1376–1377.

[42] Ueda, A., et al., "W-Band Waveguide Photomixer Using a Uni-Traveling-Carrier Photodiode with 2-mW Output," *IEEE Trans. Microwave Theory and Tech.,* Vol. 51, No. 5, May 2003, pp. 1455–1459.

[43] Ueda, A,.et al., "Ultra-Low Noise Photonic Local Oscillator at 100 GHz," *Jpn. J. Appl. Phys.*, Vol. 42, No. 6B, June 2003, pp. L704–L705.

[44] Takano, S., et al., "The First Radioastronomical Observation with Photonic Local Oscillator," *Publ. Astron. Soc. Japan*, Vol. 55, June 2003, pp. L53–L56.

[45] Shoji, Y., and H. Ogawa, "Experimental Demonstration of 622 Mbps Millimeter-Wave Over Fiber Link for Broadband Fixed Wireless Access System," *IEICE Trans. Electron.*, Vol. E86-C, No. 7, July 2003, pp. 1129–1137.

[46] Lim, C., et al., "Capacity Analysis and the Merging of a WDM Ring Fiber-Radio Backbone Incorporating Wavelength Interleaving with a Sectorized Antenna Interface," *IEICE Trans. Electron.*, Vol. E86-C, No. 7, July 2003, pp. 1184–1190.

About the Editors

Shoichi Sudo received a B.S. in electronic engineering from the University of Kanazawa in 1974. Since joining NTT Laboratories in 1974, he has mainly been engaged in research on optical fiber fabrication technology. In 1977 he and his colleagues proposed and developed a new fiber preform fabrication method named the vapor-phase axial deposition (VAD) method. Nowadays the VAD method is one of the standard methods for optical fiber fabrication along with the MCVD method and the OVD method. In 1982 he was awarded a Ph.D. from the University of Tokyo for his VAD work. In 1983 he was appointed as a manager in the Research Planning Department. After 2 years of management work, he resumed his work as a researcher and in 1985 began research on the fabrication of efficient nonlinear optical fibers and their applications. From 1986 to 1987 he was a visiting scholar at Stanford University and engaged in research on single-crystal fibers and their nonlinear device application in Bob Byer's group. After returning to NTT in 1987, he engaged in the research field of nonlinear optical devices including single-crystal fiber devices for SHG and amplification, short pulse generation by modulation instability in silica fibers, and nonlinear couplers. In 1988, while he expanded his research on nonlinear optical devices, he started research on the frequency stabilization of semiconductor laser diodes. Research in that area led to the development of laser diode frequency stabilization scheme using acetylene gas absorption lines. In 1990, he was appointed as a senior manager of NTT Opto-Electronics Laboratories, responsible for research planning and the budget. In 1992, he returned to research as a group leader in the field of optical fiber amplifiers. He placed emphasis on the research and development of 1.3-μm praseodymium-doped fiber amplifiers (PDFAs) and 1.5-μm broadband erbium-doped fiber amplifiers (EDFAs), and also studied various combinations of active ions and host glasses for fiber amplifier use/application. He was appointed the executive manager of the Research Planning Department of NTT Opto-Electronics Laboratories in 1996, and the executive manager of the planning department of NTT Science and Core Technology Laboratories in 1999. From 2001 to 2002, he was a vice president of NTT Electronics Corporation. He is currently the director of NTT Microsystem Integration Laboratories.

Dr. Sudo is a Fellow of the IEEE, a vice president of the IEEE/LEOS, and a member of the Board of Governors of the Institute of Electronics, Information, and Communication Engineers of Japan (IEICE), the Japan Society of Applied Physics, and Optical Society of America. He has been involved in society activities including serving as a program committee member for IPR'91, OEC'92, IOOC'95, CLEO/PR'95, CLEO'94-'96, ECOC'00-'03, and APOC'00-'01, and serving as a international liaison for OFC'96-'98. He also served as a editor-in-chief of *IEICE Technical Papers*. He is a recipient of the 1979 IECE Young Engineers Awards, the 1980 IECE Paper Awards, the 1982 NTT President Awards, the 1982 Kajii Awards, the 1995 IEICE Paper Awards, the 2001 IEICE Distinguished Achievement Awards, and the 2001 Ministry of Education and Science Awards.

Dr. Sudo has published 5 books and more than 100 journal articles and has presented over 150 technical talks, including 10 invited presentations and one tutorial. He has filed over 350 patents and has been granted over 100 patents, including U.S. patents.

Katsunari Okamoto received a B.S., an M.S., and a Ph.D. in electronics engineering from Tokyo University, Tokyo, Japan, in 1972, 1974, and 1977, respectively. He joined the Ibaraki Electrical Communication Laboratory, Nippon Telegraph and Telephone Corporation, Ibaraki, Japan, in 1977, and was engaged in the research on transmission characteristics of multimode, dispersion-flattened single-mode, single-polarization (PANDA) fibers and fiber-optic components. He proposed for the first time the dispersion-flattened fiber (DFF) and succeeded in a fabrication of DFF that had a chromatic dispersion of less than ±1 ps/km/nm over a wide spectral range. Since 1990, he has been working on the analysis and the synthesis of guided-wave devices, the computer-aided-design and fabrication of silica-based planar lightwave circuits (PLCs) at the Ibaraki R&D Center, NTT Photonics Laboratories. He has developed a 256×256 star coupler, various kinds of AWGs ranging from 8ch-50nm spacing AWGs to 128ch-25GHz AWGs, flat spectral response AWGs, and integrated-optic reconfigurable add/drop multiplexers.

In 2003, he started Okamoto Laboratory Ltd., a R&D consulting company that deals with the custom design of functional planar lightwave circuits. He has published more than 210 papers in technical journals and international conferences. He has authored and coauthored eight books, including *Fundamentals of Optical Waveguides*. Dr. Okamoto is a member of the Institute of Electrical and Electronics Engineers, and the Institute of Electronics Information and Communication Engineers of Japan.

Index

Recent Titles in the Artech House Optoelectronics Library

Brian Culshaw and Alan Rogers, Series Editors

Chemical and Biochemical Sensing with Optical Fibers and Waveguides, Gilbert Boisdé and Alan Harmer

*Coherent and Nonlinear Lightwave Communication*s, Milorad Cvijetic

Coherent Lightwave Communication Systems, Shiro Ryu

DWDM Fundamentals, Components, and Applications, Jean-Pierre Laude

Frequency Stabilization of Semiconductor Laser Diodes, Tetsuhiko Ikegami, Shoichi Sudo, and Yoshihisa Sakai

Fiber Bragg Gratings: Fundamentals and Applications in Telecommunications and Sensing, Andrea Othonos and Kyriacos Kalli

Handbook of Distributed Feedback Laser Diodes, Geert Morthier and Patrick Vankwikelberge

Helmet-Mounted Displays and Sights, Mordekhai Velger

Introduction to Infrared and Electro-Optical Systems, Ronald G. Driggers, Paul Cox, and Timothy Edwards

Introduction to Lightwave Communication Systems, Rajappa Papannareddy

Introduction to Semiconductor Integrated Optics, Hans P. Zappe

LC3D: Liquid Crystal 3-D Director Simulator, Software and Technology Guide, James E. Anderson, Philip E. Watson, and Philip J. Bos

Liquid Crystal Devices: Physics and Applications, Vladimir G. Chigrinov

New Photonics Technologies for the Information Age: The Dream of Ubiquitous Services, Shoichi Sudo and Katsunari Okamoto, editors

Optical Document Security, Second Edition, Rudolf L. van Renesse, editor

Optical FDM Network Technologies, Kiyoshi Nosu

Optical Fiber Amplifiers: Materials, Devices, and Applications, Shoichi Sudo, editor

Optical Fiber Communication Systems, Leonid Kazovsky, Sergio Benedetto, and Alan Willner

Optical Fiber Sensors, Volume Three: Components and Subsystems, John Dakin and Brian Culshaw, editors

Optical Fiber Sensors, Volume Four: Applications, Analysis, and Future Trends, John Dakin and Brian Culshaw, editors

Optical Measurement Techniques and Applications, Pramod Rastogi

Optical Transmission Systems Engineering, Milorad Cvijetic

Optoelectronic Techniques for Microwave and Millimeter-Wave Engineering, William M. Robertson

Reliability and Degradation of III-V Optical Devices, Osamu Ueda

Smart Structures and Materials, Brian Culshaw

Surveillance and Reconnaissance Imaging Systems: Modeling and Performance Prediction, Jon C. Leachtenauer and Ronald G. Driggers

Understanding Optical Fiber Communications, Alan Rogers

Wavelength Division Multiple Access Optical Networks, Andrea Borella, Giovanni Cancellieri, and Franco Chiaraluce

For further information on these and other Artech House titles, including previously considered out-of-print books now available through our In-Print-Forever® (IPF®) program, contact:

Artech House
685 Canton Street
Norwood, MA 02062
Phone: 781-769-9750
Fax: 781-769-6334
e-mail: artech@artechhouse.com

Artech House
46 Gillingham Street
London SW1V 1AH UK
Phone: +44 (0)20 7596-8750
Fax: +44 (0)20 7630-0166
e-mail: artech-uk@artechhouse.com

Find us on the World Wide Web at: www.artechhouse.com